TYPE 2 ISOPENTENYL DIPHOSPHATE:DIMETHYLALLYL DIPHOSPHATE ISOMERASE AND OTHER ISOPRENOID BIOSYNTHETIC ENZYMES STUDIED WITH CHEMICAL AND STATISTICAL METHODS

by

Matthew Walter Janczak

A dissertation submitted to the faculty of
The University of Utah
in partial fulfillment of the requirements for the degree of

Doctor of Philosophy

Department of Chemistry

The University of Utah

December 2014

The University of Utah Graduate School

STATEMENT OF DISSERTATION APPROVAL

The dissertation of **Matthew Walter Janczak**

has been approved by the following supervisory committee members:

C. Dale Poulter	, Chair	**12-19-2013** Date Approved
Kenneth J. Woycechowsky	, Member	**12-19-2013** Date Approved
Jennifer M. Heemstra	, Member	**12-19-2013** Date Approved
Gary E. Keck	, Member	**12-19-2013** Date Approved
Eric W. Schmidt	, Member	**12-19-2013** Date Approved

and by **Cynthia J. Burrows** , Chair/Dean of

the Department/College/School of **Chemistry**

and by David B. Kieda, Dean of The Graduate School.

ABSTRACT

Type 2 isopentenyl diphosphate:dimethylallyl diphosphate isomerase (IDI-2) catalyzes the reversible conversion of isopentenyl diphosphate (IPP) to dimethylallyl diphosphate (DMAPP). The enzyme requires a divalent cation (Mg^{2+}) and a reduced flavin mononucleotide (FMN_{red}) cofactor to be catalytically active. To probe the role of FMN_{red}, substrate analogues were incubated with enzyme-bound FMN_{red} and analyzed under various conditions by UV-vis absorption and fluorescence spectroscopy. The spectral characteristics indicated a covalent bond was formed between the analogues and flavin at either the C4a- or N5-position (dependent on the substrate analogues). Similar methodology was applied to study a flavin adduct that formed when IDI-2 was incubated with IPP or DMAPP. Furthermore, mass spectrometry demonstrated that this adduct was the result of a loss of inorganic diphosphate and yielded a single isoprene unit addition to flavin. Bond formation observed with many analogues and the natural substrates supports a role where flavin is involved with catalysis directly as a proton donor/acceptor and/or as a stabilizer of an intermediate.

Additionally, the kinetic mechanism was established for the apo form of *Streptococcus pneumoniae* IDI-2, a potential antibacterial drug target. Bisubstrate studies (where IPP and FMN were varied) and competitive inhibition experiments (with a competitive inhibitor of both substrates) were employed to determine an ordered sequential mechanism, where FMN binds first. The kinetic data appeared sigmoidal and

could only be fit when Hill coefficients where included in the mathematical models, particularly for FMN. The Hill coefficients were thoroughly evaluated statistically and their inclusion was determined to be significant, thus a possible cooperative or allosteric effect occurs upon the binding of FMN. These experiments suggest that allosteric inhibitors could be investigated to inactivate the *S. pneumoniae* IDI-2 enzyme.

In a different application of statistics, transient kinetic isotope effect studies were evaluated using the bootstrap statistical technique. While statistically significant isotope effects were determined, the values were 100 % larger than expected. Thus, the technique was successful and identified an underlying problem with the experimental design during data collection.

TABLE OF CONTENTS

CHAPTER

APPENDICES

LIST OF TABLES

Table Page

LIST OF FIGURES

LIST OF ABBREVATIONS

AACT	Acetoacetyl-CoA thiolase
ALS	Alternating least squares
BCa	Bias-corrected accelerated
BCA	Bicinchoninic acid
Bis-TBS	Bis-TRIS buffered saline
Bis-TRIS	2,2-Bis(hydroxymethyl)-2,2',2"-nitriloethanol
BSA	Bovine serum albumin
C.I.	Confidence interval
cIPP	3-Cyclopropyl-3-buten-1-yl diphosphate
5-DeazaFMN	5-Carba-5-deaza-FMN
DFT	Density functional theory
DMAPP	Dimethylallyl diphosphate
DNA	Deoxyribonucleic acid
DPM	Disintegrations per minute
DXP	1-Deoxyxyluluose 5-phosphate
DXR	DXP reductoisomerase
DXS	DXP synthase
EDTA	Ethylenediamine tetraacetic acid
eIPP	Racemic 3,4-oxido-3-methyl-1-butyl diphosphate

ESI-MS	Electron spray ionization-mass spectrometry
FAD	Flavin-adenine dinucleotide
Fl	Flavin
^{1}Fl	Singlet state of flavin
^{3}Fl	Triplet state of flavin
Fl_{ox}	Oxidized flavin
fmIPP	3-Fluoromethyl-3-buten-1-yl diphosphate
FMN	Flavin mononucleotide
FMN_{ox}	Oxidized flavin mononucleotide
FMN_{red}	Fully reduced flavin mononucleotide
FPP	Farnesyl diphosphate
FPPase	Farnesyl diphosphate synthase
G3P	Glyceraldehyde 3-phosphate
GC	Gas chromatography
GPP	Geranyl diphosphate
GTPase	Guanosine triphosphate isomerase
H_2Fl	Dihydroflavin
HEPES	4-(2-Hydroxyethyl)-1-piperazineethanesulfonic acid
HMG-CoA	β-Hydroxy-β-methylglutaryl-CoA
HMGR	3-Hydroxy-3-methylglutaryl-CoA reductase
HMGS	3-Hydroxy-3-methylglutaryl-CoA synthase
HOMO	Highest occupied molecular orbital
HPLC	High performance liquid chromatography

IDI	Isopentenyl diphosphate:dimethylallyl diphosphate isomerase
IDI-1	Type 1 isopentenyl diphosphate:dimethylallyl diphosphate isomerase
IDI-2	Type 2 isopentenyl diphosphate:dimethylallyl diphosphate isomerase
IP	Isopentenyl phosphate
IPK	Isopentenyl phosphate kinase
IPP	Isopentenyl diphosphate
IspG	2-*C*-methyl-D-erythritol-2,4-cyclodiphosphate reductase
IspH	4-hydroxyl-3-methyl-butenyl-1-diphosphate reductase
IPTG	Isopropyl β-D-1-thiogalactopyranoside
KIE	Kinetic isotope effect
KIE_{int}	Intrinsic kinetic isotope effect
LOV	Light, oxygen, voltage
m/z	Mass over charge ratio
MCR	Multivariate curve resolution
MCR-ALS	Multivariate curve resolution-alternating least squares
MECP	2C-Methyl-D-erythritol 2,4-cyclodiphosphate
MeOH	Methanol
MEP	Methylerythritol 4-phosphate
MIB	2-Methylisoborneol
MPD	Mevalonate-5-diphosphate decarboxylase
MS	Mass spectrometry
MVA	Mevalonic acid
MVK	Mevalonate kinase

MWCO	Molecular weight cut-off
NADH	Nicotinamide-adenine dinucleotide, reduced
NADPH	Nicotinamide-adenine dinucleotide phosphate, reduced
Ni-IDA	nickel-iminodiacetic acid
NIPP	*N*,*N*-dimethyl-2-amino-1-ethyl diphosphate
oIPP	Racemic 3-oxiranyl-3-buten-1-yl diphosphate
PDA	Photodiode array
PDB	Protein Data Bank
PFTase	Protein farnesyl transferase
PMD	Phosphomevalonate decarboxylase
PMK	Phosphomevalonate kinase
PP_i	Inorganic diphosphate
Red.	Reduced
R-2fIPP	(*R*)-2-Fluoro-3-methyl-3-buten-1-yl diphosphate
RNA	Ribonucleic acid
S.E.	Standard error
Semi.	Semiquinone
S-2fIPP	(*S*)-2-Fluoro-3-methyl-3-buten-1-yl diphosphate
Sp	*Streptococcus pneumoniae*
TFC	Total flavin concentration
TIM	Triosephosphate isomerase
TKIE	Transient kinetic isotope effect
TOF	Time of flight

TRP	Transient receptor potential
Tt	*Thermus thermophilus*
UPLC	Ultra performance liquid chromatography
UV-vis	Ultraviolet-visible
vIPP	3-Methylene-4-penten-1-yl diphosphate
WRC	Western corn rootworm
WT	Wild-type

ACKNOWLEDGEMENTS

I would like to thank my mentor, Dr. C. Dale Poulter for his professional and personal support during my time at the University of Utah. His advice, insight and understanding are admirable and deeply appreciated. Also, I would like to thank the past and present members of the Poulter group for whom I shared many h in the lab and learned a great deal about science. My final thank you goes to my beautiful and intelligent friend, partner, and wife, Aneta. She shared in my successes, like this dissertation, while her love sustained me through times that challenged.

The work presented here was supported by NIH grant GM 25521.

CHAPTER 1

INTRODUCTION

Biological Diversity of Isoprenoid Compounds

Isoprenoids are biological compounds derived from the five-carbon precursors isopentenyl diphosphate (IPP) and dimethylallyl diphosphate (DMAPP) (Figure 1.1). Biological diversity is introduced through chain elongation, the process of joining DMAPP to IPP with subsequent additions of IPP to the resulting products. Chain elongation forms the monoterpenes (ten-carbon structures), sesquiterpenes (fifteen-carbon structures), diterpenes (twenty-carbon structures), and so on up to natural rubber (30,000+ carbon structure). According to current estimates, there are over 60,000 isoprenoid compounds,[1] including the hemiterpenes (five-carbon units). The derivation of the term isoprene is unknown,[2] but was first introduced in 1860 to a liquid distilled from caoutchouc (rubber) with a boiling point ~ 37 °C and a formula C_5H_8.[3] The use of the word terpene to describe compounds with the empirical formula $C_{10}H_{16}$ is derived from turpentine (in German, Terpentin), the essential oil of the terebinth tree.[4] Kremers studied

Isopentenyl Diphosphate (IPP)

Dimethylallyl Diphosphate (DMAPP)

Figure 1.1. Building blocks of isoprenoid compounds.

the etymology of the word Terpene in the German chemical literature and traced its use to the early to mid-part of the nineteenth century.[5] The first use of terpene in the English chemical literature appears to be a direct use of the German word, without translation to turpene.[6] Once thought to be constituents of only plants (mainly conifer and citrus),[6] the terpenes are now known to be ubiquitous and essential throughout nature.

The isoprenoid compounds serve a wide variety of essential biological functions and serve as secondary (nonessential, but important for species survival) metabolites. Here are a brief summary of different subsets of isoprenoid compounds and a mention of their biological function. Terpenoids are used by plants as an attractant or deterrent for pollinators, defense against herbivores, and an attractant to beneficial predators.[7,8] Isoprene (a hemiterpene) (Figure 1.2) is emitted from plants during times of high temperature, serving to cool plant leaves.[9] L-, or (-)-menthol (Figure 1.2), a monoterpene produced by peppermint and cornmint (*Mentha piperita* and *arvensis* species, respectively), has a yearly worldwide demand of 25 – 30,000 metric tons.[10] Products that use menthol include toothpaste, candy, medical supplements, liquors, cigarettes, air fresheners and various cleaning products. In *Homo sapiens*, menthol activates the transient receptor potential (TRP) melastatin 8 receptor, an ion channel responsible for detection of cold environmental stimuli, which is the cause of the cooling sensation attri-

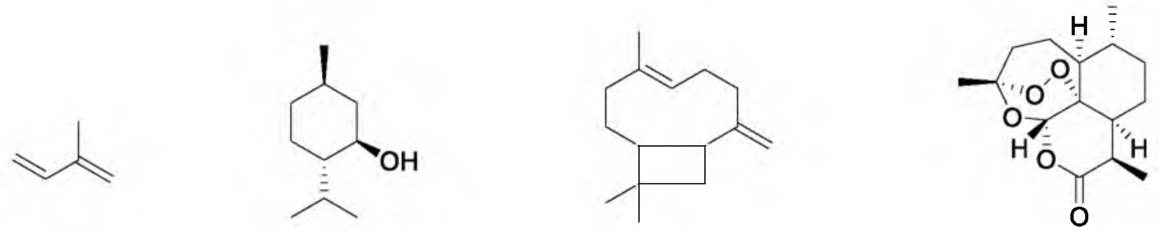

Isoprene (-)-Menthol (E)-β-Caryophyllene Artemisinin

Figure 1.2. Structures of isoprene, (-)-menthol, (E)-β-caryophyllene and artemisinin.

buted to menthol.[11]

European varieties and the wild ancestor of maize are capable of emitting (E)-β-caryophyllene (Figure 1.2) when the Western corn rootworm (WRC) invades and damages the plant.[12] The sesquiterpene attracted entomopathogenic nematodes and parasitic wasps that are natural predators of WRC.[13] Introduction of the (E)-β-caryophyllene gene into a North American variety, most of which do not produce the compound, successfully imparted the trait of attracting beneficial predators.[14] Thus, (E)-β-caryophyllene may be a natural alternative to pesticides used to control WRC.

Another sesquiterpene, artemisinin (Figure 1.2) is an antimalarial compound derived from the herb *Artemisia annua* that was used in Chinese traditional medicine to cure fever and malaria.[15] The isolated compound reduces the mortality rate of severe malaria by 35 % compared to quinine, but access to the compound is limited and the drug is cost prohibitive in economically poor areas.[16]

Two other economically important terpenes are geosmin (degraded sesquiterpene) and 2-methylisoborneol (MIB) (methylated monoterpene) (Figure 1.3) because they confer, respectively, an earthy and musty off-flavor to water, which requires expensive methods to eradicate.[17] Geosmin and MIB are responsible for the earthy odor often attributed to freshly dug, wet soil and are produced by several species of *Streptomyces*

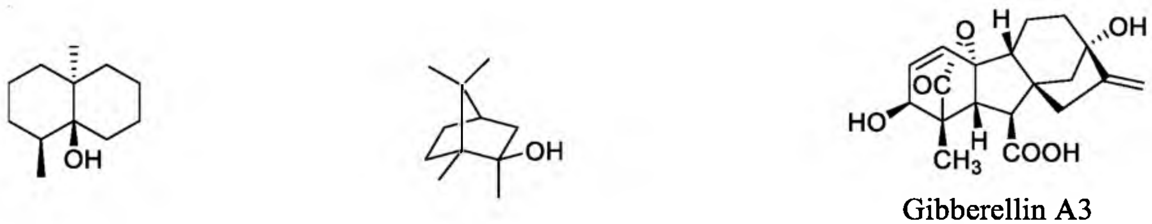

Geosmin

2-Methylisoborneol

**Gibberellin A3
(Gibberellic Acid)**

Figure 1.3. Structures of geosmin, 2-methylisoborneol and gibberellin A3.

soil bacteria as well as a number of other bacteria.[17,18] The compounds are also relevant agriculturally as geosmin is biosynthesized by the beet plant and contributes to their earthy flavor,[19] while the notes of must in Brie cheese are associated with MIB.[20]

Some longer chain terpenes include the gibberellins (diterpenes) (Figure 1.3) that function to promote plant growth in a variety of ways that include shoot elongation, flower production, seed germination and decrease of seed production.[21] The triterpene squalene is formed through a tail-to-tail condensation of two molecules of the sesquiterpene farnesyl diphosphate (FPP). Squalene (Figure 1.4) is then cyclized and rearranged in different ways to produce sterols such as cholesterol and campesterol (Figure 1.4), which serve to stabilize cell membranes in animals and plants, respectively.[22] The carotenoids are tetraterpenes found in plants that act as pigments to aid in photosynthesis and as color attractants for birds and bees.[23] In human health, β-carotene (Figure 1.4) is an antioxidant and an essential precursor to vitamin A synthesis,

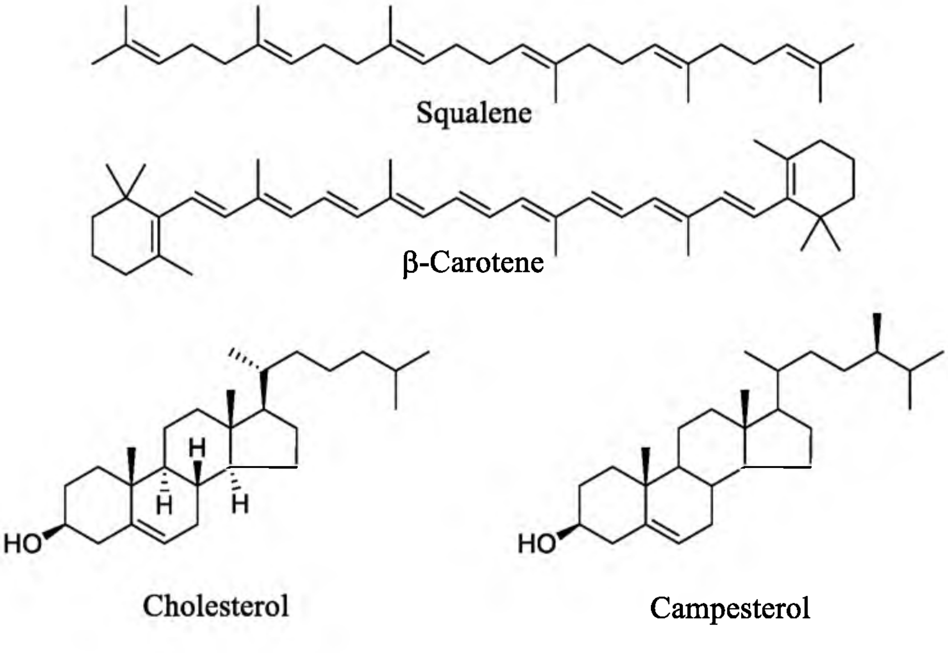

Figure 1.4. Structures of squalene, β-carotene, cholesterol and campesterol.

which is necessary for proper functioning of the human eye light receptors.[24] The polymeric nature of isoprenoid compounds extends to natural rubber, a product found in the latex from the tree, *Hevea brasiliensis* that has an average of 7000 isoprene units per molecule.[25] Beyond the chain elongation and cyclization of polyisoprene units, the prenylation of different families of natural products as well as the functionalization of isoprenoids are ubiquitous in nature.

Iridoid and secoiridoid compounds are plant defense compounds composed of a cyclopentane (iridoid) or cleaved ring (secoiridoid) fused to a six-membered ring with an oxygen (monoterpene component) and a glucose substituent (Figure 1.5).[26] The secoiridoid 3α(S)-strictosidine is the precursor to numerous monoterpene indole alkaloids, including quinine (Figure 1.5).[22]

Prenylated polyketides (or meroterpenoids) include hyperforin (Figure 1.5) from St. John's wort and the hop bitter acids. Hyperforin is responsible for the well-known antidepressant characteristics of St. John's wort, and has demonstrated antibacterial and anticancer properties.[27] Humulone is the major component of the hop bitter α-acids (35 – 70 %) and isconverted to isohumulone during the brewing process (Figure 1.5). Collectively, the hop bitter acids have anticancer, anti-inflammatory, bactericidal and antioxidant properties.[28]

The biodiversity of the isoprenoid family of compounds is extensive. Moenomycins are antibiotics with a pentasaccharide bound to an irregular isoprenoid chain through a phosphoglycerate-ether (Figure 1.5).[29] Paclitaxel (Taxol) (Figure 1.6) is a diterpene with amino acids side chains discovered in the bark of the Pacific yew that has demonstrated anticancer activity.[22] Saponins are polycyclic (four or five) triterpenoids

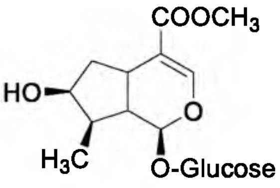

Loganin
(Iridoid)

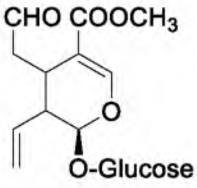

Secologanin
(Secoiridoid)

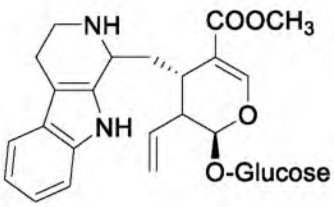

3α(S)-Strictosidine

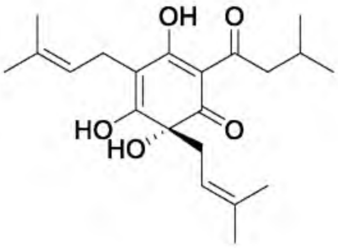

Humulone

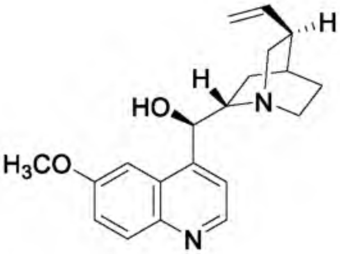

Quinine

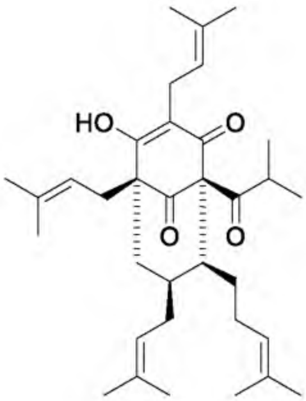

Hyperforin

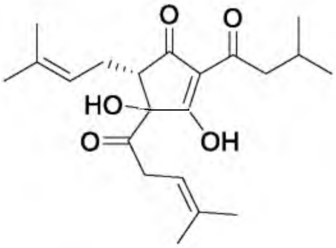

Isohumulone

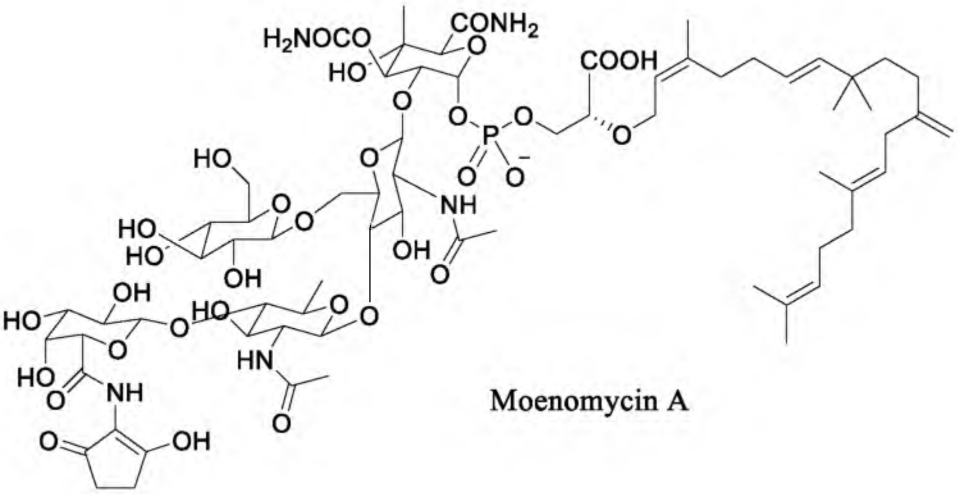

Moenomycin A

Figure 1.5. Structures of loganin, secologanin, 3α(S)-strictosidine, quinine, humulone, isohumulone, hyperforin and moenomycin A.

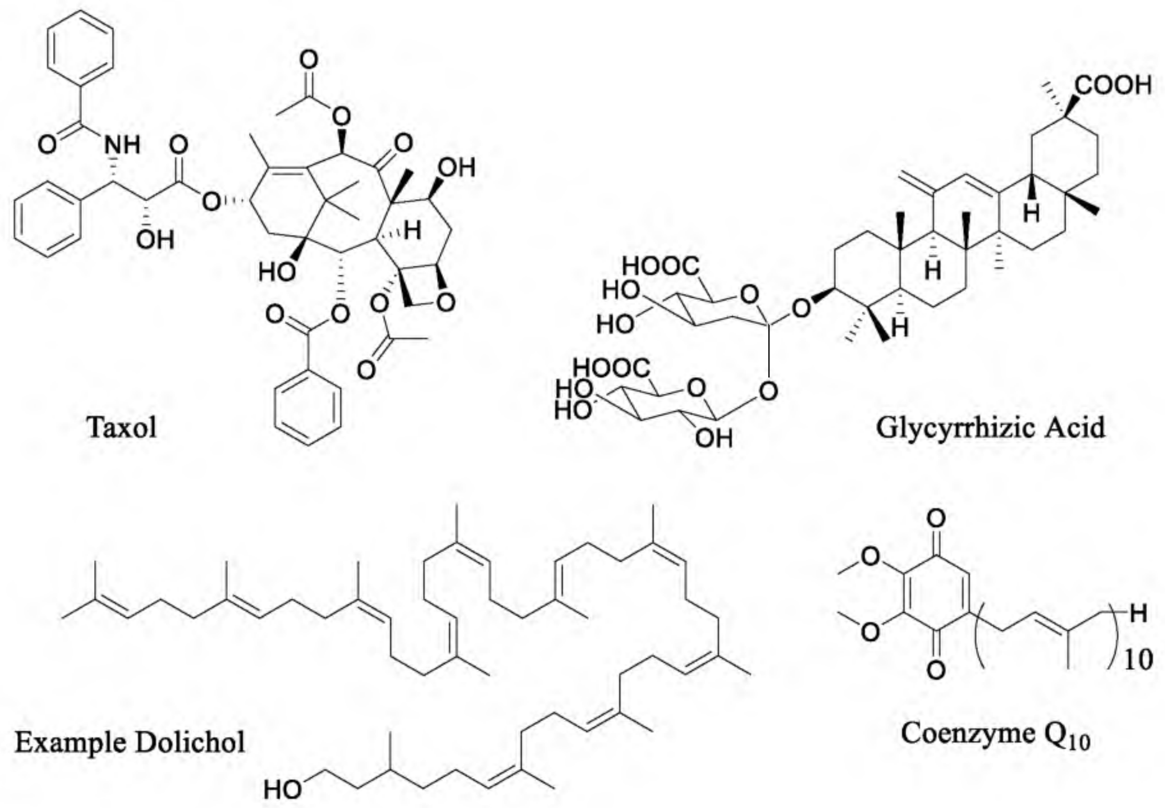

Figure 1.6. Structures of taxol, glycyrrhizic acid, a dolichol and coenzyme Q_{10}.

with one to three carbohydrate substituents that generally have a bitter taste. Glycyrrhizic acid (Figure 1.6), from licorice root, is a saponin that is sweet and has anti-inflammatory properties.[22] Beyond small molecules, dolichols (Figure 1.6) serve as the lipid component of glycolipids of eukaryotic cells and have a saturated prenol attached to 8 to 20 cis-prenyl units terminating with 2 or 3 trans-prenyl units.[30] Ubiquinones are polyprenylated benzoquinones, such as Coenzyme-Q_{10} (Figure 1.6), important compounds in the electron transfer reactions of mitochondrial respiratory chains.[31] Unique to the Archaea kingdom of life, Archaeal cell membranes (Figure 1.7) are composed of two saturated diterpene chains independently attached to glycerol through an ether linkage.[32] In addition to natural products, prenylation occurs with proteins and has been observed in RNA.

Proteins in the Ras superfamily are involved in cell growth and differentiation,

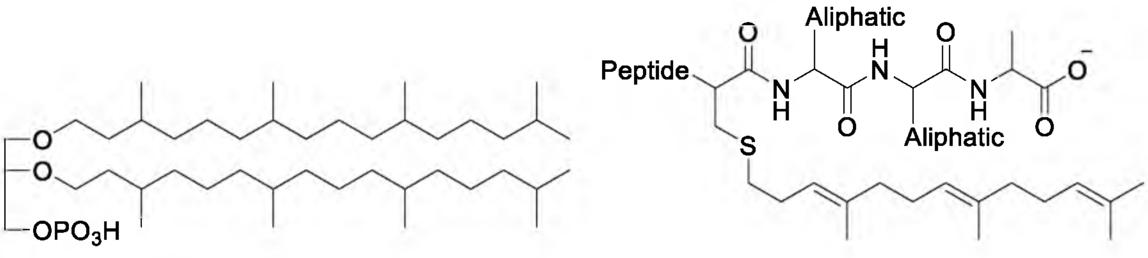

Archaeol (Archeael Membrane Lipid)   Farnesylated Peptide

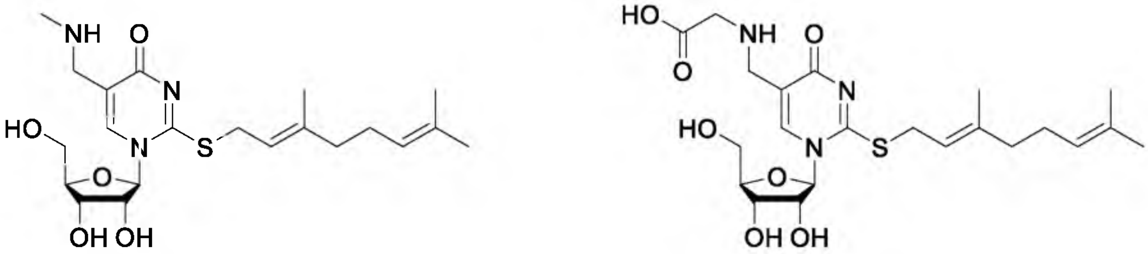

5-Methylaminomethyl-2-thiouridine   5-Carboxymethylaminomethyl-2-thiouridine

Figure 1.7. Structures of archaeol, a farnesylated peptide, 5-methylaminomethyl-2-thiouridine and 5-carboxymethylaminomethyl-2-thiouridine.

and are posttranslationally prenylated for membrane association. Farnesylation (or geranylgeranylation) occurs at a C-terminal cysteine that is a part of a CAAX motif of amino acids where A is an aliphatic residue and X is a variable group that is limited to C, S, M, Q, or A for activity (Figure 1.7).[33] The functionality of mutated Ras proteins has been associated to one-third of human cancers, with mutations in the K-Ras proteins being even more associated with colorectal and pancreatic cancers (50 and 90 %, respectively).[34] Geranylated RNA in bacteria occurs at the sulfur atom of 5-methylaminomethyl- or 5-carboxymethylaminomethyl-2-thiouridine (Figure 1.7).[35] The prenylation causes a decrease in codon bias for the glutamate UUC tRNA when GAA versus GAG codons are translated. The expansive use of isoprenoid compounds in nature is the biosynthetic result of two independent and unique pathways.

The Pathways of Isoprenoid Biosynthesis

The biosynthesis of isoprenoids occurs through either the mevalonic acid (MVA) (Figure 1.8) or the methylerythritol 4-phosphate (MEP) (Figure 1.9) pathways. The MVA pathway was discovered in the 1950s by demonstration that ^{14}C-labeled mevalonic acid led to the ^{14}C-labeled isoprenoids squalene, β-carotene, rubber, and α-pinene.[36] The first step of the MVA pathway is the condensation of two molecules of acetyl-CoA to form acetoacetyl-CoA. Acetoacetyl-CoA is then condensed with another acetyl-CoA molecule to form β-hydroxy-β-methylglutaryl-CoA (HMG-CoA). The reduction of HMG-CoA with NADPH results in mevalonic acid. Phosphorylation of mevalonate leads to 5-phosphomevalonate and the pathway then diverges for the Eukaryote and Archaea MVA pathways. Eukaryotes possess phosphomevalonate kinase, an enzyme that gives mevalonate 5-diphosphate. Diphosphomevalonate decarboxylase (or mevalonate-5-diphosphate decarboxylase) completes the isoprenoid pathway in eukaryotes to yield IPP. In Archaea, a hypothetical phosphomevalonate decarboxylase produces isopentenyl phosphate (IP) that is then phosphorylated by the well characterized isopentenyl phosphate kinase to yield IPP.[37] Archaea lack a diphosphomevalonate decarboxylase homologue and the enzyme that carries out this hypothetical reaction is still unknown.[38]

The MEP pathway (Figure 1.9) was more recently discovered. Early evidence in the late 1980s included unexpected patterns in terpenes when bacteria were fed isotopically labeled acetate.[39] In the early 1990s, [U-$^{13}C_6$]-glucose was fed to *E. coli* and labels were incorporated into ubiquinone-8 in a pattern that revealed pyruvate, not acetyl-CoA was the source an IPP two carbon unit.[40] Specifically labeled glucose, acetate, pyruvate and erythrose were fed to bacteria and the source of each carbon in IPP was

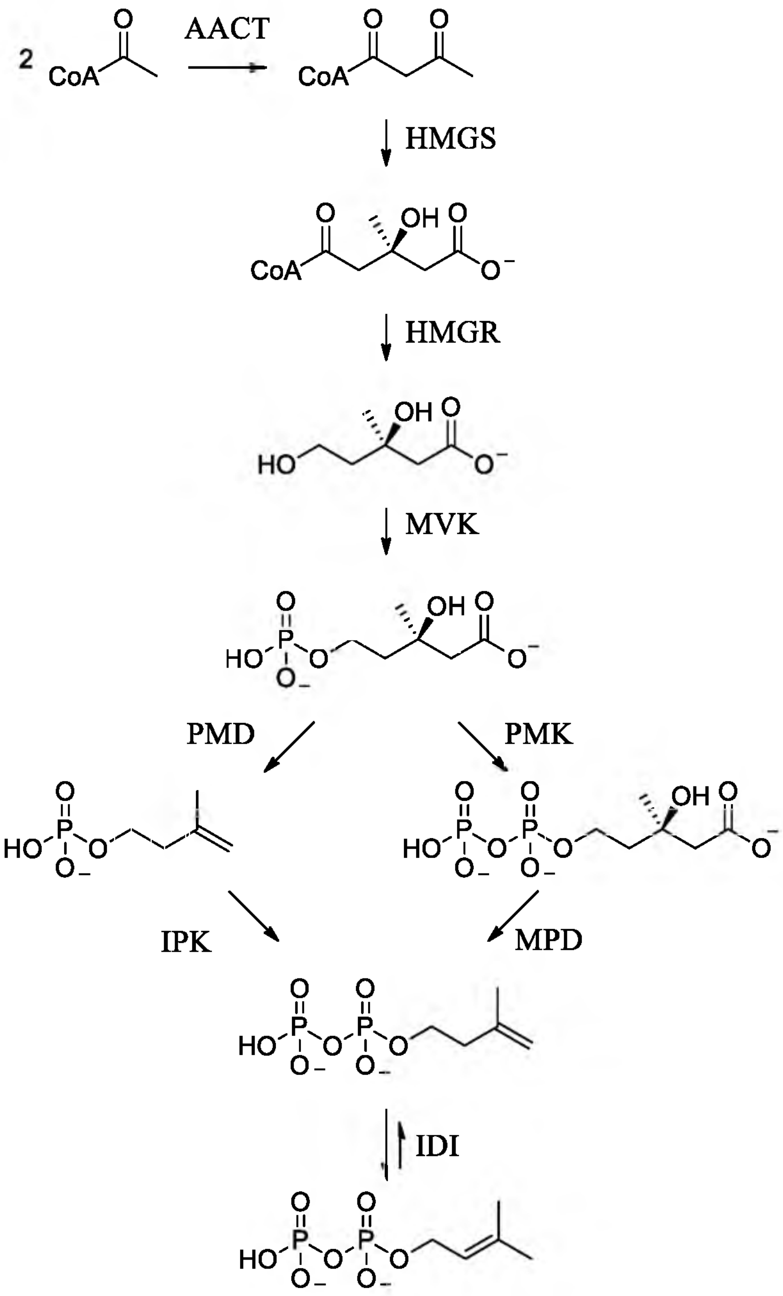

Figure 1.8. Mevalonic acid biosynthetic pathway of isoprenoid production with the enzymes responsible for each step. Enzyme abbreviations represent: AACT, Acetoacetyl-CoA thiolase; HMGS, 3-Hydroxy-3-methylglutaryl-CoA synthase; HMGR, 3-Hydroxy-3-methylglutaryl-CoA reductase; MVK, Mevalonate kinase; PMD, Phosphomevalonate decarboxylase (hypothetical); IPK, Isopentenyl phosphate kinase; PMK, Phosphomevalonate kinase; MPD, Mevalonate-5-diphosphate decarboxylase; IDI, IPP:DMAPP isomerase.

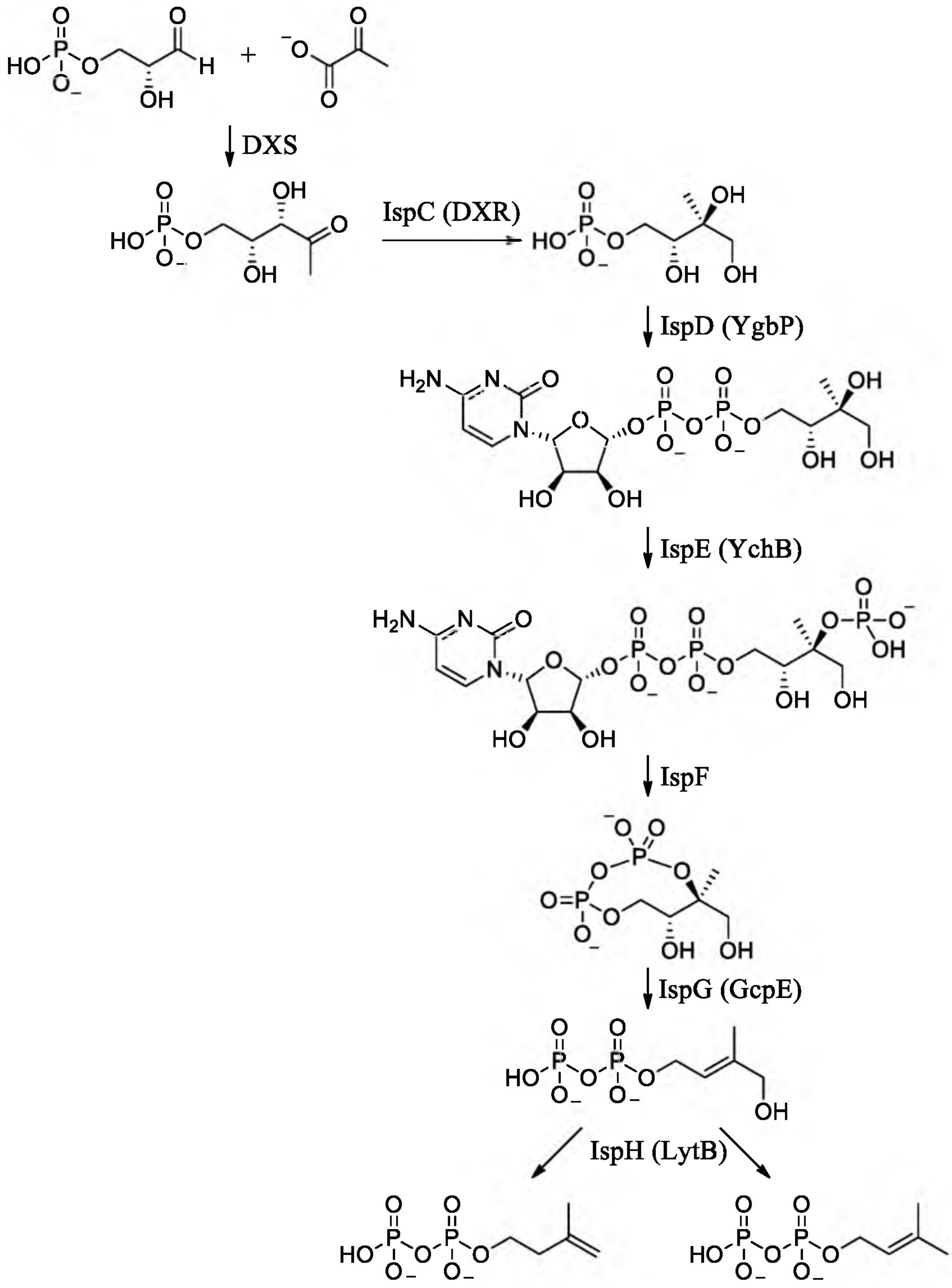

Figure 1.9. Methylerythritol phosphate biosynthetic pathway of isoprenoid production with the enzymes responsible for each step. Enzyme abbreviations represent: DXS, DXP synthase; DXR, DXP reductoisomerase; IspG, 2-*C*-methyl-D-erythritol-2,4-cyclodiphosphate reductase; IspH, 4-hydroxyl-3-methyl-butenyl-1-diphosphate reductase.

determined, which identified a source novel to that of the MVA pathway.[41] Two isoprenoid precursors were identified when isotopically labeled glycerol and pyruvate were incorporated into *E. coli* isoprenoids.[42] Sometimes called the nonmevalonate pathway, mevalonate-independent pathway or 1-deoxyxyluluose 5-phosphate (DXP) pathway, the first step of the MEP pathway is the condensation of pyruvate with glyceraldehyde-3-phosphate (G3P) to form DXP. In the next step, DXP undergoes an α-ketol rearrangement followed by reduction by NADPH to yield 2C-methyl-D-erythritol 4-phosphate, which is then condensed with cytidine diphosphate to give 4-diphosphocytidyl-2C-methyl-D-erythritol. Phosphorylation of the C2 hydroxyl group results in 4-diphosphocytidyl-2C-methyl-D-erythritol 2-phosphate that is then cyclized to 2C-methyl-D-erythritol 2,4-cyclodiphosphate (MECP). The cyclized MECP is converted to (E)-4-hydroxy-3-methyl-but-2-enyl diphosphate, which is then reduced to a mixture of IPP and DMAPP in a 5:1 ratio.[43]

Isopentenyl Diphosphate:Dimethylallyl Diphosphate Isomerase

In eukaryotes, prokaryotes, and Archaea that utilize the MVA pathway, isopentenyl diphosphate isomerase (IDI) is an essential enzyme that interconverts IPP to DMAPP (Figure 1.8). Organisms synthesizing IPP by the MEP pathway use IDI to balance cellular levels of IPP and DMAPP. The IDI enzyme is distributed in nature as two nonhomologous isofunctional (NIS)[44] forms, termed type 1 (IDI-1) and type 2 (IDI-2). Eukaryotes utilize IDI-1 exclusively; type 2 orthologs have not been observed in any eukaryotic genome sequenced to date. The type 2 NIS form is found in Archaea and Bacteria, such as the Actinobacteria, Bacillales, Cyanobacteria, Lactobacillales, and Proteobacteria phyla.[45] The majority (~ 72 %) of prokaryotic genomes that contain the

MEP pathway possess no IDI genes. Of the remainder, 17 % have IDI-1, 10 % have IDI-2, and 1 % possesses both genes. IDI-2 is a potential antibacterial drug target, since humans utilize the type 1 enzyme while type 2 is used by some pathogenic bacteria.[46]

Analogous to the MVA and MEP pathway, IDI-1 was discovered well before IDI-2. The early discovery of IDI-1 was not serendipitous but was directly related to the study of the MVA pathway. Isopentenyl diphosphate was discovered in 1958 while the pathway from mevalonate to squalene was studied.[47] IDI-1 was first isolated from a yeast extract and established that the catalyzed reaction was reversible. This study also found the enzyme in rat liver, kidney and brain tissues.[48]

The type 1 enzyme requires Mg^{2+} to coordinate the diphosphate moiety of IPP and Zn^{2+} (or Mn^{2+}) to help orient the active site amino acid side chains by coordination to three histidine and two glutamate residues (Figure 1.10).[49,50] Crystal structures of *E. coli*

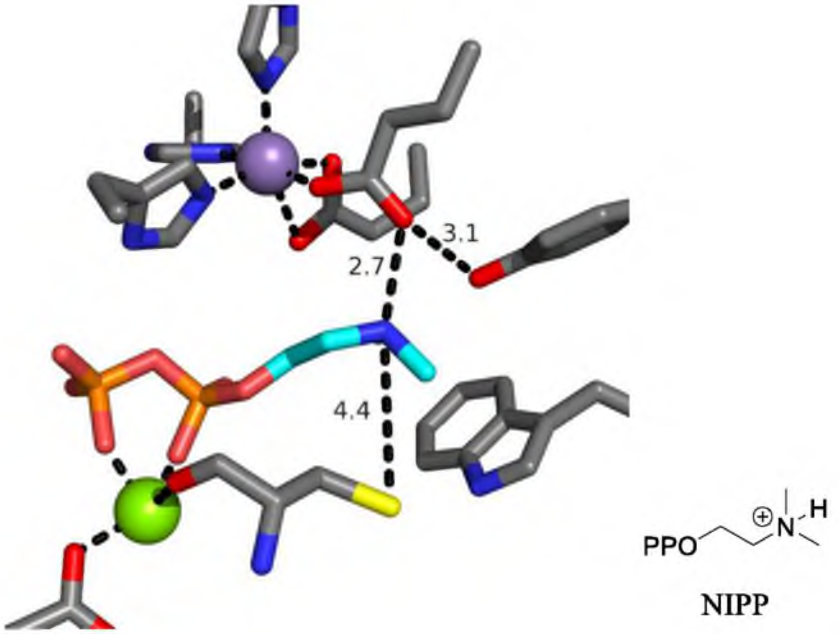

Figure 1.10. Crystal structure of *E. coli* IDI-1 with NIPP in the active site (with NIPP structure to the right). The green and purple spheres represent Mg^{2+} and Mn^{2+}, respectively. NIPP is cyan in color. PDB code 1NFS.

suggest that E116 is the proton donor, and C67 abstracts the proton to yield DMAPP. The structure in Figure 1.11 shows an epoxy analogue covalently attached to C67.[51,52] Catalysis proceeds through an antarafacial protonation/deprotonation mechanism with a carbocationic intermediate (Figure 1.12).[53–55] The carbocation is stabilized by the glutamate that donated a proton and by cation-π stabilization of the indole ring in W161.[51] An active site tyrosine (Y104) was implicated as the proton donor,[51] but later found to play an important structural role rather than a catalytic one.[56]

IDI-2 was discovered in 2000. The enzyme requires a divalent cation (Mg^{2+}) and reduced FMN cofactor for activity.[57] In contrast to the majority of flavoenzymes, which are redox active, IDI-2 catalyzes an acid/base-like reaction. The native enzyme is a tetramer or octomer in solution and has been crystallized in each form. The monomeric unit has a triosephosphate isomerase (TIM) barrel structure (Figure 1.13 for the *S.*

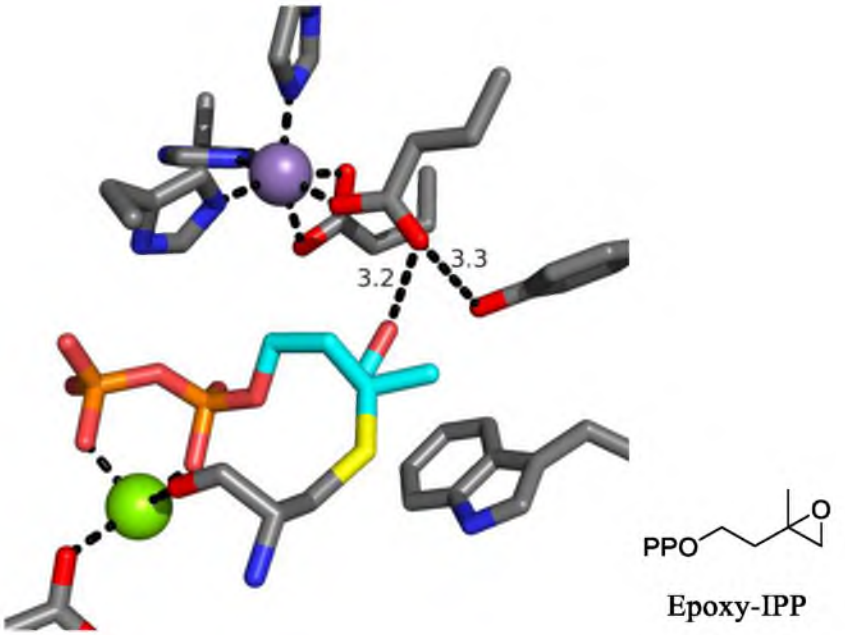

Figure 1.11. Crystal structure of *E. coli* IDI-1 with Epoxy-IPP in the active site (with Epoxy-IPP structure to the right). The green and purple spheres represent Mg^{2+} and Mn^{2+}, respectively. Epoxy-IPP is cyan in color. PDB code 1NFZ.

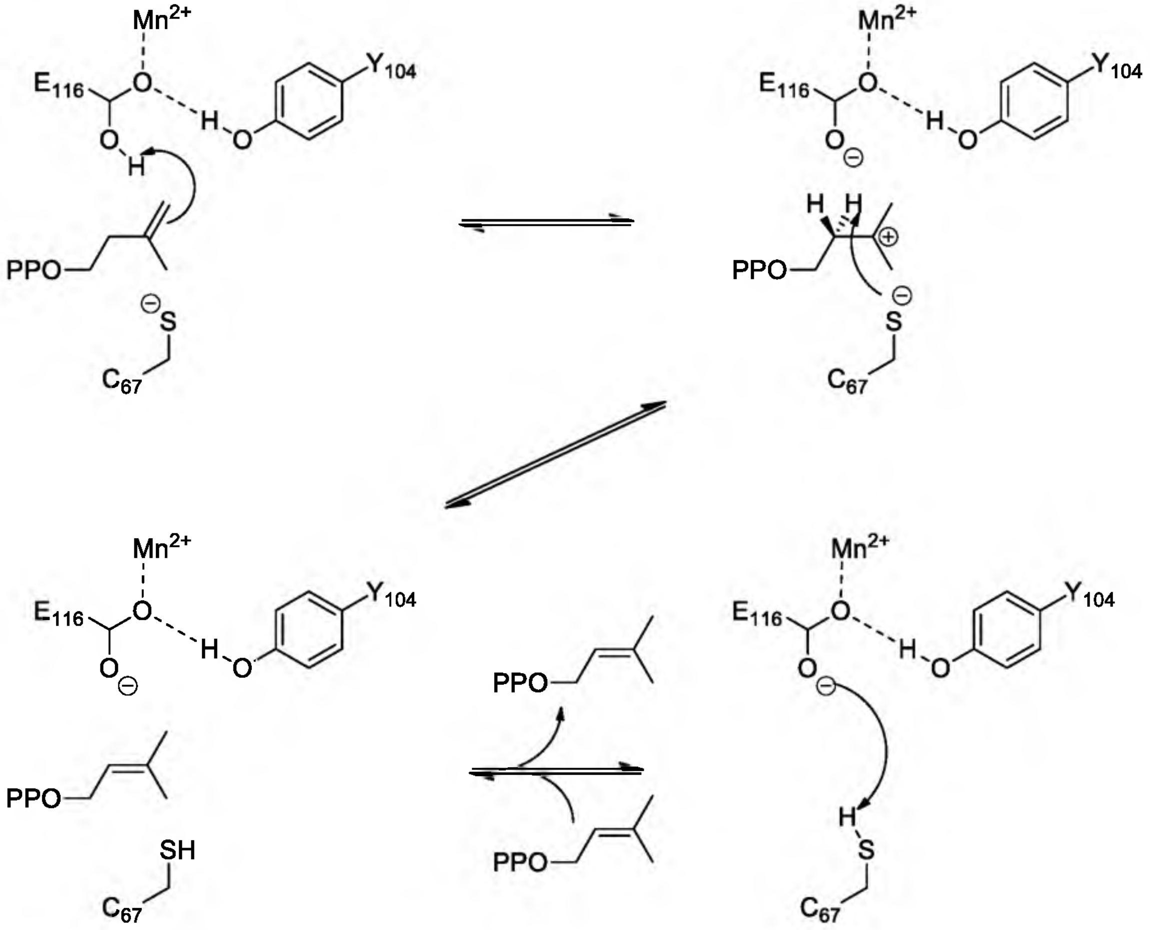

Figure 1.12. Mechanism of IDI-1 with amino acid numbering based on the *E. coli* enzyme.

shibitae tetramer).[58,59] The FMN cofactor is located in the β-sheets of the TIM barrel (Figure 1.14). The hydrocarbon moiety in IPP is in a plane parallel to and directly over the face of the isoalloxazine ring system (Figure 1.15 and Figure 1.16). The C2-C3-C4 positions of IPP are 3.3 – 3.8 Å from either N5 or C4a in FMN (Figure 1.17). Within the active site, the carbocation formed by protonation of IPP is stabilized within a box formed by FMN on the bottom. One pair of opposing walls of this box is H155 and W225 near the pyrimidyl and benzyl rings of FMN, respectively. The other pair is H11 and S195 near the diphosphate and C4/C5 of the substrate, respectively (Figure 1.18). The

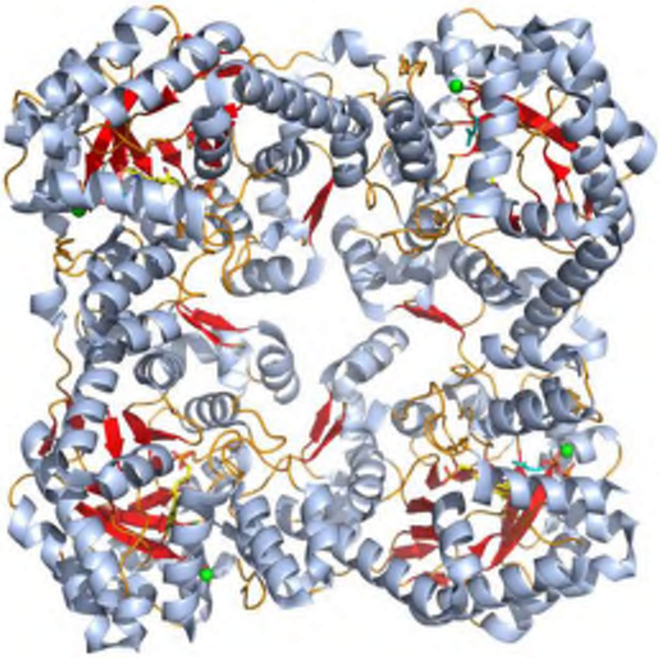

Figure 1.13. Tetrameric crystal structure of *S. shibitae* IDI-2 with IPP (cyan), FMN (yellow) and Mg^{2+} (green sphere). Structure from PDB file 3B05.

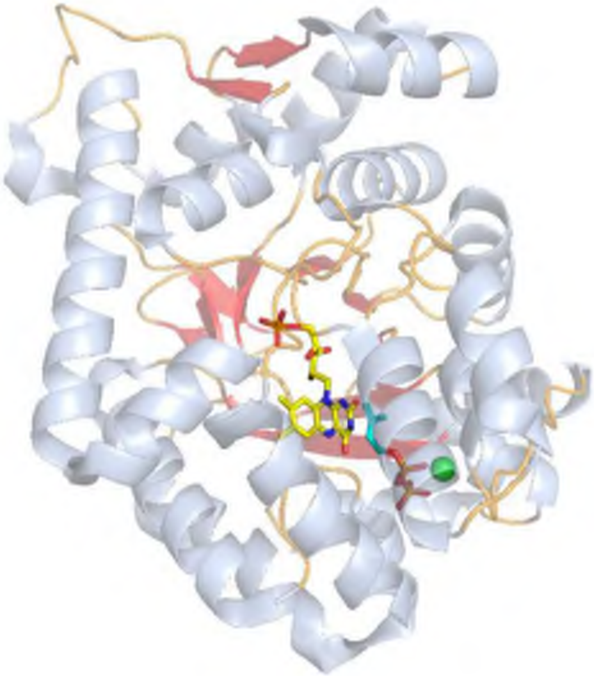

Figure 1.14. Monomer of the tetrameric crystal structure of *S. shibitae* IDI-2 with IPP (cyan), FMN (yellow) and Mg^{2+} (green sphere). Structure from PDB file 3B05.

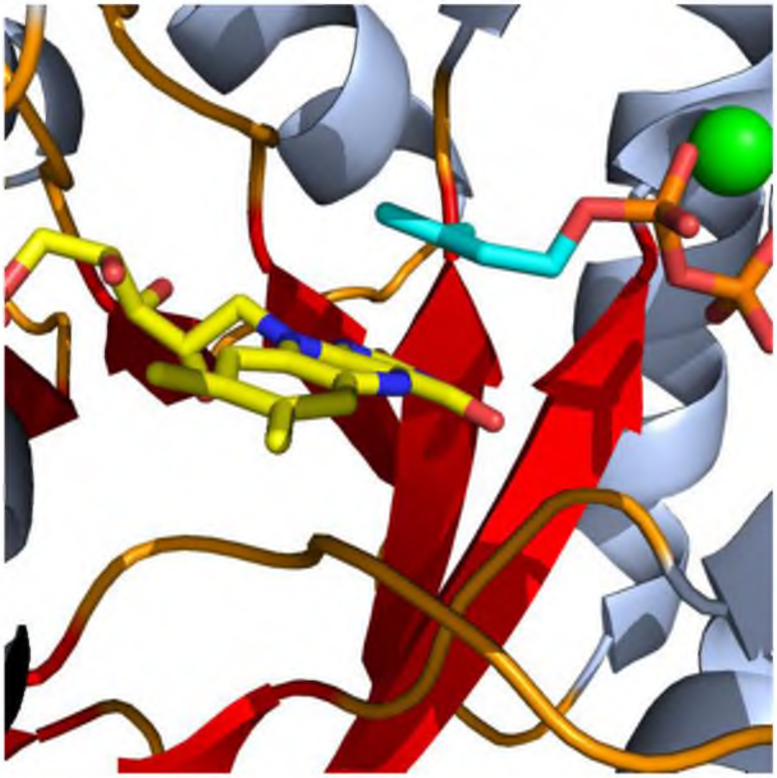

Figure 1.15. Close-up view of the positioning of FMN (yellow) and IPP (cyan) in the *S. shibitae* IDI-2 active site. The green sphere is Mg^{2+}. Structure from PDB file 3B05.

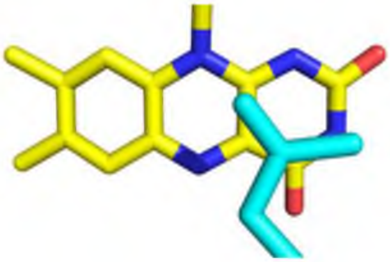

Figure 1.16. Close-up view of the positioning of IPP (cyan) directly above FMN (yellow) in the *S. shibitae* IDI-2 active site. The green sphere is Mg^{2+}. Structure from PDB file 3B05.

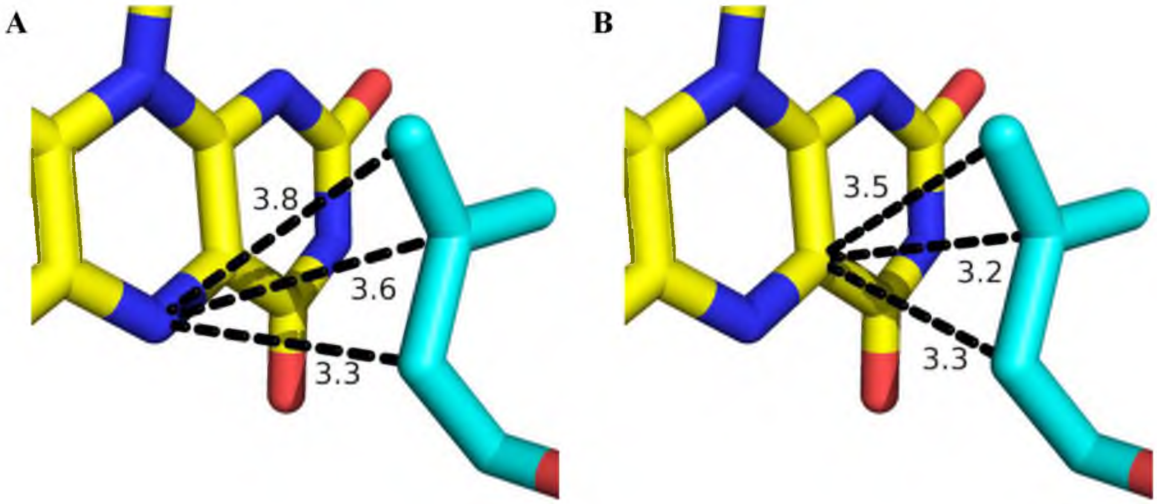

Figure 1.17. Distances between IPP carbons (cyan) and FMN (yellow) in the *S. shibitae* IDI-2 active site. A, Flavin N5; B, Flavin C4a. Structure from PDB file 3B05.

box is capped by Q160, which also stabilizes the carbocationic intermediate. Below IPP (relative to Figure 1.18) is a histidine residue and above is a serine or valine (for *S. shibitae* or *T. thermophilus*, respectively). N157 coordinates with H155, Q160 and Mg^{2+}. In the mechanistic description that follows, these amino acids will not be further discussed as their purpose is to position the substrate and stabilize the carbocation intermediate produced during catalysis.

The isomerization catalyzed by IDI-2 is highly stereoselective. The pro-*R* hydrogen of IPP is removed during isomerization of IPP to DMAPP, and a proton is removed from the *E*-methyl group of DMAPP in the reverse reaction.[60,61] Chiral methyl analysis found that with *E*- and *Z*- 4-T-IPP the allylic product E-methyl groups were (*R*) and (*S*), respectively (Figure 1.19).[62] This indicates that proton addition and abstraction is suprafacial.

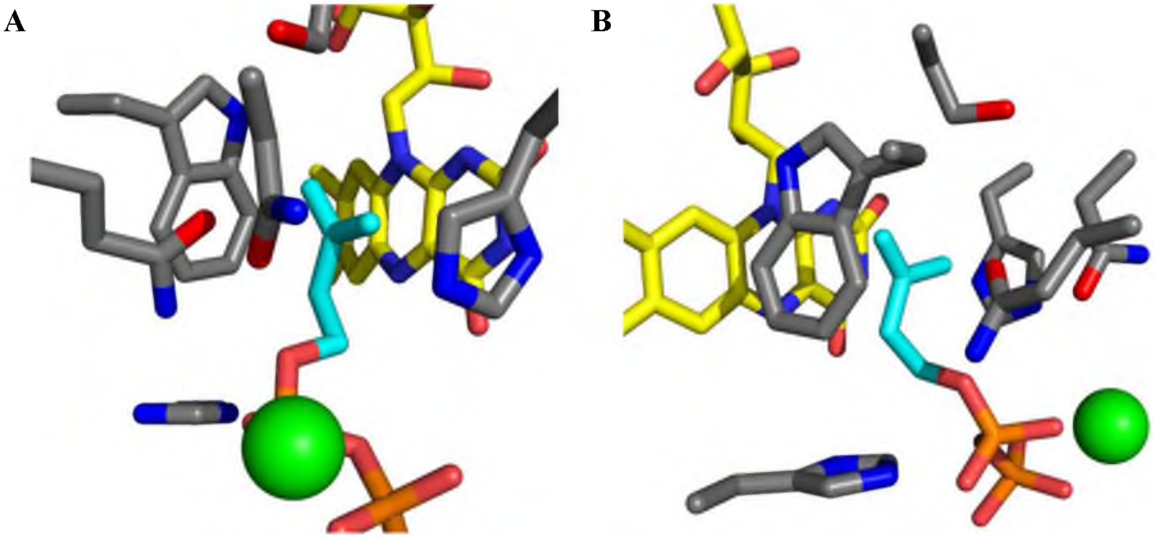

Figure 1.18. Positioning of IPP (cyan) within the active site of *S. shibitae* IDI-2 with FMN (yellow) and Mg^{2+} (green sphere). A and B are just opposing views of the same structure. Structure from PDB file 3B05.

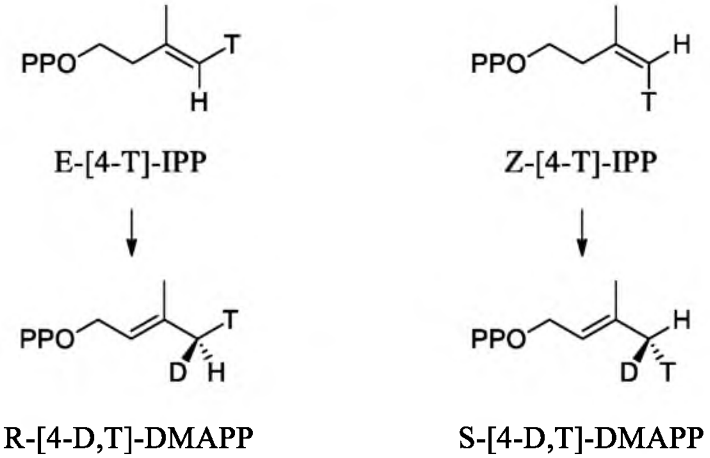

Figure 1.19. Chiral methyl analysis substrates and products.

Two mechanisms with radical or carbocationic intermediates were initially proposed for IDI-2 (Figure 1.20). UV-vis spectra indicated that when reduced, FMN was converted to the fully reduced anionic state in the absence of substrate. When IPP was incubated with IDI-2 prior to photoreduction, FMN underwent a one-electron reduction to yield the neutral semiquinone state.[63] The redox potentials for flavin bound to IDI-2 in the presence of IPP are different from those for free flavin. In *Staphylococcus aureus* IDI-2, the midpoint potential is -160 mV for the oxidized/semiquinone pair and -233 mV for the semiquinone/reduced pair.[64] In contrast, the corresponding midpoint potentials for free flavin were -313 mV and -101 mV, respectively.[65] The higher redox potentials indicated that IPP might contribute to stabilizing the semiquinone, possibly as a radical pair. EPR spectroscopy was used unsuccessfully to detect the semiquinone species.[63,66] Cyclopropyl and epoxy substrate analogues for IDI-2 (Figure 1.21) were unsuccessful in the detection of radical intermediates by "radical clock" mechanisms.[67,68] The cyclopropylcarbinyl and oxiranylcarbinyl radicals rearrange to the homoallylic isomers at rates of ~1.8 x 10^7 and 3.2 x 10^{10} s^{-1}, respectively.[69,70] When IDI-2 was incubated with the cyclopropyl analogue, NMR spectroscopy detected isomerization to cyclopropyl DMAPP without any evidence of a rearranged product. With the epoxy analogue,

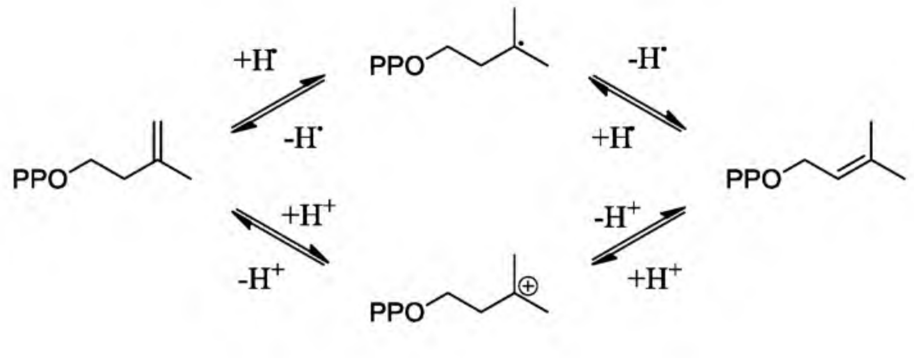

Figure 1.20. Possible general mechanisms of IDI-2.

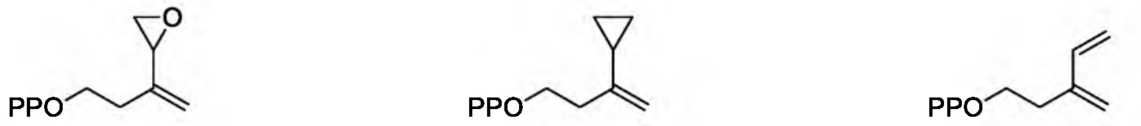

Oxiranyl-IPP Cyclopropyl-IPP Vinyl-IPP

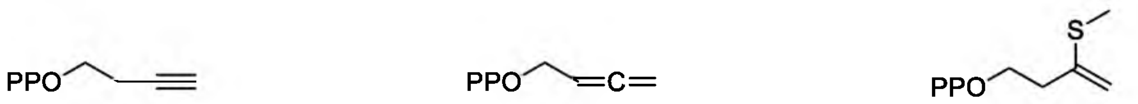

3-Butyn-1-yl PP_i 3,4-Butadien-1-yl PP_i Vinyl thioether IPP

Figure 1.21. IPP analogues discussed in the text.

epoxide opening with formation of a flavin adduct was observed without rearrangement to the homoallylic product expected for a radical reaction.

Additional evidence against a radical intermediate was found when alkyne and allene analogues of IPP were studied (Figure 1.21).[71] For both IDI-1 and IDI-2, the alkyne and allene derivatives were not alternative substrates and were not time-dependent, covalent inhibitors. The heats of reaction for formation of a carbocation by protonation of alkyne and allene derivatives was calculated to be -179 and -177 kcal/mol, respectively, while the corresponding values for formation of radicals by hydrogen atom additions were -37 and -36 kcal/mol, respectively. In comparison, the heats of protonation of 2-methyl-1-butene and 2-methyl-2-butene (-193 and -192 kcal/mol, respectively) are ~ 15 kcal/mol lower than for protonation of the related alkyne and allene derivatives. In contrast, heats of hydrogen atom addition to 2-methyl-1-butene and 2-methyl-2-butene (-34 and -33 kcal/mol, respectively), are nearly the same (~ 2 kcal/mol) as those for hydrogen atom addition. Thus, for an isomerization reaction proceeded by a radical mechanism, the alkyne/allene analogues would be good substrates or result in adduct formation to the flavin. The absence of turnover for both IDI-1 (as mentioned above proceeds through a carbocation) and IDI-2 indicates that a radical mechanism is not probable.

Another experiment with an IPP analogue demonstrated that the IDI-2 reaction is stepwise, rather than concerted with a late transition state. The vinyl thioether analogue (Figure 1.21) was found to exchange hydrogens at the methylene group with deuterium from the solvent (D_2O), with little detectable isomerized product.[72] Thus, the reaction of the vinyl thioether analogue to the carbocation was fast relative to the formation of the allylic isomer, and the IDI-2 reaction was stepwise.

Despite cumulative evidence that supports a carbocationic mechanism for the isomerization reaction, the role of flavin was still not resolved. Crystal structures of *S. shibitae* IDI-2 revealed that there were no residues that could function as a general acid or base for the respective proton addition and elimination off the substrate.[73]

Some recent mechanistic proposals suggested the N1/N5 nitrogens of flavin were general acids and O4 oxygen/N5 nitrogen were general bases for the isomerization because of their distance from the C4/C2 carbons of IPP, respectively.[58,73] However, Kittleman, et al. showed that apo-IDI-2 reconstituted with 1-deazaFMN retained full activity.[64] Since 1,5-dihydro-1-deazaFMN is not a preferred tautomer,[74] the N1 nitrogen is likely not the catalytic acid in IDI-2. A reduced, 5,5-zwitterionic flavin has been proposed by our group[63,68] as the general acid and is supported by the positioning of IPP in the IDI-2 active site.[73] The protonation at N5 of anionic reduced flavin has an estimated pK_a of ~ 4, raising the possibility of acid-base chemistry at N5.[75] Hemmi and coworkers then proposed that the flavin N5 position acts first as the general acid donating a proton to C4 of IPP, followed by deprotonation at C2 of IPP by flavin’s N5 nitrogen without any amino acid support (Figure 1.22.A).[73] While Liu and coworkers proposed flavin acting as both the general acid and base, their proposal required an active site amino acid to act as an intermediary in proton exchange (Figure 1.22.B).[66,76] However, a threonine to alanine mutation still retained ~ 6 % of the WT activity.[73]

Liu and co-workers evaluated linear free energy relationships in IDI-2 by changing the methyl substituents at the flavin 7 and 8 positions with electron withdrawing and donating groups. They found a slope of ~ -2 in the Hammett plot, indication that the rate limiting step in catalysis results in a decrease of the flavin electron density.[76] The same group explored chiral methyl analysis of the IDI-2 mechanism and found the strongest evidence to date that FMN is the proton donor that results in the substrate carbocation.[62] Based on structural models of IDI-2 with substrate bound, the

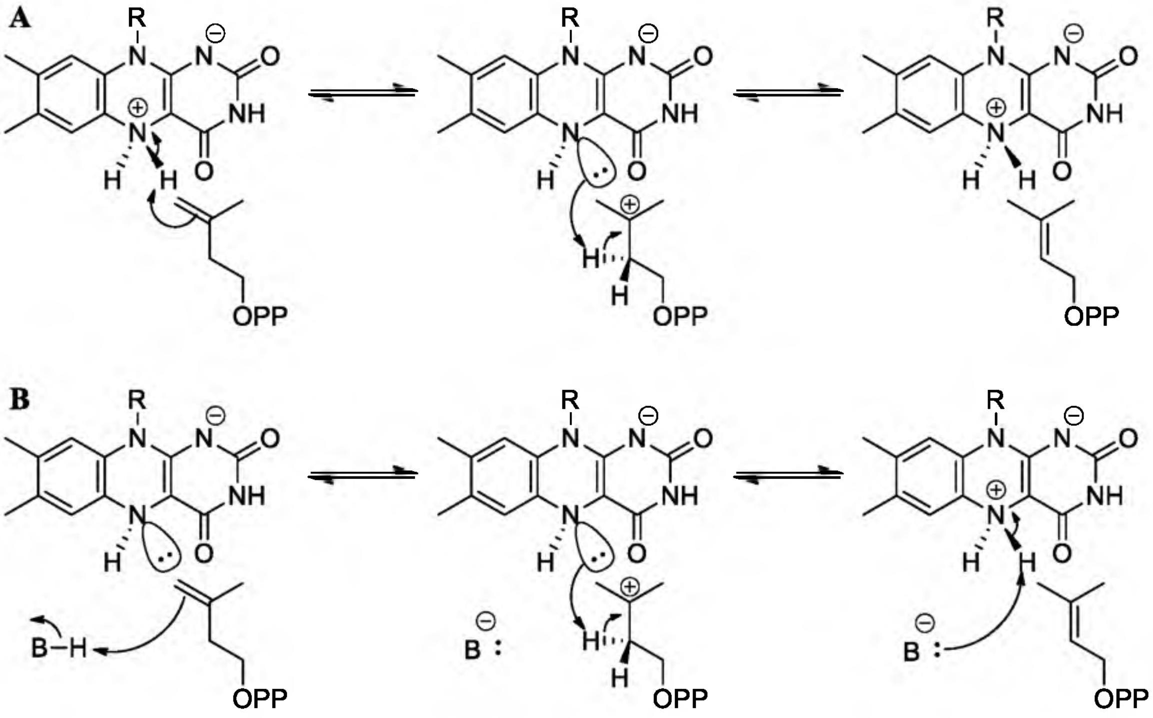

Figure 1.22. Proposed mechanisms of IDI-2. A, Flavin as both acid and base; B, Active site amino acid or water as the acid and flavin as the base.

suprafacial stereoselectivity observed in the chiral methyl analysis (described above, Figure 1.19) is consistent with FMN as the proton donor.

Another role for flavin is stabilization of the carbocation intermediate during catalysis. A delocalized HOMO surrounds the C4a-position of flavin when in the anionic reduced state,[77] which was the same flavin state of reduced FMN bound IDI-2 before addition of substrate. In support of the calculated HOMO, adduct formation of IPP analogues (vinyl-IPP and oxiranyl-IPP, Figure 1.21) occurs at the C4a-position.[58] Likely the tertiary carbocation intermediate is stabilized by the C4a-position during catalysis.

Despite these proposals and evidence of N5 involvement in catalysis, there is no definitive experimental evidence for the reduced 5,5-zwitterion of flavin. Importantly, the source of the proton that initiates catalysis is still unknown. Additionally, theoretical simulations evaluating the one- and two-electron reduction of lumiflavin have not yet explored the N5 protonation of anionic reduced flavin.[78]

Flavin Cofactors

Flavin cofactors are ubiquitous throughout nature and serve as protein structural stabilizers, light sensors, and catalysts. In general, there are three forms of flavin found in nature: riboflavin, flavin mononucleotide (FMN) and flavin adenine dinucleotide (FAD) (Figure 1.23). The conjugated ring system of flavin's isoalloxazine molecule gives a unique absorbance spectrum dependent on the redox state of flavin. The cofactor readily undergoes reversible reduction/oxidation reactions that involve 1 or 2 e^-. The major species of the flavin reduction pathway are shown in Figure 1.24 starting with oxidized flavin. With an E = -313 mV at 20°C for FMN, the first one-electron reduction yields a neutral flavin semiquinone (also called blue semiquinone) where the N5 proton has a pK_a

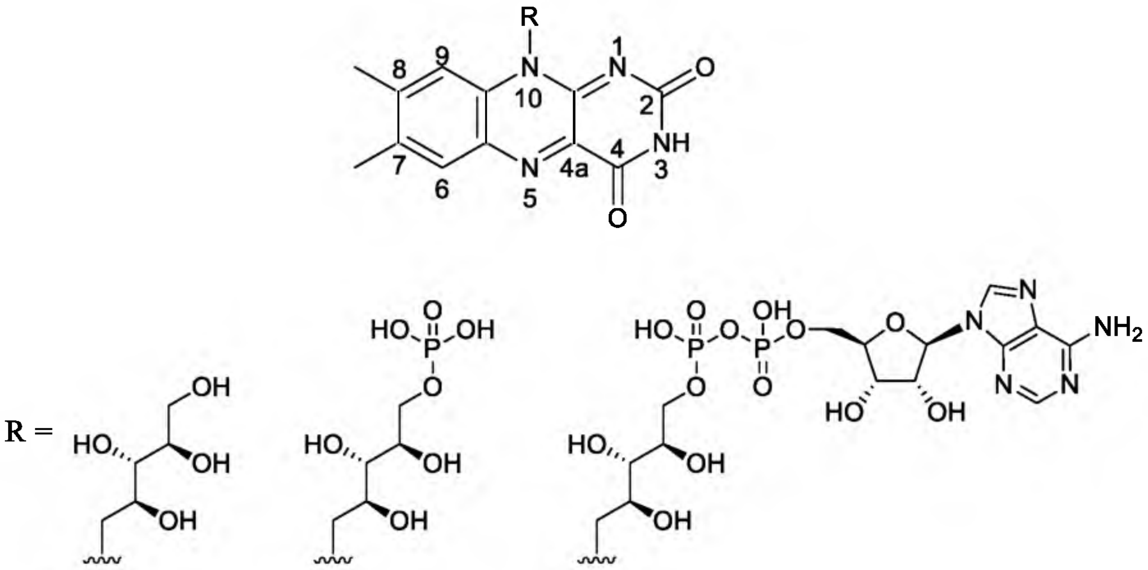

Riboflavin

Flavin Mononucleotide

Flavin Adenine Dinucleotide

Figure 1.23. Flavin structure and isoalloxazine ring numbering with explanation of different R groups.

~ 8.5.[65] Abstraction of this proton results in the anionic flavin semiquinone (also called red semiquinone). The neutral semiquinone can be further reduced by a single electron (*E* = -101 mV for FMN), to yield the reduced anionic form of flavin. Addition of a proton gives fully reduced flavin, which exists in the 1,5-dihydro or the zwitterionic 5,5-dihydro form, where the N5 proton has a pK_a of 6.7 or ~ 4, respectively.[75] In a two-electron reduction, such as a hydride transfer from the electron donor reduced nicotinamide adenine dinucleotide phosphate (NADPH), oxidized flavin is converted directly to reduced flavin with *E* = -207 mV for FMN. The redox potential of protein bound FMN (or FAD) can shift depending on how the cofactor is stabilized in the unique binding environment of the protein (because of the wide variety of flavoproteins,[79] a treatment of redox changes upon protein binding is not appropriate for this introduction).

The species highlighted in Figure 1.24, except those for fully reduced flavin, are

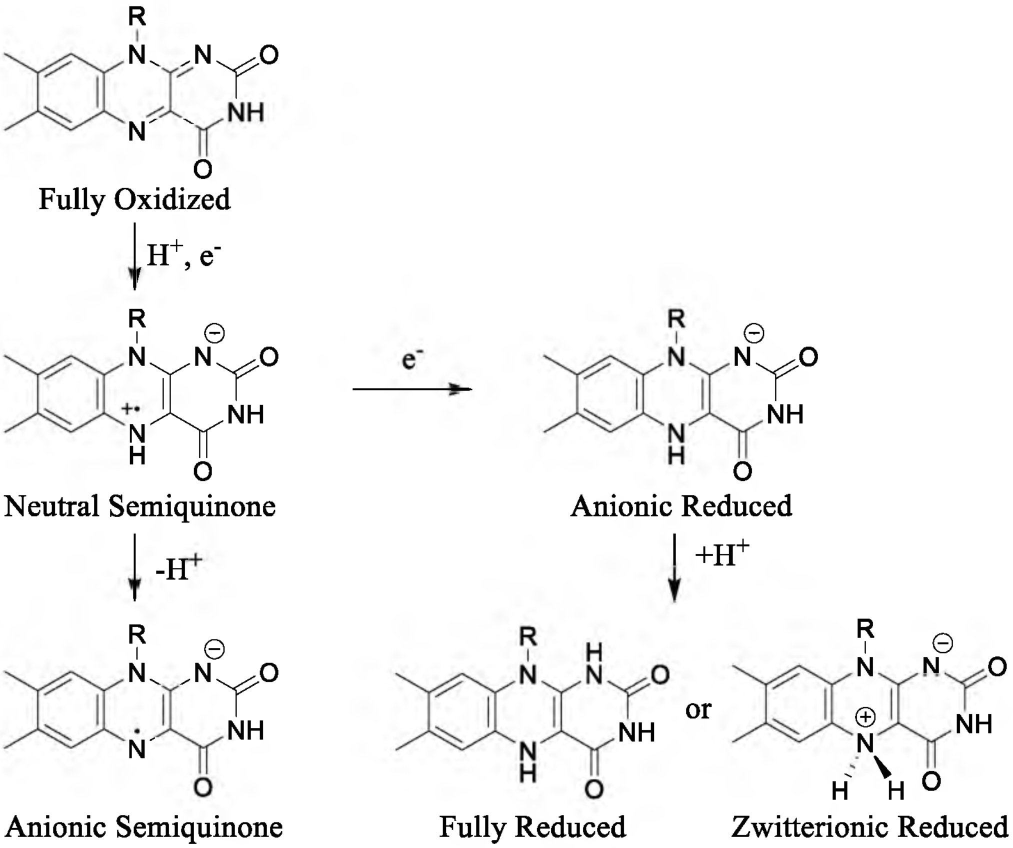

Figure 1.24. Flavin redox cycle, starting with fully oxidized flavin.

all stabilized by glucose oxidase and their corresponding absorbance spectra are shown in Figure 1.25.[80] The 1,5-dihydro species gives a spectrum similar to anionic reduced flavin, except the peak at ~ 350 nm shifts to a shoulder at 400 nm. The absorbance spectrum for the zwitterionic reduced flavin has not been determined. Fluorescent spectra of different flavin species are not as distinctive as their UV-vis spectra. Generally, oxidized flavin is fluorescent, while the neutral and cationic semiquinone, and anionic and neutral reduced flavin are nonfluorescent under ambient conditions.[81] In solution, free FMN and FAD (absorption λ_{max} 445 and 450 nm, respectively) both have fluorescence maxima at 525 nm with quantum efficiencies of 0.27 and 0.032, respectively.[82] For oxidized flavoproteins, the fluorescence excitation and emission maxima are similar to the free flavin

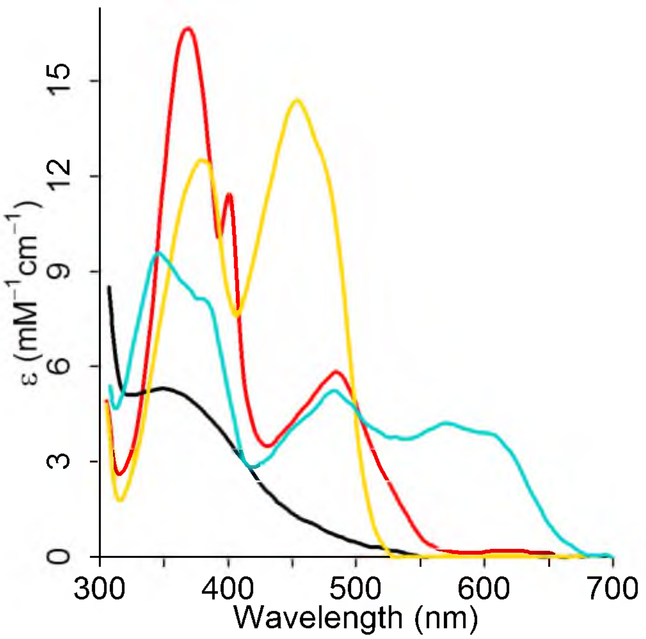

Figure 1.25. Representative UV-vis spectra of glucose oxidase with flavin in the oxidized (yellow), anionic semiquinone (red), neutral semiquinone (light blue) and anionic reduced (black) oxidation states. Data extracted from reference [80], Figure 3 with UN-SCAN-IT software.[83]

form.[82] Evidence for strong fluorescence from reduced flavins has been investigated,[84,85] but further literature is lacking, presumably because of experimental difficulties stemming from the oxygen sensitivity of reduced flavins.[86] Recently, the fluorescence emission spectra for both neutral and anionic flavin semiquinone were reported by Zhong and co-workers.[87] Table 1.1 shows a summary of fluorescence properties for flavin states other than the oxidized form.

Traditionally, flavin was implicated as the cofactor in phototropic biological processes,[88] which was recently shown to be true for the LOV (light, oxygen, voltage) domain protein.[89] In addition, two other photoreceptor proteins use flavin as a cofactor, the cryptochromes[90] and the recently discovered BLUF domain proteins.[91,92] Prior to the discovery of these proteins, chemical research involved both experimental and theoretical

Table 1.1. Summary of reduced and radical flavin cofactor absorption (excitation) and corresponding fluorescence emission properties.

Enzyme	Cofactor	Redox State	Absorbance λ_{max} (nm)	Fluorescence λ_{max} (nm)
Free in solution[87]	FAD	Anionic Reduced	360	455
Free in solution[87]	FAD	Neutral Reduced	360	480
Flavodoxin[84]	FMN	Anionic Reduced	365	530
Lactate oxidase[84]	FMN	Anionic Reduced	360	507
Photolyase[87]	FAD	Anionic Reduced	360	515 and 540
L-Amino acid oxidase[84]	FAD	Neutral Reduced	450	520
Type I cryptochrome[87]	FAD	Anionic Semiquinone	420	513
Flavodoxin mutant[87]	FMN	Neutral Semiquinone	580	700
Photolyase[87]	FAD	Neutral Semiquinone	580	715

studies of the excited state of flavins outside of a biological system. The discovery of photoreceptors prompted a revival of chemical and biological studies relevant to flavin photochemistry (the unique circumstances of FAD where the adenine moiety interacts with flavin[93,94] will not be addressed in this discussion).

Upon photoexcitation, flavin (Fl) undergoes a $\pi \rightarrow \pi^*$ transition. The possibility of a $n \rightarrow \pi^*$ transition is hidden because of the high molar absorptivities ($> 10^4$ M^{-1} cm^{-1}) of the absorption peaks in Figure 1.25 (oxidized, yellow line), along with two other peaks at 265 and 220 nm not shown in Figure 1.25.[95] The singlet state of flavin (^{1}Fl) has a lifetime of ~ 4.5 ns,[96] decaying to the triplet state (^{3}Fl) which has a lifetime of ~ 204 μs.[97] Intersystem crossing from ^{1}Fl to ^{3}Fl is highly efficient, with $\Phi = 0.7$, while ^{3}Fl phosphorescence emission is quite inefficient, $\Phi_P = 0.0012$, indicating that the triplet state decays through nonradiative relaxation.[95] The longer-lived and highly populated ^{3}Fl acts as a strong oxidant with the capacity to abstract a hydrogen or to undergo a 2e$^-$ transfer reaction resulting in the ground state reduced flavin (see Eqs. 1.1 – 1.5 in Table 1.2). In addition to the reactions in Table 1.2, ^{3}Fl can undergo photodealkylation, photooxidation, and both inter- and intraphotoaddition reactions.[98] Equations 1.1 – 1.3 are characteristic of D-D reactions of dye molecules, while equations 1.4 and 1.5 tend to be more common among flavins than other dyes.[99]

The formation of flavin semiquinone (Eq. 1.2, reverse reaction) was exploited with flavoproteins to yield enzyme stabilized flavin semiquinone using free flavin (synthetic analogues and natural forms) as a catalyst (see Eqs. 1.6 – 1.9 in Table 1.2).[100] Note that flavin is first photoreduced using EDTA as a photosubstrate and the following enzymatic reactions take place in the dark. With this technique, Massey, et al. were able to demonstrate that if an enzyme could stabilize flavin semiquinone, the reduction either stops with Eq. 1.7 or slowly proceeds to the fully reduced form (Eq. 1.8). As a special case, Massey and Hemmerich found that 5-carba-5-deazaflavins (deazaflavins) proceed through a different catalytic path, where a dimer is formed after photoexcitation of the oxidized deazaflavin (contrasting Eq. 1.6 where the fully reduced flavin is formed).[101]

Table 1.2. Summary of photoexcited flavin reactions.

Reduction	Reaction	
1e$^-$	$^3\mathrm{Fl} + \mathrm{HR} \rightarrow \mathrm{HFl}^\bullet + \mathrm{R}^\bullet$	**1.1**
	$2\mathrm{HFl}^\bullet \rightarrow \mathrm{Fl}_{\mathrm{ox}} + \mathrm{H_2Fl}$	**1.2**
	$\mathrm{HFl}^\bullet + \mathrm{R}^\bullet \rightarrow \mathrm{HFlR}$	**1.3**
2e$^-$	$^3\mathrm{Fl} + \mathrm{HR} \rightarrow \mathrm{HFlR}$	**1.4**
	$^3\mathrm{Fl} + \mathrm{HR} \rightarrow \mathrm{HFl}^- + \mathrm{R}^\bullet$	**1.5**
Enzyme	$\mathrm{Fl}_{\mathrm{ox}} \xrightarrow[h\nu]{\mathrm{EDTA}} \mathrm{H_2Fl}$	**1.6**
	$\mathrm{H_2Fl} + \mathrm{EFl} \rightarrow \mathrm{HFl}^\bullet + \mathrm{EFlH}^\bullet$	**1.7**
	$\mathrm{H_2Fl} + \mathrm{EFlH}^\bullet \rightarrow \mathrm{HFl}^\bullet + \mathrm{EFlH_2}$	**1.8**
	$2\mathrm{HFl}^\bullet \rightarrow \mathrm{Fl}_{\mathrm{ox}} + \mathrm{H_2Fl}$	**1.9**

After light exposure in the presence of a photosubstrate (EDTA or oxalate), an adduct is formed between C5 of the deazaflavin and the substrate. A second deaza-^{3}Fl displaces the substrate and a C5-C5 bond is formed between the two deazaflavins. Subsequently, this bond splits, creating two radical deazaflavins. These radical deazaflavins have a low reduction potential (~ -650 mV) which can be exploited to reduce other biological cofactors such as flavins, hemes, and iron-sulfur clusters.[101]

Flavoenzymes have also been investigated using flavin analogues as active site and mechanistic probes (while there are flavin analogues with R modifications (see Figure 1.23), for the purposes of this presentation, only analogues with isoalloxazine modifications will be discussed). With the exception of an enzyme in which flavin is covalently bound in the active site, the noncovalently bound flavin can be removed and the apoenzyme reconstituted with a coenzyme analogue (note that sometimes reconstitution is not possible because of irreversible protein denaturation). The spectral changes of these active site probes have been studied in the free and protein bound forms (see Appendix A for some example flavin analogues and their properties). One commonly used analogue is 8-chloroflavin because of its reactivity with sulfur nucleophiles. This analogue has a dual purpose, first in identifying thiolate residues in the active site near the flavin 8-position (used with lipoyl dehydrogenase and electron transfer protein)[102] and second in testing the solvent accessibility of the 8-position, both observable because of dramatic spectral changes from 8-chloro to 8-mercaptoflavin.[80] 8-Mercaptoflavins were used to study the redox state of flavin in numerous flavoenzymes, finding that the spectral and reduction properties of reconstituted enzyme mirrored that of the wild type (e.g., a stabilized red semiquinone flavin in the native enzyme was also observed with the 8-mercaptoflavoenzyme).[103] In a similar way, 4-thioflavins have been used to study the environment around the C4 carbonyl of flavin. Massey, et al. found that 4-thioflavins were reactive both as a nucleophile and an electrophile and used this knowledge to study the solvent accessibility of the O4 position of flavin in several enzymes.[104] With the increased success of crystallography, the use of flavin analogues as structural probes has diminished while they are still used as mechanistic probes.

As mechanistic probes, flavin analogues were used to assess the participation of flavin during catalysis and to alter the mechanism by using analogues with different reduction potentials. Both 1-carba-1-deaza- and 5-carba-5-deazaflavins (shortened to 1-deaza and 5-deaza, respectively, in the literature) are the most commonly used mechanistic probes.[102] 5-Deazaflavins have been used to determine whether a covalent intermediate exists in some proposed substrate carbanion intermediate reactions and if a radical flavin intermediate was involved in some reactions. In mechanisms where either flavin N5 or the substrate act as a nucleophile on each other, enzyme reconstituted 5-deazaflavin should produce a covalent adduct that can be isolated. Recently, this theory was applied to flavin-dependent thymidylate synthase to show the reaction proceeds through hydride transfer, not a covalent intermediate.[105] As described next, another example of flavin analogues as mechanistic probes involves the use of 6- and 8-position substituted analogues in free-energy relationships.

Bacterial luciferase catalyzes the reaction of fully reduced FMN, O_2 and a long chain aliphatic aldehyde to produce oxidized FMN, a carboxylic acid and emitted light. The reaction has been hypothesized to be a Baeyer-Villiger oxidation, typical of ketone monooxygenases where cyclic ketones (e.g., cyclopentanone and cyclohexanone) react with O_2, yielding water and the related lactone. The ketone monooxygenase reaction proceeds through a flavin-C4a-peroxy intermediate, which acts as the nucleophile attacking the carbonyl carbon of the ketone.[106] Francisco, et al. used six 8-substituted FMN analogues and transient kinetic studies to support their mechanism for bioluminescence by bacterial luciferase. The Hammett equation was applied to the rate of light decay and yielded a $\rho = -4$, which is inconsistent with a Baeyer-Villiger reaction expected to give $\rho = \sim (0.2 - 0.6)$.[107] Similar analyses have been performed on lactate oxidase using both 6- and 8- substituted FMN analogues[108] and 2-methyl-3-hydroxypyridine-5-carboxylic acid oxygenase using 8-substituted FAD analogues.[109]

Dissertation Overview

The work that is presented within this dissertation includes qualitative (spectral) and quantitative (kinetic) studies with the type 2 isopentenyl diphosphate:dimethylallyl diphosphate isomerase (IDI-2) and statistical analysis of kinetic isotope data from enzymes in the isoprenoid biosynthetic pathway. Chapter 2 presents data that challenge earlier conclusions of flavin adducts structures formed during incubation of substrate analogues with IDI-2 and introduces an in-depth statistical analysis of the oxidation of an FMN adduct. Chapter 3 introduces evidence for formation of a flavin adduct when IDI-2 is incubated with the natural substrates, IPP and DMAPP. Chapter 4 describes the kinetic mechanism of the *Streptococcus pneumoniae* IDI-2. To conclude, Chapter 5 gives the detailed statistical analysis of transient kinetic isotope effect data from farnesyl diphosphate synthase and protein farnesyl transferase.

CHAPTER 2

COVALENT MODIFICATION OF THE TYPE 2 ISOPENTENYL DIPHOSPHATE:DIMETHYLALLYL DIPHOSHATE ISOMERASE FLAVIN COFACTOR WITH SUBSTRATE ANALOGUES

Introduction

Some substrate analogues for IDI-2 were irreversible inhibitors that formed covalent adducts with the flavin cofactor.[68] Initially, the adducts were thought to form at N5 of flavin (Figure 2.1). These studies used UV-vis absorption spectroscopy and mass spectrometry to provide information about the adduct structures. However, the oxygen sensitivity of flavin adducts was not recognized since the adducts were exposed to oxygen when isolated from the enzyme.

When more stringent anaerobic conditions were used, some substrate analogues formed adducts at the C4a-position of flavin (Figure 2.1). In this chapter, the spectroscopic examination of several substrate analogues will be reported. The spectroscopic studies include UV-vis absorption and fluorescence spectroscopy of the adducts under different conditions, and the UV-vis absorption of the adducts while they undergo oxidation.

Oxidation of the adduct formed from 3,4-oxido-3-methyl-1-butyl diphosphate (eIPP) was studied extensively using multivariate curve resolution-alternating least

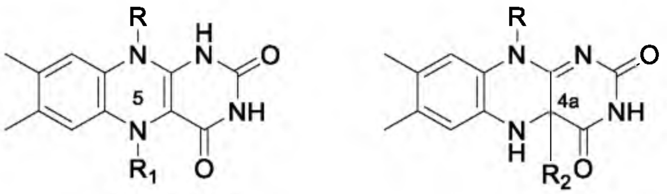

Figure 2.1. Structures of flavin adducts. R represents the ribityl or ribityl phosphate chain. R1 is a substituent at the N5-position and R2 is a substituent at the C4a-position.

squares (MCR-ALS) and genetic optimization using derivatives (Genoud). Multivariate curve resolution (MCR) is an exploratory tool that deconvolutes multicomponent spectral data with a time element.[110] For example, data collected on an HPLC with a diode array detector will have an absorption spectrum at each retention time. These data can be imagined to have m spectra collected at n wavelengths forming a matrix $\mathbf{D}_{m \times n}$, which can be equated using a multivariate form of Beer's Law (Equation 2.1),

$$\mathbf{D} = \mathbf{CS}^{\mathrm{T}} + \mathbf{E} \tag{2.1}$$

where **C** is a m x k matrix representing the concentration profile of k species for m time points, $\mathbf{S}^{\mathrm{T}}$ is a k x n matrix representing the pure spectra of k species at n wavelengths and **E** is the error matrix. With matrix algebra, the concentration profiles can be determined if the pure spectra are known (Equation 2.2) or if the concentration profiles are known, the spectra can be estimated (Equation 2.3).[111]

$$\widehat{\mathbf{C}} = \mathbf{DS}(\mathbf{S}^{\mathrm{T}}\mathbf{S})^{-1} \tag{2.2}$$

$$\widehat{\mathbf{S}} = \mathbf{D}^{\mathrm{T}}\mathbf{C}(\mathbf{C}^{\mathrm{T}}\mathbf{C})^{-1} \tag{2.3}$$

If the pure spectra and concentration profiles are not known, initial estimates must be provided. Then, the data are initially fit to either equation 2.2 or 2.3 and are optimized using least squares. The optimization continues by application of these best fits to the other equation, which is then optimized using least squares. This method is iterated until no more significant improvement in the fit is obtained in a process called alternating least squares (ALS).[112] In combination, MCR-ALS can resolve complex systems without any prior knowledge of the number of species or their pure spectra. An advantage of this method is the ability to uncover unknown intermediates that may be the result of unknown chemical pathways. However, the method may also introduce species that are not present, or may exaggerate certain components in the spectra that can introduce multimodality in the concentration profile. In addition, MCR-ALS ignores chemical kinetics. However, if the concentration profile represents a chemical process, it can be fit to a series of differential equations to determine kinetic rates.

The concentration profile described above may be quite complex as the number of species and rates increases. An added complexity is the optimization of the parameter values to fit such a complex system of simultaneous differential equations. Traditional optimization routines rely on starting or seed values and then explore the region of sample space surrounding those values with a Newton-type method (an explanation of these are beyond the scope of this chapter, however can be found in Seber and Wild).[113] The sample space may be exceedingly large for multiple parameter models. Thus if seed values are chosen far from the optimum the algorithm may never converge on a solution. Application of an evolutionary algorithm can be a solution to difficult optimizations. Given a population of values (the parents), the algorithm applies heuristic rules to adapt these values so that over the entire population, the adapted values (the children) are better than the parents.[114] Some of these rules include copying a subset of the population, applying mutations (one example is picking a random number between the lower and upper bounds of a random subset of the population) and crossovers (one example is the random swapping of parameter values between two members of the population).[114] The approach is one of brute force exploration of the sample space and requires a significant amount of computation. However, the method is meant to search the sample space in a manner more appropriate than random exploration. With a large population of values, the true optimum is more likely to be found.

Experimental Procedures

Materials. Racemic 3-oxiranyl-3-buten-1-yl diphosphate (oIPP), 3-cyclopropyl-3-buten-1-yl diphosphate (cIPP), 3-fluoromethyl-3-buten-1-yl diphosphate (fmIPP), (*R*)- and (*S*)-2-fluoro-3-methyl-3-buten-1-yl diphosphate (R-2fIPP and S-2fIPP, respectively), racemic 3,4-oxido-3-methyl-1-butyl diphosphate (eIPP) and 3-methylene-4-penten-1-yl diphosphate (vIPP) were available from previous studies (Figure 2.2).[55,68] Glycerol and guanidine·HCl were from USB Corporation. Tryptone and K_2HPO_4 were from Fisher Scientific and yeast extract was from BD Biosciences. KH_2PO_4 was from Mallinckrodt. Other reagents are from Sigma-Aldrich unless noted.

Expression and purification. His-tagged IDI-2 from *Thermus thermophilus* was expressed in *Escherichia coli* and purified as previously described[58,63] or was slightly modified as follows. Terrific broth stock (12 g tryptone with 24 g yeast extract in 900 mL H_2O) was supplemented with 0.2 g/L riboflavin. Terrific broth was prepared with 100 mL of a salt solution (170 mM KH_2PO_4 with 720 mM K_2HPO_4) and 900 mL of the Terrific broth stock solution using sterile conditions. Ampicillin and chloramphenicol were added

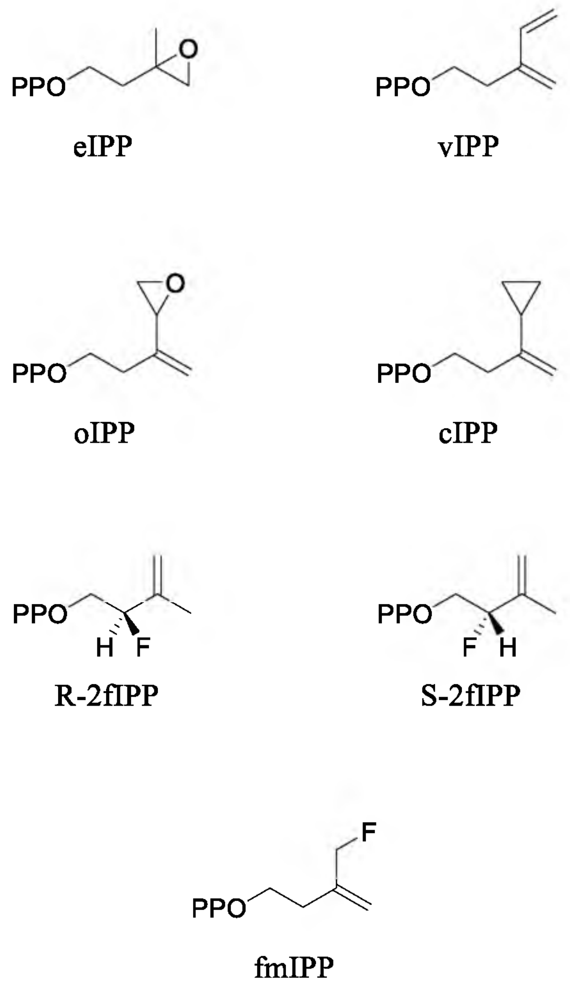
eIPP vIPP

oIPP cIPP

R-2fIPP S-2fIPP

fmIPP

Figure 2.2. Structures of IPP analogues used in adduct formation studies.

to a final concentration of 100 μg/mL and 34 μg/mL, respectively. The culture was grown at 37 °C for 4 h, and then induced with IPTG that contained FMN (final concentration 0.4 mM IPTG and 40 μg/mL FMN). After 4 h the cultures were harvested and yielded 4.3 g of cell paste per liter of media.

The only modifications to purification used a GE HisTrap HP column with a flow rate of ~5 mL/min, and the enzyme was with 500 mM imidazole (Acros) in 50 mM of Na_2HPO_4 (Mallinckrodt) pH 8, containing 300 mM NaCl (Mallinckrodt).

UV-vis assays. Assays were performed as previously described,[58,68] with the following modifications. At least 7 d before running an assay, all reagents were made O_2-free through gas exchange for one h (degassed under vacuum and then purged with argon), and then put into an anaerobic chamber (< 5 ppm O_2) (Coy Laboratories). IDI-2 and the respective substrate/inhibitor were gas exchanged and placed in the anaerobic chamber the day of experimentation. Reaction mixtures contained: 100 μM flavin-bound IDI-2 in 200 mM HEPES buffer, pH 7.0 (at 37 °C), containing 2 mM $MgCl_2$, 8 mM $Na_2S_2O_4$ and 400-800 μM substrate/inhibitor. After a minimum incubation of 4 h (or overnight) at 37 °C in the anaerobic chamber, samples were washed three times with 25 mM NH_4HCO_3, pH 7.8 at 20 °C in the anaerobic chamber through a Microcon 30 KDa MWCO ultrafiltration device to remove small molecules (Amicon/Millipore). Samples with enzyme were diluted to a final concentration of 10 mM NH_4HCO_3 buffer, pH 7.8 containing 5 % glycerol. Samples denatured with 8 M guanidine in 20 mM sodium phosphate, pH 6 or 7, were filtered (with an ultrafiltration device) to separate the protein from the adduct, and then diluted with denaturant. Samples denatured with 6 N HCl were centrifuged (without ultrafiltration) to separate protein precipitate from the adduct. The supernatant was removed and diluted with additional 6 N HCl for measurement. Samples were prepared in a twist-top cuvette (Starna Cells) and sealed with a Thermogreen™ LB-2 septum (Supelco) prior to removal from the anaerobic chamber. For oxidation studies, the cuvette was opened and the sample exposed to air by diffusion, with mixing using a stir bar (with the Agilent peltier attachment), vigorously shaking the cuvette, or pipetting air into the sample. UV-vis absorption measurements were made using an Agilent 8453 diode array spectrophotometer or Beckman Coulter DU730.

Fluorescence assays. Substrate analogue adducts were prepared as described above for the UV-vis assays. After adducts were prepared, they were diluted to a concentration of 10 μM with denaturant or for enzyme-bound adducts with 5 % glycerol. For measurements with only IDI-2 (no analogues), assays contained: 10 μM flavin-bound IDI-2 in fluorescence assay buffer (200 mM HEPES buffer, pH 7.0, (at 37 °C), containing 5 % glycerol and 2 mM $MgCl_2$). For reduced samples, $Na_2S_2O_4$ was added to a final concentration of 0.8 mM. For some samples, IPP was added to a final concentration of 100 μM. Control reactions of FMN_{ox} and FMN_{red} contained 10 μM FMN in fluorescence assay buffer, with dithionite added to the FMN_{red} control. Fluorescence measurements were made using a Horiba Jobin Yvon FluoroMax-3.

Analysis of eIPP oxidation pathway. The oxidation of the eIPP-adduct was modeled with a multivariate curve resolution-alternating least squares (MCR-ALS) analysis to estimate the time course of the flavin oxidation and to determine the spectrum of any unknown intermediates. Reference spectra were created from the initial spectrum collected at time zero (for the eIPP-adduct), the spectrum with the maximum absorbance at 600 nm (at 36.5 min, for the radical adduct), and the last spectrum that represented the final product (oxidized FMN). Unknown intermediates were assigned an arbitrary constant spectrum for all time points (absorbance = 1.0). Total flavin concentration (TFC) was determined based on the absorption of the spectrum for the fully oxidized FMN species and a reference extinction coefficient of 12,200 M^{-1} cm^{-1} at λ_{450}.[115] The initial concentration matrix was designed as shown in Table 2.1 for any number of rows.

The oxidation rates were determined for the simplified oxidation pathway in Table 2.2 based on the time course determined in the MCR-ALS analysis. Parameter estimates were supllied to differential equations that described Table 2.2 and used to

Table 2.1. Design of the initial concentration matrix for the MCR-ALS analysis. TFC = total flavin concentration.

eIPP-Adduct	Radical Adduct	Unknown Intermediate	FMN_{ox}
TFC	0	0	0
0	TFC	0	0
⋮	⋮	⋮	⋮
0	TFC	0	0
0	0	TFC	0
⋮	⋮	⋮	⋮
0	0	TFC	0
0	0	0	TFC
⋮	⋮	⋮	⋮
0	0	0	TFC

Table 2.2. Photooxidation reactions used to model the eIPP-FMN adduct oxidation where adduct formation occurs at the N5-position of flavin.

$5\text{-RFl}_{red}H + O_2 \rightarrow 5\text{-RFl}_{ox}^{+} + HO_2^{-}$, k_1	**2.4**
$5\text{-RFl}_{red}H + 5\text{-RFl}_{ox}^{+} \rightarrow 2\ 5\text{-RFl}^{\bullet} + H^{+}$, k_2	**2.5**
$5\text{-RFl}^{\bullet} + O_2 \rightarrow 5\text{-RFl}_{ox}^{+} + O_2^{\bullet -}$, k_3	**2.6**
$5\text{-RFl}_{ox}^{+} + OH^{-} \rightarrow Fl_{ox} + ROH$, k_4	**2.7**

calculate the concentration of the flavin species. The squares of the difference between these calculated values and the values determined with MCR-ALS for each species were summed. This sum of squares value was minimized with genetic optimization using derivatives (Genoud),[116] where all rate constants, as well as $[O_2]$ were allowed to float within the boundary conditions shown in Table 2.3.

Analyses for the above statistical techniques were performed using R version

Table 2.3. Boundary conditions applied to genoud algorithm.

Parameter	Lower	Upper
k_1	1×10^{-5}	1×10^{3}
k_2	1×10^{2}	1×10^{8}
k_3	1×10^{-4}	1×10^{3}
k_4	1×10^{-3}	0.1
$[O_2]$	1×10^{-6}	0.1

3.0.0 or later[117] using the packages ALS,[118] nnls,[119] Iso,[120] dichromat,[121] rgenoud,[114] nlmeODE,[122] deSolve,[123] nlme,[124] and lattice.[125]

Results

UV-vis spectroscopy of adducts. Three approaches were applied to determine the bond position of a flavin adduct. First the enzyme-bound adduct was studied and compared to both FMN•IDI-2 and IPP•FMN•IDI-2. Next, denaturation was performed with guanidine at neutral pH (6 or 7) and with 6 N HCl. The difference between the spectra collected at neutral pH versus a very low pH, along with the oxidation pathway of that isolated adduct can identify whether adduct formation occurs at the N5- or C4a-position (Table 2.4).

Table 2.4. Published trends for flavin adducts.[126-129]

	C4a-Adduct	**N5-Adduct**
Neutral pH, λ_{max} (nm)	360 – 370 and ~ 300sh	296 – 300
6 N HCl, λ_{max} (nm)	~ 400	< 300
Oxidation Requires:	O_2 + Light	Only O_2 (dark oxidation possible)
Oxidation Pathway	Adduct → $\text{Flavin}_{\text{oxidized}}$	Adduct → Radical Intermediate → $\text{Flavin}_{\text{oxidized}}$
Fluorescence Emission, λ_{max} (nm)	475	530

The results for vIPP, oIPP, eIPP and fmIPP analogues are in Table 2.5. After a 24 h incubation, the spectrum of each analogue incubated with enzyme differed from the spectrum of FMN_{red}•IDI-2. Furthermore, each spectrum was different from the initial spectrum when IPP was added to FMN_{red}•IDI-2 (Figure 2.3). The results for vIPP, oIPP, and fmIPP were similar at neutral pH (peak maxima ~365 – 375 nm and a shoulder at ~302 nm, Figure 2.4) and in 6 N HCl (peak maxima at ~ 400 nm, Figure 2.5). This bathochromic shift in the absorption maxima from a neutral to low pH was characteristic of a C4a-adduct. For eIPP, the spectrum at neutral pH has a shoulder at 324 nm that may represent a maximum. After isolation with 6 N HCl this peak at 324 nm shifted to a shoulder at 298 nm, a hypsochromic shift that indicated an N5-adduct. Both Figure 2.4

Table 2.5. UV-vis absorption properties of FMN adducts formed from IPP analogues and IDI-2 after a 24 h incubation.

Flavin Isolation Method	Assay Condition	Maxima (nm)	Minima (nm)	Shoulders
Enzyme Reference (no incubation)	**No Substrate**	352	325	
	IPP	430	367	316
Enzyme-bound	**vIPP**	404	353	315
	oIPP	342	313	416
	eIPP	350	314	-
	fmIPP	417 (broad)	393	308
8 M guanidine, pH 6	**vIPP**	256, 364	247, 331	303
	oIPP	278, 375	259, 333	303
	eIPP	258	239	304, 324, 378
	fmIPP	278, 374	257, 332	302
6 N HCl	**vIPP**	267, 402	259, 357	302
	oIPP	272, 305, 402	255, 300, 353	-
	eIPP	283, 395, 481	261, 384, 448	248, 298, 356
	fmIPP	272, 400	254, 351	302

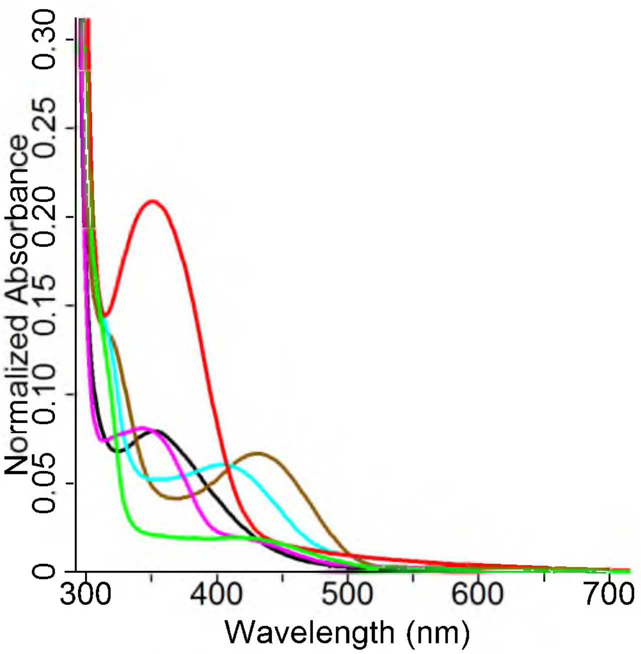

Figure 2.3. UV-vis absorption spectra of IDI-2 bound IPP analogue adducts. Lines represent vIPP- (cyan), oIPP- (magenta), eIPP- (red), and fmIPP- (green) adducts, as well as $\mathbf{FMN_{red}}$•IDI-2 (black) and IPP•$\mathbf{FMN_{red}}$•IDI-2 (brown). Spectra were normalized for absorption at 280 nm.

and Figure 2.5 have an inset displaying a small contribution from a radical species present in the eIPP spectra.

There are two characteristics of adducts that can be evaluated by observation of their oxidation pathway (Table 2.4). First, N5-adducts are O_2 sensitive, but C4a-adducts are stable after O_2 exposure until exposed to light. Second, N5-adducts oxidize through a radical intermediate detectable by an increase in absorption at 600 or 510 nm (at neutral pH or 6 N HCl, respectively), while C4a-adducts oxidize directly to the oxidized flavin species.[126] Oxidation of the vIPP-adduct is shown in Figure 2.6.A. In the first 4 min, the absorbance changed with isosbestic points at 276, 321, 368 and 415 nm, with increases in absorbance at 360 and 445 nm, characteristic of oxidized flavin. After oxidized flavin was formed, the absorbance at 445 nm decreased, likely because of photodegradation.

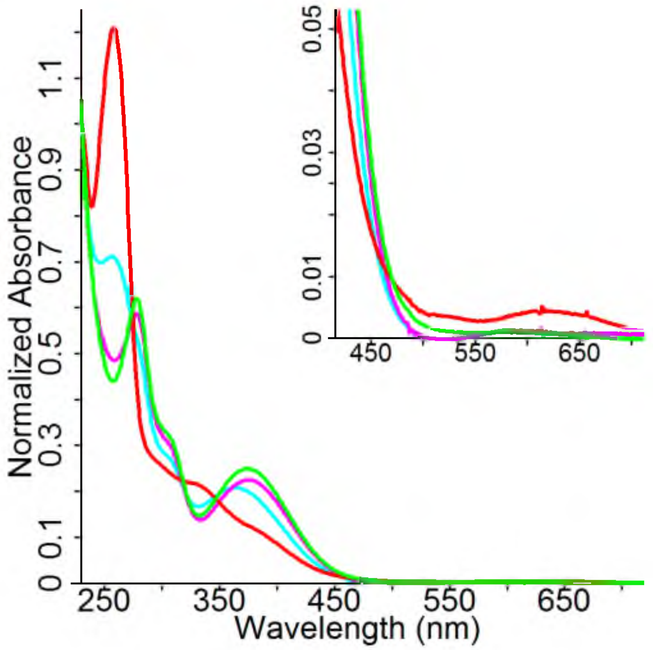

Figure 2.4. UV-vis absorption spectra of free adducts in 8 M guanidine, pH 6. Lines represent vIPP- (cyan), oIPP- (magenta), eIPP- (red), and fmIPP- (green) adducts. Inset highlights the presence of a radical species in the eIPP-adduct spectrum. Spectra were normalized for absorption at 231 nm (a common peak beyond the scale of interest).

Importantly there is no indication of a radical intermediate and no spectral change was observed when the sample was exposed to air in the absence of light. When the vIPP-adduct was oxidized in 6 N HCl, absorption peaks at ~ 270 and 400 nm increased for the first 35 min of photooxidation with isosbestic points around 290 and 320 nm (Figure 2.6.B). The pathway then proceeded through isosbestic points at 276 and 342 nm with a peak that appeared at 294 nm and the peak at ~ 400 nm shifted a few nanometers. The observed pattern matched that of a 4a-alkylated lumiflavin analogue photooxidized in 6 N HCl that resulted in protonated oxidized flavin with a sharp peak maximum at 395 nm.[128]

The oxidation pathway of the oIPP-adduct in pH 6 (Figure 2.7.A) was similar to that of vIPP-adduct oxidation under the same conditions. In the first 10 min, there were increases in absorption at ~ 360 and 445 nm with isosbestic points at 274, 318 and 415

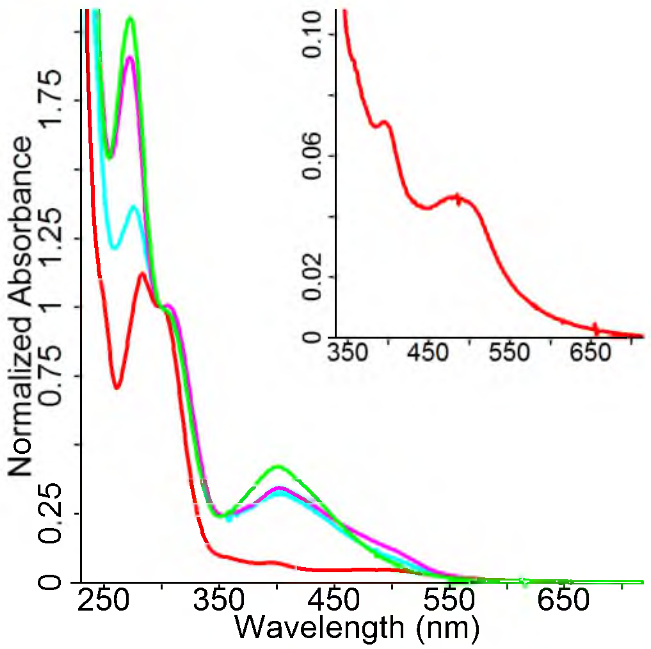

Figure 2.5. UV-vis absorption spectra of free adducts in 6 N HCl. Lines represent vIPP- (cyan), oIPP- (magenta), eIPP- (red), and fmIPP- (green) adducts. Inset highlights the presence of a radical species in the eIPP-adduct spectrum. Spectra were normalized for absorption at 300 nm (a common peak/shoulder).

nm. After 10 min, absorption continued to increase without any significant spectral changes. As with the vIPP-adduct, there was no evidence for a radical intermediate and light was required. For the oIPP-adduct oxidation in 6 N HCl (Figure 2.7.B), there was a slight increase in absorption at ~ 500 nm, possibly indicating a radical intermediate. Otherwise the spectral changes were similar to those of the vIPP-adduct. There is no clear isosbestic point that led to the ~ 500 nm peak and importantly, the protonated N5-alkylated flavin intermediate has a sharp peak at ~ 500 nm.[128,130] Thus, the observed species is likely a small proportion of N5-adduct or some unknown intermediate.

Oxidation of the eIPP-adduct is unique from the other oxidation pathways because light was not necessary to observe a spectral change. At pH 6, the oxidation proceeded through a radical intermediate detected by a broad peak around 600 nm

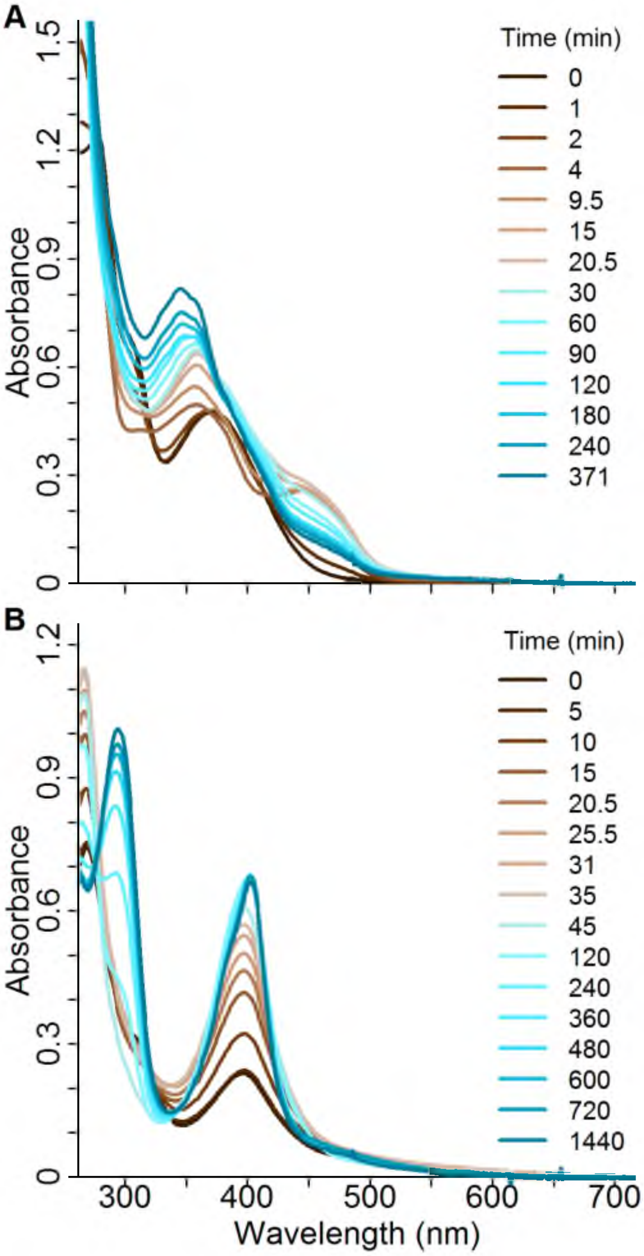

Figure 2.6. UV-vis absorption spectra of vIPP-adduct oxidation. A, In 8 M guanidine, pH 6; B, In 6 N HCl. Time represents the amount of time exposed to light. Modified from reference 58.

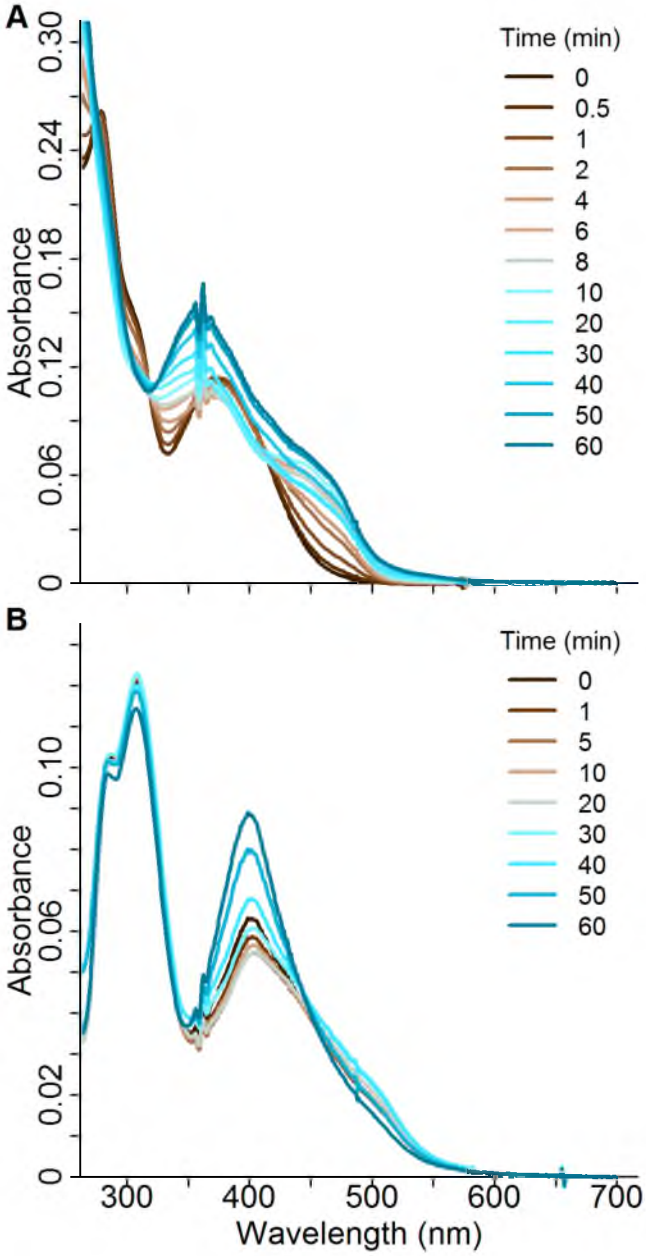

Figure 2.7. UV-vis absorption spectra of oIPP-adduct oxidation. A, In 8 M guanidine, pH 6; B, In 6 N HCl. Time represents the amount of time exposed to light.

(Figure 2.8.A), followed by further oxidation of the intermediate giving isosbestic points at 302, 350 and 500 nm, and finally producing fully oxidized flavin with peaks at 375 and 445 nm (Figure 2.8.B). A similar pattern was observed for the oxidation in 6 N HCl. A radical intermediate formed through a series of spectra with an isosbestic point at 320 nm, and a final spectrum for the radical with peaks at 355, 396 and 510 nm (Figure 2.9.A). After formation of the radical intermediate, oxidation continued with isosbestic points at 280, 360 and 445 nm to give a spectrum of protonated fully oxidized flavin product with a peak at 396 nm (Figure 2.9.B).

Photooxidation of the fmIPP-adduct at pH 6 produced a spectrum of fully oxidized FMN (Figure 2.10.A). For this experiment, the sample was exposed to O_2 (air) for almost 6 h before light exposure. For clarity, only the initial (no O_2) and final (5.8 h of exposure to air) spectra are shown in Figure 2.10.A. Only a small increase in absorption was observed at 600 nm, which may have been caused by residual light in the laboratory and is not considered significant. Once the sample was exposed to light, the sample rapidly oxidized in 35 min to give fully oxidized FMN, without evidence for formation of a radical intermediate. Spectra gave two isosbestic points at 290 and 329 nm during this photooxidation. The final spectrum for fully oxidized flavin had peaks at 375 and 445 nm.

In the absence of light, oxidation of the fmIPP-adduct in 6 N HCl gave a radical intermediate that was photooxidized to protonated oxidized flavin (Figure 2.11.A and .B). In the absence of light, the radical slowly formed over a period of 19 h with poorly defined isosbestic points at ~ 340 and ~ 450 nm (Figure 2.11.A). Peaks seen at 358 and 505 nm were characteristic of a protonated N5-alkylated flavin.[130] The radical was then

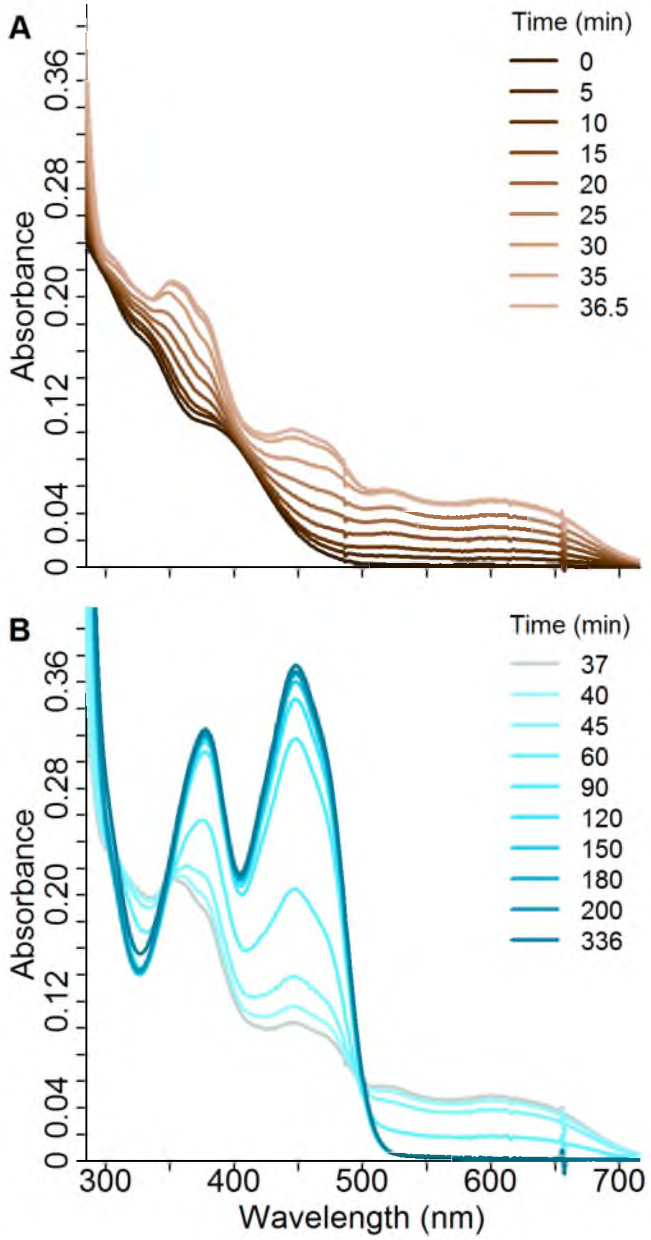

Figure 2.8. UV-vis absorption spectra of eIPP-adduct oxidation in 8 M guanidine, pH 6. A, Displaying the absorption change leading to the intermediate; B, Continuation of A, from the intermediate to product. Time represents the amount of time exposed to oxygen.

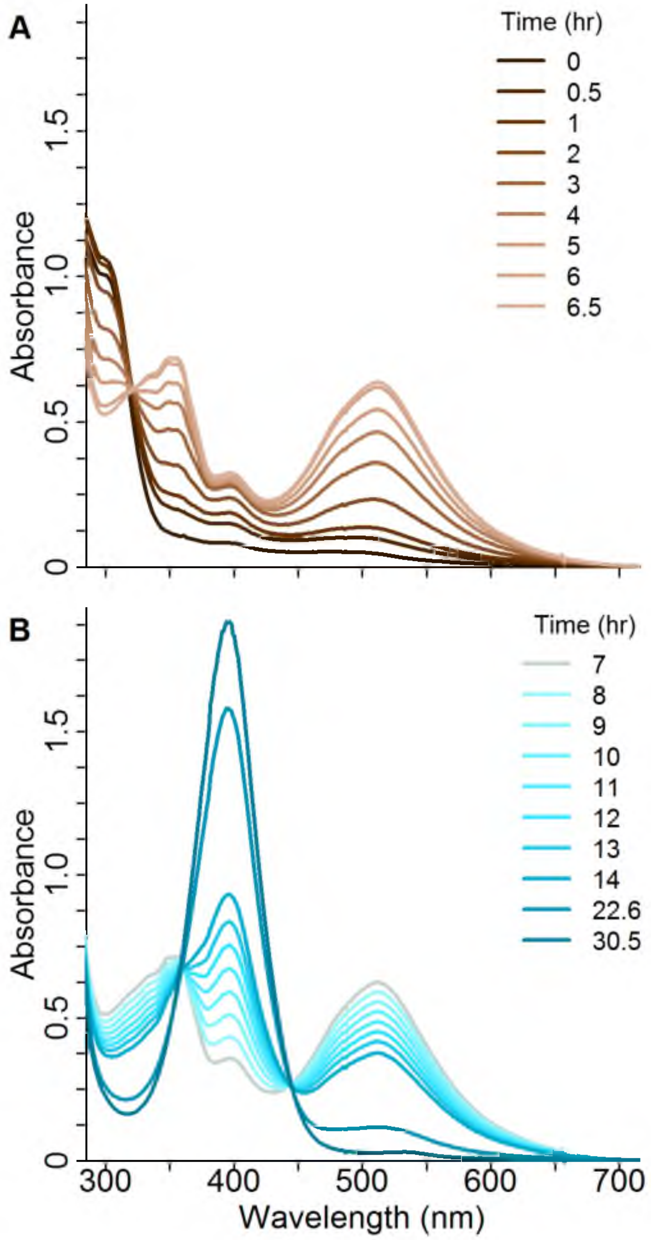

Figure 2.9. UV-vis absorption spectra of eIPP-adduct oxidation in 6 N HCl. A, Displaying the absorption change leading to the intermediate; B, Continuation of A, from the intermediate to product. Time represents the amount of time exposed to oxygen.

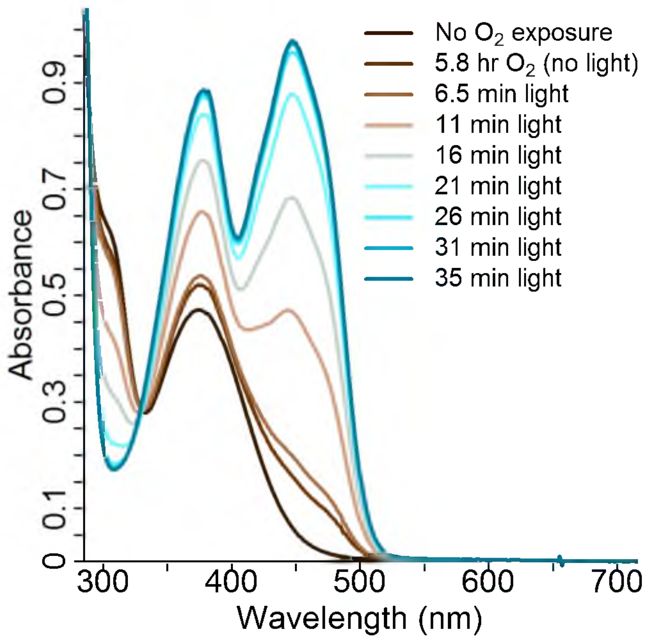

Figure 2.10. UV-vis absorption spectra of fmIPP-adduct oxidation in 8 M guanidine, pH 6.

slowly photooxidized and gave a series of spectra with well-defined isosbestic points at 293, 356 and 445 nm and a final spectrum with a peak at 395 nm, characteristic of a protonated fully oxidized flavin product (Figure 2.11.B). For the fmIPP-adduct, the oxidation results were inconsistent and present an argument against reliance on just one type of spectral evidence to conclude the position of flavin adduct formation.

Fluorescence spectroscopy of adducts. In solution, free FMN_{ox} has a fluorescence emission maximum at 525 nm and oxidized flavoproteins have similar fluorescence properties.[82] Evidence for strong fluorescence from reduced flavins has been investigated,[84,85] but further literature is lacking, presumably because of experimental difficulties that stem from the oxygen sensitivity of reduced flavins and the need for low temperatures (77 K).[86] The fluorescence emission spectra for both neutral and anionic flavin semiquinone were reported by Zhong and co-workers (Table 1.1).[87]

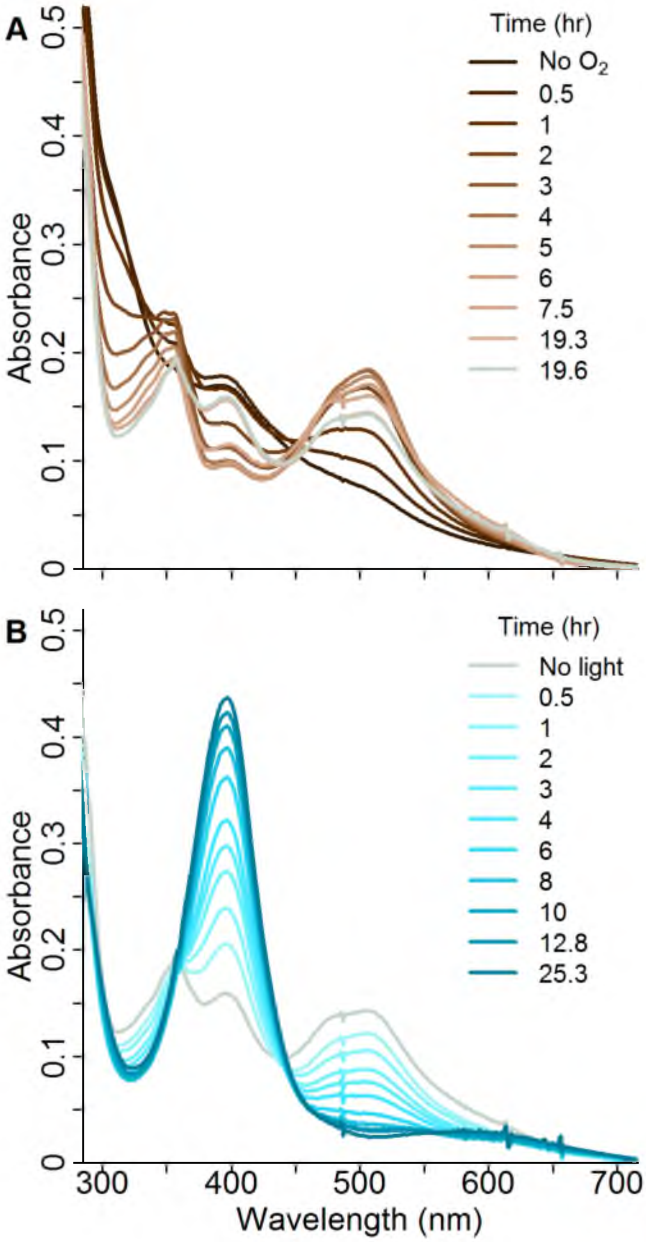

Figure 2.11. UV-vis absorption spectra of fmIPP-adduct oxidation in 6 N HCl. A, Oxidation in the absence of light; B, Continuation of A, after light exposure.

The emission spectra of a flavin adduct differs whether the bond occurs at N5 or C4a. However literature on the subject is scant. One of the few examples studied adducts isolated from lactate oxidase at 293 K and demonstrated that N5- and C4a-adducts have a fluorescence maximum at ~ 475 and 530 nm, respectively.[85] Only the adducts formed from vIPP, oIPP and eIPP were measured with fluorescence. For comparison, the fluorescence properties of IDI-2 were evaluated and are presented first.

As a control, the emission maximum for FMN_{ox} was confirmed to be 528 nm without any other unique characteristics. However, for FMN_{ox}•IDI-2, a peak at 660 nm was very intense in the presence or absence of IPP (Table 2.6 and Figure 2.12). When reduced, this peak shifted to 700 nm and the intensity diminished by about 96 %.

When emission at 530 nm was monitored, IPP•FMN_{red}•IDI-2 had a poorly defined excitation maximum at ~ 418 nm (Figure 2.13.A), similar to the absorption maximum at 426 nm (Figure 2.3). Excitation at 420 nm, gave an emission maximum at 540 nm (Figure 2.13.B). Interestingly, emission from the reduced state in the presence of IPP was about five times more intense than from the oxidized form of the enzyme.

Fluorescence spectra were collected for flavin adducts bound to IDI-2, and free from enzyme by denaturation of the complex with 8 M guanidine, pH 7 or by 6 N HCl (Table 2.7). Excitation of enzyme-bound adducts at 295 nm yielded similar results to

Table 2.6. *Tt*-IDI-2 fluorescence properties.

Flavin State	Substrate	Excitation λ_{max} (nm)	Emission λ_{max} (nm) λ_{excite} = 295 nm	Emission λ_{max} (nm) λ_{excite} = 420 nm
Oxidized	None	348	660	520
	IPP	354	660	515
Reduced	None	366	700	515
	IPP	418	538, 700	540

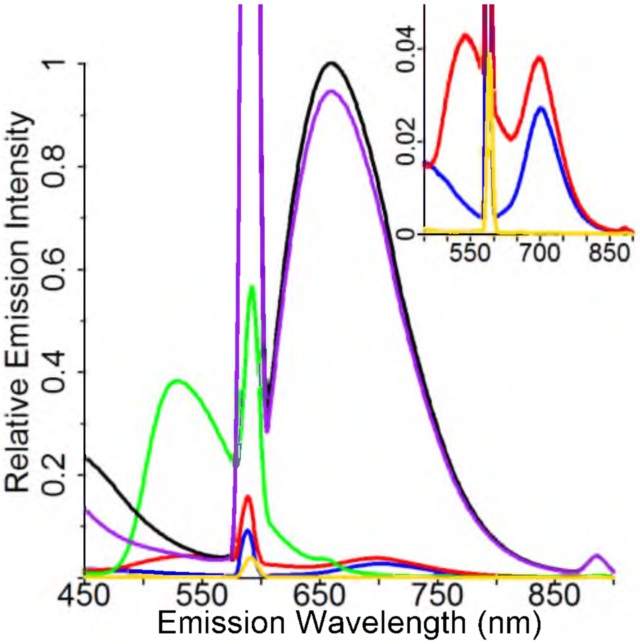

Figure 2.12. Fluorescence emission spectra with excitation at 295 nm of *Tt*-IDI-2 under various conditions. Inset is scaled in to highlight the characteristics of the less intense spectra. Lines represent: FMN_{ox} (green), FMN_{red} (yellow), FMN_{ox}•IDI-2 (black), IPP•FMN_{ox}•IDI-2 (purple), FMN_{red}•IDI-2 (blue), IPP•FMN_{red}•IDI-2 (red). Note: sharp peaks in around 580 nm are Raman peaks for water.

FMN_{OX}•IDI-2, where a very intense emission was seen at 660 nm. Additionally, the vIPP-adduct had a shallow peak at 523 nm and the eIPP-adduct had an intense peak at 470 nm (Figure 2.14.A). In 8 M guanidine, pH 7, each adduct fluoresced at ~ 530 nm with a second peak at ~ 664 nm that overlapped with a Raman peak from water (Figure 2.14.B). For the spectra in 6 N HCl, each adduct fluoresced at 460 nm. However these peaks were not considered significant because of their low intensity (Figure 2.14.C).

Additional emission spectra were collected with excitation at 350 nm, which was an excitation maximum for FMN_{ox}•IDI-2 when emission was monitored at 530 nm (Figure 2.12.B). With 350 nm excitation, enzyme-bound adducts fluoresced at ~ 450 – 470 nm, and were intense compared to the FMN_{red}•IDI-2 and IPP•FMN_{red}•IDI-2 species (Figure 2.15.A). The adducts in pH 7 each fluoresced at 530 nm with a smaller peak at

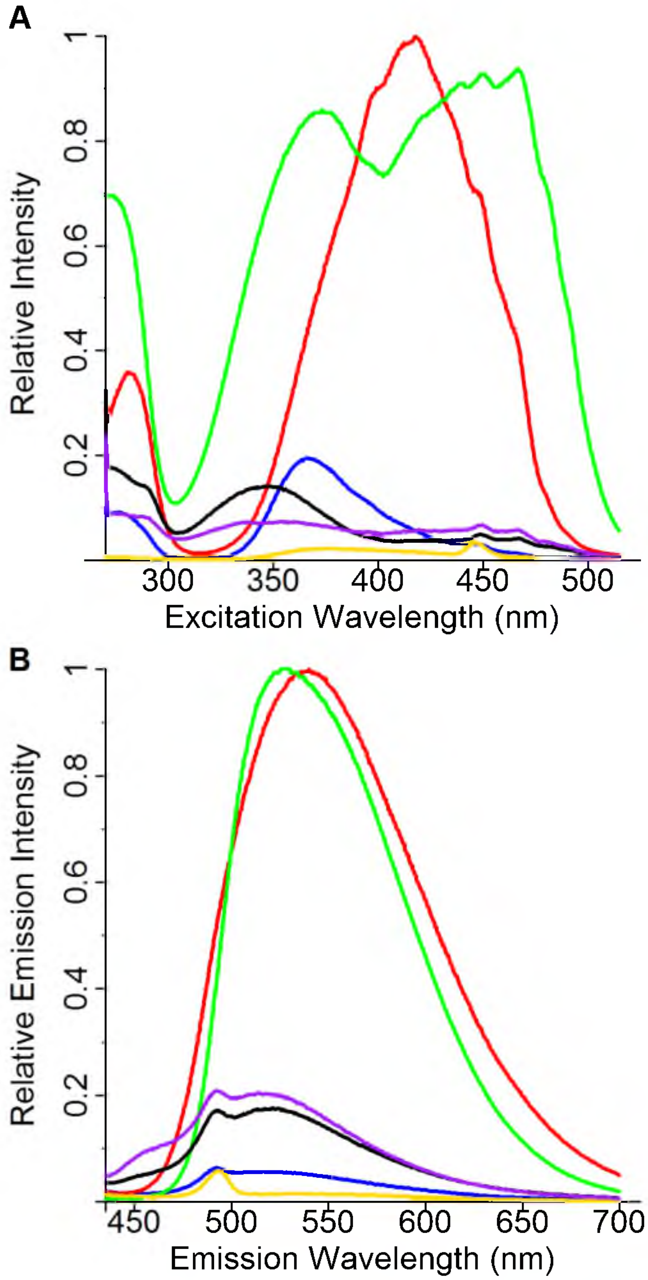

Figure 2.13. Fluorescence excitation spectra of *Tt*-IDI-2 under various conditions. A, Monitoring emission intensity at 530 nm (FMN_{ox} spectrum decreased 85 %); B, Emission spectrum with excitation at 420 nm (FMN_{ox} spectrum normalized to have the same peak height as IPP•FMN_{red}•IDI-2, ~ 87% decrease). Lines represent: FMN_{ox} (green), FMN_{red} (yellow), FMN_{ox}•IDI-2 (black), IPP•FMN_{ox}•IDI-2 (purple), FMN_{red}•IDI-2 (blue), IPP•FMN_{red}•IDI-2 (red).

Table 2.7. Fluorescence properties of adducts formed from substrate analogues.

Condition	Substrate Analogue	Emission λ_{max} (nm) $\lambda_{excite} = 295$ nm	$\lambda_{excite} = 350$ nm	$\lambda_{excite} = 420$ nm
Bound	vIPP	523, 664	450	537
	oIPP	664	457	525
	eIPP	470, 664	470	475
pH 7	vIPP	531, ~664	430, 530	529
	oIPP	537, ~664	435, 530	530
	eIPP	528, ~664	432, 531	533
6 N HCl	vIPP	460	453	~460
	oIPP	460	451	553
	eIPP	460	452	-

~ 430 nm. Control spectra were collected for FMN_{ox} and FMN_{red} at pH 7, with excitation at 350 nm and they fluoresced at ~ 430 and 530 nm, respectively (Figure 2.15.B). It appears that the adducts possess characteristics of both flavin redox species, which would indicate that the adducts were a population of both N5- and C4a-adducts. In 6 N HCl (Figure 2.15.C), the peak intensities were ~ 1 % or less than the most intense peak observed at 350 nm excitation and were not considered significant.

The emission seen upon excitation at 420 nm revealed an important difference between the vIPP- and oIPP-bound adducts and the eIPP-bound adduct. Emission maxima for vIPP and oIPP were observed at ~530 nm, while the eIPP maximum was 475 nm (Figure 2.16.A). These values correspond to C4a- (530 nm) and N5- (475 nm) adducts as observed for a C4a-adduct in D-amino acid oxidase and an N5-adduct in lactate oxidase.[84] Contrary to the enzyme-bound observations, when these adducts were isolated and measured in pH 7, each fluoresced at ~ 530 nm. The fluorescence spectra collected for the adducts in 6 N HCl have an insignificantly small intensity (Figure 2.16.C).

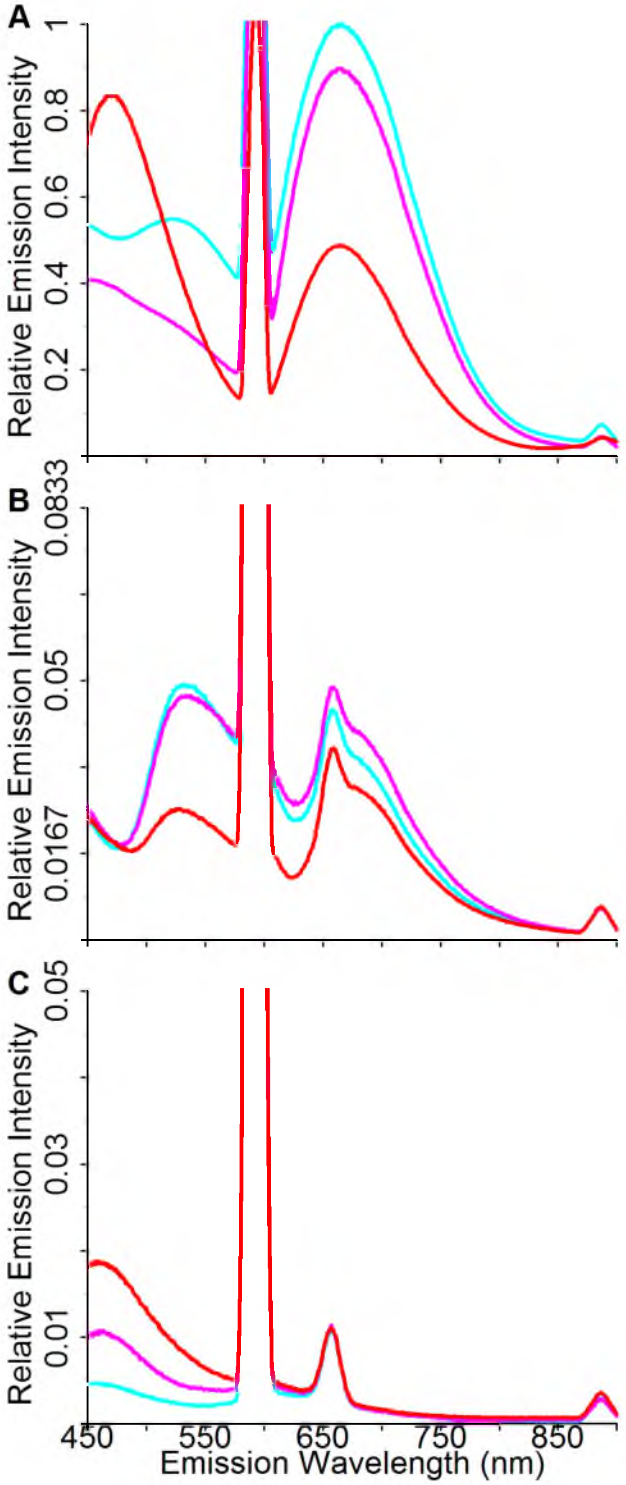

Figure 2.14. Fluorescence spectra of *Tt*-IDI-2 adducts formed from substrate analogues under various conditions with excitation at 295 nm. A, Emission spectra of bound adduct; B, Emission spectra of adduct isolated with 8 M guanidine, pH 7; C, Emission spectra of adduct isolated with 6 N HCl. Lines represent: vIPP- (cyan), oIPP- (magenta), and eIPP- (red) adducts.

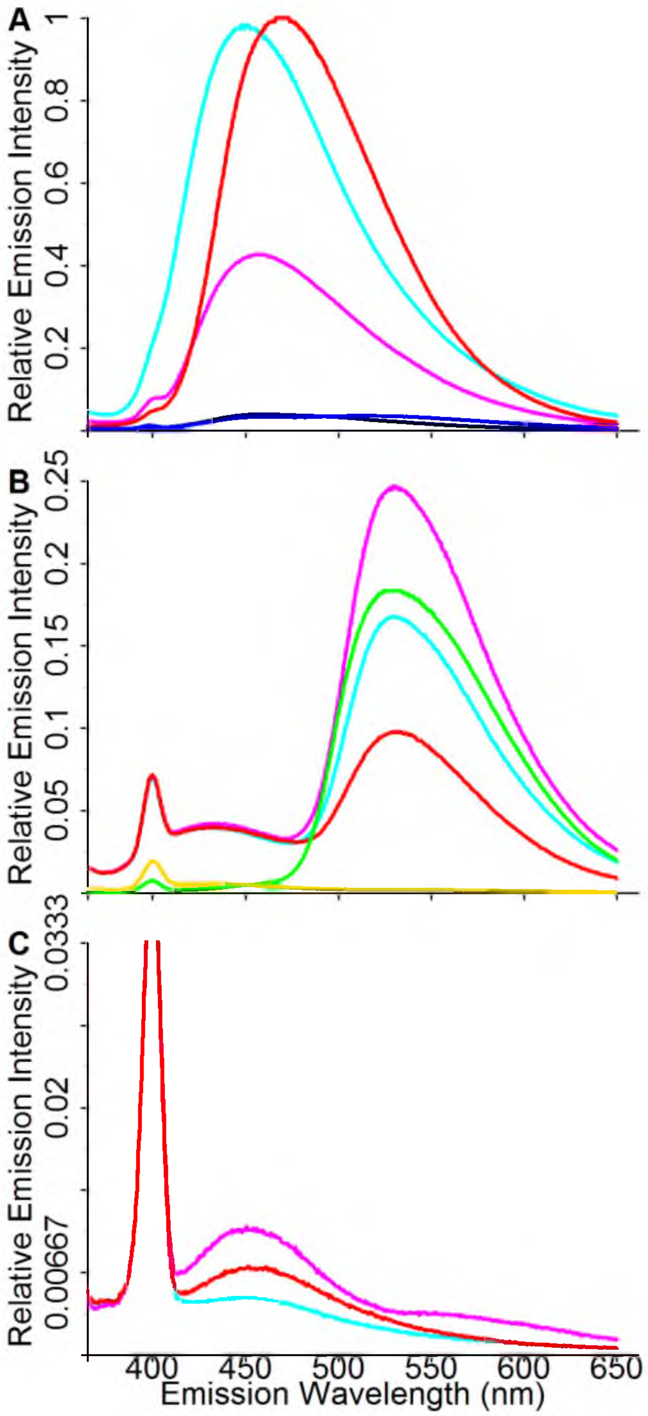

Figure 2.15. Fluorescence spectra of *Tt*-IDI-2 adducts formed from substrate analogues under various conditions with excitation at 350 nm. A, Emission spectra of bound adduct with FMN_{red}•IDI-2 (black) and FMN_{red}•IDI-2•IPP (blue); B, Emission spectra of adducts isolated with 8 M guanidine, pH 7 with FMN_{red} (yellow) and FMN_{ox} (green) (spectrum decreased by 80 %); C, Emission spectra of adduct isolated with 6 N HCl. Lines represent: vIPP- (cyan), oIPP- (magenta), and eIPP- (red) adducts.

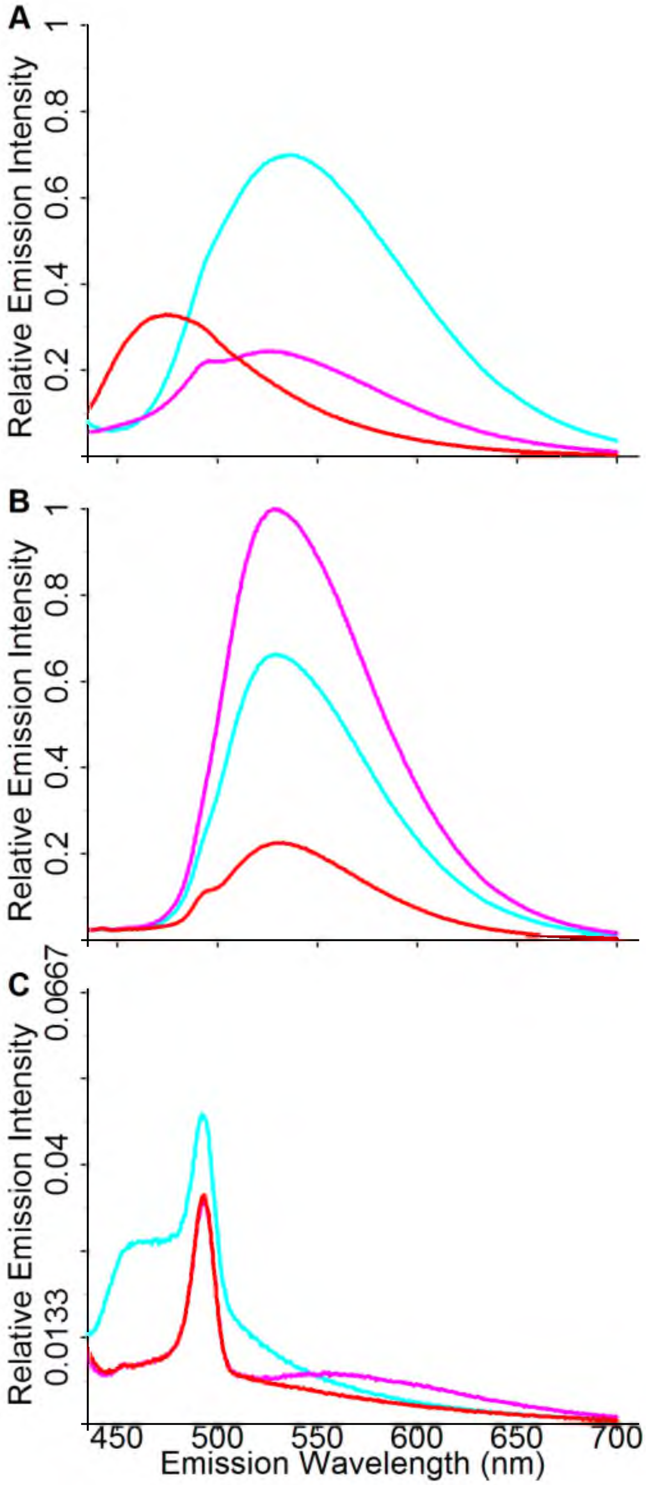

Figure 2.16. Fluorescence spectra of *Tt*-IDI-2 adducts formed from substrate analogues under various conditions with excitation at 420 nm. A, Emission spectra of bound adduct; B, Emission spectra of adduct isolated with 8 M guanidine, pH 7; C, Emission spectra of adduct isolated with 6 N HCl. Lines represent: vIPP- (cyan), oIPP- (magenta), and eIPP- (red) adducts.

UV-vis spectroscopy of non-adduct forming substrate analogues. In addition to the analogues described above, other substrate analogues did not show evidence of adduct formation. The (*R*)- and (*S*)-2fIPP compounds were not irreversible inhibitors for IDI-1.[55] cIPP was an alternate substrate for IDI-2 and did not covalently modify the flavin cofactor as determined by mass spectrometry (Figure 2.17).[68] For these compounds, UV-vis absorption assays provided sufficient evidence that adduct formation did not occur.

After a 24 h incubation, the enzyme was washed with buffer and the collected spectrum for each analogue was similar to that of FMN_{red}•IDI-2 (Figure 2.18 and Table 2.8). The (*R*)- and (*S*)-2fIPP analogues were further evaluated with guanidine denaturation. The spectra of the isolated flavin product resemble that of neutral reduced flavin with shoulders at ~ 280 and ~ 400 nm (Figure 2.19).[130] The products isolated by denaturation with 6 N HCl resemble protonated radical flavin with peaks at 258, 358, and 488 nm (Figure 2.20).[130] Based on the other spectral evidence, the partial oxidation in 6 N HCl was not likely the result of degradation of an N5-adduct, but rather an artifact due to the long-lived radical stabilized in 6 N HCl as observed in Figure 2.9 for the degradation of the eIPP-adduct.

Analysis of eIPP oxidation pathway. The oxidation pathway of the eIPP-adduct isolated with guanidine (Figure 2.8) was modeled with MCR-ALS to determine the

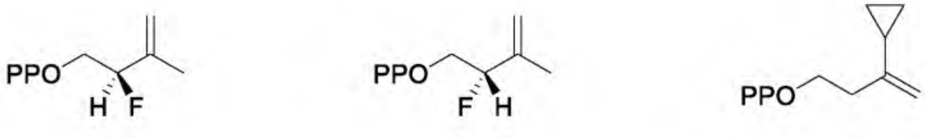

R-2fIPP S-2fIPP cIPP

Figure 2.17. IPP analogues that did not produce FMN-adducts.

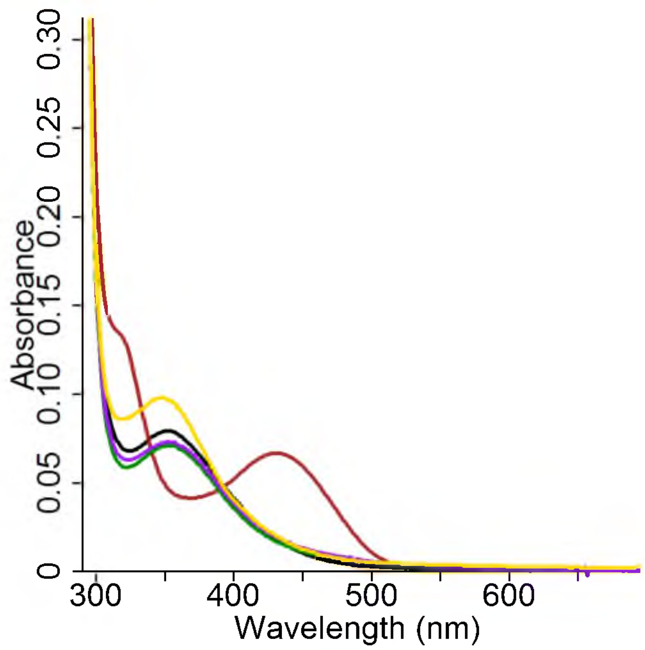

Figure 2.18. UV-vis absorption spectra of IDI-2 bound IPP analogues. Lines represent R-2fIPP (dark green), S-2fIPP (purple), cIPP (yellow), FMN_{red}•IDI-2 (black) and IPP•FMN_{red}•IDI-2 (brown). Spectra were normalized for absorption at 280 nm.

Table 2.8. UV-vis absorption properties of IPP analogues that do not form FMN adducts in IDI-2.

Flavin Isolation Method	Assay Condition	Maxima (nm)	Minima (nm)	Shoulders
Enzyme-bound	**R-2fIPP**	354	322	
	S-2fIPP	354	323	
	cIPP	347	318	
8 M guanidine, pH 6	**R-2fIPP**			292, 353
	S-2fIPP			291, 353
	cIPP	n.p.	n.p.	n.p.
6 N HCl	**R-2fIPP**	315, 492	299, 394	251, 280, 352
	S-2fIPP	315, 492	295, 393	260, 355
	cIPP	315, 492	264, 391	356

n.p. = not performed

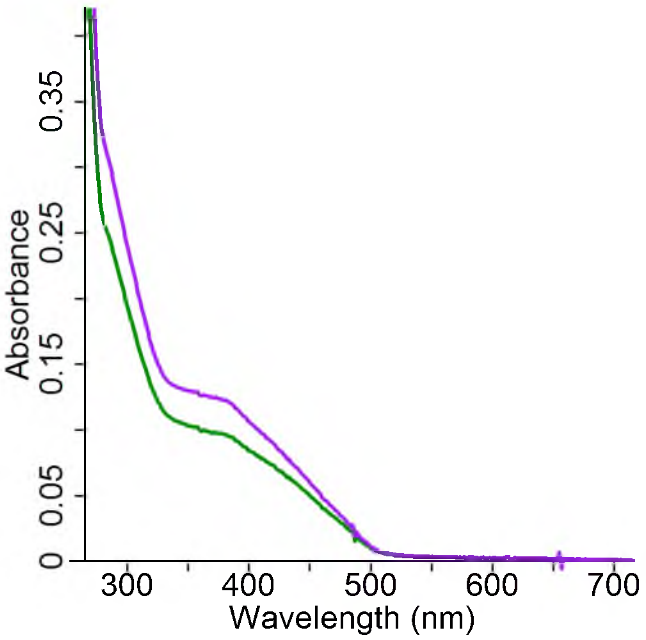

Figure 2.19. UV-vis absorption spectra of isolated FMN product in 8 M guanidine, pH 6. Lines represent R-2fIPP (dark green), S-2fIPP (purple).

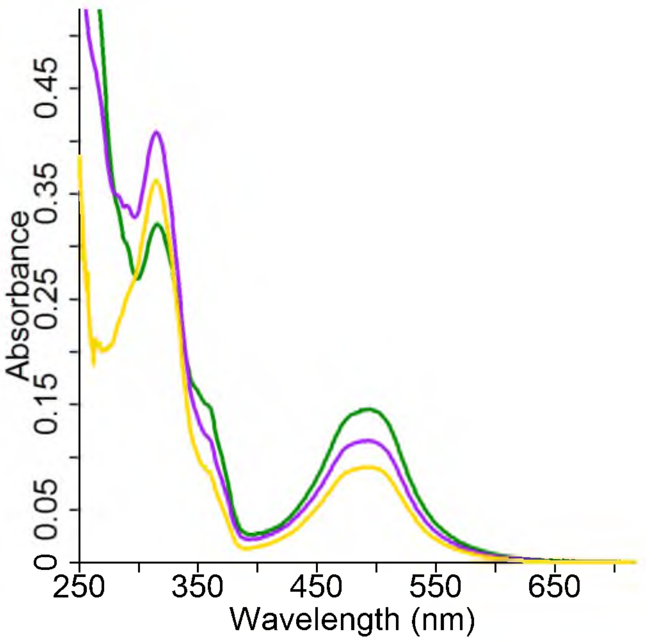

Figure 2.20. UV-vis absorption spectra of isolated FMN product in 6 N HCl. Lines represent R-2fIPP (dark green), S-2fIPP (purple) , and cIPP (yellow).

number of species that are observed spectroscopically and how their concentrations change with time. Spectra were truncated at 300 nm to simplify the analysis. When only three species were assumed in the oxidation pathway, the time course obtained is shown in Figure 2.21.A and the corresponding spectra of the major species are shown in Figure 2.21.B. While the optimized spectra correspond well to the eIPP-adduct, radical and oxidized flavin species, the time course revealed a bimodal concentration profile for the eIPP-adduct, where the adduct is converted to the radical intermediate, which then decays to FMN_{ox} and then back to the reduced adduct. However, oxidation of a reduced FMN species is considered to be essentially irreversible,[131] and formation of a large population of FMN_{red} in the presence of O_2 is unlikely. Therefore, the bimodal model was rejected and a four species model was evaluated.

When four species were evaluated, the optimization still resulted in a bimodal appearance for the eIPP-adduct (Figure 2.22.A). The spectrum of the unknown species had an absorption maximum at 375 nm with a smaller peak at 450 nm (Figure 2.22.B). These peak positions corresponded well to the spectrum of FMN_{ox}, but had different intensities (Figure 1.25). To correct for the bimodal eIPP-adduct concentration, another MCR-ALS analysis was performed with the concentrations for the radical adduct and FMN_{ox} as they appear in Figure 2.22.A. For the eIPP-adduct, only the concentration values up to the appearance of the second peak were used, and the concentration after that point was fixed at zero. The unknown intermediate concentration was determined by subtracting the summation of all the flavin concentration values from the TFC. Next, these concentration values were fixed so only the spectra were optimized in a single iteration MCR-ALS analysis. This analysis resulted in a time course with four distinct

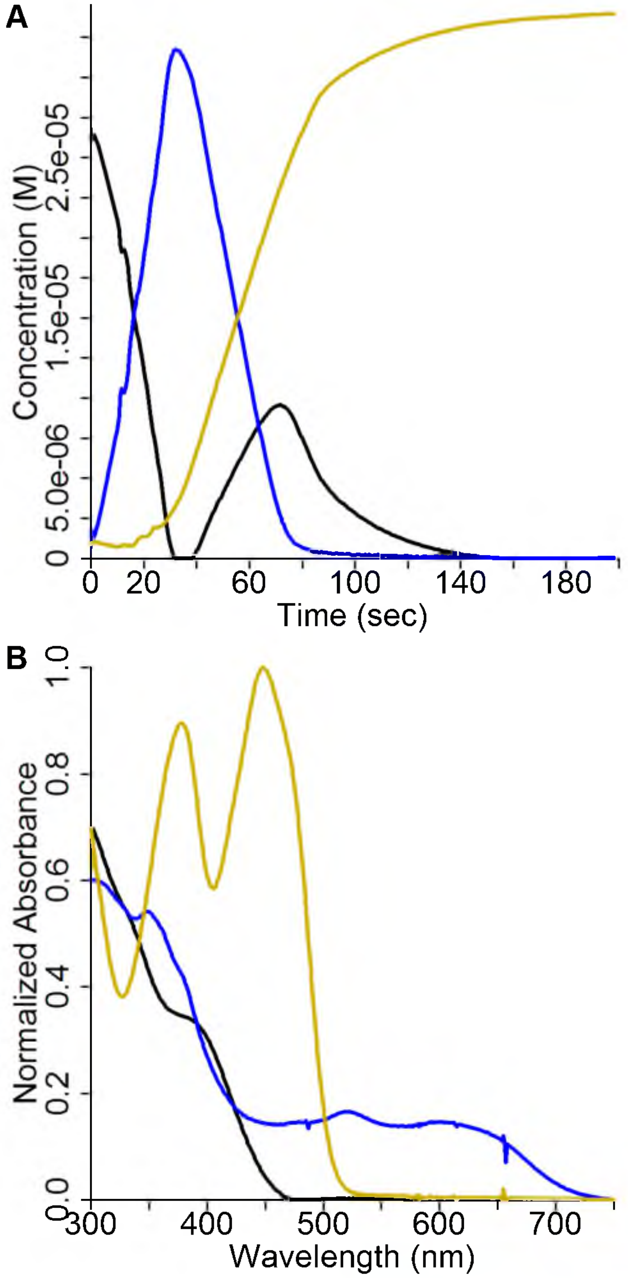

Figure 2.21. MCR-ALS results for the oxidation of the eIPP-FMN adduct with three species. A, Time course; B, Spectra of the species in the time course. Lines represent eIPP-FMN adduct (black), eIPP-FMN radical (blue), FMN_{ox} (gold).

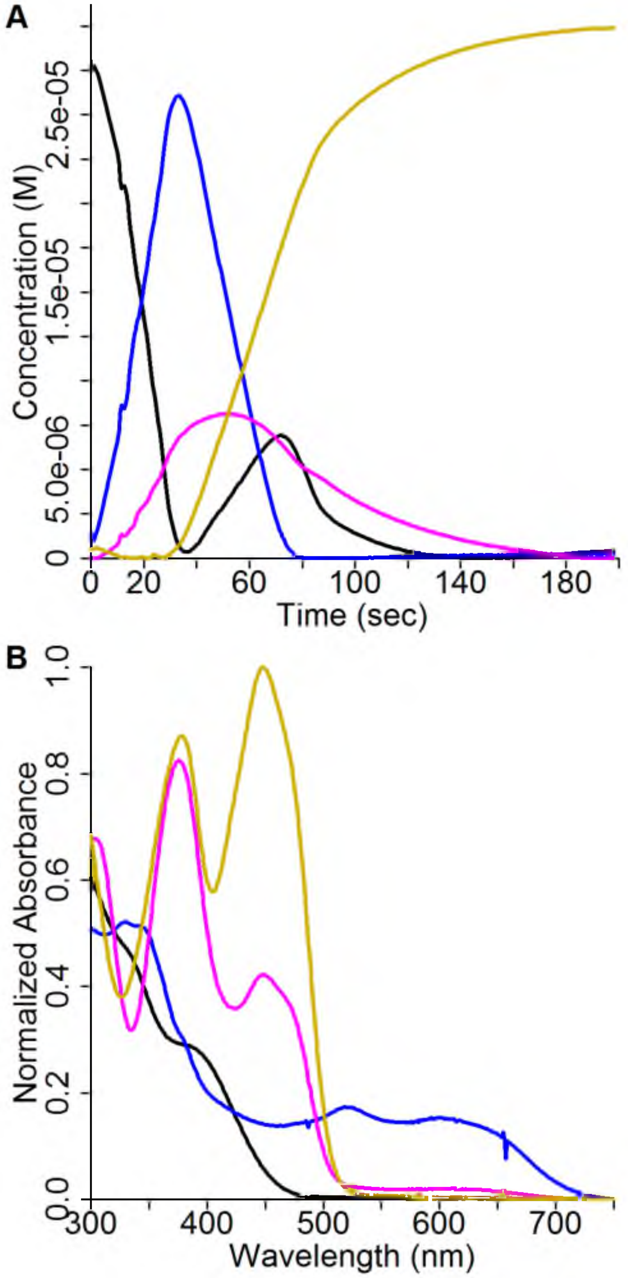

Figure 2.22. MCR-ALS results for the oxidation of the eIPP-FMN adduct with four species, optimized model. A, Time course; B, Spectra of the species in the time course. Lines represent eIPP-FMN adduct (black), eIPP-FMN radical (blue), FMN$_{ox}$ (gold) and unknown intermediate (magenta).

species and spectra that all differ from one another (Figure 2.23).

While the time course was not completely optimized (restricted to a single iteration), the spectrum of the unknown intermediate had some characteristics of reported flavin species. The peak at ~ 450 nm had noticeably decreased from Figure 2.22.B, but the peak at 375 nm remained and a peak or shoulder at ~ 300 nm was more intense (Figure 2.23.B). N5-alkylated flavins with a 4a-OOH or 4a-OCH_3 group have peak maxima at 374 and 363, respectively, along with another peak at ~ 310 nm (in methanol).[132] A peroxy-adduct or pseudobase have been proposed as intermediates in the oxidation of N5-alkylated flavins.[132] Since the spectrum was calculated and not directly observed, no conclusions will be drawn other than the species is an N5-eIPP-FMN adduct with a 4a-peroxy or hydroxyl group.

An attempt was made to model the calculated time course in Figure 2.23.A based on Table 2.2. Differential equations based on this scheme were used to estimate the rate of change in the concentration of the eIPP-adduct, radical adduct and FMN_{OX}. From these, the concentration of the unknown intermediate (5-RFl_{OX}^{+}) could be calculated by subtracting the summation of the other three flavin species from the TFC. For this experiment, oxygen concentration was a variable to avoid any assumptions about the rate of oxygen diffusion. A stir bar mixed the solution in the cuvette and the introduction of oxygen was not monitored. The optimum parameter values are in Table 2.9, without error terms. The traces formed from these rate constants are shown in Figure 2.24, overlaid with the traces from the time course of Figure 2.23.A.

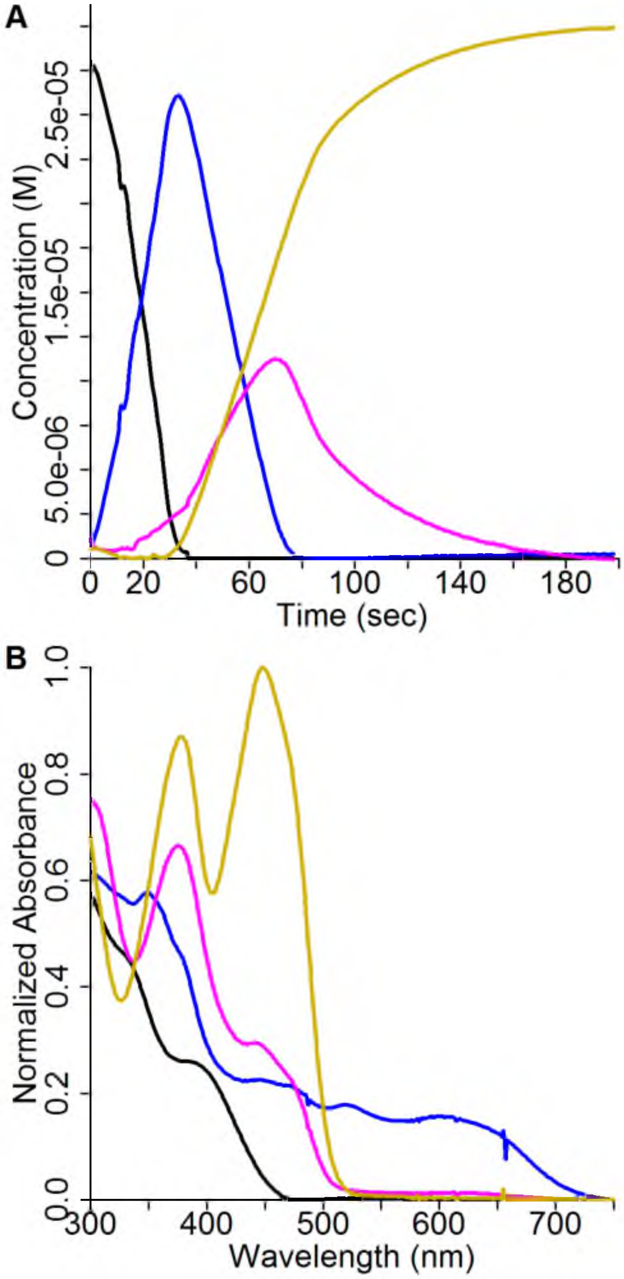

Figure 2.23. MCR-ALS results for the oxidation of the eIPP-FMN adduct with four species, model correcting for bimodal eIPP-FMN adduct trace. A, Time course; B, Spectra of the species in the time course. Lines represent eIPP-FMN adduct (black), eIPP-FMN radical (blue), FMN$_{ox}$ (gold) and unknown intermediate (magenta).

Table 2.9. Parameter estimates for the oxidation of the eIPP-FMN adduct according to Table 2.2.

Parameter	Value (units)
k_1	10 $M^{-1} min^{-1}$
k_2	5.2 x 10^4 $M^{-1} min^{-1}$
k_3	300 $M^{-1} min^{-1}$
k_4	4.5 x 10^{-2} $M^{-1} min^{-1}$
[O_2]	1.0 x 10^{-4} M
TFC	3.01 x 10^{-5} M

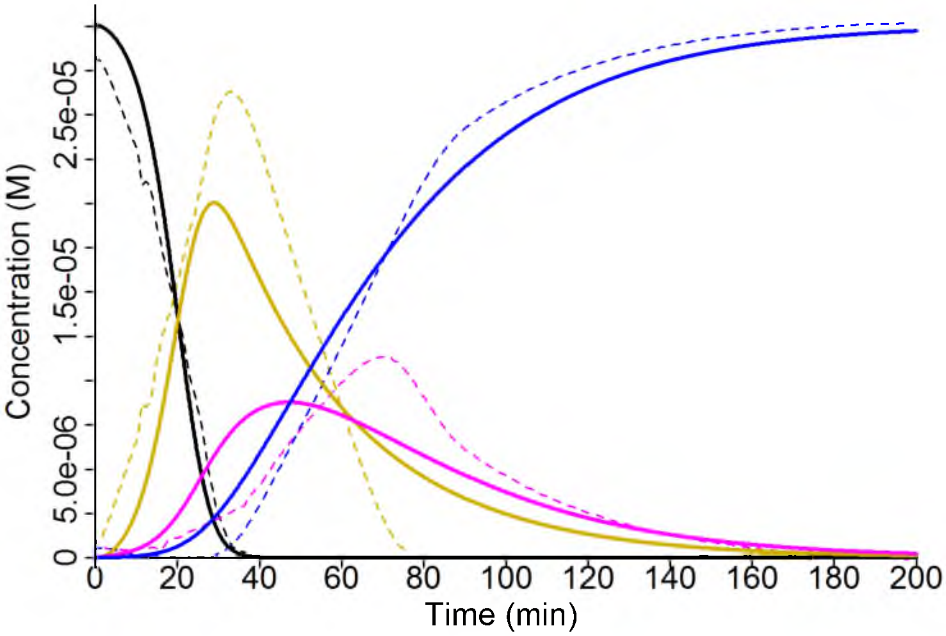

Figure 2.24. Overlaid time course for the oxidation of the eIPP-FMN adduct with four species. Solid lines are the genoud fit to the MCR-ALS time course of the oxidation of the eIPP-FMN adduct according to Table 2.2 with parameter values in Table 2.9. Dotted lines are traces from the MCR-ALS analysis (Figure 2.23.A). Lines represent eIPP-FMN adduct (black), eIPP-FMN radical (blue), FMN_{ox} (gold) and unknown intermediate (magenta).

Discussion

Previous studies indicated that the IPP analogues vIPP, oIPP, eIPP and fmIPP formed N5 adducts with flavin when incubated with IDI-2. In these experiments, FMN was reduced photochemically or with NADPH and samples were washed with buffer that was not O_2-free.[68] However, these flavin adducts were O_2 sensitive and required anaerobic conditions for comprehensive study. In addition, the adducts that were isolated by denaturation of the enzyme in acidic conditions were previously measured in 5 % trifluoroacetic acid, pH 0.5. The pKa value for the N1-position of oxidized flavin is 0, while the pKa value for the N5-position is < 0.[133] Thus, a lower pH was needed to protonate flavin.

Spectroscopic reevaluation of the adducts in strict anaerobic conditions determined adduct formation for vIPP, oIPP and fmIPP at the C4a-position, while the eIPP-adduct was at the N5-position. In agreement with these findings, crystal structures performed by Hemmi and co-workers found that the C4a-position resulted in a better fit to the electron density map for the vIPP- and oIPP-adducts.[58]

The fluorescence properties of the adducts indicate that at room temperature, isolated adducts have spectral properties that are misleading. When enzyme-bound, the properties are consistent with those reported in the literature and are likely a result of the enzyme environment that prevents movement of the isoalloxazine backbone of flavin. One improvement to the measurement of isolated adducts would be to observe them at low temperatures (77 K).

During catalysis, there is a proposed tertiary carbocationic intermediate at C3 of IPP. Based on crystal structures of the *S. shibitae* IDI-2, the carbocation is 3.1 Å from the

C4a-position of flavin.[58] The positive charge is stabilized by a partial negatively charged carbon atom at the 4a-position in the flavin ring system. For some of the substrate analogues above, the C4a carbon acted as a nucleophile. vIPP is initially an alternative substrate where the C5 methylene abstracts a proton from FMN, which yields a delocalized carbocation that undergoes nucleophilic attack by the flavin C4a carbon to the vIPP C6 carbon (Figure 2.25.A).[58] The oIPP-adduct forms by first protonation of the epoxide ring,[67] followed by nucleophilic attack by the flavin C4a carbon which causes the oxiranyl ring to open (Figure 2.25.B).

These conclusions can be extended to inhibitors that formed adducts and do not yet have structural information. For fmIPP, protonation of the double bond likely does

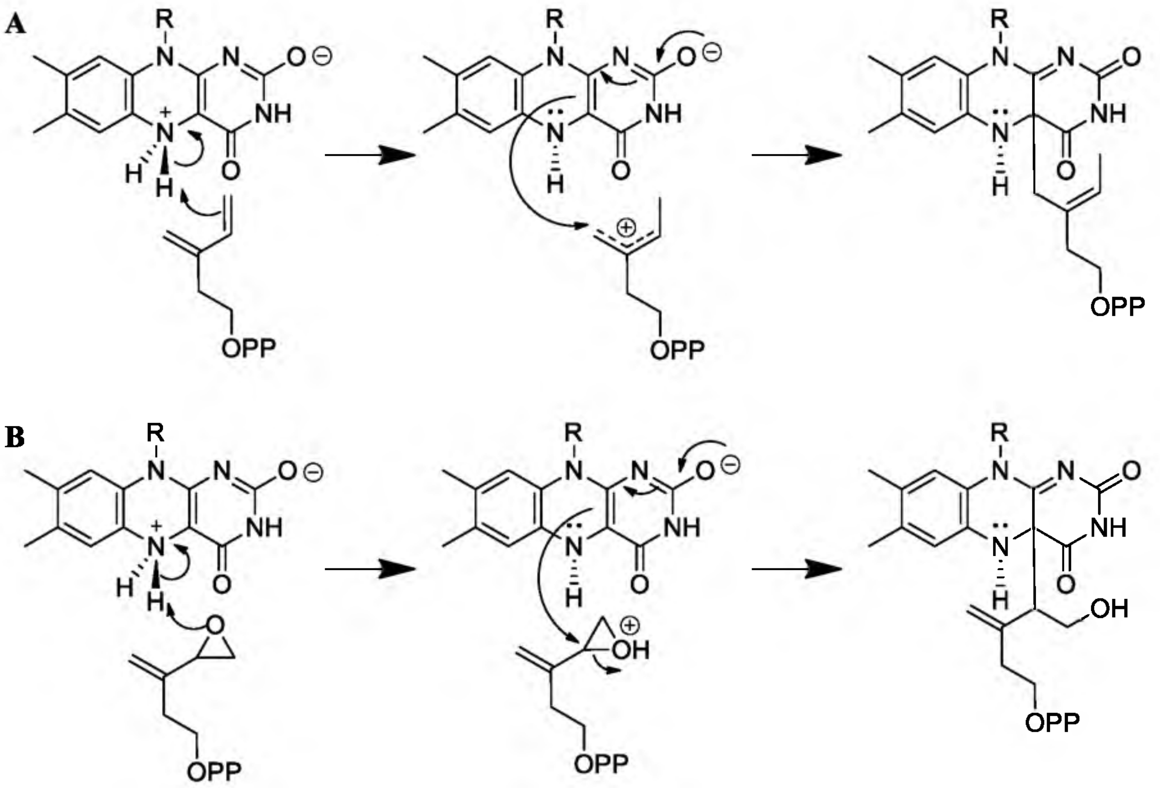

Figure 2.25. Proposed mechanisms for the formation of a flavin adduct with: A, vIPP; and B, oIPP.

not occur because of the electron withdrawing fluorine. Direct nucleophilic attack of the flavin C4a carbon occurs at the fmIPP methylene carbon, which causes the double bond to shift to the C3-C5 bond with subsequent release of fluoride (Figure 2.26). Another possible mechanism is the direct attack of the flavin C4a to the fmIPP 5-methyl carbon with fluoride as the leaving group (Figure 2.26).

A different mechanism must take place for eIPP, which results in an N5-adduct. Based on studies performed by our group, the covalent adduct is formed by the S-eIPP enantiomer.[134] As expected, UV-vis studies with this enantiomer results in an identical spectrum as the racemic eIPP.[134] The proposed mechanism involves proton abstraction from the N5-position by the epoxide oxygen, which opens the ring and yields a tertiary carbocation (Figure 2.27). The compact active site positions the carbocation near N5, rather than near C4a, which is the normal position for IPP. The lone pair of electrons above N5, which are posed to abstract a proton from C2 of the substrate, instead act as a nucleophile and attack the carbocation to form a bond (Figure 2.27).

The formation of adducts between the FMN cofactor and substrate analogues of IDI-2 are direct evidence that FMN is involved in catalysis. With the different adducts

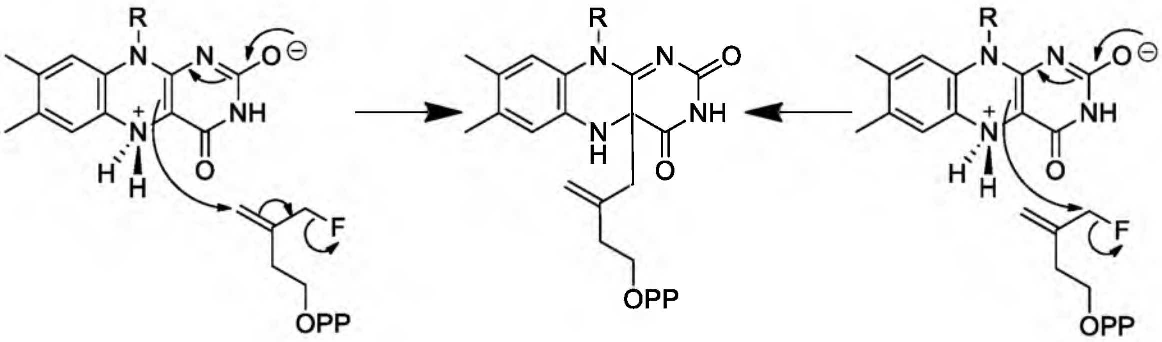

Figure 2.26. Proposed mechanisms for the formation of a flavin adduct with fmIPP.

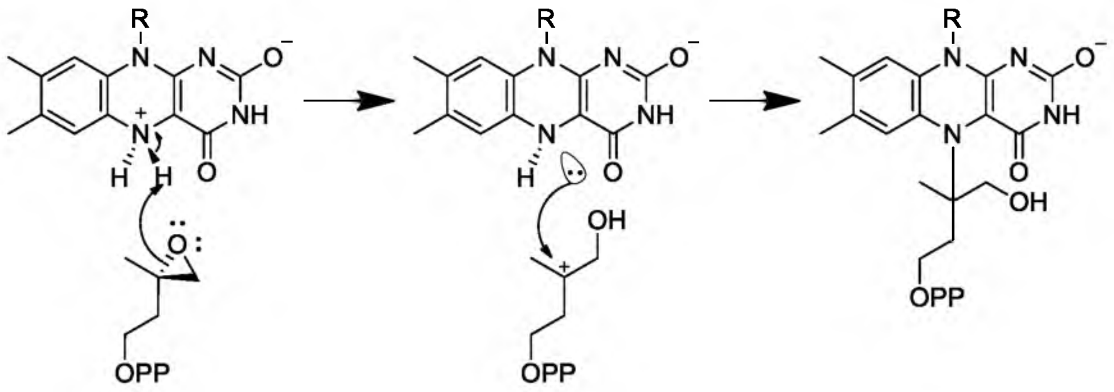

Figure 2.27. Proposed mechanism for the formation of a flavin adduct with eIPP.

that are formed, the electronic structure around the flavin N5-C4a bond can be distinguished. The evidence supports a C4a carbon with a partial negative charge that likely stabilizes a carbocationic intermediate during catalysis. The N5 nitrogen donates a proton to yield a carbocationic intermediate that is subsequently attacked by a nucleophile nearest the positive charge. Future experimentation would include exploration of flavin analogues similar to those discussed in Chapter 1 or isotopically labeled at the N5 and C4a positions. The reactions in Table 2.2 are an oversimplification of the true oxidation of a flavin adduct but support the statistical analysis. The chemistry involved in flavin adduct oxidations has been studied,[126] but not comprehensively. Comparatively, the oxidation of reduced flavins/flavoproteins has been studied extensively and is a well-known seven step process.[131]

The equilibrium of the comproportionation reaction for an N5-adduct (Eq. 2.5) lies heavily towards radical formation.[126] The calculated results agree with this observation since the rate of radical formation was fast compared to the other rates (Table 2.9). If a parameter was included to account for the disproportionation (the reverse reaction of Eq. 2.5), no significant improvement in the fit was observed. The rate of oxygen reactivity toward the reduced and radical N5-adducts (k_1 and k_3) appeared to be significantly slower than that observed in the literature. 3,5-Dimethyl-dihydrolumiflavin and 1-carba-1-deaza-5-ethyl-dihydrolumiflavin reacted with oxygen at rates of 0.6 – 1.8 x 10^3,[132] and 3.9 x 10^3 M^{-1} min^{-1},[135] respectively. When in the radical oxidation state, these same compounds reacted with oxygen at rates of 24 and 37.8 x 10^3 M^{-1} min^{-1}, respectively. Note that the 3,5-dimethyl-dihydrolumiflavin radical is less reactive towards oxygen than the eIPP-adduct. The differences observed are likely a result of the method of oxygen addition. For the eIPP-adduct, oxygen was allowed to diffuse into solution, while for the lumiflavin adducts, anaerobic solutions that contained the adduct were added to aerobic solutions via syringe or a stopped-flow apparatus. Another difference may be the form of flavin that was studied. Lumiflavin lacks the ribityl phosphate group present in FMN. Decay rates of several minutes and hours were observed for the oxidation of N5-FMN adducts formed with lactate oxidase.[129]

The original hypothesis was that the spectra collected for the oxidation of an eIPP-adduct could be deconvoluted and that estimates for the rates of oxidation could be calculated. The deconvolution was possible, but based on the rate results, there are inadequacies that require improvement. Future experiments would benefit from greater restriction over the introduction of oxygen; such restrictions would include monitoring the oxygen concentration, the introduction of oxygen into the cuvette (control of the stirring rate), and monitoring the amount of light being received by the sample. The lack of strict control limits the confidence in the rate values as general descriptors of oxidation rates for N5-flavin adducts.

CHAPTER 3

MECHANISM-BASED INACTIVATION OF ISOPENTENYL DIPHOSPHATE:DIMETHYLALLYL DIPHOSPHATE ISOMERASE BY THE NATURAL SUBSTRATES ISOPENTENYL DIPHOSPHATE AND DIMETHYLALLYL DIPHOSPHATE

Introduction

Spectroscopic evidence indicated that when FMN is bound in *Tt*-IDI-2 and reduced, the cofactor is in the anionic state.[63] Based on density functional theory (DFT) calculations, a delocalized HOMO is directly above C4a of the anionic reduced isoalloxazine flavin backbone.[77] The discovery that catalytically active IDI-2 produces FMN adducts with inhibitors is an indication that the partially negative C4a carbon may help stabilize a tertiary carbocationic intermediate (Chapter 2).[58]

In this chapter, a description of the same experiments of Chapter 2 is presented but with IPP and DMAPP, the natural substrates of IDI-2. After overnight incubations of the substrates with IDI-2, a substantial change was seen in the UV-vis absorption spectrum. Based on characteristics in UV-vis spectra, the position of the adduct was determined to be at the C4a-carbon of flavin. Mass spectrometry revealed that two different adducts formed. However, these adducts were formed after long-term incubations (overnight for one type and more than 3 weeks for the second type). While the reaction may not be biologically relevant, the one isoprene unit adduct was observed in all mass spectra, including controls and those previously collected by our group.

Experimental Procedures

Materials. IPP, DMAPP, GPP and FPP were available from previous experiments. $^{13}C_5$-IPP was provided by Dr. Aquiles E. Leyes. Powdered TiO_2, ZrO_2, Nb_2O_5 and graphite were from SkySpring Nanomaterials, Inc. Guanidine was from usb/Affymetrix. NADPH was from rpi. Other chemicals were from Sigma-Aldrich.

IDI-2 adduct preparation, isolation and UV-vis spectroscopic analysis. His-tagged *Tt*-IDI-2 was expressed and purified as previously described (Chapter 2).[58] Adduct preparation assays and analyses were performed as previously described,[58] with the following modifications (similar to Chapter 2). All assays were performed in an anaerobic chamber (O_2 < 5 ppm) with solutions degassed by cycling argon purging with gas evacuation and allowed to equilibrate in the chamber for a minimum of 7 d. Enzyme and substrate were transferred to the anaerobic chamber the day of reaction. Assay solutions were 100 μM FMN•IDI-2 and 800 μM substrate, in 200 mM HEPES, pH 7.0 containing 2 mM $MgCl_2$ and 8 mM $Na_2S_2O_4$, and were incubated overnight up to 7 d at 37 °C. Isolation of the adduct was performed in the following ways: 1) Denaturation of the enzyme in 3.6 M guanidine/2 M KBr (denaturation buffer) followed by filtration through a 30kD MWCO ultrafiltration device (Amicon) or 2) His-tagged IDI-2 was applied to a Ni-IDA column (Affymetrix) and washed with denaturation buffer. Denaturation was also performed using 6 N HCl. Freshly prepared 6 N HCl was critical. Otherwise the sample would degrade before a spectrum could be measured.

Sample preparation for ESI-MS analysis. Initially, the same mass spectrometry method was used as for previous adduct studies.[68] However, for a pure spectrum of the adduct, IDI-2 was washed 5 times with 50 mM ammonium acetate and then washed with denaturation buffer and filtered through a 30kD MWCO ultrafiltration device (Amicon). Excess metal oxide (TiO_2, ZrO_2 or Nb_2O_5) was added to the flow through that contained the FMN-adduct and the sample was vortex shaken for 30 min. The metal oxide was spun down at 15,000 *g* and the supernatant removed. Impurities were removed with three cycles of washing the metal oxide with 10 mM Bis-Tris, pH 6.0 containing 150 mM NaCl (Bis-Tris buffered saline, or Bis-TBS), vortexing to resuspend the powder then centrifuging at 4000 *g* to remove the supernatant. To elute the adduct, 200 mM sodium phosphate, pH 6.0 was added and the sample was vortex shaken for 5 min. The metal oxide was separated by centrifugation at 15,000 *g*, and the supernatant that contained the adduct was removed. As an additional enrichment step, the solution was applied to graphite powder, washed three times with 50 mM ammonium acetate and the adduct eluted with 50 mM ammonium acetate in 30 % acetonitrile. In a different enrichment procedure, the metal oxide step was skipped, and the deflavination solution was directly applied to graphite and eluted as above.

Samples subjected to TOF ESI-MS (Waters LCT Premier XE) were analyzed with the following parameters, in negative ion mode: capillary 2.5 kV, cone 55 – 100 V, scanned from *m*/*z* 50 – 1000 and for positive ion mode: 3.5 kV, 150 V and *m*/*z* 400 – 2000, respectively. Samples from graphite purification were analyzed in negative ion mode, with parameters: capillary 2.5 – 2.8 kV, cone 10 V, scanned from *m*/*z* 50 – 1100.

Samples were also subjected to UPLC (Waters Aquity with PDA detector) under the conditions: negative ion capillary 2 kV, cone 30.0 – 35 V, extractor 3 – 4.6 V. Mobile phase A: 50 mM ammonium acetate, pH 7.0; B: Acetonitrile. Gradient conditions in % A (time elapsed in min): 99 (0), 99 (1), 0 (5), 0 (6), 99 (8). Flow rate 0.5 mL/min. 10 μL injection volume. Column: Waters Aquity UPLC BEH Phenyl 1.7 μm. Diode array collection from 200 – 460 nm, scanned from *m/z* 100 – 1000.

Kinetics of adduct formation. Inactivation experiments were performed in an anaerobic chamber with solutions pre-equilibrated for a minimum of 7 d in the chamber. Enzyme (500 nM) was incubated with IPP (0 and 0.28 – 97 mM) at 37 °C up to 7 d in 200 mM HEPES, pH 7.0 containing 2 mM $MgCl_2$ and 40 μM dithionite. Aliquots were removed at set time points and assayed using the acid lability assay,[63] with 50 μM ^{14}C-IPP in 200 mM HEPES, pH 7.0 containing 2 mM $MgCl_2$, 2 mM NADPH and 40 μM FMN. Activity was determined for all samples and then added to the activity lost at each time point because of enzyme degradation (the 0 mM IPP sample). First order rate constants were determined for each [IPP]; these observed rates were then plotted against [IPP] and fit to the Michaelis-Menten equation to calculate k_{inact} and K_i.

Isoprene production. Assays were prepared as for the UV-vis adduct assays described above, except were reduced with NADPH and were performed without anaerobic conditions. Reagents were mixed in headspace GC vials and were sealed with an air-proof screw-top cap. Incubations were performed for various times (each time point used a separate vial), and reactions were terminated by placing the vial on ice. Conditions varied both substrate (IPP or DMAPP) and presence or absence of the reductant. Headspace GC-MS analysis was performed at Danisco US Inc. (a division of Genencor), monitoring for both total ions and a $[M+1]^+$ of 69 for isoprene.

Results

UV-vis spectroscopic analysis. Control spectra were collected with enzyme reduced in an anaerobic chamber, then washed 5 times with 25 mM NH_4CO_3 to remove reductant. A spectrum was collected of FMN_{red}•IDI-2 without IPP and immediately after addition of IPP (Figure 3.1). The adduct was observed when reduced enzyme was incubated with IPP for 24 h in an anaerobic chamber. The enzyme was washed to remove excess and unbound IPP and both the adduct bound IDI-2 and the control FMN_{red}•IDI-2 (without IPP) were measured. A peak shift from 353 nm for FMN_{red}•IDI-2 to 344 nm for FMN_{red}•IDI-2 with IPP indicated that a change in the flavin cofactor occurred during the incubation (Figure 3.1).

The cofactor was isolated with a deflavination solution (3.6 M guanidine/2 M

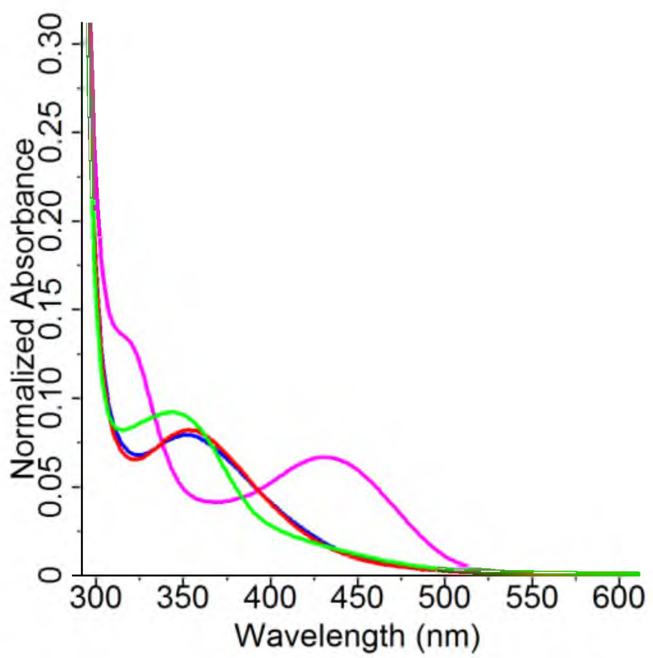

Figure 3.1. UV-vis absorption plots of FMN•IDI-2 after reduction. Prior to measurement, samples were washed 5 times with 25 mM NH_4CO_3, pH 7.8, to remove reductant. Lines represent: No substrate (blue); Addition of IPP after washing with NH_4CO_3 (magenta); 24 incubation without substrate (red); and 24 incubation with IPP (green). Spectra normalized at 280 nm.

KBr) or 6 N HCl. A study evaluated the type of reductant (dithionite or NADPH) and the change in absorption over time (0.5, 4, 24 and 72 h). The guanidine isolated adduct appeared to be well formed after 24 h for either reductant (Figure 3.2.A and .C). However, isolation with 6 N HCl revealed the gradual appearance over time of a peak at 400 nm. This peak corresponds to a C4a-adduct (Table 2.4) and indicates the adduct was not fully formed until about 72 h (Figure 3.3.A and .C). For both reductants and adduct isolation methods, if no substrate was added, there were no significant changes in absorption (Figure 3.2.B and .D and Figure 3.3.B and .D). The characteristics for the spectra collected at 72 h are reported in Table 3.1.

Oxidation of all three forms of the modified cofactor (enzyme-bound, guanidine freed and HCl freed) was studied when sample was exposed to O_2 and light. The enzyme-bound adduct oxidized to a stable neutral radical intermediate, characteristic of the broad absorption peak around 600 nm with an isosbestic point at 485 nm (Figure 3.4). Oxidation continued to fully oxidized flavin with a maximum at 450 nm. However, the final product absorption was extremely weak and may have represented a population of FMN•IDI-2 that was not completely oxidized but existed in some other unidentifiable state.

No radical intermediate was detected for guanidine isolated adduct since there was no absorption change at 600 nm (Figure 3.5). However, there is a change with isosbestic points at 322 and 424 nm during the first 11 min. Afterwards, there appears to be a collection of different states without any distinct isosbestic points. The initial change is likely the oxidation of the adduct which leads to photodegradation at 11 min.

For the 6 N HCl isolated adduct, oxidation begins with a small peak at 400 nm

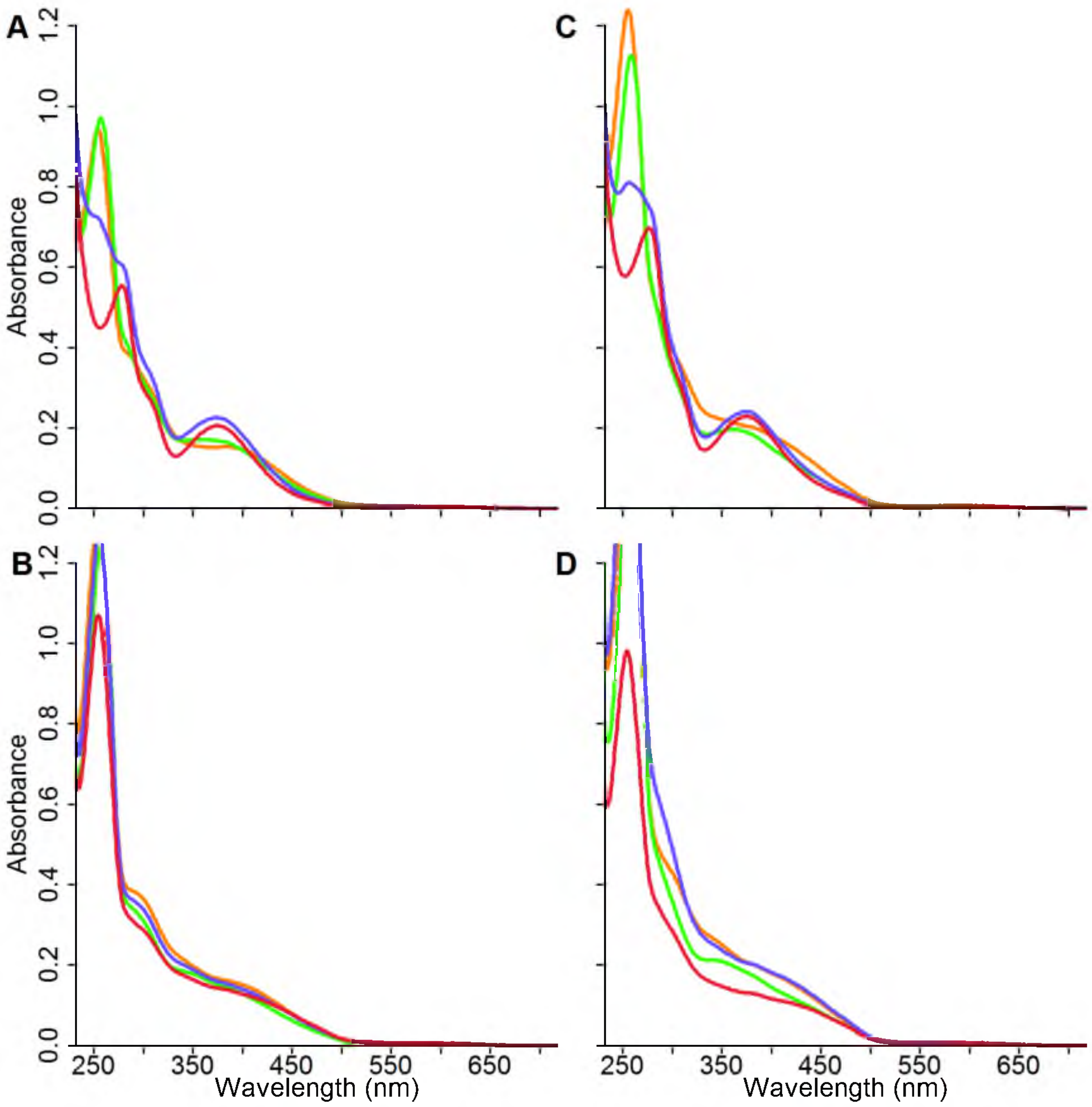

Figure 3.2. UV-vis absorption plots of isolated FMN from IDI-2 at pH 6.0 under the following conditions. A, IPP + dithionite; B, Dithionite only; C, IPP + NADPH; D, NADPH only. Lines represent 0.5 (orange), 4 (green), 24 (purple) and 72 (red) h.

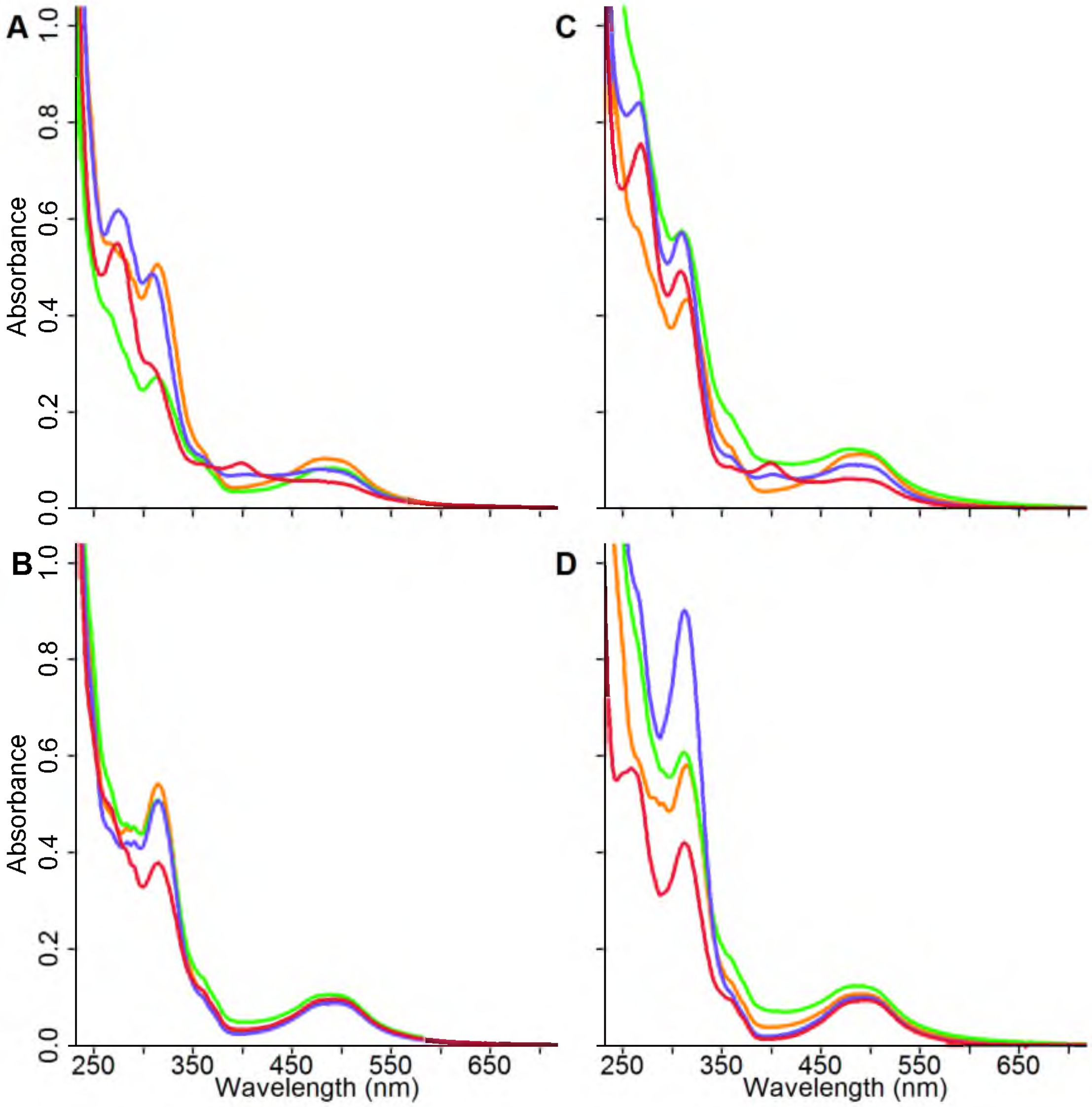

Figure 3.3. UV-vis absorption plots of isolated FMN from IDI-2 in 6 N HCl under the following conditions. A, IPP + dithionite; B, Dithionite only; C, IPP + NADPH; D, NADPH only. Lines represent 0.5 (orange), 4 (green), 24 (purple) and 72 (red) h.

Table 3.1. Absorption characteristics for deflavinated FMN under the following conditions.

Flavin Isolation Method	Assay Condition	Maxima (nm)	Minima (nm)	Shoulders (nm)
3.6 M guanidine/2 M KBr, pH 6	**Dithionite Only**	221, 254	234	296
	IPP + Dithionite	220, 278, 374	256, 332	304
	NADPH	254	233	296
	IPP + NADPH	220, 276, 375	252, 332	304
6 N HCl	**Dithionite Only**	314, 492	299, 399	262, 279, 357
	IPP + Dithionite	272, 398	257, 278	304, 356, 460
	NADPH	259, 312, 493	243, 288, 394	356
	IPP + NADPH	268, 308, 399, 489	249, 295, 377, 445	356

that results in a sharp, large (absorbance >> 2) peak at 400 nm with a noticeably bright yellow color (Figure 3.6). This transition occurs in two steps: the first gives spectra with isosbestic points at 287 and 329 nm and a spectrum with a peak at 500 nm. In the second step, the transition gives spectra with isosbestic points at 290, 354, and 447 nm and a final spectrum of protonated oxidized flavin.

The UV-vis absorption profile of FMN_{red}•IDI-2 was further examined immediately and after a long (21 d) incubation of substrate (IPP, DMAPP, GPP and FPP). Control spectra were collected immediately after addition of substrate. IPP•FMN_{red}•IDI-2 and DMAPP•FMN_{red}•IDI-2 have identical spectra with a peak maximum at 430 nm and a shoulder at 316 nm, which differ from FMN_{red}•IDI-2 that has

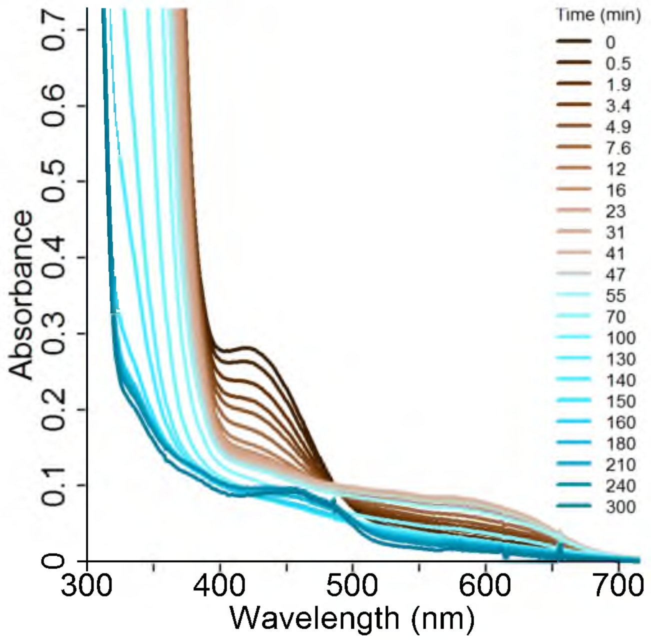

Figure 3.4. UV-vis absorption plots of FMN$_{\text{adduct}}$•IDI-2 oxidation. Time represents the time of exposure to both oxygen and light.

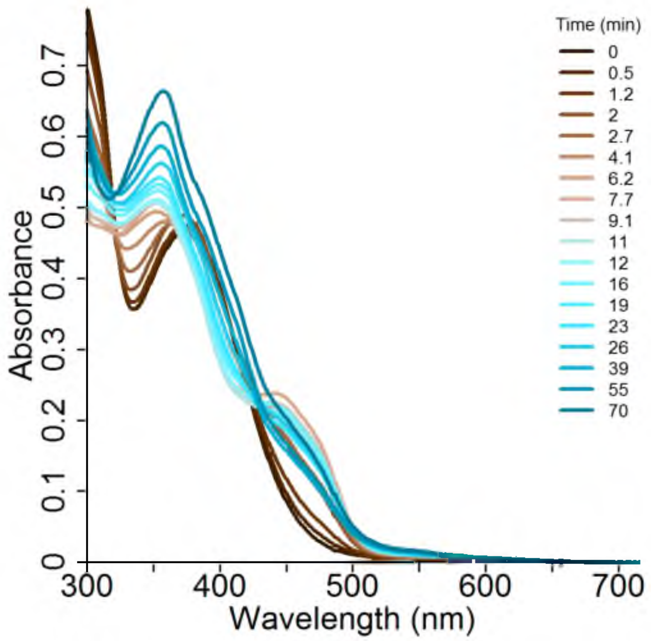

Figure 3.5. UV-vis absorption plots of oxidation of FMN$_{\text{adduct}}$ isolated using 3.6 M guanidine/2 M KBr, pH 6. Time represents the time of exposure to oxygen and light.

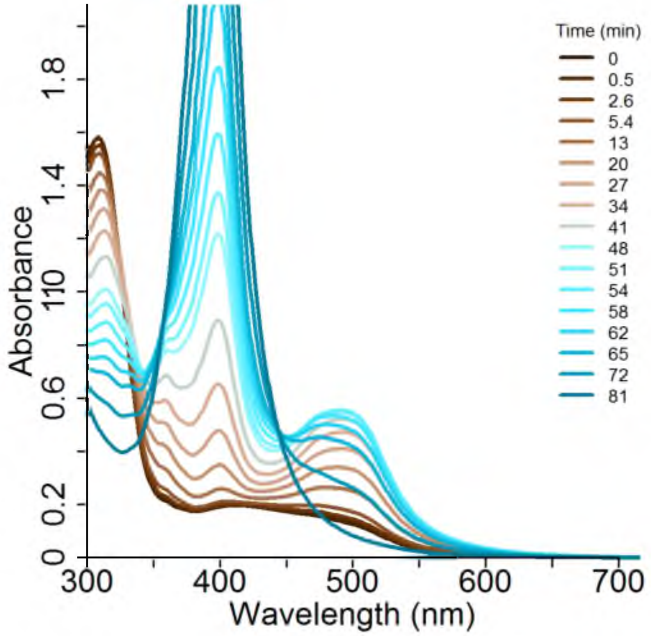

Figure 3.6. UV-vis absorption plots of oxidation of FMN$_{\text{adduct}}$ isolated using 6 HCl. Time represents the time of exposure to both oxygen and light.

a maximum at 352 nm (Figure 3.7). The absorption spectrum for GPP with FMN$_{\text{red}}$•IDI-2 has a maximum at 348 nm, similar to FMN$_{\text{red}}$•IDI-2. The solution with FPP was turbid and the absorption spectrum was void of any characteristics, perhaps because of FPP micelle formation at the high concentration needed for the adduct assays. After a 24 h incubation, the IPP•FMN$_{\text{red}}$•IDI-2 spectrum had a peak shift to 344 nm, while both FMN$_{\text{red}}$•IDI-2 and GPP with FMN$_{\text{red}}$•IDI-2 were void of a peak shift with a maximum at ~ 350 nm (Figure 3.8).

ESI-MS analysis. For mass spectrometry, the adduct isolated with denaturation buffer was enriched using a phosphoproteomics procedure.[136,137] Each metal oxide (TiO_2, ZrO_2 and Nb_2O_5) appears vibrant white in color. When FMN was added, the disappearance of yellow color in solution with subsequent yellowing of the metal oxide provided qualitative evidence of adsorption. FMN was not observed to desorb during

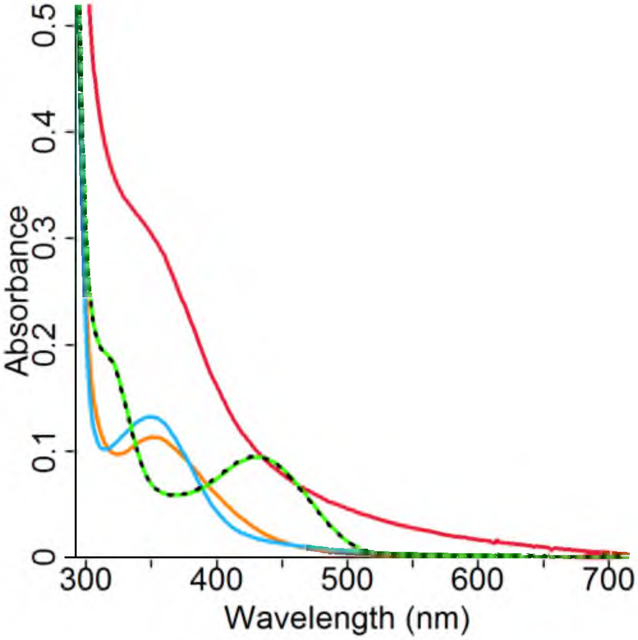

Figure 3.7. UV-vis absorption plots of FMN$_{red}$•IDI-2. Lines represent immediate addition of nothing (orange), IPP (green), DMAPP (dotted black), GPP (blue), and FPP (red).

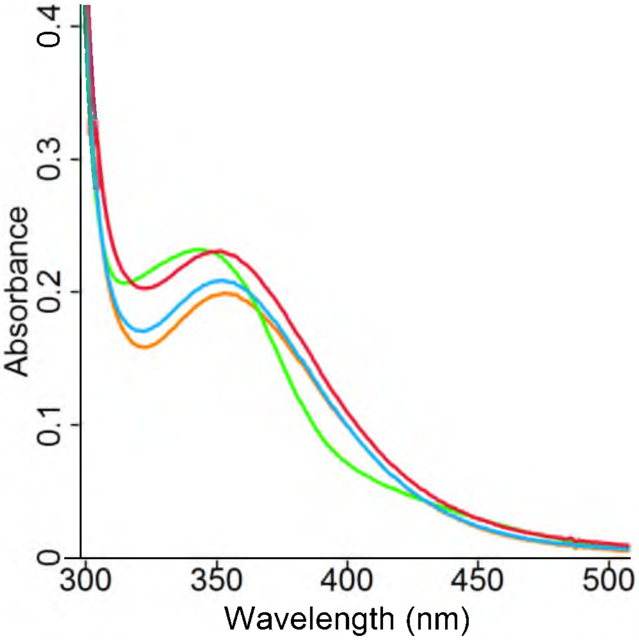

Figure 3.8. UV-vis absorption plots of FMN$_{red}$•IDI-2 after 24 h incubation. Lines represent nothing (orange), IPP (green), GPP (blue), and FPP (red).

washes. While elution is typically performed under basic conditions,[138] elution can be performed near neutral pH by including NaCl in a sodium phosphate buffer.[139] Elution with Bis-TBS, pH 6.0 resulted in ~ 60 % recovery of FMN from TiO_2 and ZrO_2, but only 8 % recovery from Nb_2O_5. Attempts to adsorb and elute IPP were unsuccessful, perhaps because of the bidentate binding of phosphate to metal oxides.[140]

To eliminate phosphate from the metal oxide elution, a second enrichment on graphite was performed.[141] Successfully used to enrich phosphoproteins for mass spectrometry,[142] and for separation of nucleosides and their corresponding phosphates,[143] the technique was modified and applied to enrich FMN. Following the metal oxide enrichment step, the graphite step resulted in a total recovery of 13.4%. When the graphite step was performed without metal oxide enrichment, recovery was 13.5%. Either the metal oxide or graphite procedures produced similar MS results (Figure 3.9).

Six different incubations with IDI-2 were performed: no substrate (control), IPP, $^{13}C_5$-IPP, DMAPP, GPP and FPP. Each spectrum contained peaks at *m*/*z* 255.2 and 455.1, which represent lumiflavin and fully oxidized FMN, respectively. The expected neutral mass of an IPP-FMN adduct would be 702.1 or 704.1 (Figure 3.10). However, no peak was observed that corresponded to either mass. Instead, a peak at *m*/*z* 525.2 was consistently observed for incubations of IPP and DMAPP with IDI-2 for different lengths of time (Figure 3.11.A and .B). The mass increase from *m*/*z* 455.1 to 525.2 corresponded to a single isoprene unit increase (Figure 3.10). To verify that isoprene was the source of this increase, IDI-2 was incubated with $^{13}C_5$-IPP. As expected, a 5-unit peak shift to *m*/*z* 530.2 was observed, which supports an isoprene-FMN adduct (Figure 3.11.D). Interestingly, the *m*/*z* 525.2 was observed in both the control, where no substrate was

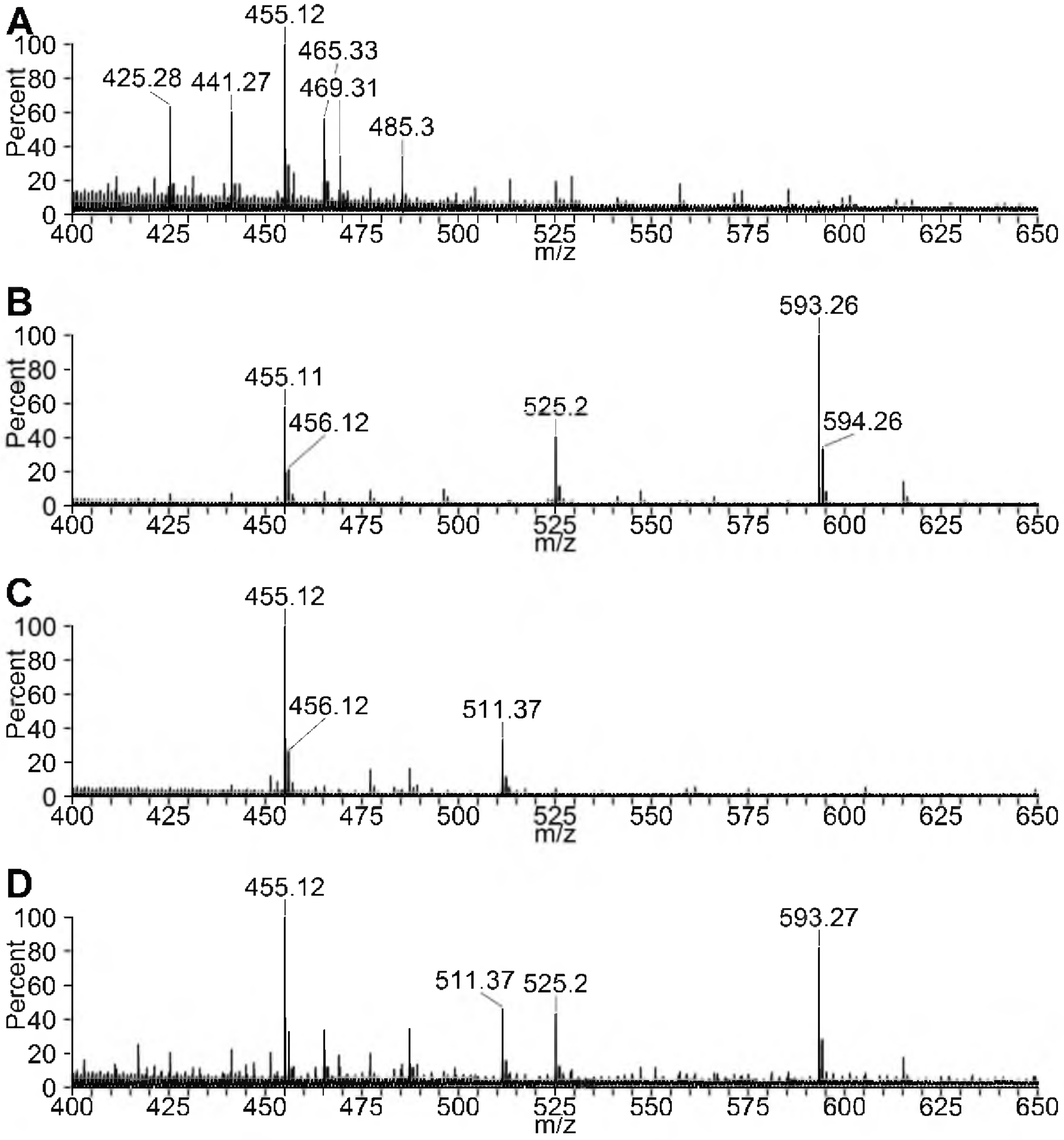

Figure 3.9. Negative ion TOF ESI mass spectrum of purified FMN from *Tt*-IDI-2 after a 21 d incubation. A, No Substrate (graphite purified); B, IPP (graphite purified); C, No Substrate (ZrO_2 purified); D, IPP (ZrO_2 purified). Note: Full spectra available in Appendix B.

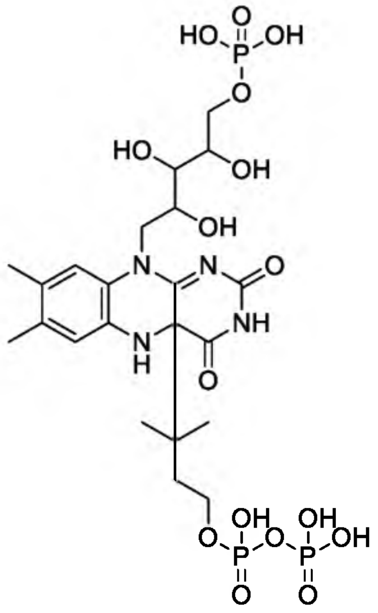

Chemical Formula: $C_{22}H_{35}N_4O_{16}P_3$
Exact Mass: 704.13

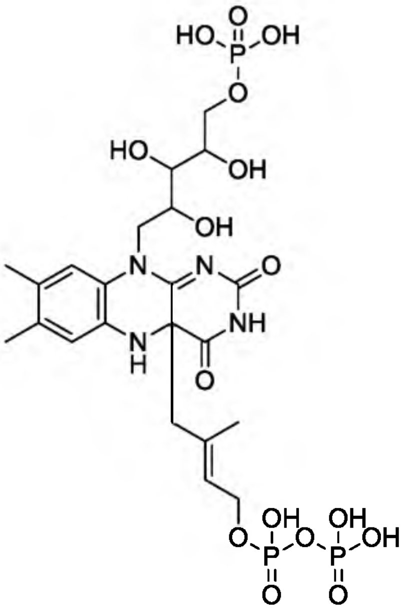

Chemical Formula: $C_{22}H_{33}N_4O_{16}P_3$
Exact Mass: 702.11

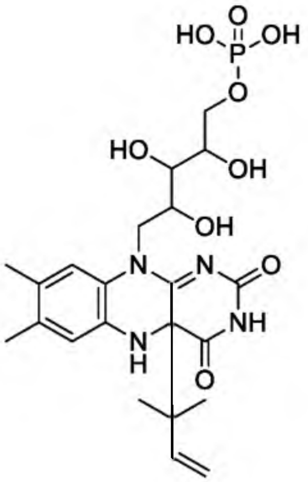

Chemical Formula:
$C_{22}H_{31}N_4O_9P$
Exact Mass: 526.18

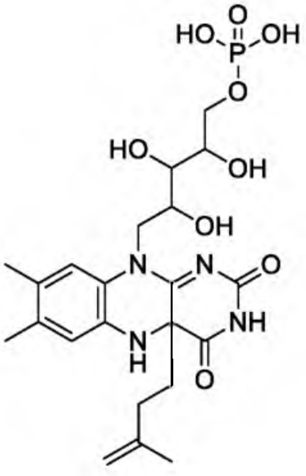

Chemical Formula:
$C_{22}H_{31}N_4O_9P$
Exact Mass: 526.18

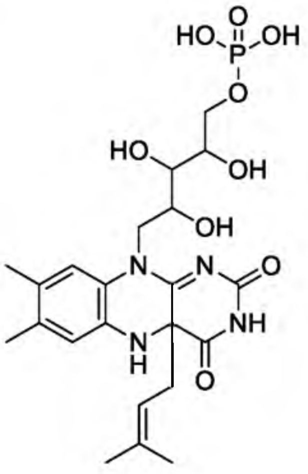

Chemical Formula:
$C_{22}H_{31}N_4O_9P$
Exact Mass: 526.18

Figure 3.10. Chemical structures and neutral masses of possible FMN adducts with IPP and isoprene. Based on UV-vis spectral evidence, only adducts at the C4a-position of FMN are displayed.

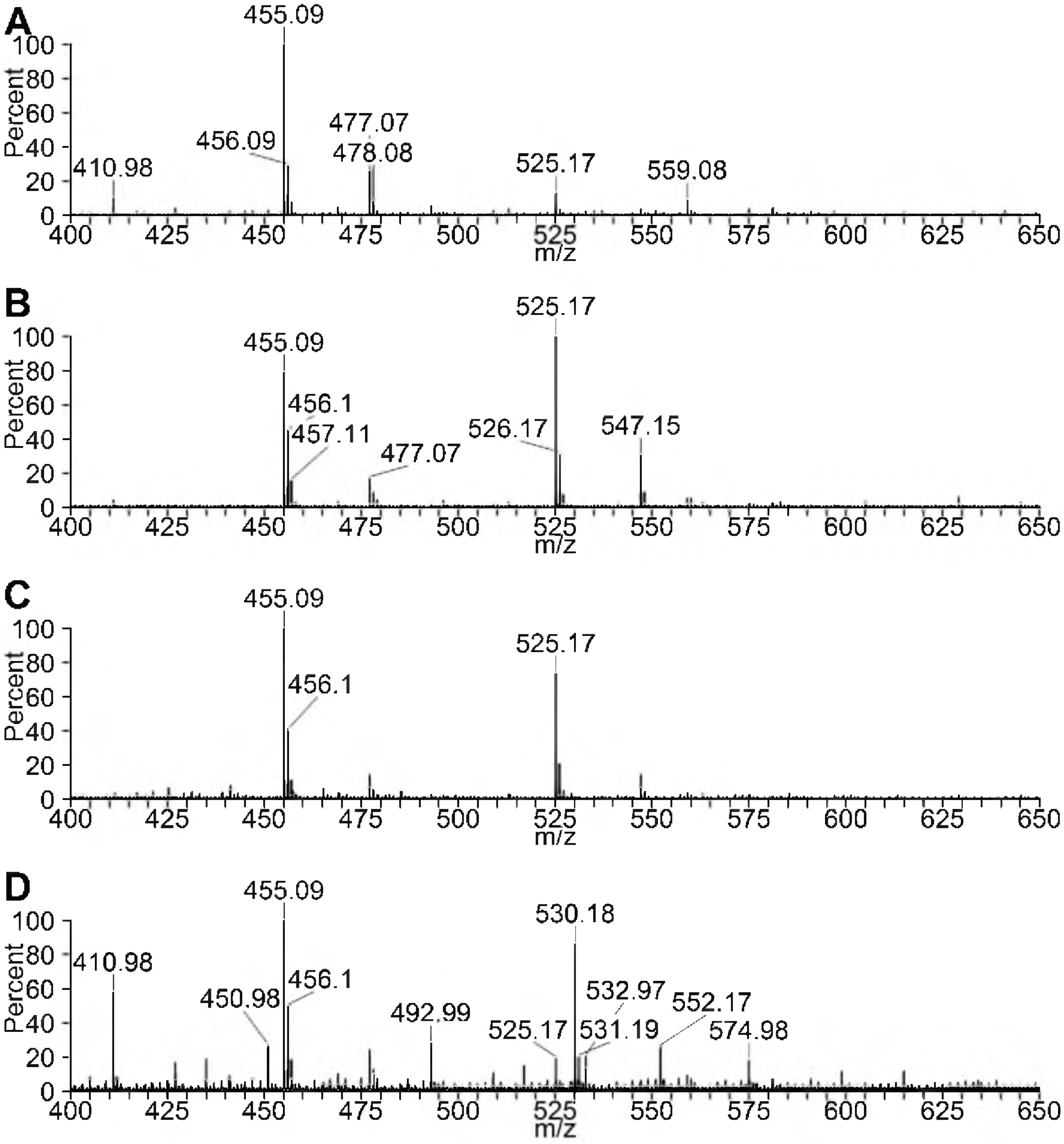

Figure 3.11. Negative ion TOF ESI mass spectrum of isolated FMN after a 24 h incubation of *Tt*-IDI-2 with different substrates. A, No Substrate; B, IPP; C, DMAPP; D, $^{13}C_5$-IPP. Note: Full spectra available in Appendix B.

incubated with IDI-2 and the $^{13}C_5$-IPP incubation (Figure 3.11.A and .D). This peak likely corresponds to adduct formation in vivo.

Another investigation involved a longer incubation of 27 d. When IPP was incubated for several weeks, a new peak appeared at *m/z* 593.2 (Figure 3.12.A) and corresponded to the addition of a second isoprene unit to the isoprene-FMN adduct (Figure 3.13). To investigate whether IDI-2 was involved with chain elongation and formation of a C_{10} prenyl unit adduct, IDI-2 was incubated with GPP or FPP. However, no adduct formation was observed (Figure 3.12.B and .C).

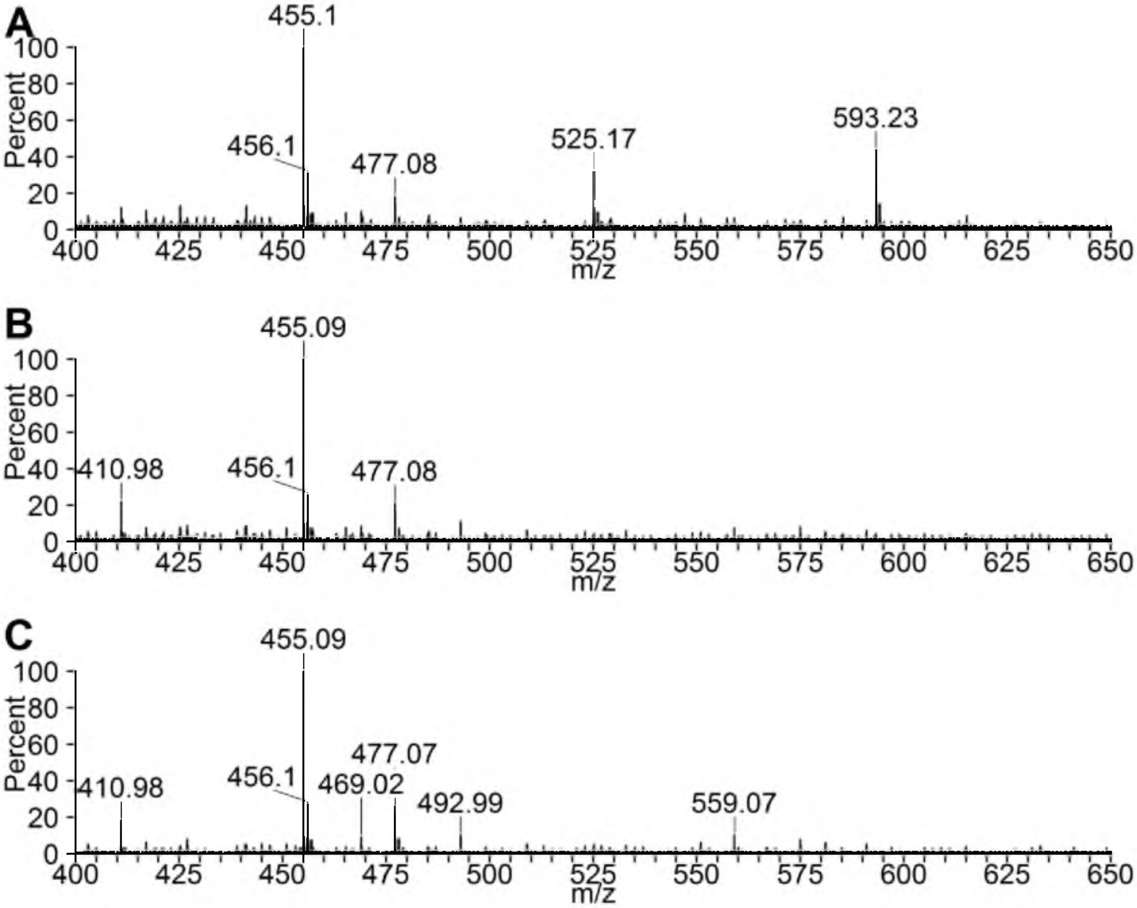

Figure 3.12. Negative ion TOF ESI mass spectrum of isolated FMN after a 27 d incubation of *Tt*-IDI-2 with different substrates. A, IPP; B, GPP; C, FPP. Note: Full spectra available in Appendix B.

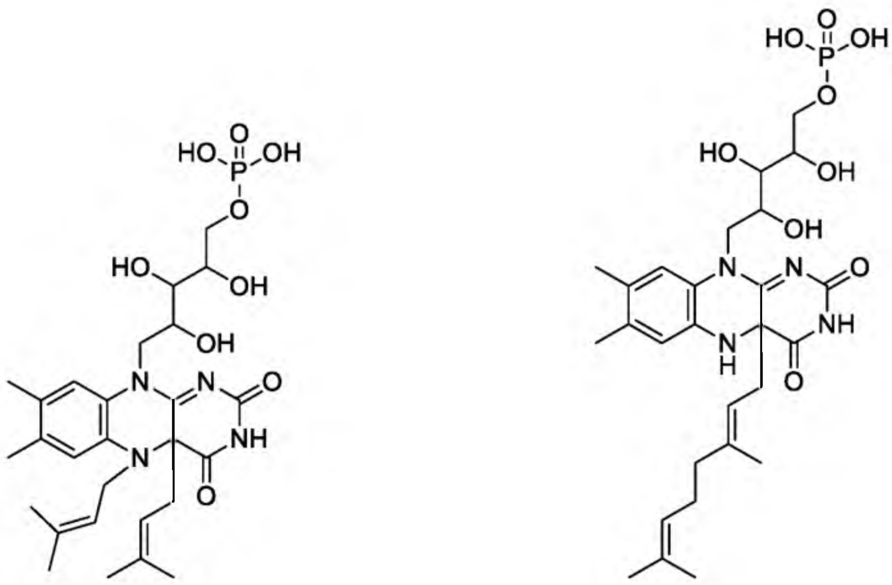

Chemical Formula: $C_{27}H_{39}N_4O_9P$
Exact Mass: 594.25

Chemical Formula: $C_{27}H_{39}N_4O_9P$
Exact Mass: 594.25

Figure 3.13. Chemical structures and neutral masses of possible FMN diprenylated adducts.

UPLC-MS analysis. The same samples studied with negative ion TOF ESI-MS were also studied with UPLC. Four different flavin species were detected and could be separated in an 8 min run. Figure 3.14 highlights the normalized chromatograms of the four different masses and their retention times. Figure 3.15 shows the corresponding mass spectra for the chromatograms in Figure 3.14. Lumiflavin (*m/z* 255.1), a light degradation product of FMN, was found in every sample and eluted around 4.0 min. In the chromatograms, fully oxidized FMN (*m/z* 455.1) was the first species to elute around 2.4 min and the isoprene-FMN adduct (*m/z* 525.2) eluted at 2.8 min. The diprenylated adduct species (*m/z* 593.2) eluted at 3.1 min. Fully oxidized riboflavin (*m/z* 374.1) was not detected. As hydrophobicity increased, the retention time increased as expected using a phenyl column with reverse phase conditions. This indicates that the suspected diprenylated adduct is more hydrophobic than the FMN-isoprene adduct.

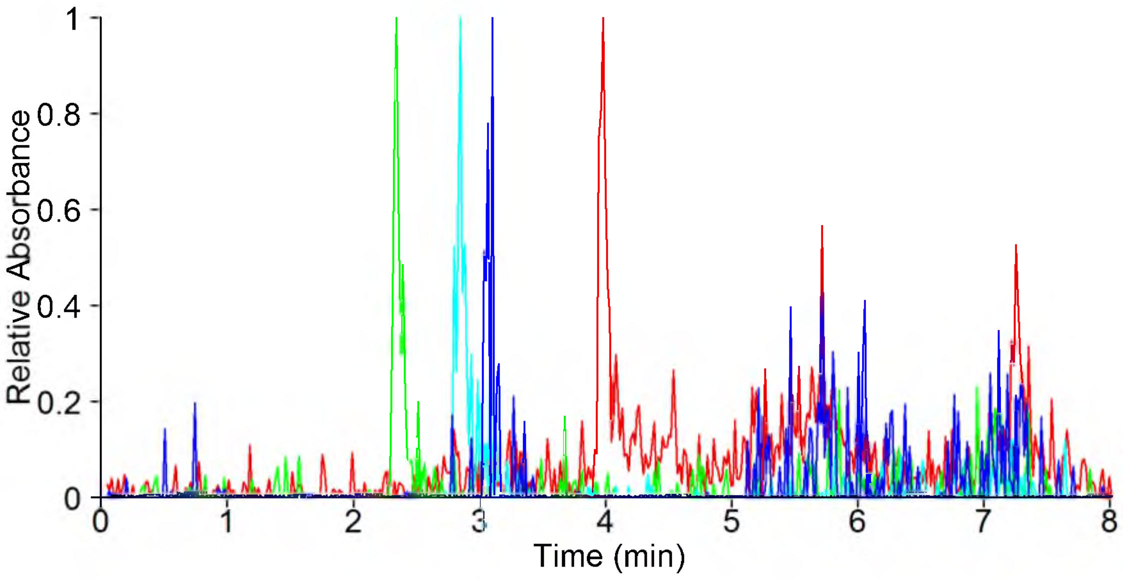

Figure 3.14. UPLC-MS chromatogram highlighting masses (minus H) of different flavin species. Lines are *m/z* 255.2 (lumiflavin, red), 455.1 (FMN, green), 525.2 (isoprene-FMN adduct, cyan), and 593.2 (diprenyl-FMN adduct, blue).

Kinetics of adduct formation. Data fit to a first over exponential equation started at 90 min through 60 h. Earlier data did not improve the fit and data collected after 60 h maintained the same level of activity as earlier time points. The best fit, first order exponential curves are shown in Figure 3.16.

The observed rate of decay was plotted against IPP concentration to determine the rate of inactivation (Figure 3.17). The parameters for the best-fit line are in Table 3.2. The rate of inactivation is extremely slow, a probable reason why the adduct was not detected earlier.

Isoprene production. Calibrated peak area was used to determine the molarity of isoprene collected from 1.8 mL of vial headspace. Without enzyme, the rate of DMAPP degradation into isoprene was faster over 90 min than when IDI-2 was incubated with IPP or DMAPP (Figure 3.18). However, in the first few time points, isoprene was produced more readily with IDI-2 and DMAPP than the other conditions. In these first

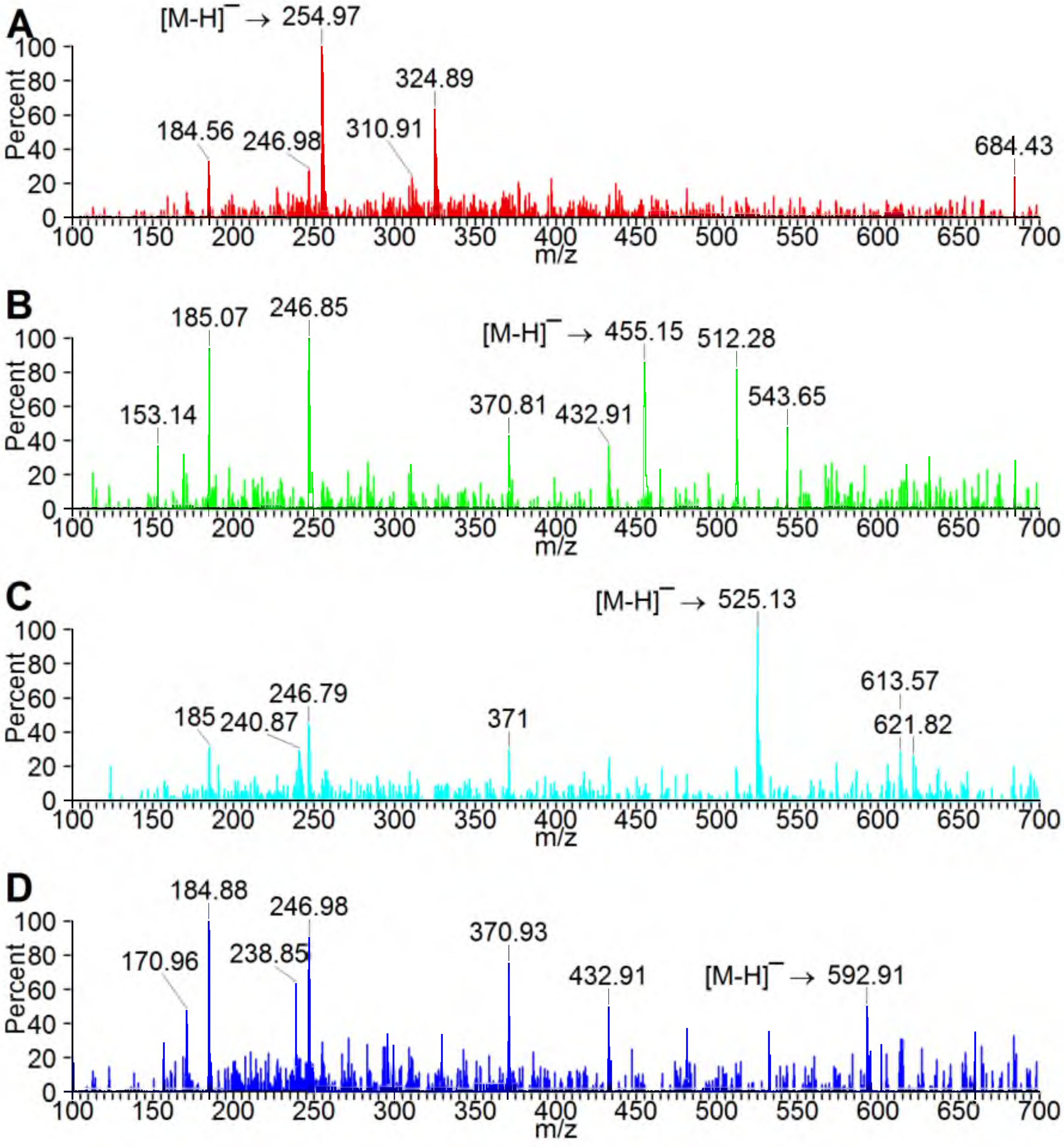

Figure 3.15. Negative ion ESI mass spectra corresponding to the UPLC chromatograms in Figure 3.14. A, Lumiflavin; B, FMN; C, isoprene-FMN adduct; D, Potential diprenylated FMN adduct.

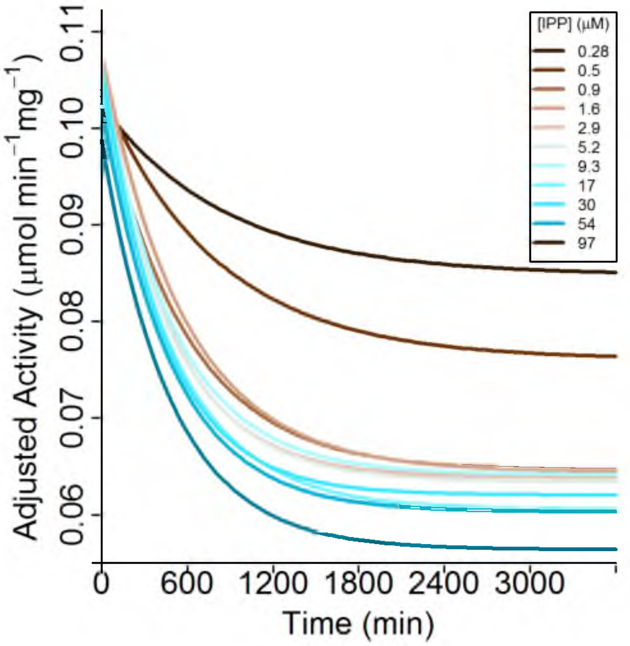

Figure 3.16. Best fit curves of the activity of IDI-2 after incubation with IPP. Adjusted activity corrects for enzyme activity loss over time.

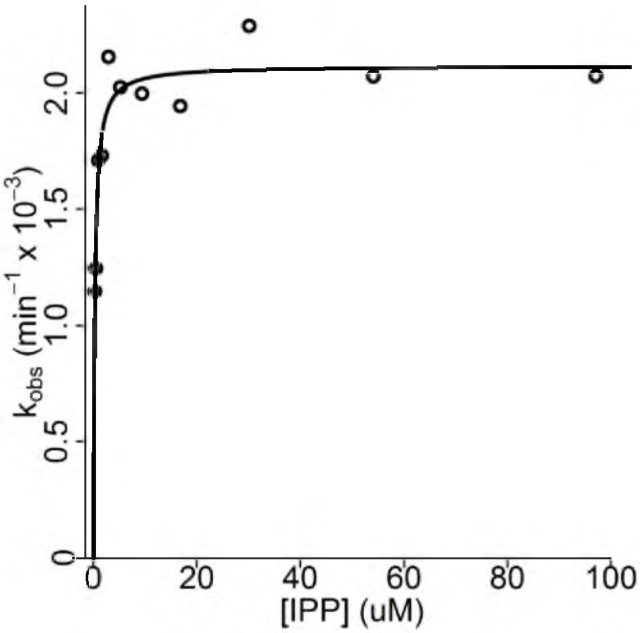

Figure 3.17. Observed rates plotted against IPP concentration.

Table 3.2. Kinetic parameters of the inactivation of IDI-2 by IPP.

	Mean	**S.E.**	**95% C.I.**
k_{inact} (min^{-1})	2.12×10^{-3}	6×10^{-5}	(1.99×10^{-3}, 2.25×10^{-3})
K_i (μM)	0.264	0.036	(0.188, 0.352)

few time points an estimate of the rate of isoprene synthase activity was determined to be 2.1×10^{-4} nmol isoprene/(min•mg). In Figure 3.18.B, the standardized residuals of the best fit lines have curvature. For samples with enzyme, the curvature indicates a better fit would be hyperbolic, so the rate of isoprene production is plateauing. Meanwhile, the curvature of the DMAPP without IDI-2 residuals indicates that an exponential fit would be a better fit and the rate is exponentially increasing.

For a longer incubation, the most obvious result is that DMAPP without enzyme produces more isoprene than when IDI-2 was included (Figure 3.19). Without enzyme, the fastest rate of isoprene production from DMAPP occurred when NADPH was included in the assay. When IDI-2 was incubated with IPP and NADPH, there was a steady rate of isoprene production, which is reasonable considering that the enzyme is catalytically active and producing DMAPP. Some other conditions that were not included in the figure did not produce any detectable isoprene. These conditions include only assay solution (no IDI-2 and no substrates) and IDI-2 with or without NADPH (no substrates). After 42 h there was a small amount of isoprene production from an incubation of IPP (no IDI-2), with or without NADPH (43 or 50 nM, respectively).

Discussion

The discovery of flavoenzymes involved in the well-studied isoprenoid pathway introduced a new area of chemistry for flavoenzymes. Recent evidence implies the N5-

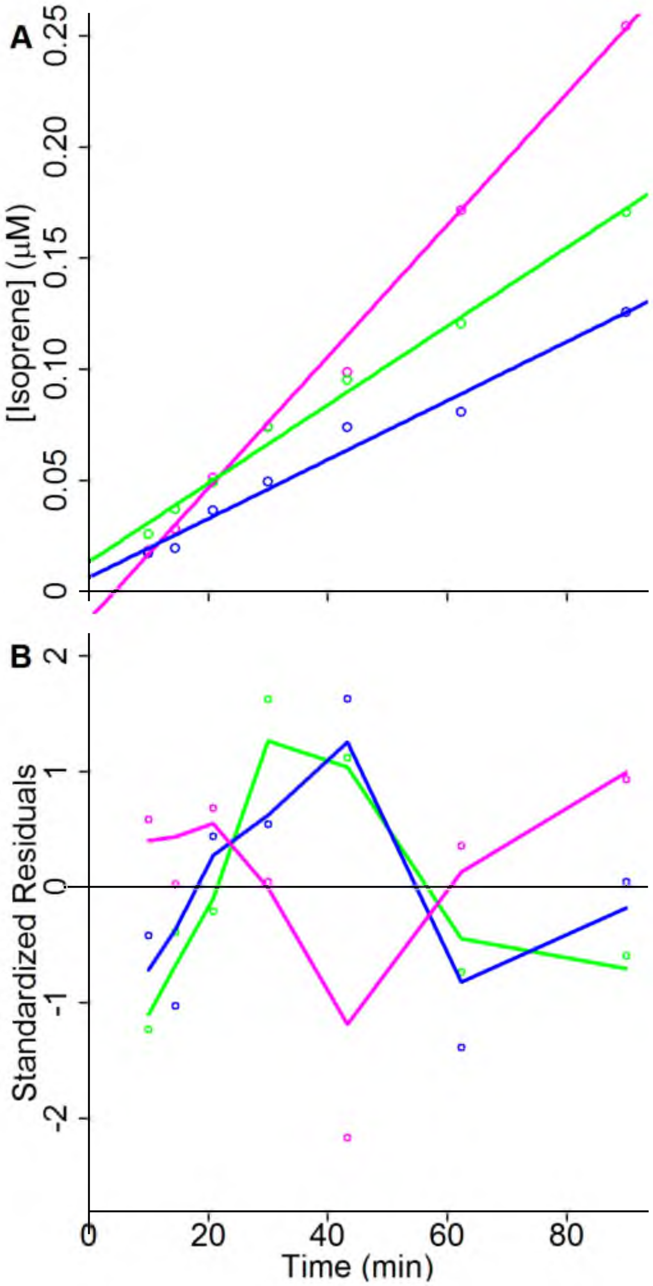

Figure 3.18. Best fit linear lines of isoprene production with NADPH in a short incubation. Lines represent IDI-2 and DMAPP (green), IDI-2 and IPP (blue) and only DMAPP (magenta). A, Isoprene production versus time; B, Standardized residuals of the best fit lines in A.

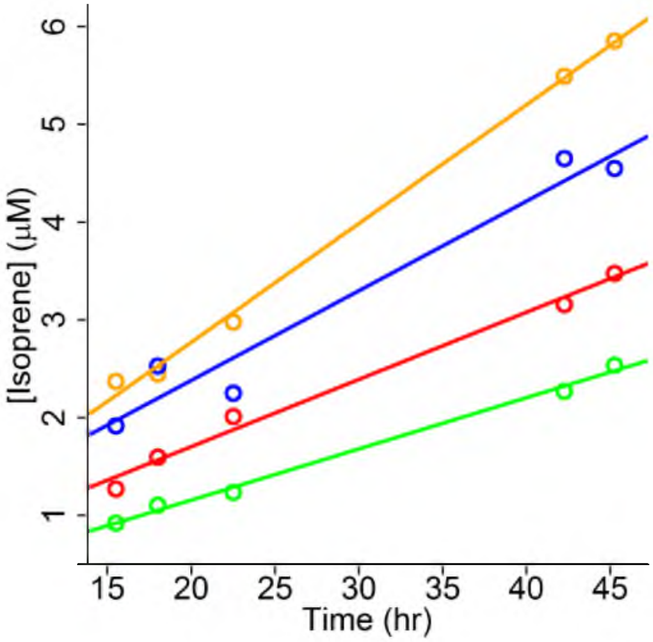

Figure 3.19. Best fit linear lines of isoprene production with NADPH in a long incubation. Lines represent IDI-2 and DMAPP (red), IDI-2 and IPP (green), DMAPP with no enzyme (orange) and DMAPP with no enzyme or NADPH (blue).

position of flavin participates in both proton donation and abstraction during the isomerization of IPP to DMAPP.[62,76] Also, crystal structures and spectroscopic observations indicate that the C4a flavin position covalently bonds to substrate analogues.[58] Together, these indicate that flavin is actively participating in catalysis.

In crystal structures of IDI-2 with IPP, the C3-position of IPP is poised directly above the C4a-position of flavin.[58,73] Calculations have shown that the C4a-position of flavin has a delocalized HOMO when in the anionic reduced state.[77] Thus, during carbocation formation of IPP, there could be complex formation between the substrate and cofactor. During an overnight incubation with IPP and IDI-2, an FMN-adduct was observed. There is a bathochromic shift (375 → 399 nm) when the adduct is guanidine denatured at neutral pH compared to the protonated adduct in 6 N HCl. Oxidation of the free adduct in either solution required both oxygen and light and results in direct oxidized

FMN without any intermediates. These results are characteristic of an adduct at the C4a-position (Table 2.4). Interestingly, when enzyme-bound, the adduct proceeds through a radical intermediate, a characteristic of an N5-adduct. A radical was observed for *Tt*-IDI-2 when IPP was incubated with the enzyme prior to reduction.[63] In this case, the radical was evidence only that *Tt*-IDI-2 was capable of stabilizing the neutral radical intermediate and not evidence of a radical intermediate in catalysis. Likewise, one would speculate that the FMN adduct observed was oxidized to a radical flavin that could be stabilized by the enzyme, and not that the radical is a critical intermediate.

A peak increase from *m/z* 455.1 of oxidized FMN to *m/z* 525.2 for the FMN-adduct confirmed that only a single isoprene unit was added to FMN. However, the diphosphate group was retained when adducts formed between FMN and substrate analogues of IDI-2.[68] The expected neutral mass of an adduct with FMN and IPP of 702 or 704 (depending on which IPP carbon adduct formation was occurring) was not observed in any experiments. Thus, the diphosphate group is likely a leaving group during adduct formation. The mass increase was also observed with DMAPP as the substrate. When $^{13}C_5$-IPP was the substrate, the mass increased an additional 5 units, as would be expected if the source of the adduct was the carbon backbone of IPP. With UPLC-MS, FMN was separated from the isoprene-adduct.

In both the control, where no substrate was incubated with IPP, and incubation with $^{13}C_5$-IPP, there was a peak at *m/z* 525.2. The source of this mass was expected to be from the IPP pool of *E. coli*, the expression organism; however this hypothesis was not evaluated any further.

When incubation time was increased to several weeks, rather than just a few days, a new peak at *m*/*z* 593.2 was observed. Initially thought to be contamination, the mass corresponds to a two-isoprene unit adduct with FMN. LC-MS separated the two-isoprene unit adduct from both FMN and the one-isoprene unit adduct. The fragmentation pattern of the 593.2 mass had the characteristic pattern for FMN, with a major peak at *m*/*z* 371 (corresponds to the ribityl group, benzyl and piperazinyl rings, Figure 3.20). The *m*/*z* 593.2 FMN mass was either caused by chain elongation or diprenylation. In order to determine which was true, ion source fragmentation of the cofactor adduct was explored.[144] However results were inconclusive.

One concern with the observation of adduct formation in the presence of dithionite is the possibility of sulfoxide, sulfite or dithionite adduct formation with the isoalloxazine ring system of FMN.[145,146] However, when NADPH was used as a reductant, absent dithionite, adduct formation still occurred. In addition, $^{13}C_5$-IPP increased the mass of the adduct by 5 mass units. The several-week-long incubation that resulted in a new mass could be the result of the equilibrium between dithionite and two sulfoxylate radical ions.[147] Numerous sulfoxide, sulfite and dithionite adducts can be hypothesized (Figure 3.21) and their masses can be searched for in the measured mass

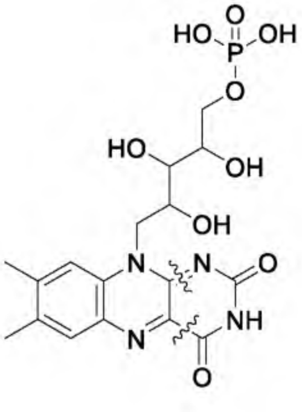

Figure 3.20. FMN with the location of fragmentation that leads to a mass of 372.

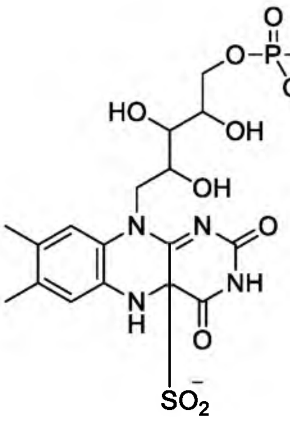

Chemical Formula:
$C_{17}H_{22}N_4O_{11}PS^-$
Exact Mass: 521.07

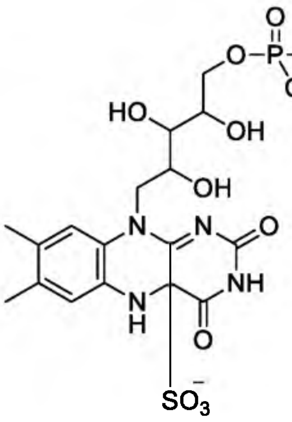

Chemical Formula:
$C_{17}H_{22}N_4O_{12}PS^-$
Exact Mass: 537.07

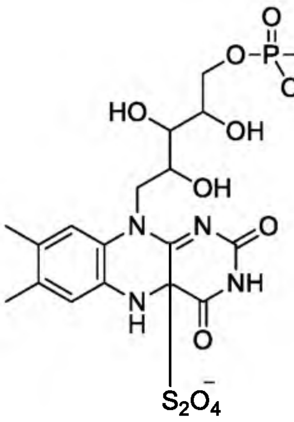

Chemical Formula:
$C_{17}H_{22}N_4O_{13}PS_2^-$
Exact Mass: 585.04

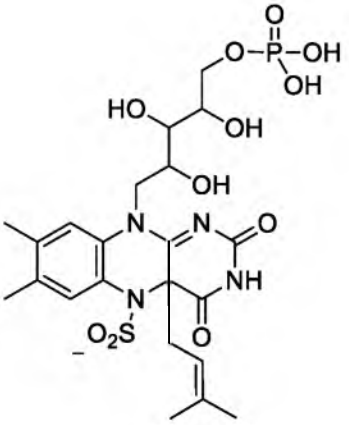

Chemical Formula:
$C_{22}H_{30}N_4O_{11}PS^-$
Exact Mass: 589.14

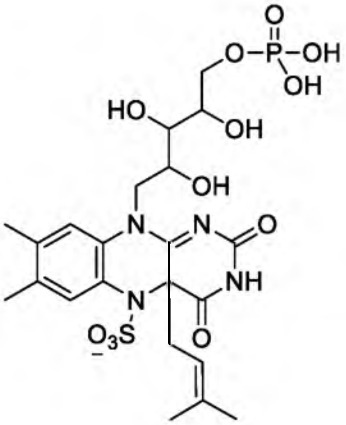

Chemical Formula:
$C_{22}H_{30}N_4O_{12}PS^-$
Exact Mass: 605.13

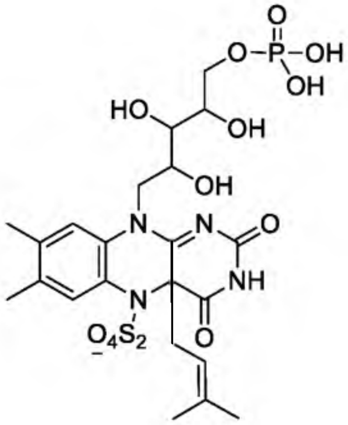

Chemical Formula:
$C_{22}H_{30}N_4O_{13}PS_2^-$
Exact Mass: 653.10

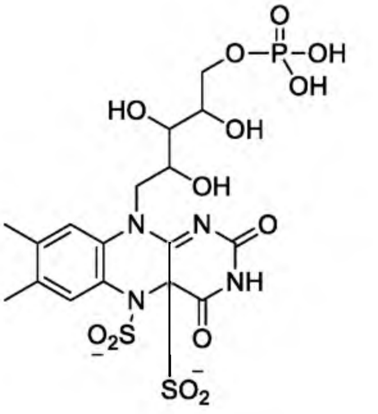

Chemical Formula: $C_{17}H_{21}N_4O_{13}PS_2^{2-}$
Exact Mass: 584.03

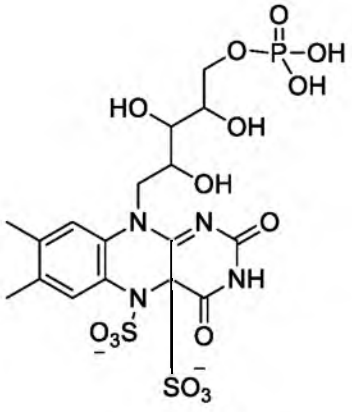

Chemical Formula: $C_{17}H_{21}N_4O_{15}PS_2^{2-}$
Exact Mass: 616.02

Figure 3.21. Possible adducts between FMN and isoprene-FMN adducts with sulfoxide, sulfite and dithionite with their neutral masses.

spectra. Importantly, none of the masses in Figure 3.21 correspond to peaks at *m/z* 526.2 or 594.2, further evidence that the observed adduct was not derived from dithionite.

The rate of inactivation was studied to quantify this slow process. Interestingly, the enzyme always retained some activity (Figure 3.16). Based on the spectroscopic evidence (Figure 3.2 and Figure 3.3), there appeared to be complete enzyme inactivation when [IPP] > [IDI-2]. In the inactivation studies, as [IPP] increased, [IPP] >> [IDI-2]; however there was still activity perhaps a result of DMAPP hydrolysis because of the lengthy incubation times. Any isoprene (bp = 34 °C) would not stay in solution at 37 °C, therefore equilibrium with the enzyme is unlikely. Furthermore, the DMAPP hydrolysis product, 3-methyl-2-buten-1-ol, would lack the diphosphate group, a necessity for substrate binding in IDI-2. Thus, these products would be unavailable for catalysis and enzyme was still available to catalyze the radioactive substrate when tested for activity. While the IDI-2 manufactured adduct may be biologically irrelevant, prenylated flavins have been identified from two different sources.

The first identified example of a prenylated flavin was from visible light irradiated riboflavin in the presence of isohumulones in a N_2-flushed environment.[148] Humulones are prenylated phloroglucinol natural products from the hop plant and are isomerized to isohumulones during the process of brewing beer (Chapter 1).[28] When beer is exposed to light, riboflavin in the triplet excited state transfers an electron to isohumulone, which then undergoes a bond cleavage resulting in a 3-methyl-2-butenyl radical. This radical reacts with a thiol group to form 3-methyl-2-butene-1-thiol, the compound responsible for 'skunky' beer.[149] In the decreased O_2 environment, recombination between the flavin semiquinone radical and the 3-methyl-2-butenyl radical results in the prenylated flavin at both the C4a- and N5-positions.

The other example is not believed to be a direct prenylation of riboflavin, but rather of a riboflavin degradation product. The prenylation occurs at the N5-position and then undergoes a cyclization with the benzyl side of what remains of the isoalloxazine backbone to yield hunanamycin A.[150] The compound was isolated from a *Bacillus* strain and mimics synthetic riboflavin synthase inhibitors, but did not show significant antimicrobial activity.

The biological relevance of adduct formation by IDI-2 seems to be one of irrelevance and serendipity. One explanation for adduct formation would be that IDI-2 produces isoprene. However the low isoprene synthase activity excludes this possibility. Another explanation would involve a feedback mechanism, but the slow rate of adduct formation restricts in vivo observation of the adduct to an instance of induced recombinant protein expression. Recombinantly expressed enzymes can be catalytically active in the cell, particularly in the case of an enzyme in the early isoprenoid pathway because IPP and DMAPP are ubiquitous in the cell. The high number of expressed enzyme increases the chance that this adduct would be observed. The sluggish nature of IDI-1 may exist in IDI-2, causing isomerization to fluctuate prior to product release.[151] If this were the case, adduct formation may be a result of a rare catalytic mistake.

CHAPTER 4

KINETIC MECHANISM OF *Streptococcus pneumoniae* TYPE 2 ISOPENTENYL DIPHOSPHATE:DIMETHYLALLYL DIPHOSPHATE ISOMERASE

Introduction

The first published phylogenetic relationships of organisms with a gene for IDI-2 located the gene in the Bacteria and Archaea domains of life.[45] IDI-2 has been cultured and studied from the species, *Bacillus subtillus*,[45] *Streptomyces* sp. strain CL190,[57] *Thermus thermophilus*,[63] *Staphylococcus aureus*,[64] and *Sulfolobus shibatae*.[152] While the extremophilic organisms *T. thermophilus* and *S. shibatae* have proved to be useful enzymes to study the chemical intricacies of IDI-2, they fail to model IDI-2 as a potential drug target.

With the advent of genomic technologies, enzymes that are essential and unique to human pathogens could be investigated as potential antibacterial drug targets. The isoprenoid biosynthetic pathway has been targeted since humans use the mevalonate (MVA) pathway and IDI-1 to produce isoprenoids, while several pathogens utilize the methylerythritol phosphate (MEP) pathway and/or IDI-2.[153] For example, fosmidomycin inhibits two enzymes in the MEP pathway and has been used successfully as an antibiotic against *E. coli* and *Plasmodium falciparum* (malaria parasite).[154] *Streptococcus pneumoniae* produces isoprenoids via the MVA pathway with IDI-2.[153] A currently studied drug target in the MVA pathway of *S. pneumoniae* is the mevalonate kinase enzyme. The enzyme is inhibited at an allosteric site by diphosphomevalonate, whereas the human mevalonate kinase is unaffected.[155] From this study, mevalonate analogues were studied and the authors found characteristics in the analogues that were preferred by mevalonate kinase.[156]

IDI-2 from *S. pneumoniae* has not yet been explored as a drug target. Presented here are the kinetic characteristics of *S. pneumoniae*, which are the initial steps towards a better understanding of the enzyme and its viability as a drug target.

Experimental Procedures

Materials. HEPES, HEPES sodium salt and NADH were purchased from rpi. Magnesium chloride hexahydrate, molecular biology grade and FMN (97% pure) were purchased from Sigma-Aldrich. ^{14}C-IPP (60 $\mu C_i/\mu$mol) was purchased from Perkin-Elmer. NIPP (*N,N*-dimethyl-2-amino-1-ethyl diphosphate) was available from earlier experimentation.[63] 5-Deaza-FMN was provided by Dr. Seoung Choi.

Expression and purification. E. coli M15 cells with plasmid coding for *Streptococcus pneumoniae* IDI-2 (*Sp*-IDI-2) were expressed and purified as previously described for the *T. thermophilus* IDI-2,[58] with the following modifications. Frozen cells were thawed with binding buffer (20 mM sodium phosphate, pH 7.4, with 20 mM imidazole and 500 mM NaCl), lysed with sonication and centrifuged. The lysate supernatant was applied to a HisTrap FF Crude Ni^{2+} affinity column (GE Healthcare). Purification was performed at 4 °C with a step gradient of binding buffer that contained increasing imidazole (20, 40, 500 mM). After the protein was loaded onto the affinity column, the enzyme was deflavinated with a wash of 2 M KBr in binding buffer. Enzyme concentration was determined using the BCA assay (Pierce).

Kinetic assays. The acid-lability assay, with modifications described previously, was used to determine kinetic parameters.[63] Briefly, assay buffer was equilibrated at 37 °C and the reaction initiated with the addition of *Sp*-IDI-2 diluted in 0.14 mg/mL BSA in 10 mM HEPES, pH 7.0. After 10 min, the reaction was quenched with 200 µL MeOH:HCl (4:1) and incubated for another 10 min. Samples were removed and 1 mL ligroin added and vigorously vortexed, allowed to separate for 10 min, then 500 µL of the organic layer was added to scintillation fluid (UltimaGold, Perkin-Elmer). The assay sample disintegrations per minute (DPM) were counted, along with total count and blank samples (TriCarb 2910TR, Perkin-Elmer). Blank samples were performed as described above, but instead of enzyme, reactions were initiated with H_2O. Total count samples were the same volume of assay buffer, without enzyme, used in the reaction added directly to scintillation fluid. The assay sample order for each replicate was randomly assigned. FMN, 5-deaza-FMN and NADPH or NADH stock solutions were prepared the day of experimentation. FMN and 5-deaza-FMN stock concentrations were determined with UV-vis spectroscopy and the extinction coefficients of 12,200 M^{-1} cm^{-1} at λ_{450},[115] and 12,000 M^{-1} cm^{-1} at λ_{396},[157] respectively.

Single substrate saturation assays. Single substrate experiments were replicated three times. The general assay conditions were 60 nM apo-*Sp*-IDI-2 in 200 mM HEPES (pH 7.0 at 37 °C) containing 2 mM $MgCl_2$, 2 mM NADPH and 0.14 mg/mL BSA in 10 mM HEPES (pH 7.0). For variable FMN (constant IPP), the conditions included 150 µM IPP (spiked with [^{14}C]-IPP) and 0.25 – 5.0 µM FMN. For variable IPP (constant FMN), the conditions were 8 µM FMN and 15 – 400 µM IPP (spiked with [^{14}C]-IPP).

Bisubstrate assays. Bisubstrate kinetic experiments were replicated four times. Assays were prepared as a grid of varying IPP (5.0 – 200 μM, spiked with [^{14}C]-IPP) and FMN (0.51 – 4.1 μM) concentrations in 100 mM HEPES (pH 7.0 at 37 °C) containing 25 mM $MgCl_2$, 10 mM NADH and 0.14 mg/mL BSA in 10 mM HEPES (pH 7.0) and were initiated with the addition of 7.5 nM apo-*Sp*-IDI-2.

Inhibition assays. Inhibition kinetic experiments were replicated three times, for each inhibition experiment. The general assay conditions were 100 mM HEPES (pH 7.0 at 37 °C) containing 25 mM $MgCl_2$, 10 mM NADH and 0.14 mg/mL BSA in 10 mM HEPES (pH 7.0). Experiment specific conditions are listed below.

NIPP inhibition studies. For variable FMN, assay buffer contained 61.2 μM IPP (spiked with [^{14}C]-IPP) and a grid of FMN (0.93 – 2.6 μM) and NIPP (0, 3.8 – 12.9 μM). For variable IPP, assay buffer contained 1.5 μM FMN and a grid of IPP (spiked with [^{14}C]-IPP) (72 – 300 μM) and NIPP (0, 6.7 – 52 μM). 20 nM apo-*Sp*-IDI-2 was added for both conditions.

5-DeazaFMN inhibition studies. For variable FMN, 7.5 nM apo-*Sp*-IDI-2 was added to assay buffer with 23.3 μM IPP (spiked with [^{14}C]-IPP) and a grid of FMN (0.56 – 3.5 μM) and 5-deazaFMN (0, 0.02 – 0.16 μM). For variable IPP, 15 nM apo-*Sp*-IDI-2 was added to assay buffer with 1.6 μM FMN and a grid of IPP (spiked with [^{14}C]-IPP) (18 – 225 μM) and 5-deazaFMN (0, 0.05 – 0.25 μM).

Data analysis. Single substrate data were fit to the Michaelis-Menten equation with an additional term for substrate inhibition (Equation 4.1). Bisubstrate kinetic data were fit to the following: the standard sequential ordered and random equations (Eqs. 4.2 and 4.3),[158] a modified Multiple Essential Activator Site velocity equation (Eq. 4.4),[158] and a standard sequential ordered model with Hill coefficients (Eq. 4.5). Eqs. 4.6 – 4.9 were used to fit the inhibition data. Analysis was performed using R version 3.0.0,[117] with the packages nlstools,[159] calibrate,[160] and dichromat.[121]

$$\upsilon = \frac{k_{cat}[\mathrm{E}]}{1 + \frac{K_m}{[\mathrm{S}]} + \frac{[\mathrm{S}]}{K_i}} \tag{4.1}$$

$$\upsilon = \frac{k_{cat}[\mathrm{E}][\mathrm{A}][\mathrm{B}]}{K_A K_B + [\mathrm{A}]K_B + [\mathrm{A}][\mathrm{B}]} \tag{4.2}$$

$$\upsilon = \frac{k_{cat}[\mathrm{E}][\mathrm{A}][\mathrm{B}]}{K_A K_B + [\mathrm{A}]K_B + [\mathrm{B}]K_A + [\mathrm{A}][\mathrm{B}]} \tag{4.3}$$

$$\upsilon = \frac{k_{cat}[\mathrm{E}]\frac{[\mathrm{S}]^m[\mathrm{A}]^n}{{K_S}^m K_A^n}}{\left(1 + \frac{[\mathrm{A}]}{K_A}\right)^n + \frac{[\mathrm{S}]^m[\mathrm{A}]^n}{{K_S}^m K_A^n}} \tag{4.4}$$

$$v = \frac{m k_{cat}[\mathrm{E_T}]\left(\frac{[\mathrm{B}]}{K_B}\right)^m\left(\frac{[\mathrm{A}]}{K_A}\right)^n}{1 + \left(\frac{[\mathrm{A}]}{K_A}\right)^n + \left(\frac{[\mathrm{B}]}{K_B}\right)^m\left(\frac{[\mathrm{A}]}{K_A}\right)^n} = \frac{m k_{cat}[\mathrm{E_T}]}{1 + \left(\frac{K_B}{[\mathrm{B}]}\right)^m\left(1 + \left(\frac{K_A}{[\mathrm{A}]}\right)^n\right)} \tag{4.5}$$

$$v = \frac{k_{cat}[\mathrm{E}]}{1 + \left(\frac{K_m}{[\mathrm{S}]}\right)^n\left(\left(\frac{[\mathrm{I}]}{K_i}\right)^d + 1\right)} \tag{4.6}$$

$$v = \frac{k_{cat}[\mathrm{E}]}{\left(1 + \left(\frac{[\mathrm{I}]}{K_i}\right)^n\right)\left(\left(\frac{K_m}{[\mathrm{S}]}\right)^m + 1\right)} \tag{4.7}$$

$$v = \frac{k_{cat}[\mathrm{E_T}]}{1 + \frac{K_s}{[\mathrm{S}]} + K_s\left(\frac{[\mathrm{I}]}{K_i}\right)^d\left(\frac{1}{K_{si}} + \frac{1}{[\mathrm{S}]}\right)} \tag{4.8}$$

$$v = \frac{k_{cat}[\mathrm{E}]}{1 + \left(\frac{[\mathrm{S}]}{K_s}\right)^n + \frac{[\mathrm{I}]}{K_i}} \tag{4.9}$$

Results

Overexpression and purification. The purification step for the *Sp*-IDI-2 was crucial to obtain partial holoenzyme or pure apoenzyme. Inconsistent results were obtained by deflavination when Ni^{2+} bound His_6-*Sp*-IDI-2 was only washed with binding buffer. To avoid any ambiguity in the final form of the *Sp*-IDI-2 enzyme, a 2 M KBr wash step was introduced to completely deflavinate the enzyme and this was confirmed with UV-vis spectroscopy where no flavin peaks were observed at ~360 and 450 nm (data not shown). The residual activity of the apoenzyme, without added FMN, resulted in only 0.3% activity compared to fully active enzyme with FMN in the assay buffer.

Kinetic assays. For purposes of proper statistical analysis, all equations were modified according to the following procedure. To calculate velocity from raw data, it was necessary to first compute the ratio of sample DPM to the DPM from the total counts (product ratio). This ratio was multiplied by IPP concentration to yield the concentration of product, DMAPP. The concentration of product divided by time in seconds equals the velocity of the reaction (Eq. 4.10).

$$\upsilon = \left(\frac{\mathrm{DPM_{sample}}}{\mathrm{DPM_{total}}}\right)\left(\frac{[\mathrm{IPP}]}{\mathrm{time}}\right) \qquad \mathbf{4.10}$$

Substitution of equation 4.10 into the equations presented in the Experimental Procedures section allowed for each equation to be solved for in terms of the product ratio. Each analysis was performed on the substituted equations, but figures are presented with velocity, rather than ratio on the y-axis.

Residual analyses of the fitted equations indicated that the residuals were not randomly distributed. A logarithmic transformation of both the response and model successfully randomized the residuals. Figure 4.1 shows an example of the residuals before and after transformation. The horn pattern in Figure 4.1.A indicates residual heteroscedasticity (meaning the residuals are heterogeneously distributed). The nearly homogeneous distribution of the residuals in Figure 4.1.B is indicative of a properly fit model with proper statistical assumptions. After transformation and an initial fit, if there were any standardized residuals with an absolute value greater than four, these were considered significant outliers and were removed so a new initial fit could be conducted. For the new initial fit (and any fit without significant outliers), any standardized residuals with an absolute value greater than two were removed and a final fit was performed. After the final fit, further diagnostics were performed for informational purposes only and no further modifications were made.

The choice of residual elimination was based on the standard normal curve for

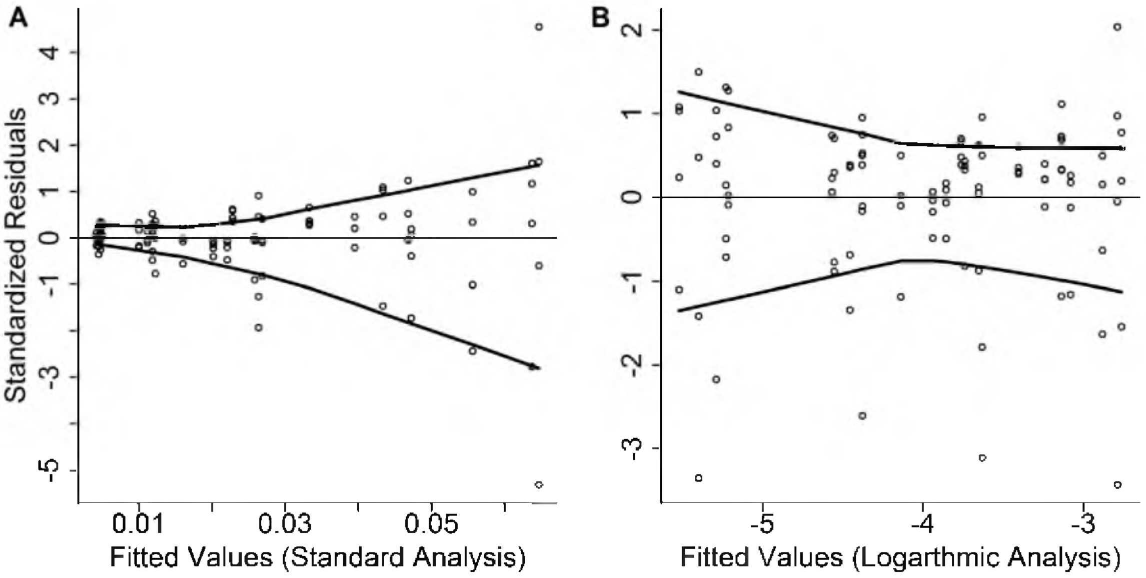

Figure 4.1. Standardized residual plots comparing data sets. A, Untransformed data; B, Transformed data. The data set and model are identical. However the right hand model has undergone a logarithmic transformation. The lines represent smoothing curves of the maximum and minimum points at each fitted value.

residuals (Figure 4.2). A standardized residual with an absolute value greater than 4 has a probability of occurrence less than 1 out of 10,000. With such a low likelihood, these values are true outliers. Standardized residuals with absolute values greater than 2 have a probability of less than 5 out of 100. These are considerably more likely values; however, their elimination is reasonable for smaller data sets and ultimately improves the overall error associated with parameter values.

Single substrate kinetics. Saturation of apo-*Sp*-IDI-2 with either IPP or FMN and variation of the other substrate gave Michaelis-Menten curves that taper at high substrate concentration (Figure 4.3). The data were fit to Eq. 4.1 to include substrate inhibition. The kinetic parameters are described in Table 4.1 and Table 4.2.

The k_{cat} values are similar to those obtained for the *T. thermophilus* enzyme of

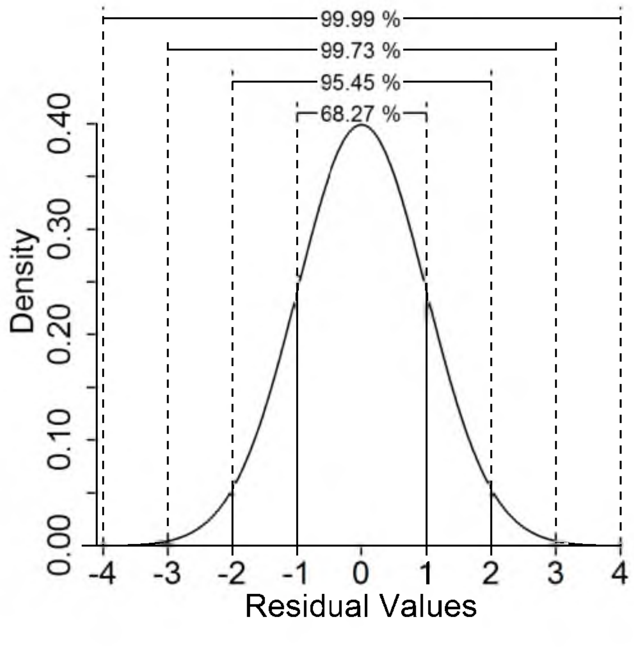

Figure 4.2. Standard normal curve for standardized residuals with mean of 0 and standard deviation of 1. Lines represent probabilities (shown as percentages) of the standard normal curve. For example, data have a probability of 0.6827 of being found within one standard deviation of the mean.

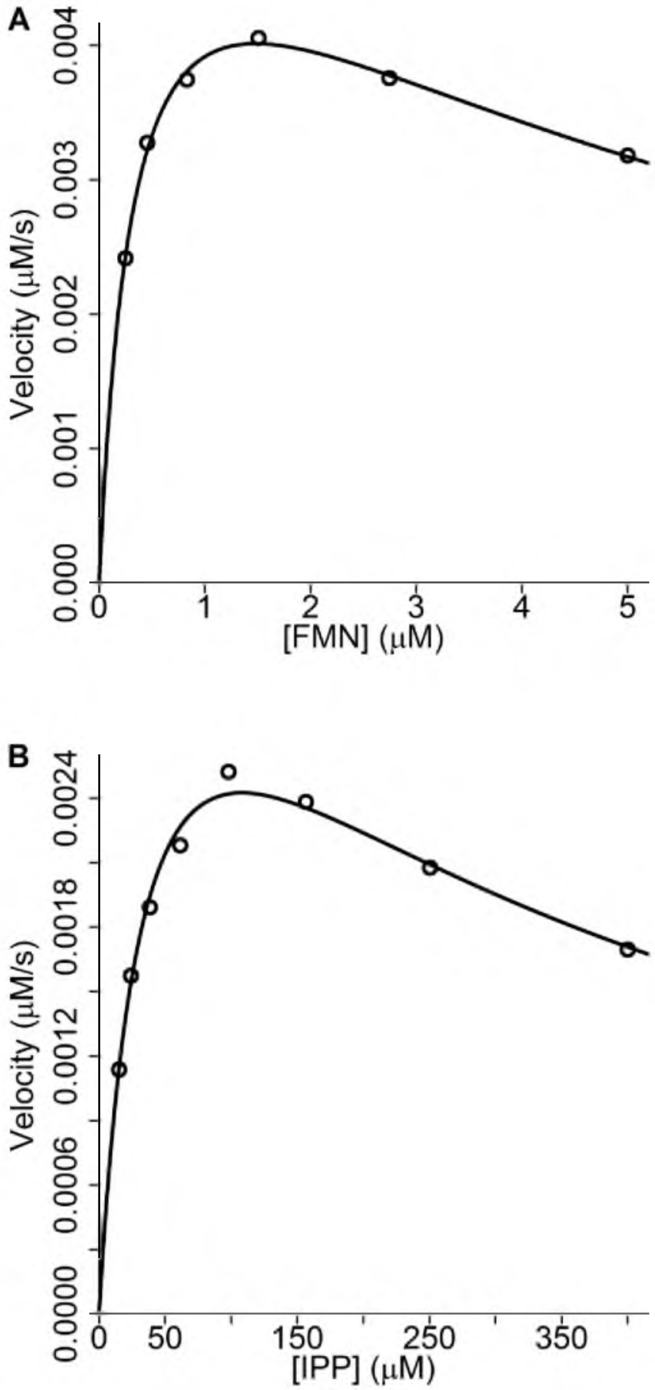

Figure 4.3. Single substrate kinetics plots for *Sp*-IDI-2. A, Variable FMN, [IPP] = 150 μM; B, variable IPP, [FMN] = 8 μM. Points are the average of three separate experiments and the line is the best fit line through the data.

Table 4.1. Kinetic parameters for *Sp*-IDI-2 with variable FMN (constant IPP).

	Mean	**S.E.**	**95% C.I.**
k_{cat} (s^{-1})	0.196	0.011	(0.174, 0.223)
K_{fmn} (μM)	0.343	0.044	(0.259, 0.450)
K_i (μM)	6.40	1.01	(4.61, 9.17)

Table 4.2. Kinetic parameters for *Sp*-IDI-2 with variable IPP (constant FMN).

	Mean	**S.E.**	**95% C.I.**
k_{cat} (s^{-1})	0.141	0.009	(0.125, 0.161)
K_{ipp} (μM)	40.0	4.1	(32.5, 49.7)
K_i (μM)	292	39	(221, 388)

0.13 and 0.18 s^{-1} for variable FMN and IPP, respectively.[63] Likewise, the K_m for variable IPP is similar to the *S. aureus* enzyme (17 μM),[64] but larger than the *T. thermophilus* enzyme (5.6 μM).[63] The K_m for variable FMN differs from the *T. thermophilus* enzyme (4.7μM).[63] There were no similar studies with other IDI-2 enzymes that indicated substrate inhibition, so a comparison could not be made for the K_i parameter.

Bisubstrate kinetics. The bisubstrate kinetics of *Sp*-IDI-2 were investigated to determine the *Sp*-IDI-2 mechanism. The assay conditions used for the single substrate kinetics were not suitable for the bisubstrate studies and required reoptimization.

Initial bisubstrate experiments exhibited substrate inhibition at high substrate concentrations. At lower substrate concentrations, reproducibility was an issue. To resolve these problems, the reductant and Mg^{2+} used in the assay were investigated. NADPH powder was stored at -20 °C in a desiccator for up to a year and 100 mM stock solutions were prepared with a 7 d expiry and stored at -20 °C. However, literature studies found that using optimized conditions (lyophilization from a solution of 200 mM NaCl in pH 9.0 Tris buffer), NADPH degradation at -20 °C was 20% over one week.[161] The half-life of NADPH in solution at 37 °C is only 71 min in pH 6.0 buffer (interpolated from rate constant determinations at 30 and 41 °C).[162] While these conditions were suitable for the *Tt*-IDI-2 enzyme,[63] *Sp*-IDI-2 was more sensitive to reductant. Steady state kinetic curves of NADPH and NADH gave similar results with hyperbolic curves (k_{cat} = 8.7 x 10^{-2} and 7.3 x 10^{-2} sec^{-1}, respectively) (Figure 4.4). The dithionite reduced data required a sigmoidal fit yielding a k_{cat} = 2.6 x 10^{-2} sec^{-1}. Dithionite was not suitable and appeared to degrade within the span of the experiment, as the assay samples were visibly yellow when enzyme was added to initiate the reaction. Compared to the half-life of NADPH at 41 °C (55 min), NADH is considerably more stable (half-life of 400 min)

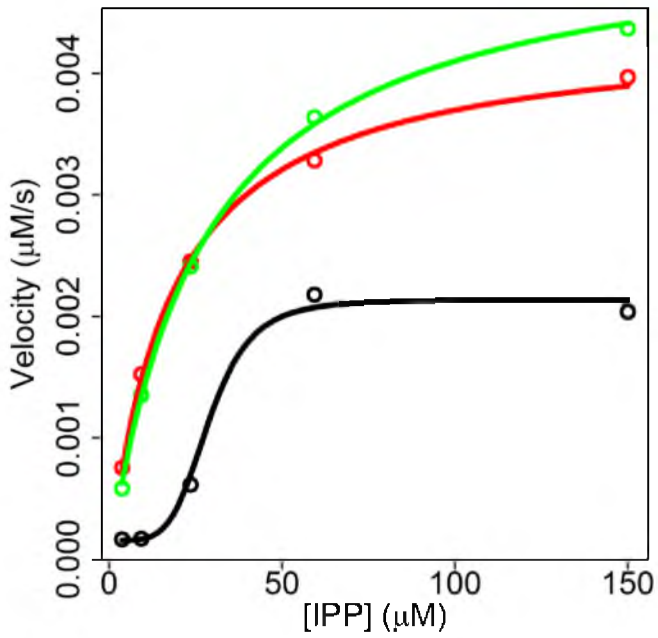

Figure 4.4. Steady state kinetics of *Sp*-IDI-2 with NADPH (green), NADH (red) and dithionite (black) as reductants. Each point represents the average of three data points. Both NADPH and NADH were fit to the Michaelis-Menten equation. The dithionite data were fit to a modified Michaelis-Menten equation that included a Hill coefficient and a baseline correction parameter.

(unfortunately data were not available to interpolate these results to 37 °C).[162] Based on the greater stability of NADH, this was chosen as the reductant for the *Sp*-IDI-2 enzyme. Next, by comparing enzyme activity, the optimum concentration of NADH was determined as 10 mM (Figure 4.5). After optimization of the reductant, the dication concentration was investigated.

Formerly, stock solutions of 200 mM $MgCl_2$ were prepared with an old supply of $MgCl_2 \cdot 6H_2O$ and several drops of 5 N HCl and gave a solution with pH ~ 1 – 2. Without any acid, a 1 M solution, pH ~ 5 – 6, could be prepared with newly purchased $MgCl_2 \cdot 6H_2O$. With the new material, optimum enzyme activity was achieved with 25 mM $MgCl_2$ (Figure 4.6). An interesting consequence of increasing Mg^{2+} concentration was that blank readings decreased (Figure 4.7).

With the optimized conditions, the activity of *Sp*-IDI-2 was studied as both a

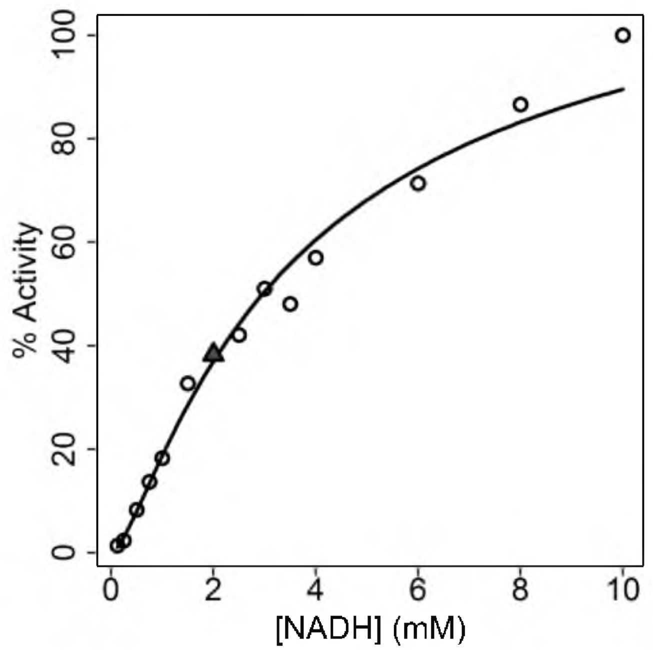

Figure 4.5. Dependence of *Sp*-IDI-2 activity on [NADH]. The curve represents the best fit through the data using the Richards equation and is for visualization purposes only. The dark triangle represents the original [NADPH].

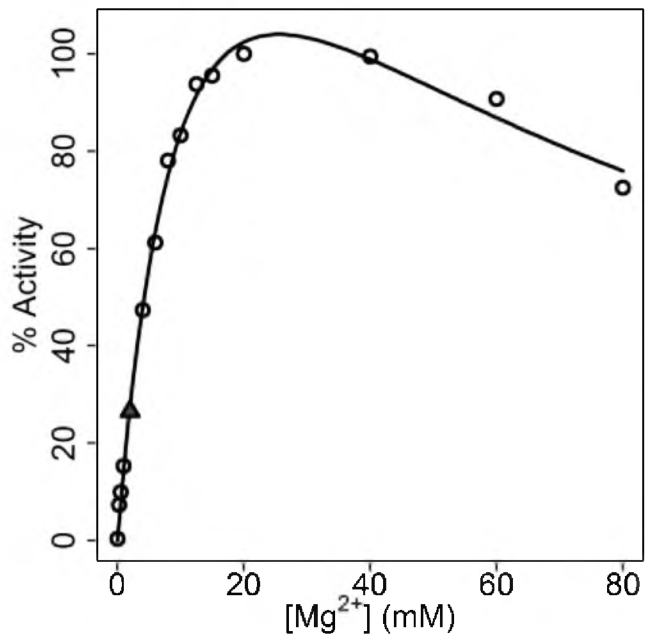

Figure 4.6. Dependence of *Sp*-IDI-2 activity on [Mg^{2+}]. The curve represents the best fit through the data using a substrate inhibition curve and is for visualization purposes only. The dark triangle represents the original [Mg^{2+}].

function of IPP concentration at different concentrations of FMN and as a function of FMN concentration at different concentrations of IPP. A ping-pong type mechanism was immediately excluded because the data in the reciprocal plots tend towards a common point of intersection, rather than parallel as in a ping-pong mechanism. The data and best fit lines to Eq. 4.2, a sequential mechanism with FMN binding first (evidence for this model will be elaborated in the inhibitor kinetic studies results) are shown in Figure 4.8.A and Figure 4.9.A. The residual plots for these best-fit lines are shown in Figure 4.8.B and Figure 4.9.B. In addition to the poor fits as shown in Figure 4.8.A and Figure 4.9.A, the parameters for the fit were $k_{cat} = 1.58 \pm 0.18$, $K_{ipp} = -42.3 \pm 9.8$, and $K_{fmn} = -12.2 \pm 2.5$. In a previous study, negative values excluded the model that was fit and a different model was necessary to describe the data.[163]

Likewise, the simple model of an ordered mechanism with FMN binding first was

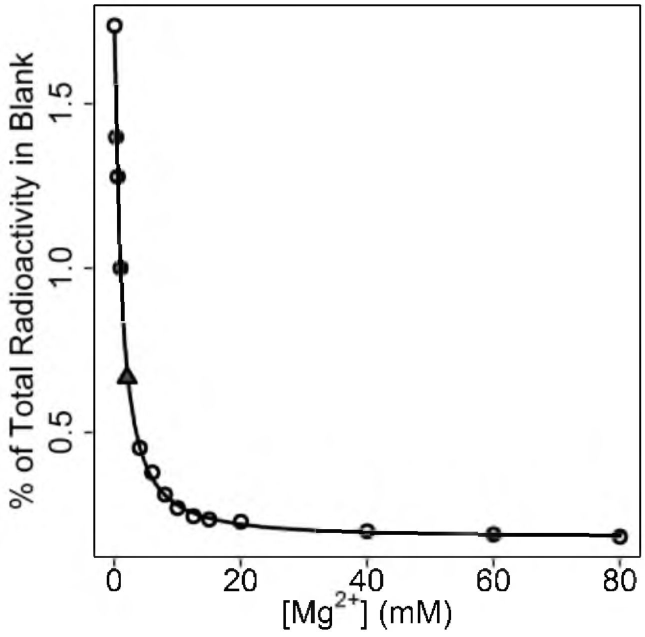

Figure 4.7. Dependence of radioactivity in blanks on [Mg^{2+}]. The curve represents the best fit through the data using an exponential curve and is for visualization purposes only. The dark triangle represents the original [Mg^{2+}] used in early experiments.

not accepted as a reasonable model. In Figure 4.8.B, a clear pattern is observed where the residuals move from negative at low reciprocal values, to positive then to negative at higher reciprocal values. The trend one would expect for a good fit would be a nearly linear line around 0 with slope 0. Thus, the observed trend indicates the true model has curvature. There is no obvious trend in Figure 4.9.B. However, the residuals of the individual concentrations of IPP are not randomly distributed around zero. Instead, they tend to be either all negative or all positive, an indication that the best-fit lines are not actually going through the data points. Examination of the Michaelis-Menten plots based on the above parameters shows that the fits are very poor (Figure 4.10.A and Figure 4.10.B). A better fit was achieved when the data were fit with a sigmoidal function (Figure 4.10.C and Figure 4.10.D). Together, this evidence excludes the sequential,

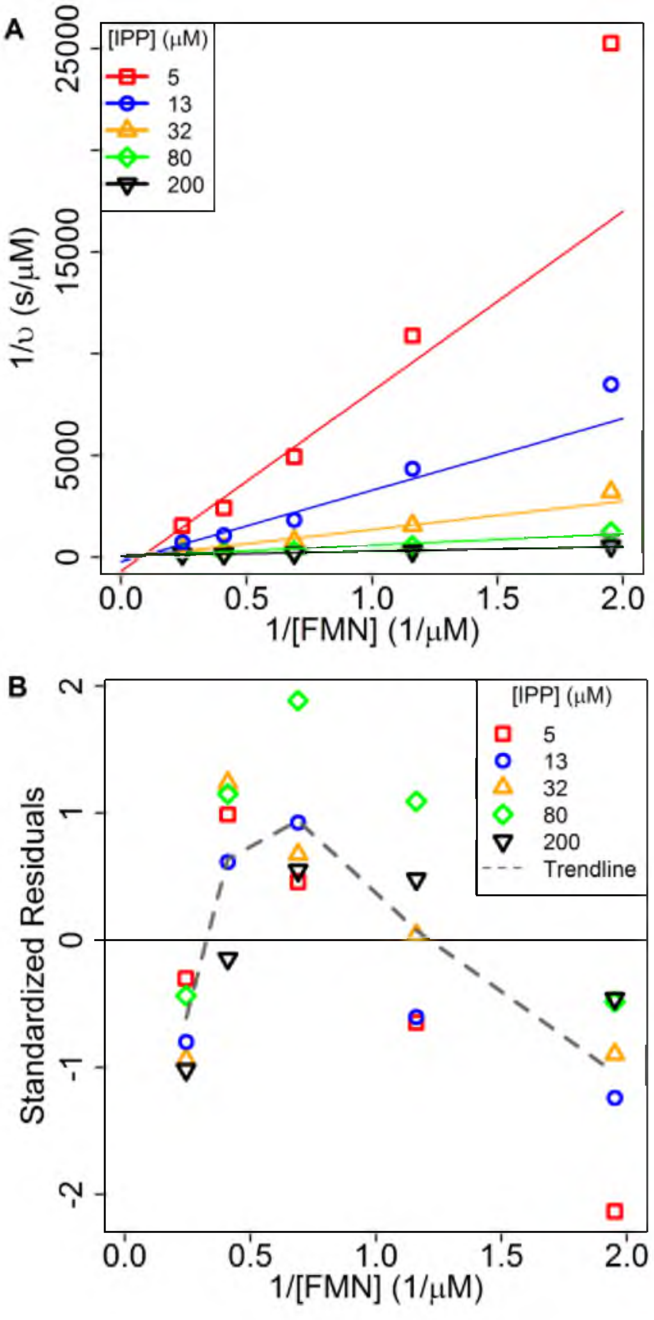

Figure 4.8. Reciprocal plots for *Sp*-IDI-2 bisubstrate kinetics with variable FMN. A, Reciprocal plot with best fit lines for an ordered mechanism with FMN binding first; B, Residual plot of the residuals from the fit in A with a trend line displaying the patterns of residuals for varying FMN concentration.

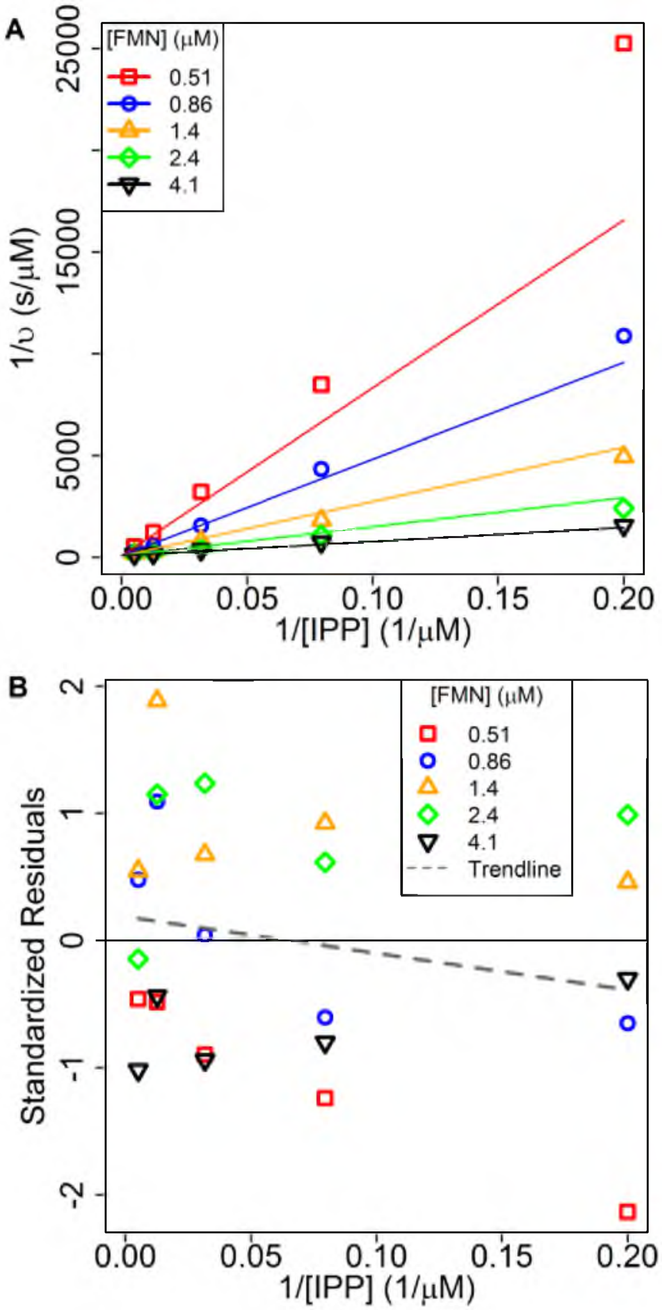

Figure 4.9. Reciprocal plots for *Sp*-IDI-2 bisubstrate kinetics with variable IPP. A, Reciprocal plot with best fit lines for an ordered mechanism with FMN binding first; B, Residual plot of the residuals from the fit in A with a trend line displaying the patterns of residuals for varying IPP concentration.

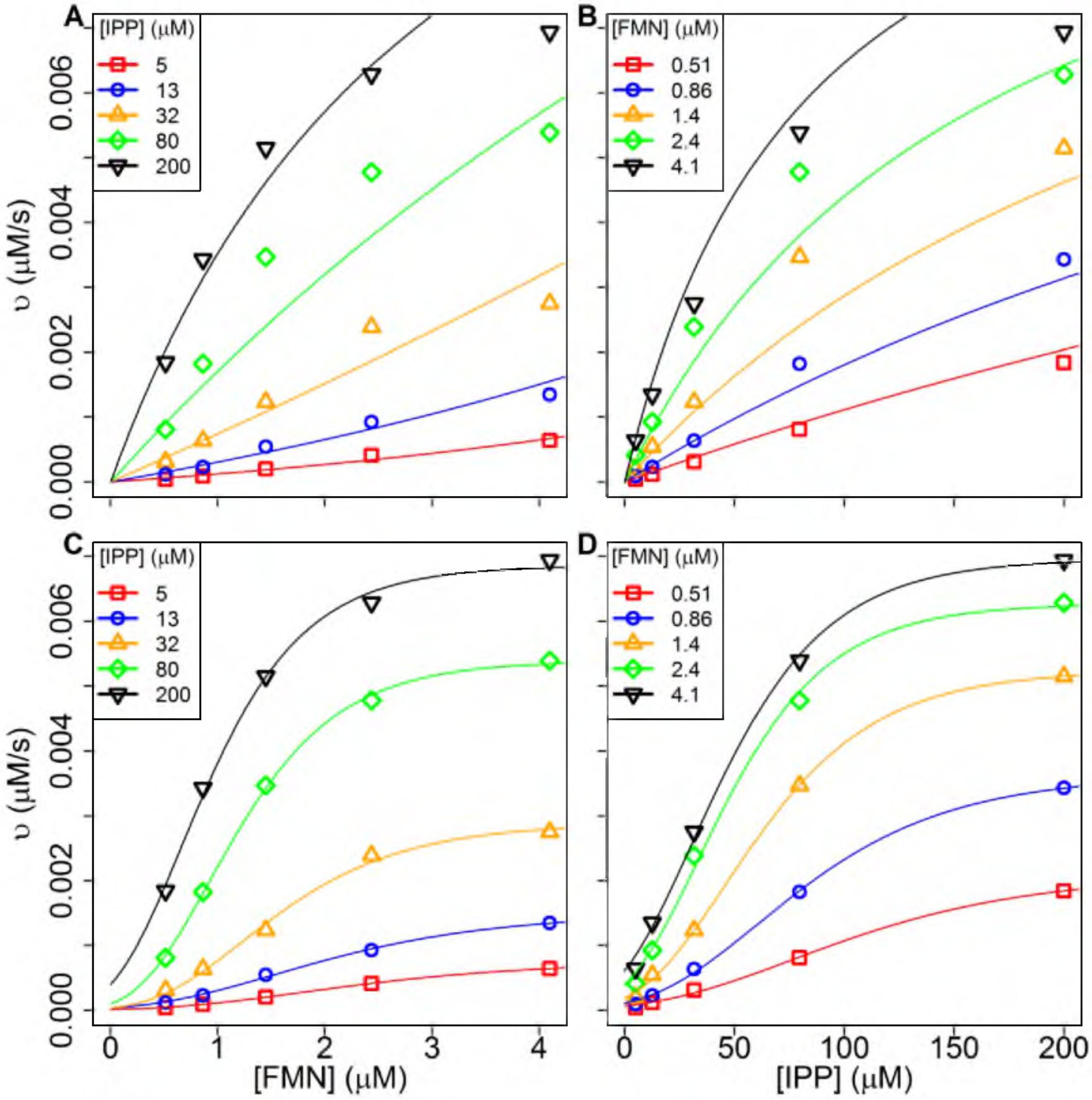

Figure 4.10. Michaelis-Menten plots for the bisubstrate kinetics of *Sp*-IDI-2. A, Best fit lines for variable FMN using the parameters in the text for a sequential ordered model with FMN binding first; B, Best fit lines for variable IPP using the parameters in the text for a sequential ordered model with FMN binding first; C, Best fit lines for variable FMN using a Gompertz growth model; D, Best fit lines for variable IPP using a Gompertz growth model. Note: the fits to the Gompertz equation were not multivariate fits and are for visualization only.

ordered model with FMN binding first as an inadequate description for the kinetic mechanism of *Sp*-IDI-2.

Two models were used that more appropriately describe the bisubstrate kinetic data. The first model is a modified ordered multiple essential activator and multiple substrate binding site model (Eq. 4.4), where A represents FMN, S represents IPP, and *n* and *m* are Hill coefficients.[158] With this model, FMN is treated as an activator such that *n* molecules of FMN bind before any IPP binds. In other words, *n* molecules of FMN are independently in equilibrium with IDI-2 and *m* molecules of IPP bind only to the FMN_n•IDI-2 complex. The parameters from this fit are shown in Table 4.3. The Michaelis-Menten plots and reciprocal plots are shown in Figure 4.11.

The next model fitted to the data was the common ordered binding equation, with FMN binding first, modified to include Hill coefficients (Eq. 4.5). As in the previous model, A represents FMN, S represents IPP, and *n* and *m* are Hill coefficients. With the modification, the assumption is that *n* molecules FMN are simultaneously in equilibrium with IDI-2 and bind before IPP. Then *m* molecules of IPP are simultaneously in equilibrium with the FMN_n•IDI-2 complex. The results from this fit are in Table 4.4. The

Table 4.3. Kinetic parameters for *Sp*-IDI-2 fit to a modified ordered multiple essential activator and multiple substrate binding site model.

	Mean	**S.E.**	**95% C.I.**
k_{cat} (s^{-1})	1.11	0.08	(0.98, 1.29)
K_{ipp} (μM)	23.3	4.0	(16.0, 32.4)
K_{fmn} (μM)	1.61	0.49	(0.89, 2.99)
m	1.14	0.02	(1.10, 1.19)
n	2.59	0.34	(2.07, 3.45)
Residual Sum of Squares	2.167		

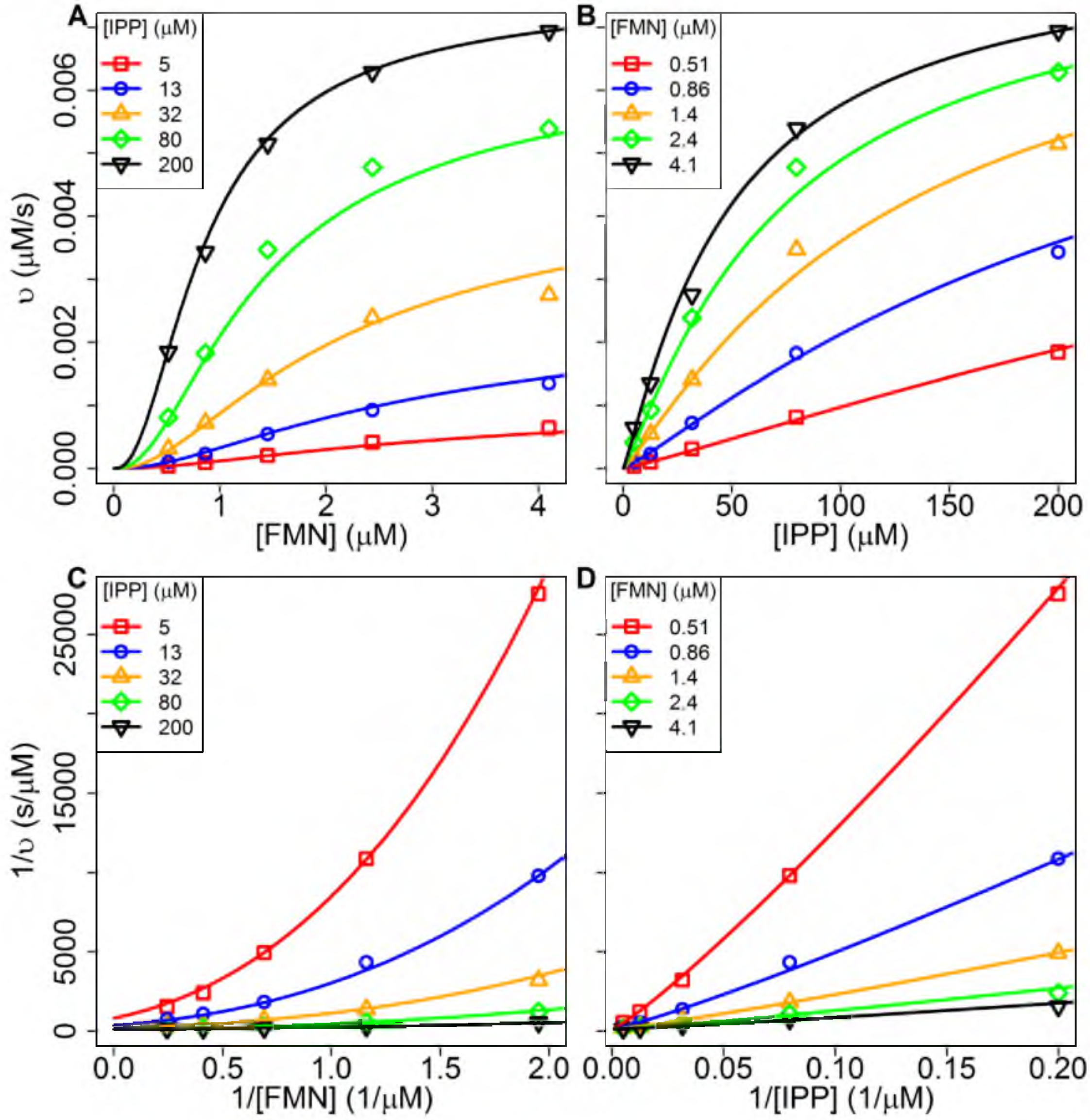

Figure 4.11. Plots for *Sp*-IDI-2 bisubstrate data with best fit lines to the modified ordered multiple essential activator and multiple substrate binding site model. A, and B, Michaelis-Menten plots for variable FMN and IPP, respectively; C, and D, Reciprocal plots for variable FMN and IPP, respectively.

Table 4.4. Kinetic parameters for *Sp*-IDI-2 fit to a modified ordered multiple substrate binding site model.

	Mean	S.E.	95% C.I.
k_{cat} (s^{-1})	0.983	0.078	(0.845, 1.162)
K_{ipp} (μM)	40.8	5.6	(30.8, 53.5)
K_{fmn} (μM)	2.39	0.26	(1.98, 3.07)
m	1.15	0.02	(1.10, 1.19)
n	1.95	0.09	(1.79, 2.12)
Residual Sum of Squares	1.978		

plots of Michaelis-Menten and reciprocal fits are shown in Figure 4.12. Both models fit the bisubstrate data well with low residual sums of squares. The parameter values for both models are similar. Thus, models that require a Hill coefficient and treat FMN as the first substrate to bind support the data.

Inhibition studies were performed that comprehensively described the *Sp*-IDI-2 kinetic mechanism and supported the previously described bisubstrate fits. Adonitol was examined as a competitive inhibitor of FMN, however was not inhibitory even at millimolar concentrations. Lumichrome was also studied as it successfully inhibited NADH:flavin oxidoreductase, an enzyme that uses FMN as a substrate.[164,165] Solubilization of lumichrome in pyridine resulted in a 90 % decrease in catalytic efficiency. When dissolved in NaOH, no change in kinetic parameters was observed for the control, but an inhibitor was desired that did not require changing the assay conditions. Thus, 5-deazaFMN was explored.

In order to fit the data obtained from 5-deazaFMN inhibition of FMN, the standard competitive inhibition equation was modified to include Hill coefficients (Eq. 4.6) to yield the curves shown in Figure 4.13. From this fit, 5-deazaFMN was a potent

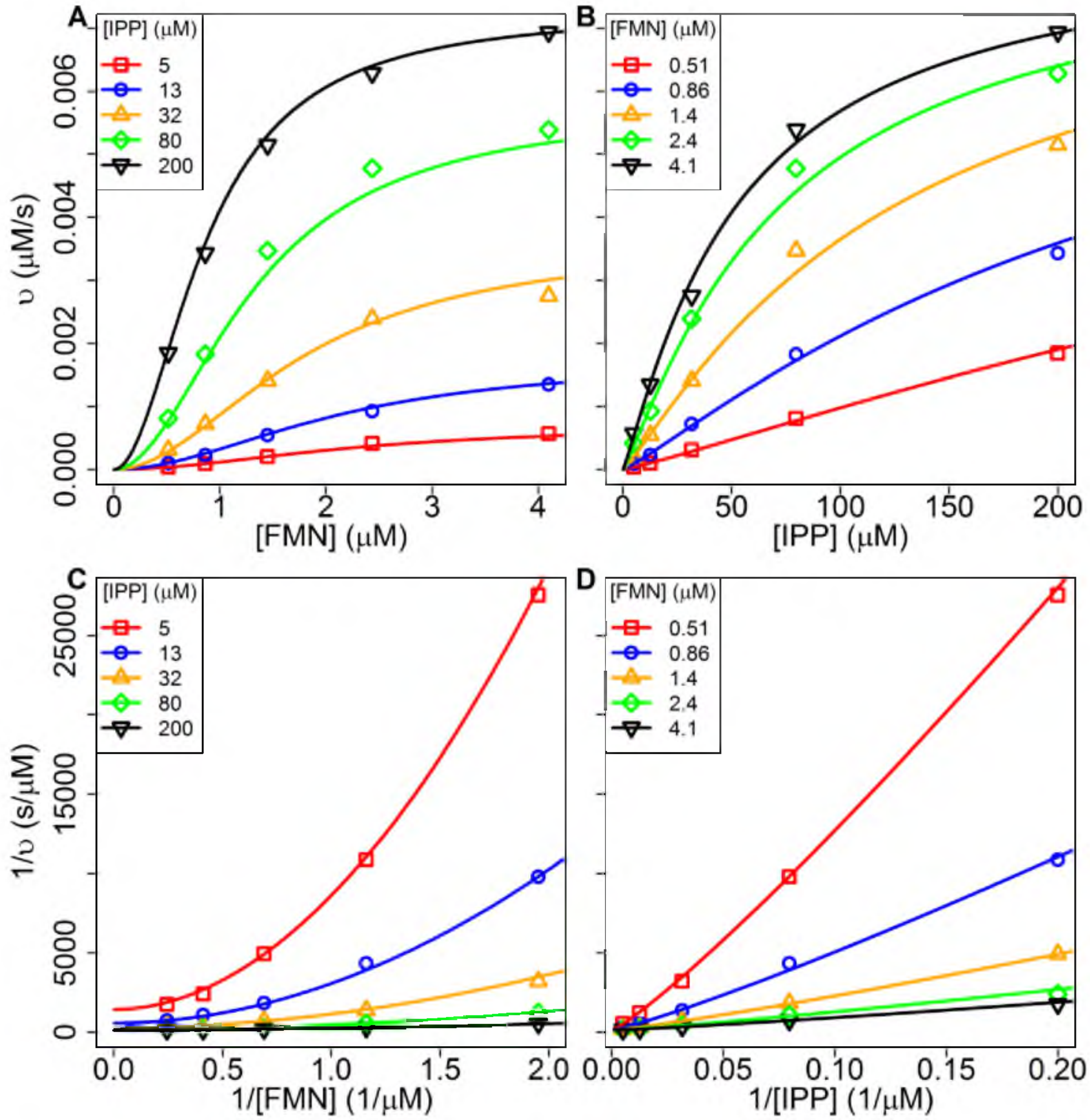

Figure 4.12. Plots for *Sp*-IDI-2 bisubstrate data with best fit lines to the modified ordered with FMN binding first model. A, and B, Michaelis-Menten plots for variable FMN and IPP, respectively; C, and D, Reciprocal plots for variable FMN and IPP, respectively.

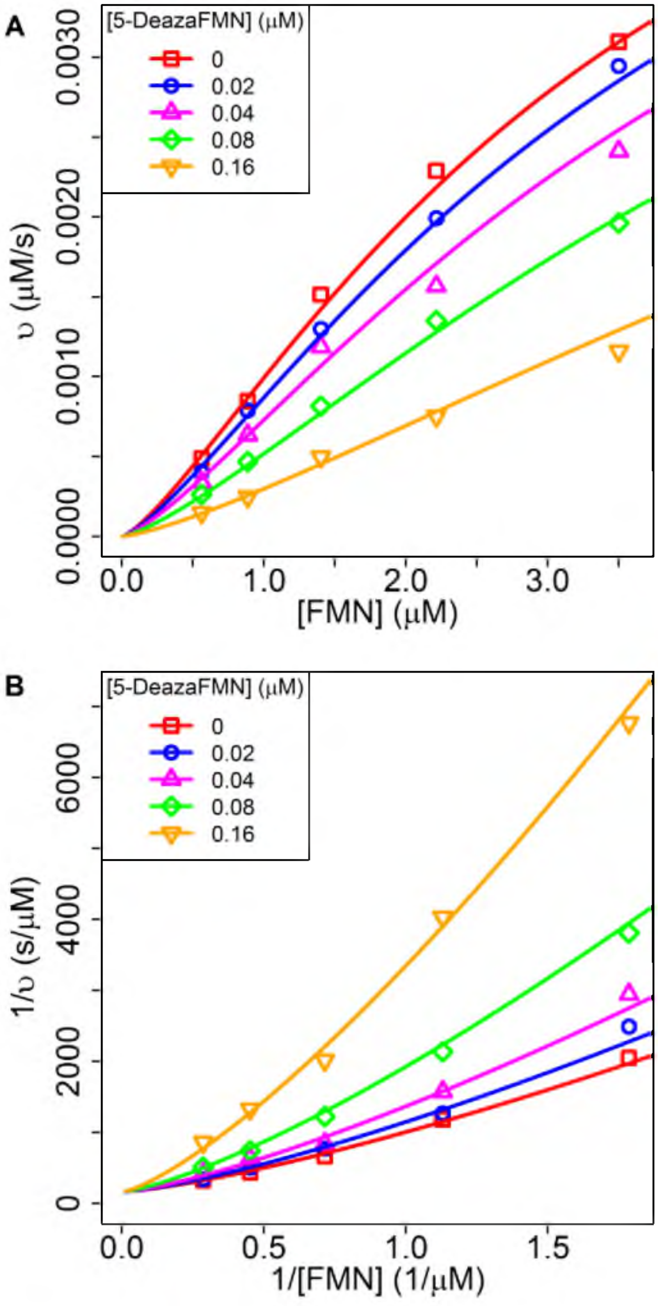

Figure 4.13. Plots of *Sp*-IDI-2 inhibition with 5-deazaFMN and variable FMN with data fit to a modified competitive inhibitor equation. A, Michaelis-Menten plot; B, Reciprocal plot.

inhibitor of FMN with a K_i of 75 nM (Table 4.5). Each Hill coefficient for FMN and 5-deazaFMN is the same, and each is half the Hill coefficient for FMN in the bisubstrate essential activator model (Table 4.3). Whether this is significant or just a coincidence is unclear.

When 5-deazaFMN was evaluated with IPP as the varied substrate, data were fit to a modified noncompetitive inhibitor model (Eq. 4.7, Figure 4.14). With this fit, the Hill coefficient of IPP had a 95% confidence interval of (0.72, 1.43), which includes 1.0. Thus, this parameter was not included and the data were refit to give the results in Table 4.6 under the "Original Analysis" column. The fits to the data reveal a problem where the fit poorly matches the data at no or low 5-deazaFMN concentrations. To account for this, a new term, K_{ippi}, was included to account for equilibrium binding of IPP to the 5-deazaFMN•IDI-2 complex as shown in Figure 4.15. Here IPP is assumed to bind differently to the active FMN•IDI-2 compared to the inhibitor complex.

When the new term was included (Eq. 4.8), the residual sum of squares decreased by half (Table 4.6, “Subsequent Analysis”). However, the parameter values shifted from the previously observed results in the bisubstrate studies. For example, the original K_{ipp} parameter increased from 61 to 224 μM when the new parameter was added, while for the bisubstrate study the value was 41 μM. While adding a new parameter improved the fit, the changes in the parameter values may be an indication that Figure 4.15 is not an appropriate model either.

To complement the results of the FMN competitive inhibitor pattern, a competitive inhibitor for IPP was evaluated. First, cyclopropyl-IPP was evaluated, but because it functions as an alternate substrate,[166] the results were more convoluted than

Table 4.5. Kinetic parameters for 5-deazaFMN inhibition of FMN for *Sp*-IDI-2 fit to a modified competitive inhibition model.

	Mean	S.E.	95% C.I.
k_{cat} (s^{-1})	0.833	0.134	(0.636, 1.261)
K_i (nM)	75.0	5.8	(63.6, 86.9)
K_{fmn} (μM)	3.55	0.71	(2.53, 5.86)
n	1.31	0.05	(1.22, 1.42)
d	1.34	0.08	(1.18, 1.53)

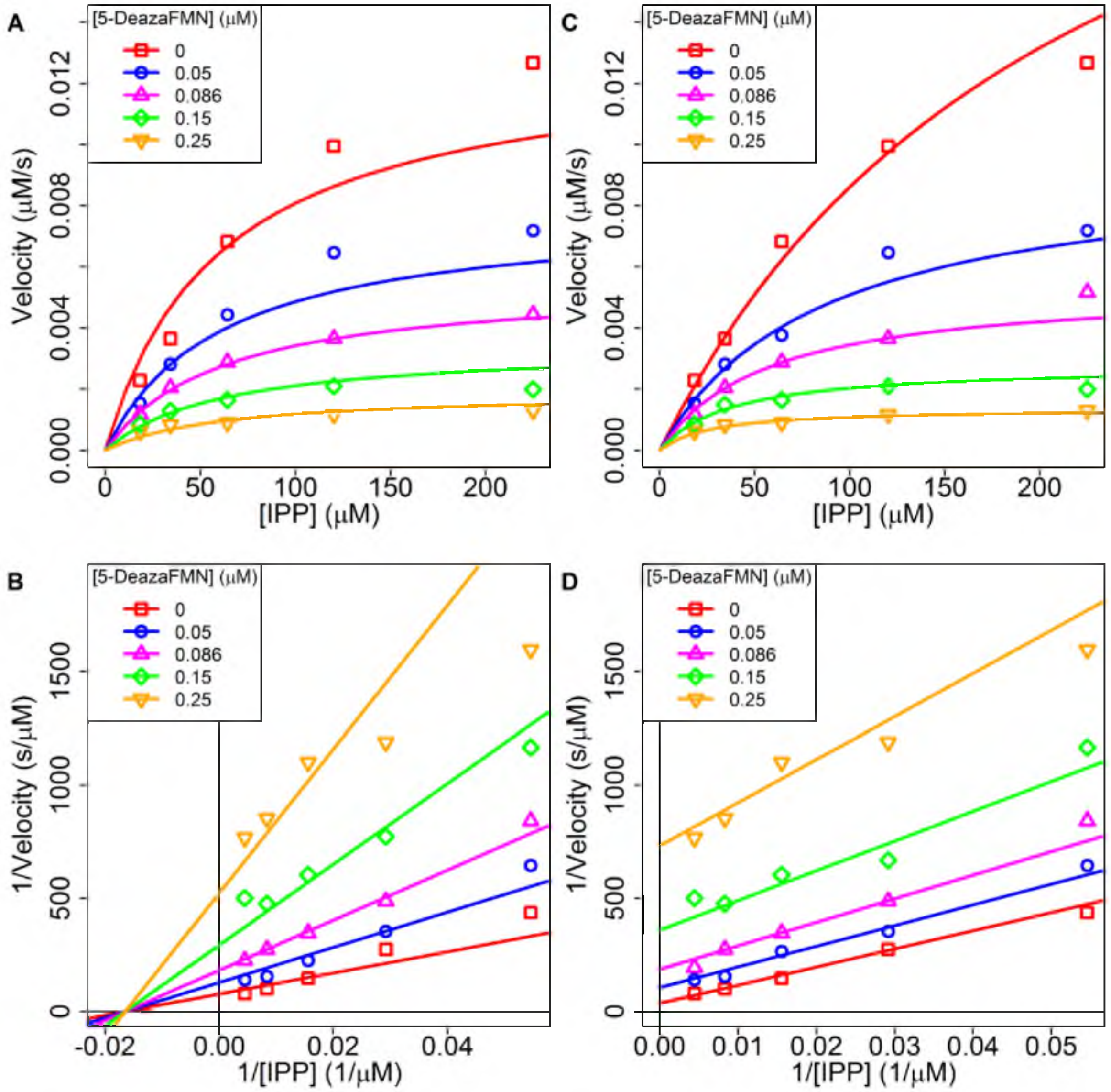

Figure 4.14. Plots of *Sp*-IDI-2 inhibition with 5-deazaFMN and variable IPP with data fit to a modified competitive inhibitor equation. A, Michaelis-Menten plot of the Original Analysis; B, Reciprocal plot of the Original Analysis; C, Michaelis-Menten plot of the Subsequent Analysis; D, Reciprocal plot of the Subsequent Analysis.

Table 4.6. Kinetic parameters for 5-deazaFMN inhibition of IPP for *Sp*-IDI-2. Original Analysis are results from a fit to Eq 7. Subsequent Analysis are results from a fit to Eq 8.

	Original Analysis			**Subsequent Analysis**		
	Mean	**S.E.**	**95% C.I.**	**Mean**	**S.E.**	**95% C.I.**
k_{cat} (s^{-1})	0.866	0.070	(0.740, 1.021)	1.86	0.32	(1.38, 2.77)
K_{ipp} (μM)	60.7	7.6	(47.2, 77.8)	224	51	(149, 369)
K_i (nM)	68.3	6.8	(55.8, 82.2)	201	37	(143, 318)
d	1.35	0.09	(1.19, 1.54)	1.44	0.07	(1.31, 1.57)
K_{ippi} (μM)	--			15.8	4.3	(7.9, 25.6)
Residual Sum of Squares	3.198			1.456		

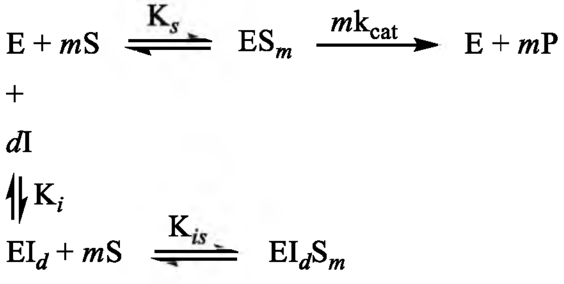

Figure 4.15. Proposed model for the noncompetitive inhibition of IPP by 5-deazaFMN.

desired. The *T. thermophilus* IDI-2 potent inhibitor Cl-IPP was examined, but as previously described, reproducibility was a problem.[167] Previously, NIPP was a demonstrated inhibitor of *T. thermophilus* IDI-2 with a K_i = 5.1 μM,[63] and thus was evaluated for the *S. pneumoniae* enzyme.

The data from NIPP inhibition of IPP could be fit to the standard competitive inhibition model (Eq. 4.6, without the *n* and *d* parameters) to yield the best-fit curves in Figure 4.16. When Hill coefficient parameters were included, either the fit did not

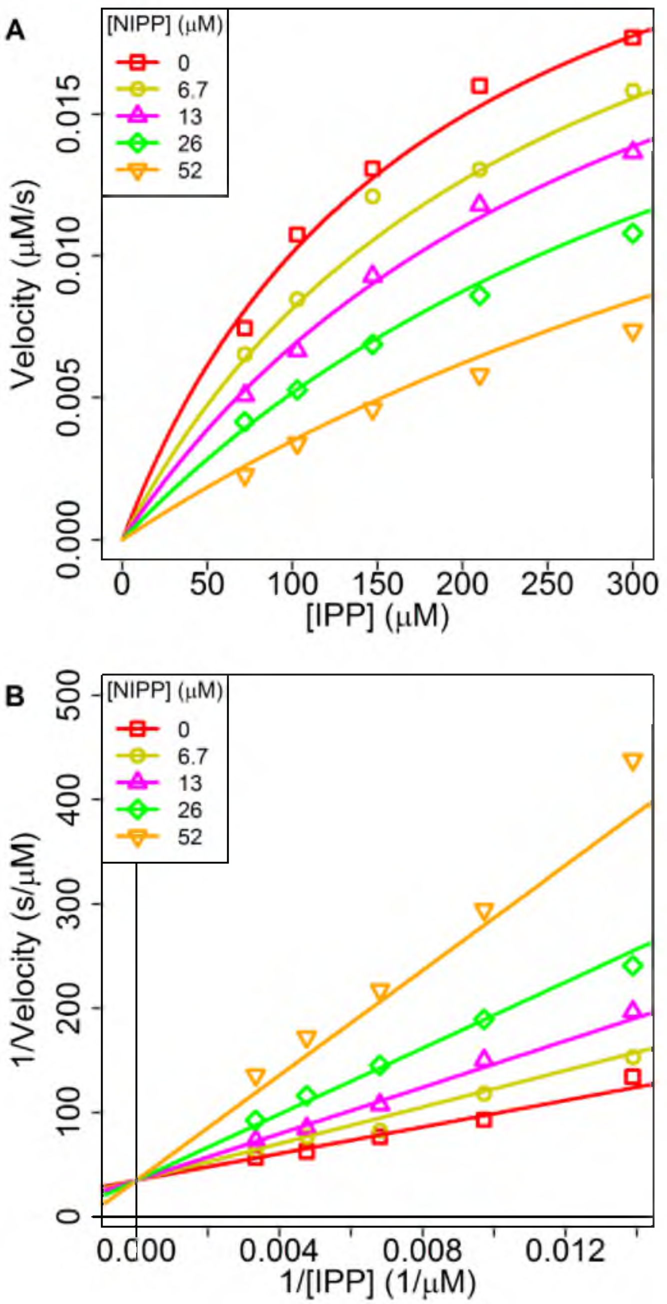

Figure 4.16. Plots of *Sp*-IDI-2 inhibition with NIPP and variable IPP with data fit to a competitive inhibitor equation. A, Michaelis-Menten plot; B, Reciprocal plot.

improve significantly or the 95% confidence interval of that parameter included 1.0 (an indication the parameter was insignificant). Here, the large K_{ipp} is similar to the value obtained for the 5-deazaFMN inhibition experiment under the "Subsequent Analysis" fit (Table 4.7).

Assessing NIPP as an inhibitor of FMN, the reciprocal plots showed data that were parallel at different NIPP concentrations but curved (Figure 4.17). Thus the data were fit to a modified uncompetitive model to account for the curvature (Eq. 4.9). As observed with all studies of variable FMN, an exponent was needed to properly fit the data and the value was ~ 2 (Table 4.8).

Cumulatively, the pattern of the FMN competitive inhibitor (competitive for FMN and noncompetitive for IPP) and the pattern of the IPP competitive inhibitor (competitive for IPP and uncompetitive for FMN) indicate that the sequential binding occurs with FMN binding first followed by IPP binding.[168]

Discussion

The discovery of the MEP pathway of isoprenoid biosynthesis has introduced a number of new enzyme antibacterial drug targets. These enzymes are necessary for the pathogenic organisms that express them, but are not found in *Homo sapiens*. While not exclusive to the MEP pathway, IDI-2 is found in several pathogenic organisms, including *Staphylococcus aureus*, *Enterococcus faecalis*, and *Streptococcus pneumoniae*.[45] Like the enzymes of the MEP pathway, IDI-2 has been proposed as a potential drug target due to the absence of a homologue in humans. Despite the appeal of IDI-2 as a drug target, there have been limited studies on the enzyme from pathogenic organisms.

The *Sp*-IDI-2 enzyme was previously selected as a potential antibacterial agent

Table 4.7. Kinetic parameters for NIPP inhibition of IPP for *Sp*-IDI-2 fit to a competitive inhibition model.

	Mean	S.E.	95% C.I.
k_{cat} (s^{-1})	1.47	0.10	(1.29, 1.70)
K_i (μM)	15.5	1.2	(13.3, 18.0)
K_{ipp} (μM)	184	23	(144, 236)

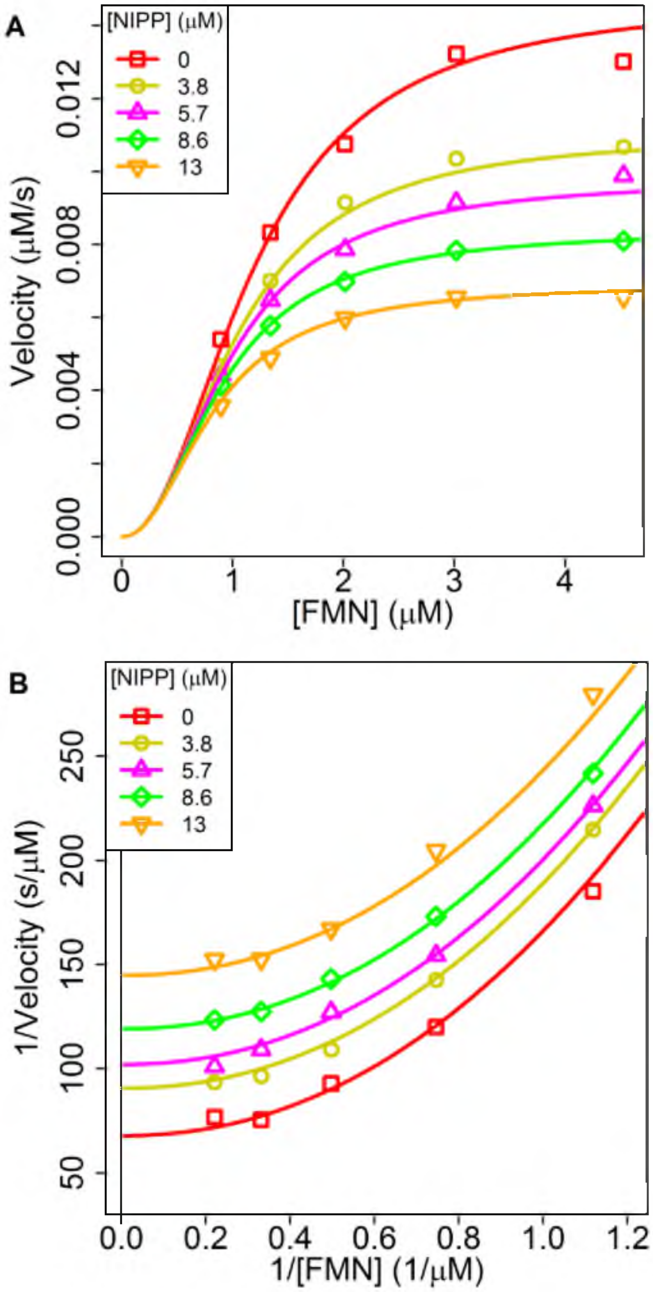

Figure 4.17. Plots of *Sp*-IDI-2 inhibition with NIPP and variable FMN with data fit to a modified uncompetitive inhibitor equation. A, Michaelis-Menten plot; B, Reciprocal plot.

Table 4.8. Kinetic parameters for NIPP inhibition of FMN for *Sp*-IDI-2 fit to a modified uncompetitive inhibition model.

	Mean	S.E.	95% C.I.
k_{cat} (s^{-1})	0.736	0.021	(0.699, 0.782)
K_i (µM)	11.4	0.6	(10.4, 12.6)
K_{fmn} (µM)	1.19	0.04	(1.12, 1.28)
n	2.12	0.13	(1.88, 2.37)

and crystallized.[163] During preliminary studies, flavin was released from the enzyme while purified on a Ni^{2+} affinity column. However, these results were inconsistent and not reproducible with different columns and wash procedures. To ensure complete deflavination, a 2 M KBr wash was added to the purification method. Reconstitution, if necessary, required incubation with FMN and washes with buffer through an ultrafiltration device.[163] These properties of *Sp*-IDI-2 differ from the *T. thermophilus* enzyme in that the *Tt*-IDI-2 lost the ability to be reconstituted once deflavinated.

The ease at which FMN released from *Sp*-IDI-2 introduced the possibility that FMN functions as a substrate in the overall reaction. Bisubstrate kinetic studies have a long history used in conjunction with competitive substrate inhibitors to elucidate the overall bisubstrate kinetic mechanism.[168] Applying these techniques, a mechanism was uncovered that is both well described by the data (a sequential, ordered mechanism, with FMN binding first) and unique (Hill coefficients were necessary for proper fitting).

Based on crystal structures of the *S. shibitae* IDI-2, it seemed apparent that FMN bound in the active site before IPP because FMN was located deeper in the binding pocket.[58,73] Furthermore, IDI-2 has routinely been purified with FMN still bound from some organisms including *Methanocaldococcus jannaschii*,[169] and *Thermus thermophilus*.[63]

The bisubstrate kinetics of *Sp*-IDI-2 exhibited curvature that a simple bisubstrate model could not explain. Likewise, when substrate concentration was plotted against velocity, the data did not approach zero in a direct hyperbolic manner. A simple equation was desired that would describe the data without including complex or unnecessary characteristics. In one attempt to fit the data, a multiple essential activator equation was applied. However, the meaning of the coefficients differed from those of the inhibition results. While the multiple essential activator fit may help explain some characteristics of the mechanism, the model is not completely adequate. Modification of the sequential, ordered bisubstrate equation with Hill coefficients improved the fit and made all the results consistent. For example, the Hill coefficient for FMN in every study was ~ 2, except when inhibited by 5-deazaFMN when it was 1.3. The literal, but unrealistic interpretation of the Hill coefficients would be that two molecules of FMN simultaneously bind with apo-IDI-2. More reasonable is the idea that two molecules of FMN bind before IPP based on the successful fitting of the multiple essential activator model with a coefficient of 2.6. Here the value represents a summation of the population in the steady state and thus, there are two or three FMN molecules bound to IDI-2 before IPP binds.

The addition of Hill coefficients was one way to describe the data, but these results will not be used to extrapolate the exact mechanism. While Hill coefficients are convenient to mathematically fit data, their ineffectiveness to establish a definitive mechanism is well described.[170] The complexity of data and nonlinear fits provides confidence that the system undergoes cooperativity or allostery. The results are consistent with a type of cooperativity that would be positive in nature. Since the *Sp*-IDI-2 enzyme is a tetramer in solution,[163] these subunits likely interact in a process that is necessary for catalysis. Hemmi and coworkers found that addition of substrate caused the octomer of *S. shibatae* IDI-2 to degrade into a tetramer.[59] Based on unpublished results from our group, a monomer can be produced that is also active, which supports an allosteric rather than a cooperative effect.

The presence of an allosteric effect raises new possibilities beyond just active site targeted drugs. To date, there are no crystal structures of an IDI-2 enzyme without FMN bound. Determination of the effects that take place upon FMN binding may be important to understand the observed bisubstrate kinetics.

CHAPTER 5

BOOTSTRAP ANALYSIS OF TRANSIENT KINETIC ISOTOPE EFFECTS IN FARNESYL SYNTHASE AND PROTEIN FARNESYL TRANSFERASE

Introduction

Farnesyl diphosphate (FPP) synthase catalyzes a head-to-tail condensation of IPP and DMAPP to form geranyl diphosphate (GPP). In a similar manner, FPP synthase (FPPase) can condense GPP and another molecule of IPP to form FPP, which begins the isoprenoid chain-elongation pathway. The FPPase enzyme contains a core scaffold of 10 α helices that have been termed the "isoprenoid fold" because of their ubiquity in the isoprenoid family of enzymes.[171] The universality of the structural fold found in FPPase leads it to be an ideal model to understand the chemistry of reactions in the isoprenoid biosynthetic pathway.

Based on protein sequences in the human genome, hundreds of prenylated proteins have been predicted that vary in their function from processes such as centromeric proteins, proteins involved with cell cycle regulation and apoptosis, glycogen metabolic enzymes, and GTPases of the Ras superfamily.[172] The Ras proteins, which are part of the signaling pathway that controls cell proliferation, are substrates of protein farnesyl transferase (PFTase). Nearly one-third of human cancers are linked to mutated Ras proteins and within that, K-Ras mutations are found in half the colorectal cancers and almost all (90 %) of pancreatic cancers.[34] PFTase catalyzes the farnesylation of a cysteine residue at the C-terminal of a protein that contains a motif called the CAAX box, where A represents an aliphatic amino acid and X is a variable amino acid site. The reaction occurs as the cysteine's zinc coordinated sulfur displaces the phosphate oxygen from C1 of FPP. Evidence that describes the nature of this displacement supports both dissociation,[173,174] and association,[175–177] or is substrate dependent.[178] Understanding the transition state structure of PFTase will help investigation into inhibitors that may be used as anticancer drugs.

Currently, investigations into the FPPase and PFTase transition state structures focus on transient kinetic studies, particularly transient kinetic isotope effects (TKIE). The time and signal dependency of transient kinetics requires a different analytical approach than when steady state kinetic isotope effects (KIE) are studied. Fisher and co-workers developed a set of rules that can be applied to transient kinetics to determine the intrinsic KIE (KIE_{int}) with stopped-flow experimentation.[179] While they neglected a quantitative determination of error in their examples, variability of TKIEs can be described using the bootstrap.

The bootstrap is a computer intensive statistical technique that, for the purposes of this chapter, is nonparametric (no assumptions are made regarding the nature of the population distribution). With this technique, a sample is made (with replacement) from a given set of data, and the parameter of interest is calculated. As an example, a dataset is in Table 5.1 where the linear relationship between X and Y is of interest. In this simplified example, the slope (0.244 ± 0.029 calculated from Eq. 5.1 and 5.2) and intercept (0.448 ± 0.177 calculated from Eq. 5.3 and 5.4) are easily calculated since each

Table 5.1. Example linear regression data (Original columns) with samples of those data taken with replacement.

Original		Sample 1		Sample 2	
x	y	x	y	x	y
1	0.803	2	0.863	7	2.19
2	0.863	7	2.19	7	2.19
3	1.32	8	2.12	8	2.12
4	1.48	3	1.32	3	1.32
5	1.76	9	2.99	8	2.12
6	1.38	9	2.99	10	2.98
7	2.19	2	0.863	8	2.12
8	2.12	10	2.98	5	1.76
9	2.99	5	1.76	3	1.32
10	2.98	5	1.76	8	2.12
Slope		0.267		0.196	
Intercept		0.381		0.713	

Sample 3		Sample 4		Sample 5	
x	y	x	y	x	y
6	1.38	4	1.48	8	2.12
5	1.76	10	2.98	1	0.803
7	2.19	1	0.803	2	0.863
7	2.19	6	1.38	9	2.99
7	2.19	6	1.38	6	1.38
10	2.98	6	1.38	2	0.863
3	1.32	10	2.98	4	1.48
7	2.19	5	1.76	6	1.38
10	2.98	1	0.803	6	1.38
10	2.98	7	2.19	10	2.98
0.257		0.242		0.243	
0.369		0.548		0.312	

has an explicit solution.

$$slope = m = \frac{\sum(X_i - \bar{X})(Y_i - \bar{Y})}{\sum(X_i - \bar{X})^2} \qquad \textbf{5.1}$$

$$slope\ standard\ deviation = \sqrt{\frac{MSE}{\sum(X_i - \bar{X})^2}} \qquad \textbf{5.2}$$

$$intercept = b = \bar{Y} - m\bar{X} \qquad \textbf{5.3}$$

$$intercept\ standard\ deviation = \sqrt{MSE\left(\frac{1}{n} + \frac{\bar{X}^2}{\sum(X_i - \bar{X})^2}\right)} \qquad \textbf{5.4}$$

$$MSE = \frac{\sum\left(Y_i - \hat{Y}_i\right)^2}{n-2} = \frac{\sum e_i^2}{n-2} \qquad \textbf{5.5}$$

Also in Table 5.1 are five random samples from the original dataset. These samples were taken with replacement, so each data point could be sampled multiple times. For example, in Sample 1 data points (9, 2.99) and (5, 1.76) were each sampled twice. The slope and intercept for each sample are also shown in Table 5.1 below the sampled data (for the bootstrap, the variability is not determined at this stage). Next, the mean and standard deviations of these slope and intercept values are calculated. For this example, the slope is 0.241 ± 0.027 and intercept is 0.465 ± 0.164. These are the bootstrap statistics and are an estimate of the sample distribution; note how similar the parameters and their variability are compared to the explicitly determined values above.

The original data could be sampled any number of times, but usually a good estimate is achieved quickly, as in the above example with only five samples of the data. With 100 samples (not shown), the slope is 0.240 ± 0.031 and the intercept is 0.457 ± 0.140. A bootstrap replicate is performed each time the original data are sampled and a parameter calculated. The collection of these values will form a distribution that approximates the true distribution (Figure 5.1). From a collection of bootstrap replicates, the mean and variability can be approximated. In a bootstrap analysis, an influential data point is one that causes the distribution to shift significantly in one direction. For example, an influential data point may cause a bias where slope values are calculated only when it is selected in the bootstrap replicate (slope < 0.15, Figure 5.1.B). Removal

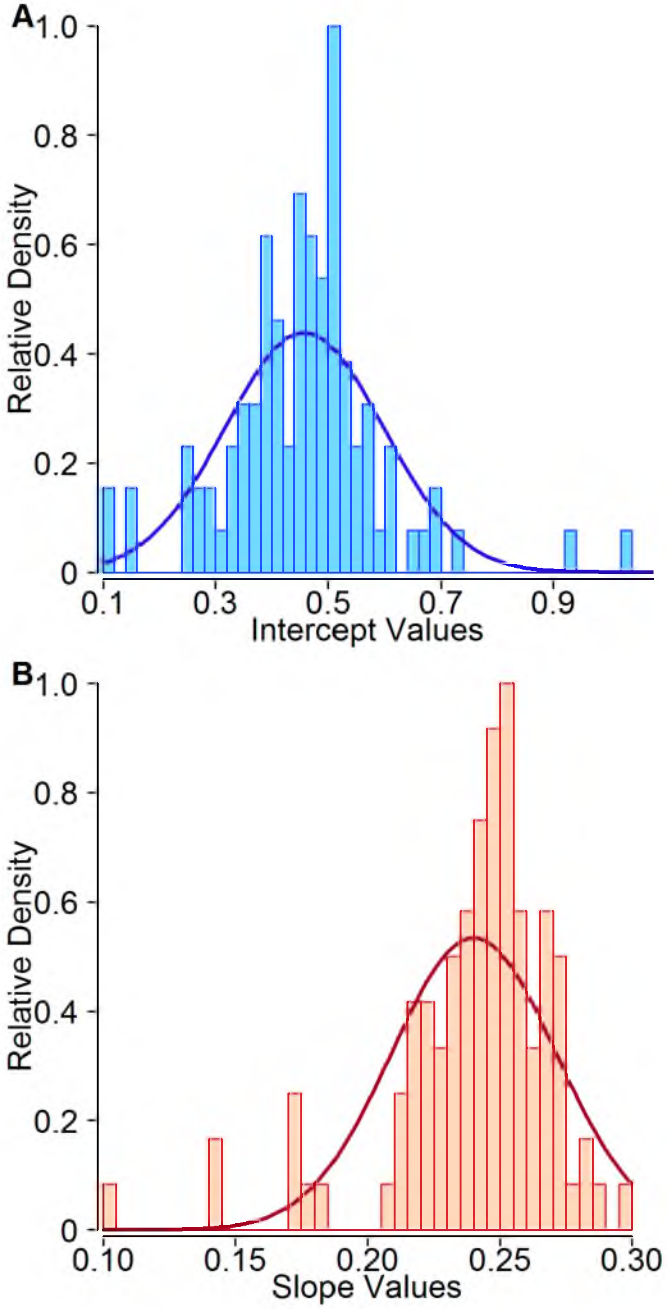

Figure 5.1. Histograms of the 100 bootstrap values from the linear regression example. Curves represent the normal curves with mean and standard deviations discussed in the test. A, Intercept values; B, Slope Values.

of this point would correct the skew in the distribution and provide for a more realistic approximation to the true distribution.

Importantly, some considerations were overly simplified for the previous example. In the previous example, it would be desirable to perform the experiment another four to six times to have an appropriate dataset. Even though the parameters were well approximated, replicates on the entire experiment will help the analyst understand the experiment-to-experiment variability. Another consideration is that the bootstrap does not create data. It just examines the data in a different way than traditionally performed.

While simple statistics, such as slope, have a well-known and understood formula and associated error structure, many parameters such as a KIE (because it is a combination of individually determined parameters, see Experimental Procedures), deviate from that ideal situation. In moving away from ideality, the associated theory and statistical foundation for the variability of a parameter become convoluted, complicated, and in some situations impossible to explicitly determine. A primary advantage of the bootstrap to other statistical methods is its simplicity and the use of data that have already been generated to estimate a statistic that may otherwise be extremely difficult to solve.

The following describes the application of the bootstrap to determine the $\mathrm{KIE}_{\mathrm{int}}$ for both FPPase and PFTase. The error and confidence limits associated with the $\mathrm{KIE}_{\mathrm{int}}$ parameter will be presented. The importance of an appropriate determination of error will be discussed.

Experimental Procedures

Source of data. The farnesyl synthase data were provided by Dr. Leigh-Anne Ferguson-Ihnken (APPENDIX A). Data for the farnesyl transferase experiments were provided by Dr. Seoung Choi (APPENDIX B).

Derivation of transient kinetic isotope effect equation. The turnover ratio was fit to a first order growth model Eq. 5.6 that forced an intercept at the origin, where: y_i, t_i, and ε_i, are the response, time and error, respectively, for data point i; m is the response from the deuterated (D) or unlabeled (H) substrates; and a_m and k_m are parameters of the exponential function.

$$y_i = a_m(1 - \exp^{-k_m t_i}) + \varepsilon_i \qquad \textbf{5.6}$$

Finding the derivative of Eq. 5.6 with respect to time, gives Eq. 5.7.

$$dy_i/dt = -a_m k_m \exp^{-k_m t_i} + \varepsilon_i' \qquad \textbf{5.7}$$

The TKIE model (Eq. 5.8),[179] is only dependent on the derivatives of the signals s_H and s_D for the unlabeled and deuterated substrate, respectively. The derivative 5.7 is substituted into 5.8 to yield 5.9.

$$TKIE_x = \frac{d[s_H]/dt}{d[s_D]/dt} \qquad \textbf{5.8}$$

$$TKIE_i = \frac{a_H k_H \exp^{-k_H t_i} + \varepsilon_{H,i}'}{a_D k_D \exp^{-k_D t_i} + \varepsilon_{D,i}'} = \frac{a_H k_H \exp^{-k_H t_i}}{a_D k_D \exp^{-k_D t_i}} + \varepsilon_{H,i}'' \qquad \textbf{5.9}$$

Taking the limit as $t \to 0$, gives Eq. 5.10 which, according to the First Rule of Transient-State KIEs, is equal to the intrinsic KIE.[180]

$$\lim_{t \to 0} TKIE = \frac{a_H k_H}{a_D k_D} = KIE_{Intrinsic} \qquad \textbf{5.10}$$

Statistical analysis. Data analysis was performed using the boot package in R version 2.11.0 or later,[117] with the additional packages boot,[181,182] dichromat,[121] ggplot2,[183] grid,[117] nlstools,[159] and spatstat.[184]

Results

Source of data and statistical analysis. A single turnover kinetic study was performed with both FPPase and PFTase using unlabeled and CD_3-labeled substrates (Figure 5.2). The amount of unlabeled and CD_3-labeled substrates and products that remained after a reaction were separated with HPLC and quantified as disintegrations per minute (DPM) from a scintillation counter. The turnover ratio (the signal) was calculated and fit to a single exponential growth model, Eq. 5.6. The choice of model fit to the data is irrelevant, as long as the model is the same for both the labeled and unlabeled analysis, and the derivative can be calculated.[179] No intercept correction was included in the single exponential growth model because the confidence interval of the intercept parameter included zero, an indication that it was an unnecessary parameter.

A balanced approach was used to ensure that over the entire analysis, regardless

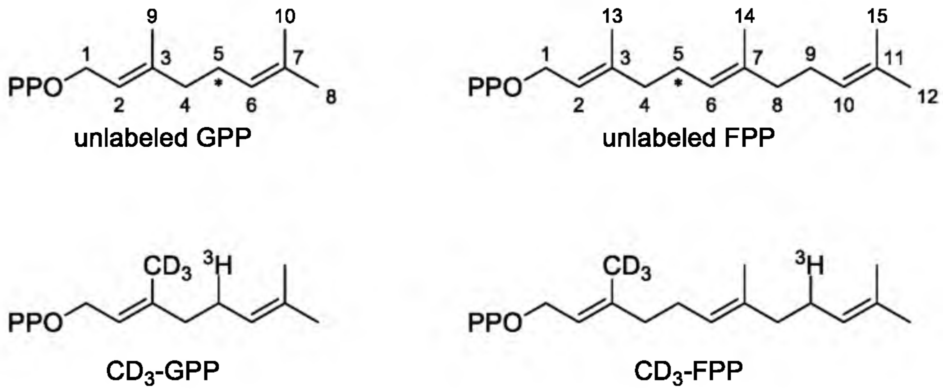

Figure 5.2. Structures of unlabeled GPP and FPP (* denotes a ^{14}C label) and deuterated methyl-GPP and FPP with a ^3H label. The unlabeled term refers to the C9 and C13 methyl groups only and does not refer to the radioactive labels.

of the number of bootstrap replicates, each data point was used an identical number of times. Sampling with time-point stratification retained the initial number of time points for each bootstrap replicate, which ensured that full exponential curves were evaluated (this would exclude a hypothetical bootstrap replicate that contains only sampling from a single time point).

For each analysis, an initial fit was performed to both the deuterated and unlabeled data and residuals were identified (Figure 5.3.A and Figure 5.4.A). While the bootstrap analysis is resistant to outliers, three points in the farnesyl synthase dataset had standardized residuals with absolute values > 3. Closer inspection revealed that one point was an outlier for both experiments and the others were outliers in just one of the experiments. The fit was repeated where the paired outlier was kept in the analysis while the individual outliers were considered statistically significant outliers and were removed (Figure 5.3.B). Initial analyses with the bootstrap indicated that influential data were present and should be removed, similar to an outlier in a regression analysis. The removal of influential data was only performed once (Figure 5.3.C and Figure 5.4.B). A number of bootstrap replicates were evaluated for each study, ranging from 100 – 250,000. However, 10,000 replicates were satisfactory and produced results that were identical to three significant digits of different numbers of replicates. Thus, all following results and discussion will refer to the 10,000 replicate results.

The $\mathrm{KIE}_{\mathrm{int}}$ values for both enzymes were determined to be significantly greater than 1 (Table 5.2), an indication that a kinetic isotope effect was observed. Several plots are presented as diagnostic checks on the bootstrap analysis to ensure that the bootstrap was both properly executed and the results obtained are statistically relevant. Plots of the

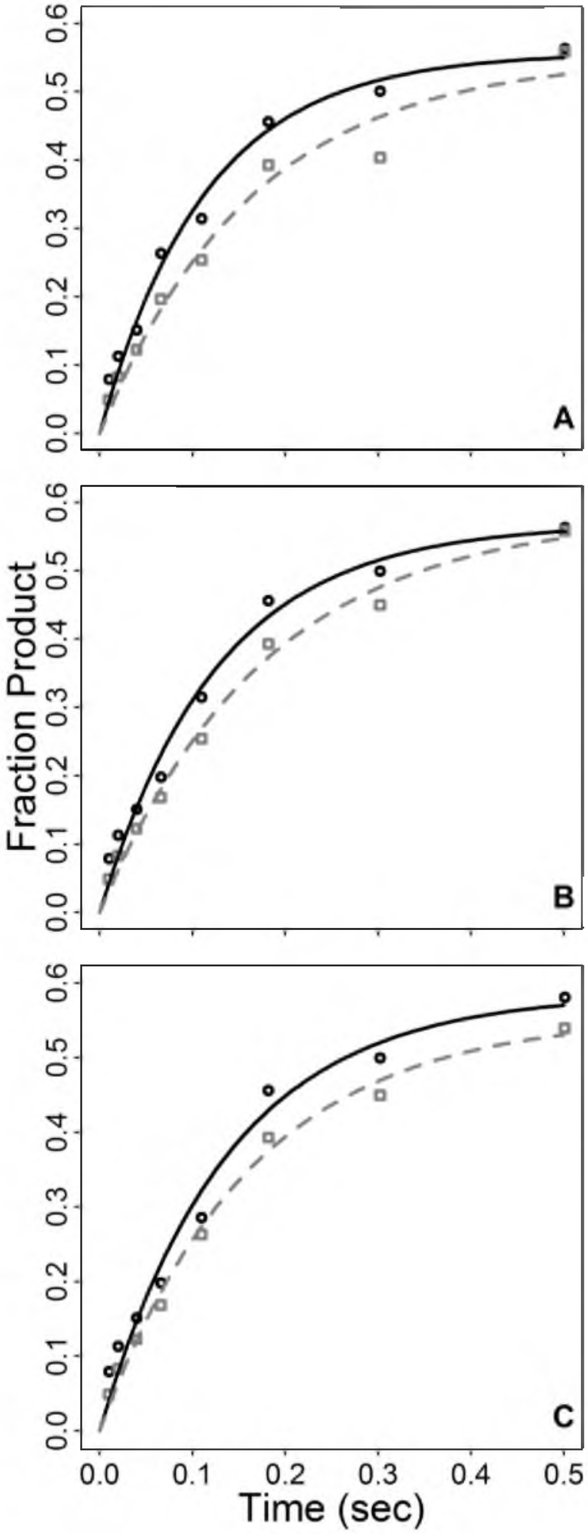

Figure 5.3. Product formation plots for FPPS. Dark solid lines and circles represent unlabeled GPP results. Gray, dashed lines and squares represent CD_3-GPP results. A, First plot of the data; B, Plot after removing two outliers; C, Final plot after removing influential data.

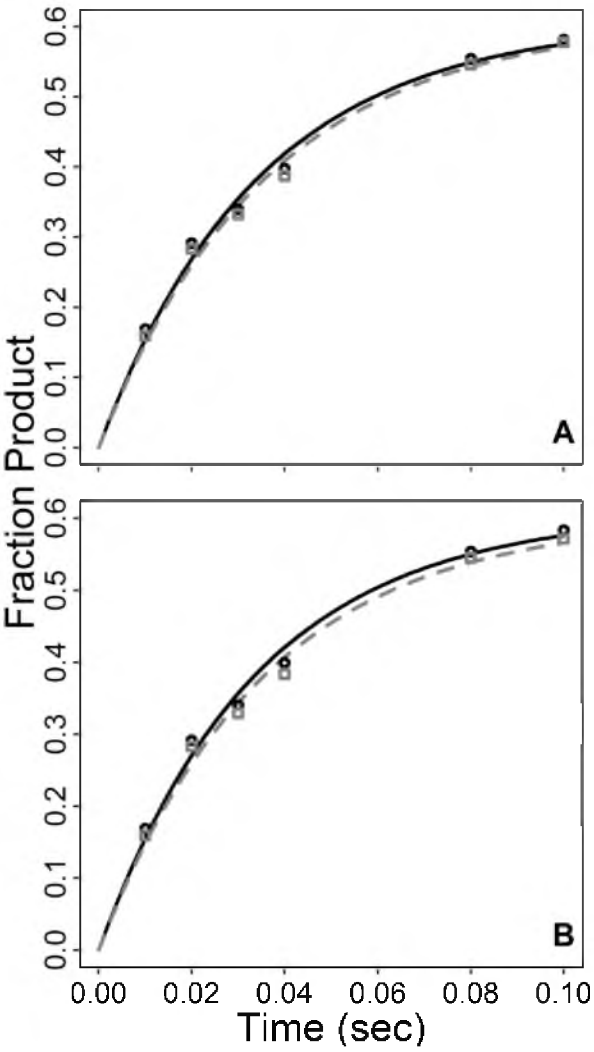

Figure 5.4. Product formation plots for PFTase of the average result at each time point and the best fit lines. Dark solid lines and circles represent unlabeled FPP results. Gray, dashed lines and squares represent CD_3-FPP results. A, First plot of the data; B, Plot after removing influential data.

jackknife values for the initial and final analysis for both enzymes are shown in Figure 5.5. These plots identify influential data in a bootstrap analysis. In Figure 5.5.A, the first analysis of the FPPase data revealed two points that were significantly influencing the distribution (37 and 55). Likewise, with the PFTase data, Figure 5.5.B shows three influential points (31, 43 and 60). After these points were removed and the bootstrap repeated, some more points were revealed as influential. However, the analysis was

Table 5.2. Summary of results comparing the bootstrap to a nonlinear analysis. Nonlinear indicates a nonlinear determination of the KIE_{int} based on all the data pooled together. Initial is the parameter value before any data were removed (for FPPase bootstrap, after outliers were removed). Final is the parameter value after outliers (for Nonlinear analysis) and influential data (for Bootstrap analysis) were removed. S.E. is standard error of the KIE_{int}. 95% BCa C.I. is the 95% bias-corrected accelerated confidence interval.

Enzyme	Analysis	Stage of Analysis	KIE_{int}	S.E.	95% BCa C.I. Low	95% BCa C.I. High
Farnesyl Synthase	Nonlinear	Initial	1.461			
		Final	1.371			
	Bootstrap	Initial	1.374	0.115	1.207	1.690
		Final	1.242	0.057	1.142	1.371
Farnesyl Transferase	Nonlinear	Initial	1.046			
		Final	1.053			
	Bootstrap	Initial	1.047	0.019	1.009	1.085
		Final	1.053	0.013	1.029	1.081

stopped after the second bootstrap. Histograms of all KIE_{int} values from the bootstrap replicates are shown in Figure 5.6. The initial data were not expected to be normally distributed because of the presence of influential data that will skew the distribution. Once the points described above were removed and the analysis repeated, and in support of properly produced results, the final plots of both enzymes studied appear normally distributed. Note that for the FPPase enzyme (Figure 5.6.A), the influential points in the first analysis skewed the results and caused a high KIE_{int} value, visible by the poor fit of the normal curve over the distribution. For the PFTase enzyme (Figure 5.6.B), the influential points caused a low KIE_{int} value. However the poor fit of the normal curve is not as visible.

The collection of curves produced in all 10,000 bootstrap replicates are in Figure 5.7 and Figure 5.8 for the FPPS data and Figure 5.9 and Figure 5.10 for the PFTase data. The impact of these plots is one's ability to see the trending behavior of the derivative

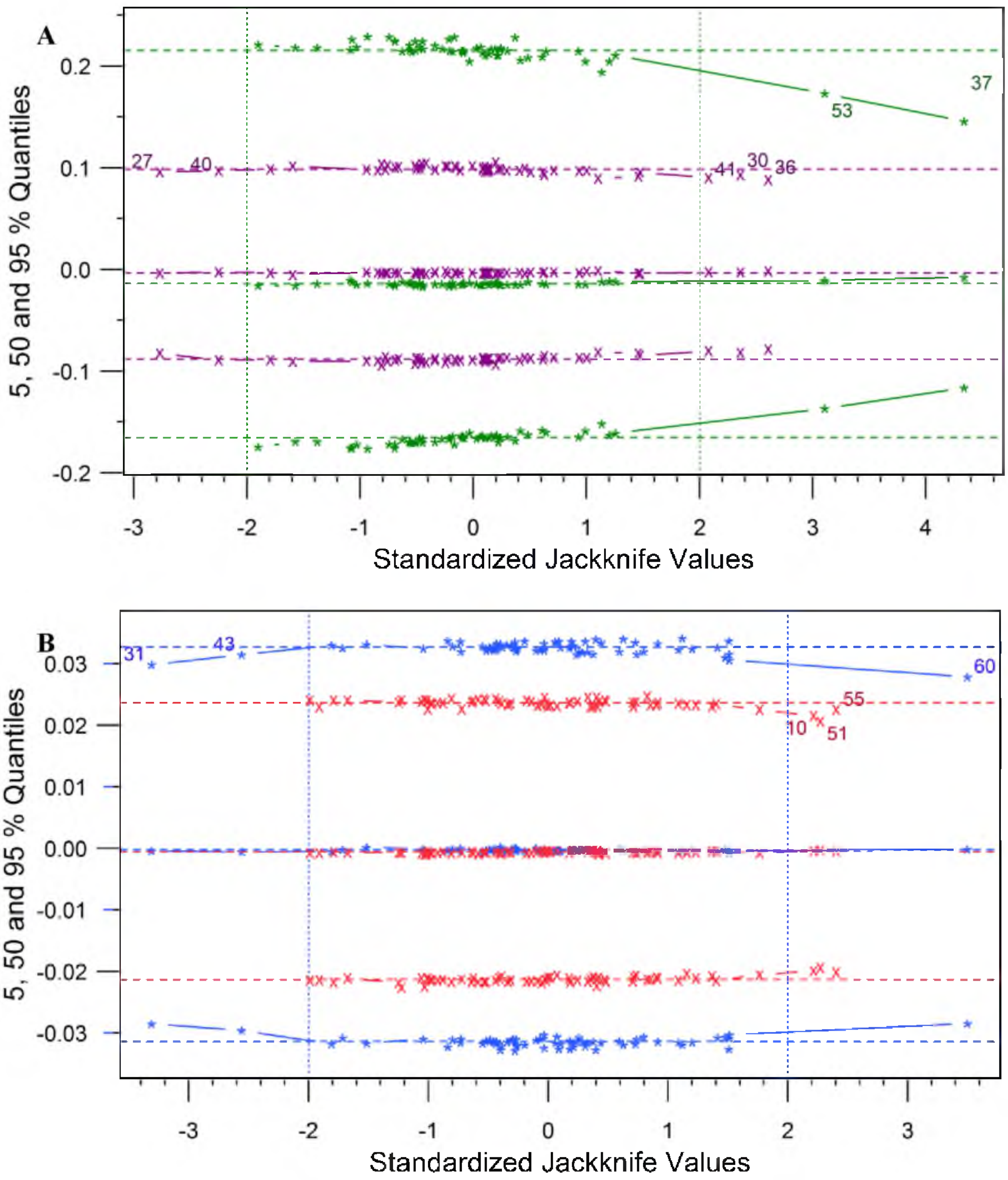

Figure 5.5. Jackknife-after-boot plots. A, FPPase. The first (after outliers were removed) and final bootstraps are indicated by * and x, respectively; B, PFTase. The first (after outliers were removed) and final bootstraps are indicated by * and x, respectively. Numbers indicate the number of the ordered data points.

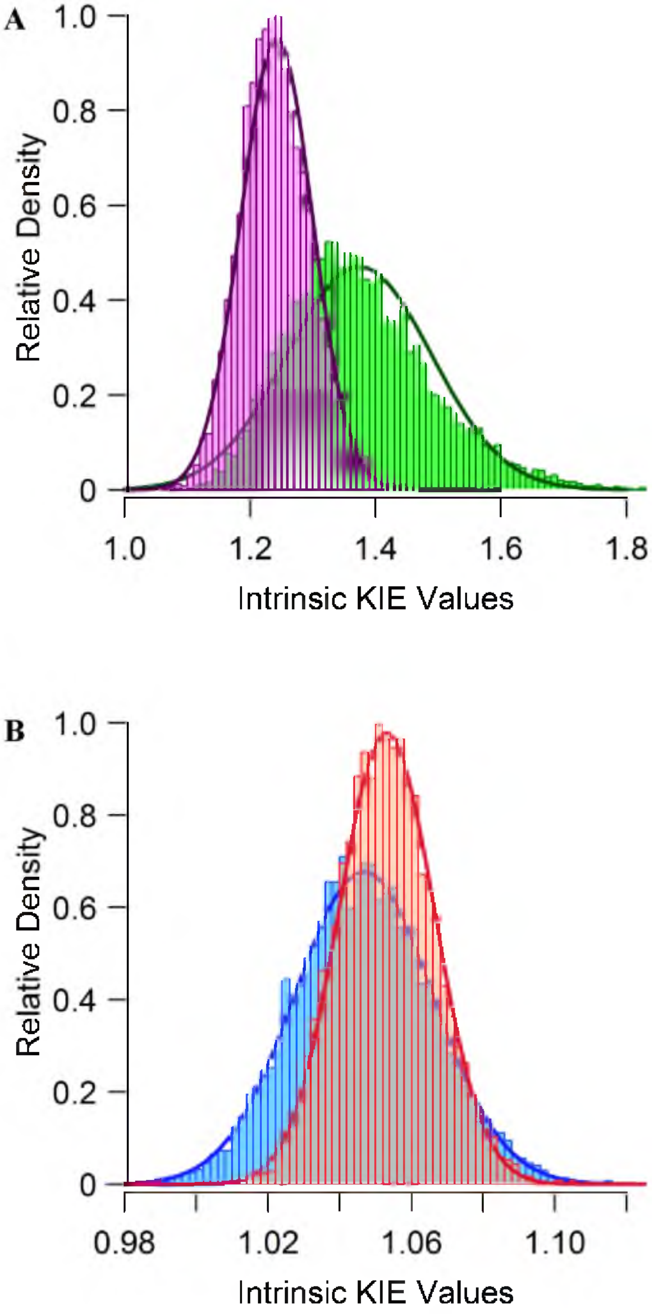

Figure 5.6. Histograms of bootstrap results. A, FPPase. The first bootstrap (after removing outliers) is in green. The second bootstrap (after removing influential data) is in magenta; B, PFTase. The first bootstrap is in blue. The second bootstrap (after removing influential data) is in red. Curves represent a normal curve with mean and standard deviation of the corresponding data.

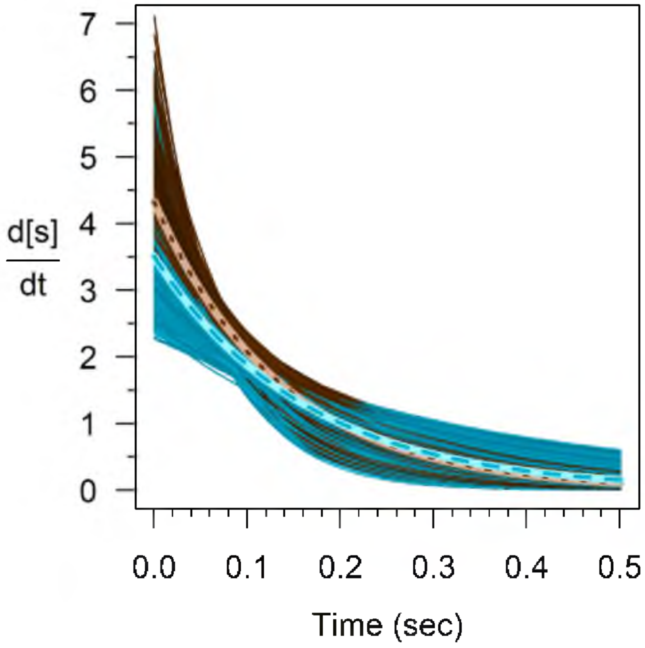

Figure 5.7. Signal derivative curves for the final analysis of FPPase. Unlabeled substrate curves are in brown, CD_3-GPP curves are blue. The bold dotted (unlabeled) and dashed (deuterated) curves represent the average of their respective curves.

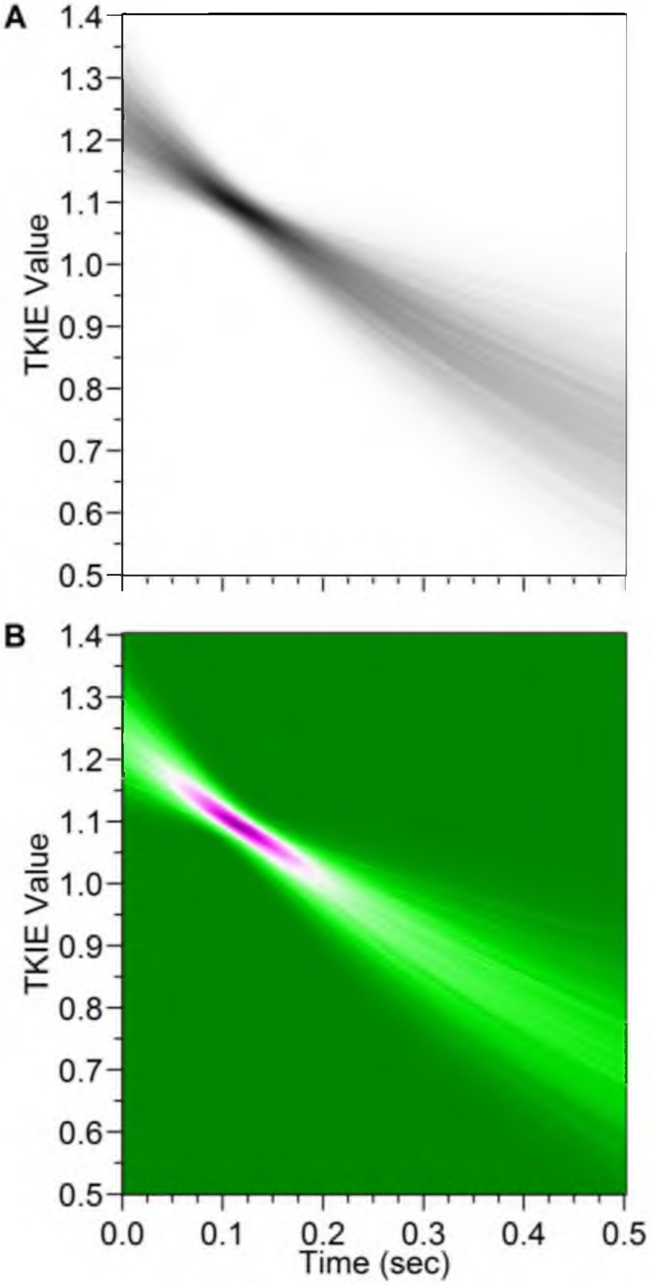

Figure 5.8. Superimposed TKIE curves for the final analysis of FPPase. A, Black represents the highest density and white represents the lowest; B, Dark purple represents the highest density and green represents the lowest. The individual curves represent one bootstrap replicate.

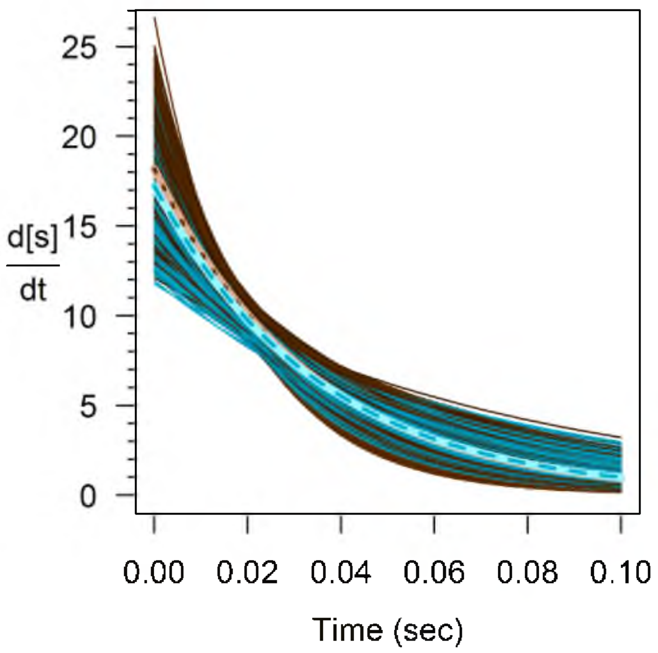

Figure 5.9. Signal derivative curves for the final analysis of PFTase. Unlabeled substrate curves are in brown, CD_3-FPP curves are blue. The bold dotted (unlabeled) and dashed (deuterated) curves represent the average of their respective curves.

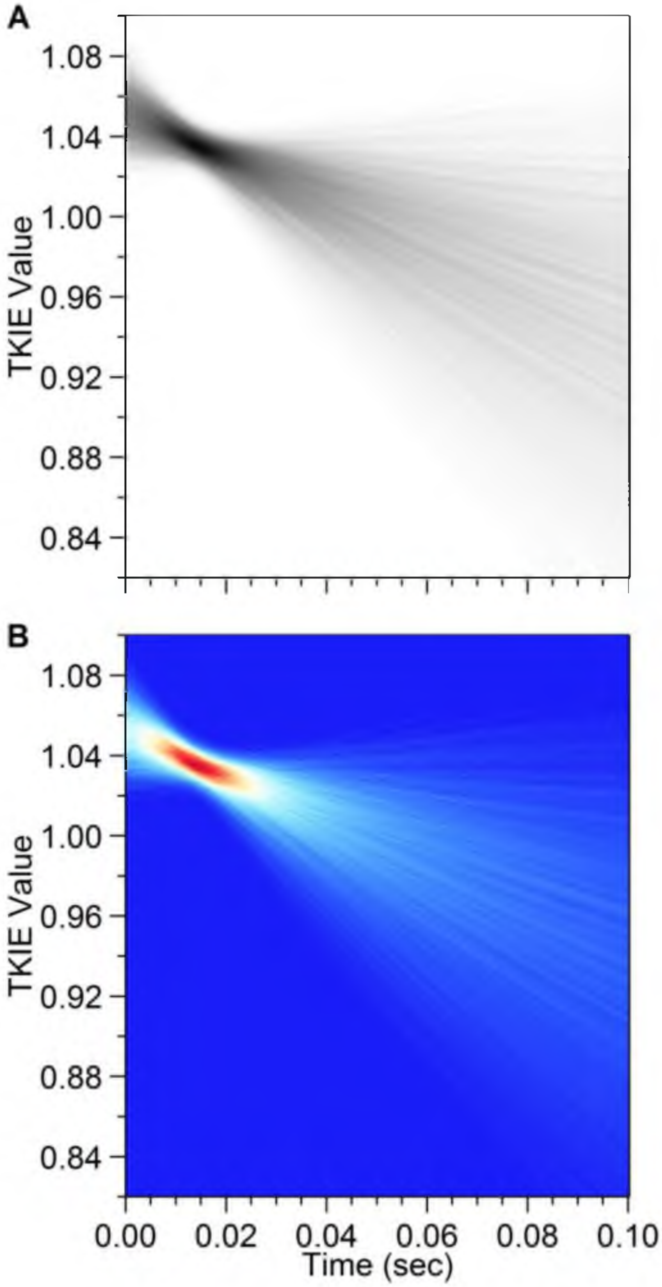

Figure 5.10. Superimposed TKIE curves for the final analysis of PFTase. A, Black represents the highest density and white represents the lowest; B, Dark red represents the highest density and blue represents the lowest. The individual curves represent one bootstrap replicate.

functions and the TKIE function. With the derivative functions of both enzymes, the unlabeled substrate curves are larger at lower time points as they go to zero, indicating an observed normal KIE. The functions then decrease until they intersect and switch positions so the deuterated substrate curves are larger than the unlabeled curves. This pattern in the relationships of deuterated and unlabeled substrates in the derivative curves is visible in the TKIE plots.

The TKIE plots show the density of the curves from the bootstrap analysis. Here the majority of TKIE values start out larger than 1.0, then pass through 1.0 (where the derivative functions intersect) and continue decreasing, while some appear to continuously increase (Figure 5.10). Notice that these curves are not uniformly distributed across time. In both datasets, the curves start out dispersed around t = 0, then condense into a collection of curves that appear darker and then spread out at higher time points.

Discussion

The bootstrap technique, first described in 1979,[185] now has a well-established and rigorously studied history. The bootstrap is frequently applied in designing phylogenetic trees, a result of a classic paper that resolved the problem of relating organisms with only a single DNA sequence sample from a species.[186] Other fields have also incorporated the bootstrap, such as psychology,[187] economics,[188] and ecology.[189] While there is literature precedence for the application of the bootstrap to problems of a chemical nature, the application is sparse. One reason for this limited application may be the vigorous, explicit solutions desired by the physical sciences. The bootstrap is a nonparametric technique, meaning that there is not necessarily an explicit solution to a parameter of interest. The unavailability of an explicit solution may be the result of a yet unsolved, complex or impossible analytical solution to a parameter. For example, with equation 5.10, each parameter has an associated error, which can be determined from a nonlinear fit. However, when each parameter is combined as in equation 5.10, the TKIE variability becomes convoluted. Visually, we can see the heterogeneous variability in Figure 5.8 and Figure 5.10.

The transient-state kinetic isotope effect approach has received limited acknowledgement in the literature, perhaps because of the difficulty in determination of the error associated with the TKIE parameter. In early papers that evaluated TKIE values, estimates of error were made with an assumption of only 2% error caused by pipetting.[179,190] Another paper added and subtracted standard error from the mean value of fitted parameters to determine maximum and minimum TKIE values.[191] To my knowledge, the exploration of error in transient-state kinetic isotope effect studies has not been further evaluated or estimated.

The bootstrap approach was applied to estimate the intrinsic KIE in a transient-state KIE experiment. Furthermore, the body of data collected in the bootstrap replicates was used to visualize the confidence intervals. With PFTase, all data had been collected before analysis started, but with FPPase, data were collected and immediately analyzed. Once enough data were collected to obtain a consistent KIE_{int} value, experimentation was ceased.

Based on unpublished results from our group, the KIE_{int} values obtained with the bootstrap technique are 100 % greater than predicted using computational techniques. For example, the computed KIE was 1.1 for the predicted reaction that occurs with the

FPPase enzyme (a resonance stabilized [9-D_3]-geranyl cation, see Figure 5.2). However, the bootstrap determined a value of 1.24 with a 95 % BCa C.I. of (1.14, 1.37). Knowledge of the error in this parameter helped to reexamine the experimental design. Future experiments will attempt a different approach than using radiolabeled compounds.

While the approach presented here focused on the analysis of transient-state KIE experiments, the methodology may be extended to steady-state KIE experiments. Steady-state KIE values are by their nature a complicated parameter to determine with numerous sources of error. Unfortunately, there is limited description of how to determine the error of in a KIE value. A suggestion, and perhaps the practice, is to conduct separate KIE experiments, calculate KIE for each, then average these values for the mean and standard deviation.[192] While this is a reasonable approach, there is a loss of information when the within experiment error is ignored.

An important note must be addressed about careful data fitting with the transient kinetic isotope effect equations. One powerful aspect of equation 5.8 is the inherent model independence, meaning that the model fit to the observed signal is irrelevant, as long as that model is the same for the numerator and denominator and a limit exists as $t \to 0$. For example, there are many models that can be used to describe a growth curve such as an exponential, biexponential, Gompertz, logit, Richards and so on. The caution concerns overfitting and appropriately fitting the observed data. The first data analysis with the FPPase data revealed a lag phase that fit well to the three-parameter Gompertz equation (Eq. 5.11). Following a similar analysis as above, a KIE_{int} of

$$y_i = a\exp\big(b\exp(ct_i)\big) + \varepsilon_i \qquad \textbf{5.11}$$

1.217 ± 0.063 was determined. These results concur with the results in Table 5.2 for FPPase. However, a lag phase indicates that chemistry is not the rate limiting step and instead the binding of enzyme and substrate are rate limiting. The single turnover kinetics of DNA helicase yield a lag phase, the magnitude of which is dependent on the length of double stranded DNA that is unwound.[193] Thus, the process of DNA unwinding has multiple steps, some of which are rate limiting. In another case, a lag phase was observed in single turnover kinetic studies of tryptophan synthase when both substrates of the bisubstrate reaction were simultaneously added to the enzyme.[194] However, with preincubation of the first substrate that binds with the enzyme before addition of the second substrate, the lag phase was eliminated. Similarly, our group determined that preincubation was necessary for the same reason, and thus no lag phase should be present. Upon further examination, a discovery was made that a blank correction was omitted during data analysis. Once the correction was applied, the results listed in Table 5.2 were obtained. If the blank corrected data were analyzed using the Gompertz equation, after outlier and influential data elimination (the same points were determined to be outliers and influential as that for the single exponential model), the result is a KIE_{int} = 1.248 ± 0.068. This result is nearly the same as that in Table 5.2, but the uncertainly is higher for the three-parameter model, an indication that the model is overfit. Practically, the Gompertz model was not the correct model for the chemistry taking place and thus the single exponential model was used.

APPENDIX A

SPECTRAL DATA OF FLAVIN ANALOGUES

	Potential	λ_{max} (nm)*		Fluorescence (nm)		
Synthetic Analogue	**(mV)**	**Oxidized**	**Reduced**	λ_{ex}	λ_{em}	**F**†
5-deaza-5-thia-lumiflavin[195]	+380	380	284			
7,8-a,a,a-hexa-fluororiboflavin[196]	+20					
8-phenylsulfonyl-riboflavin[197]	-30	452 (10.0) 338 (10.1)	379 (9.3)	455	531	0.43
8-methylthiosulfonyl-8-norFMN[198]	-50					
8-methylsulfonyl-riboflavin[197]	-50	457 (10.8) 333 (10.2) 271 (38.9)	362 (10.5) 310 (15.3) 265 (39.8)			
8-cyano-8-norriboflavin[199]	FAD: -50	456, 338	Anionic (pH 7): 312, 372 Neutral (acidic): 316, 362	338 and 456	530	
4-thio-riboflavin[104] Neutral	FAD: -55	496, ~370	333 (8.6) 485 (6.4)	Non-fluorescent in either form		
Anionic		503, 370	328 (10.2) 425 (5.7)			
8-formyl-8-norriboflavin[196]	-90					
8-sulfonyl-riboflavin[197]	-122	457 (10.8) 333 (10.2) 271 (38.9)	362 (10.5) 310 (15.3) 265 (39.8)	450	531	0.70
7,8-dichloro-7,8-norFAD[196]	-126					
7-chloro, 8-desmethylFAD[200]	-128					
7-chlororiboflavin[201]	-128	447 (9.8) 334 (7.3)				

* Extinction coefficient (mM^{-1} cm^{-1}) in parenthesis

† Fluorescence emission relative to riboflavin, unless noted.

Synthetic Analogue	Potential (mV)	λ_{max} (nm)[*]		Fluorescence (nm)		F[†]
9-azariboflavin[201]	-135	437 (21.2) 313 (6.5)				
8-chloro, 7-desmethylFAD[200]	-144					
8-chlororiboflavin[201]	-144	432 (12.1) 356 (8.6)				
8-chloro-8-norFAD[200]	-152					
8-methylthiosulfinyl-8-norFMN[198]	-161					
8-carboxy-8-norriboflavin[196]	-165					
8-(phenylmercapto)-riboflavin[197]	-166	474 (26.0) 456 (24.4)	354 (5.3) 300 (10.0)	475	528	0.0123
8-fluoro-8-norFAD[198]	-167					
8-isopropyl riboflavin[202]	-168	448 (12.5)				
8a-hydroxy riboflavin[196]	-170					
8-H-8-norFMN[198]	-180					
8-(*N*-acetylcysteinyl)-riboflavin[197]	-180	475 (28.0) 456 (25.7)	354 (7.9) 300sh (14.5)	470	525	0.11
6-methyl-8-norFMN[198]	-200					
7,8-didemethyl riboflavin[202]	-203	436 (12.5)				
8-(mercapto propionyl)-riboflavin[197]	-203	477 (25.3) 458 (22.3) 251 (49.3)	355 (6.0) 300sh (11.4) 257 (45.2)	478	525	0.032
8-thiomethyl-8-norFAD[198]	-204					
8-(mercaptoacetyl)-riboflavin[197]	-208			478	526	0.05

[*] Extinction coefficient (mM^{-1} cm^{-1}) in parenthesis

[†] Fluorescence emission relative to riboflavin, unless noted.

Synthetic Analogue	Potential (mV)	λ_{max} (nm)*		Fluorescence (nm)		F†
8-thiomethyl-riboflavin[197]	-208	474 (28.5) 460 (26.0)	353 (5.8) 292 (11.4)	478	527	0.040
6-methylFAD[200]	-219					
6-methylriboflavin[201]	-219	447 (11.5) 396 (19.2)				
RoseoFMN (8-dimethyl aminoFMN)[201]	-222	505 (32.8) 314 (6.8)				
3-deaza-3-carbariboflavin[201]	-240	421 (20.0)				
8-ethoxy-8-norFMN[198]	-246					
6-hydroxyFAD[196]	-255					
8-methoxy-8-norFMN[198]	-260					
1-deaza-1-carbariboflavin[201]	-280	535 (6.8) 365 (4.0)				
8-mercapto-riboflavin[197]	-290	523 (30.0) 310 (9.8) 277 (48.8)	351 (5.8) 282sh (21.5)	Non-fluorescent		
6-aminoFAD[196]	-297					
8-amino-8-norFMN[198]	-310					
8-hydroxy-FAD[203] pH 7:	-340[200]	478 (36.7) 302 (9.9) 265sh (39.9) 252.5 (61.2)		440	500	1.3‡
pH 3:		445 (27) 280sh (19.4) 261 (44.6) 238 (42.2)		475	535	1.3‡
1,5-deaza-1,5-carbariboflavin[201]	-370	476 (9.5) 344 (4.2)				

* Extinction coefficient (mM^{-1} cm^{-1}) in parenthesis

† Fluorescence emission relative to riboflavin, unless noted.

‡ Fluorescence emission relative to lumiflavin 3-acetate.

APPENDIX B

MASS SPECTRA AND CHROMATOGRAMS OF ISOPRENE-FMN ADDUCT

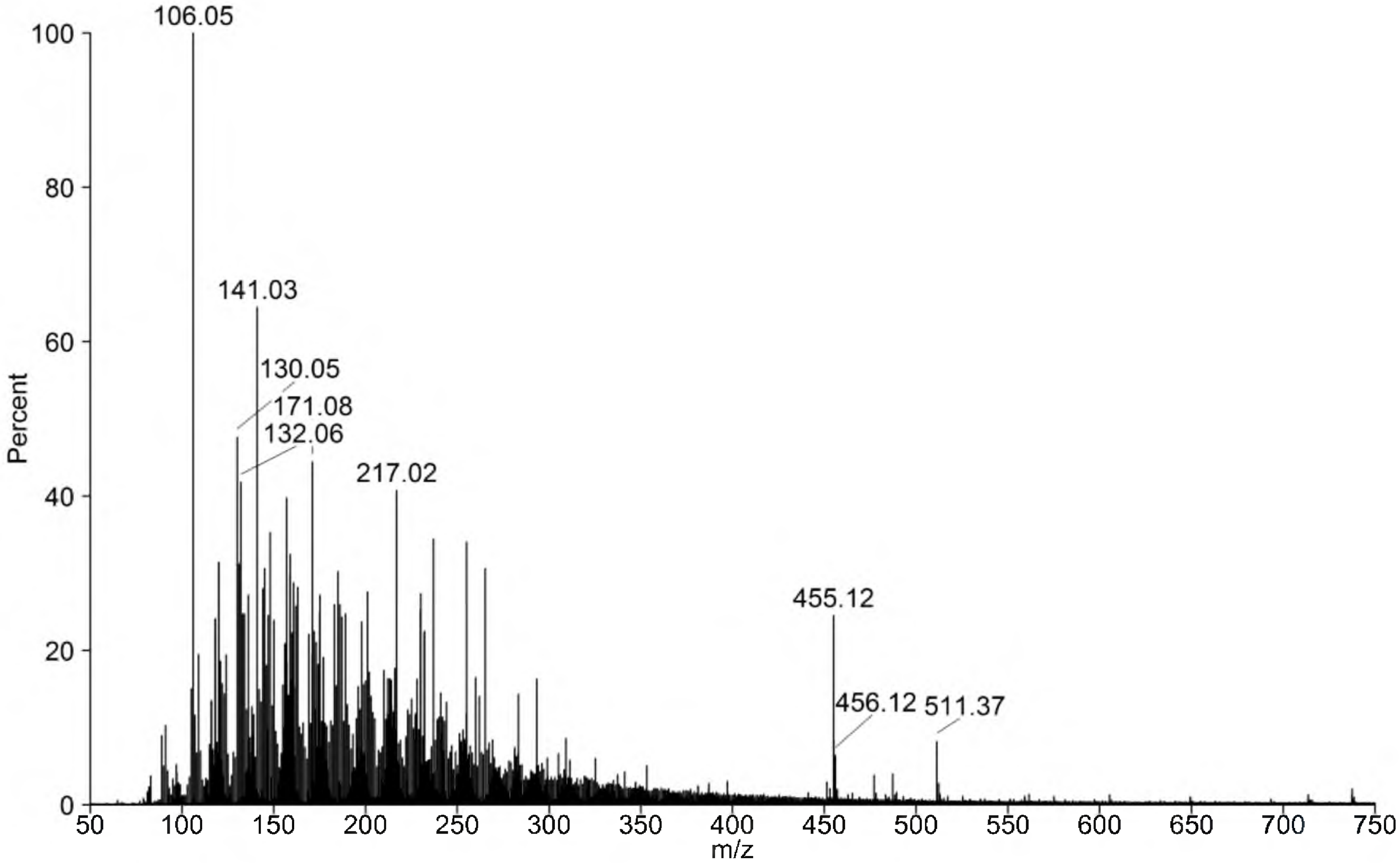

MS 1. Negative ion TOF ESI Mass spectrum of ZrO_2 purified FMN from IDI-2 after a 21 d incubation without substrate.

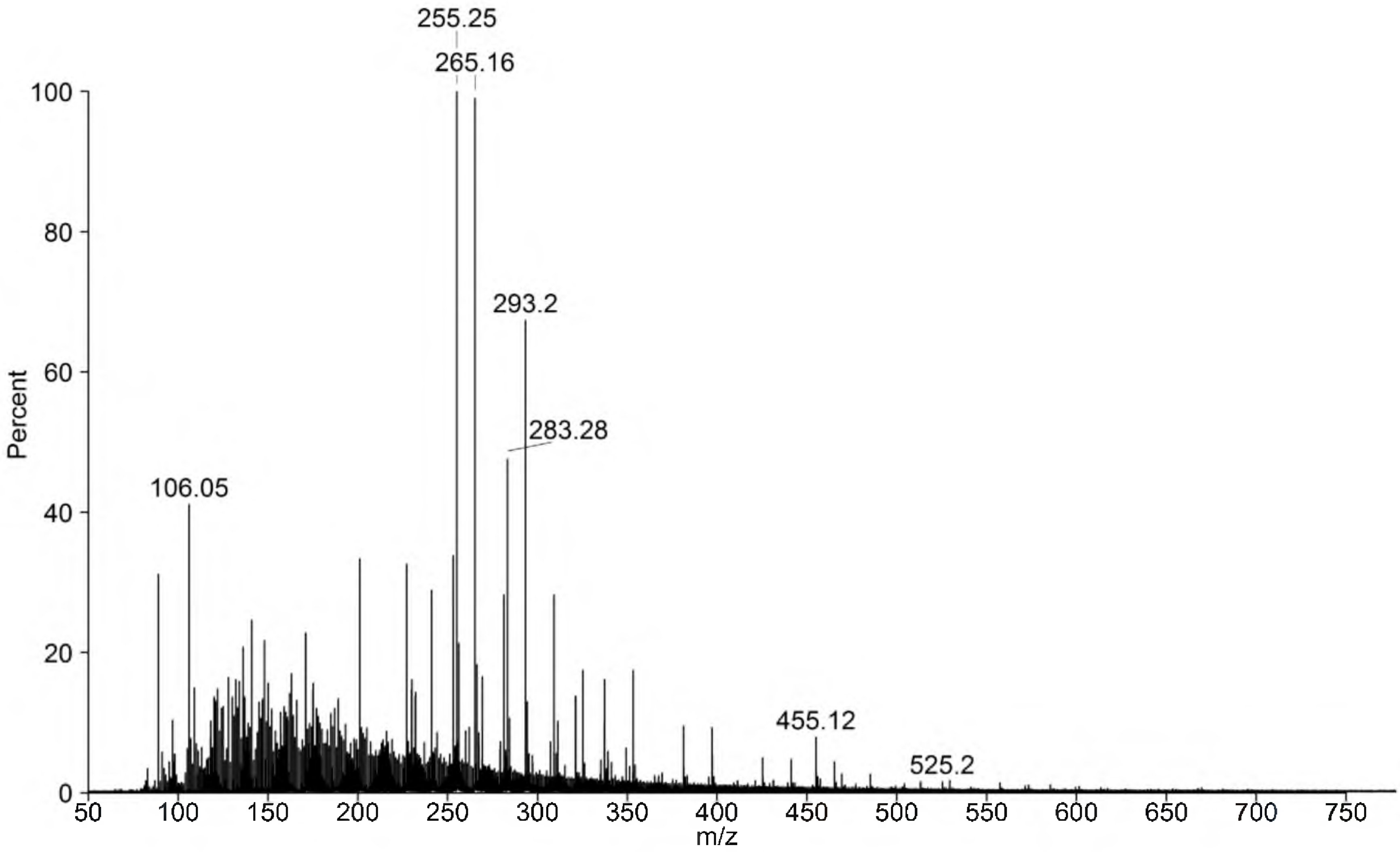

MS 2. Negative ion TOF ESI Mass spectrum of graphite purified FMN from IDI-2 after a 21 d incubation without substrate.

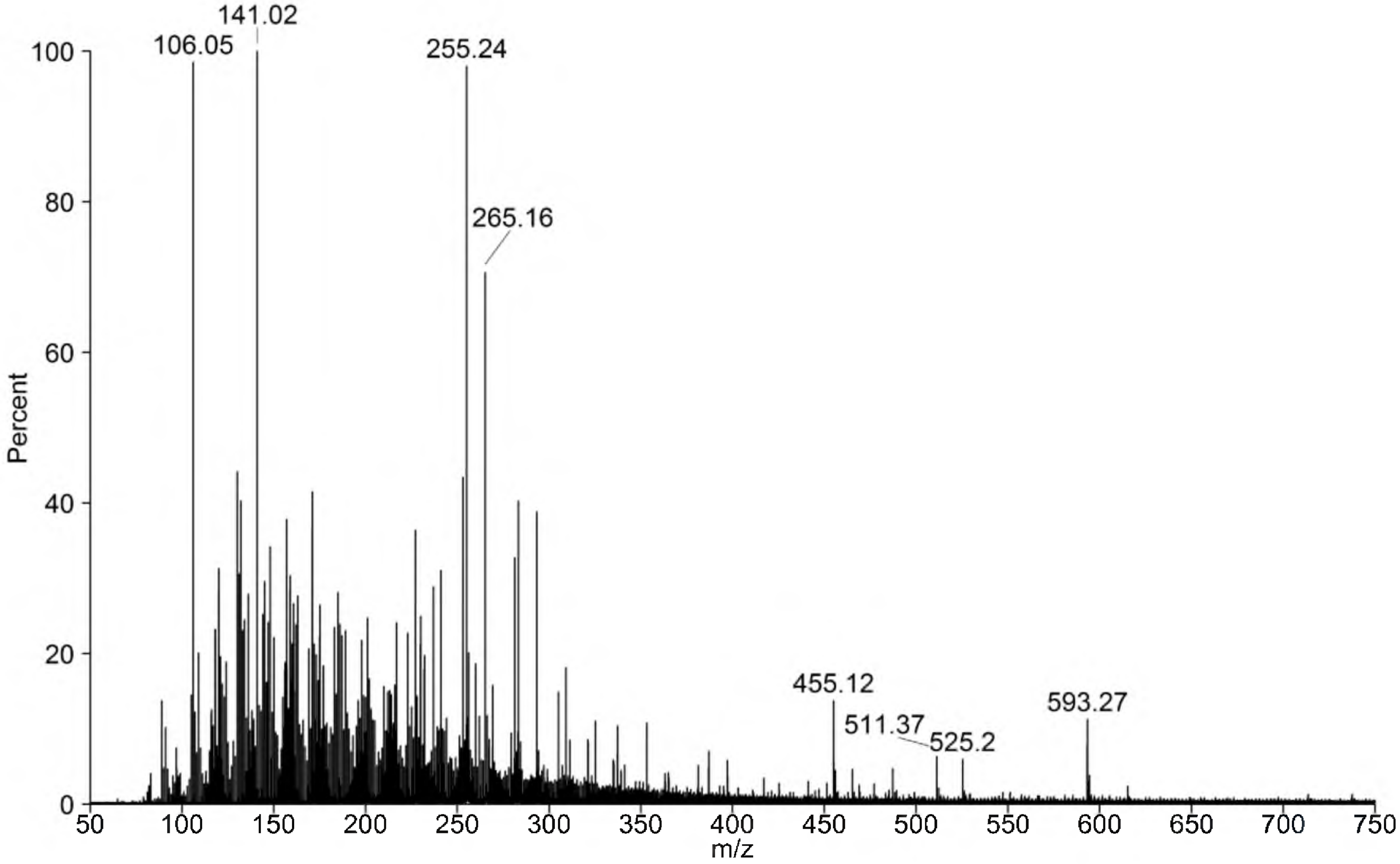

MS 3. Negative ion TOF ESI Mass spectrum of ZrO_2 purified FMN from IDI-2 after a 21 d incubation with IPP.

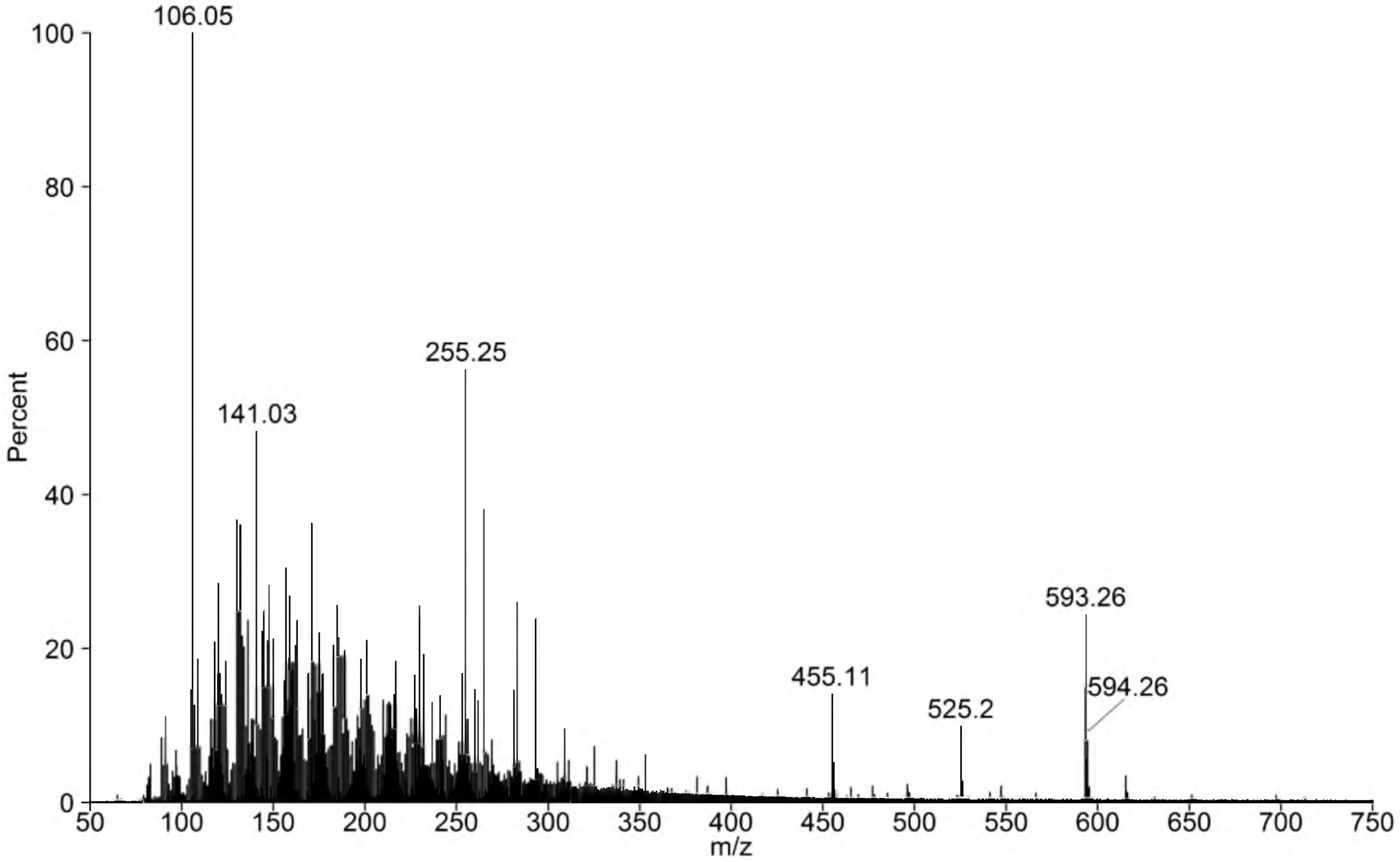

MS 4. Negative ion TOF ESI Mass spectrum of graphite purified FMN from IDI-2 after a 21 d incubation with IPP.

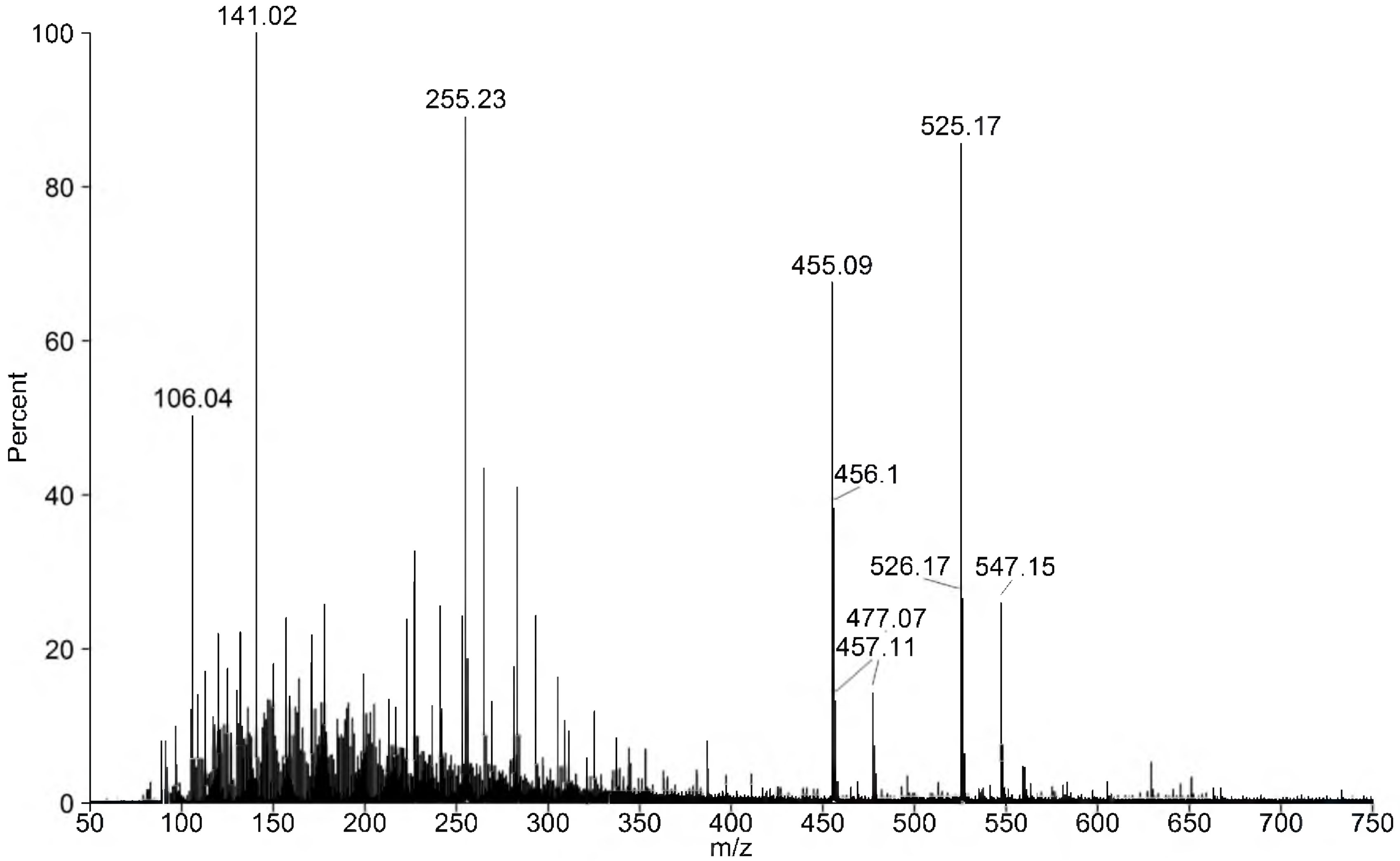

MS 5. Negative ion TOF ESI Mass spectrum of FMN isolated from IDI-2 after a 24 h incubation with IPP.

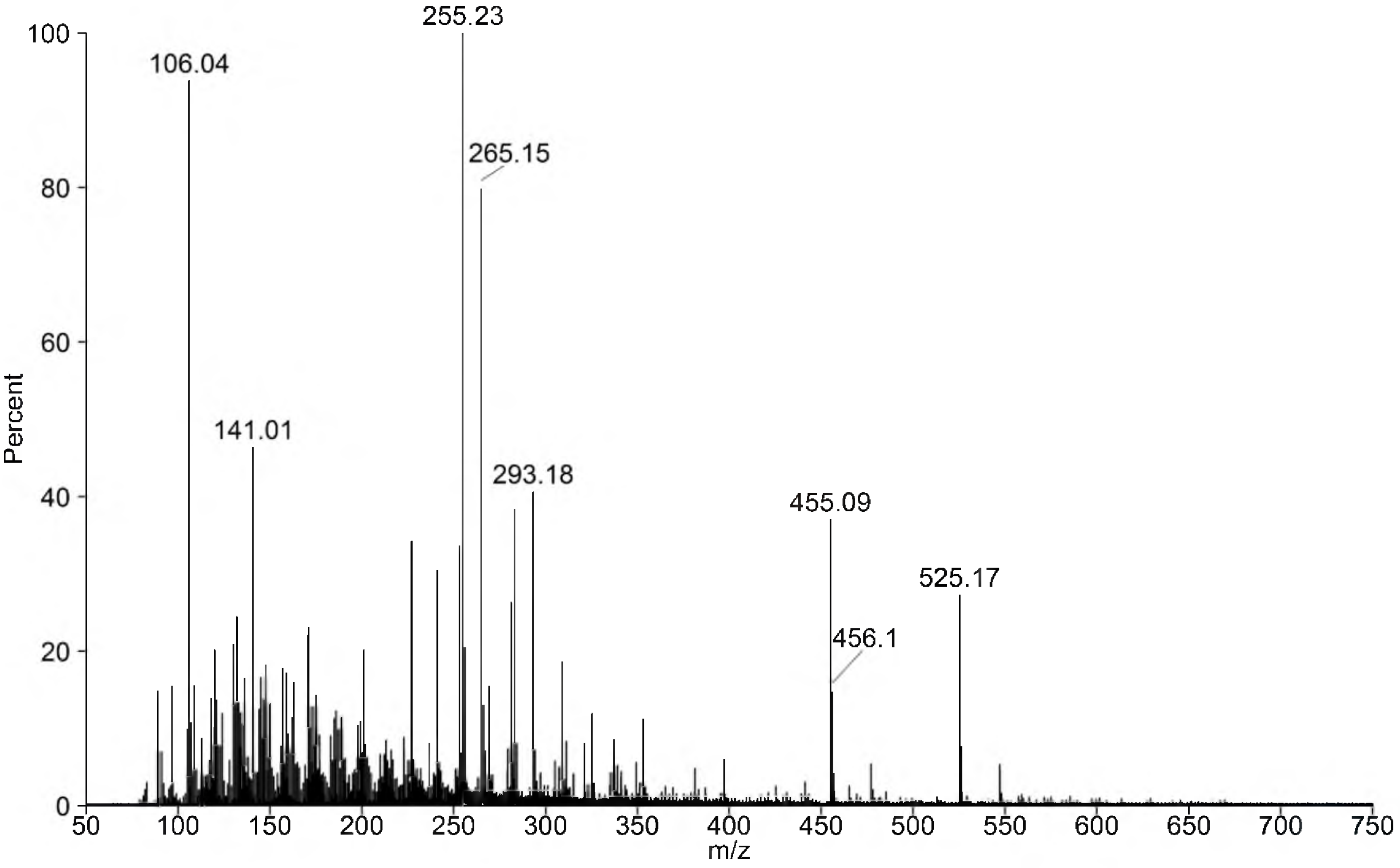

MS 6. Negative ion TOF ESI Mass spectrum of FMN isolated from IDI-2 after a 24 h incubation with DMAPP.

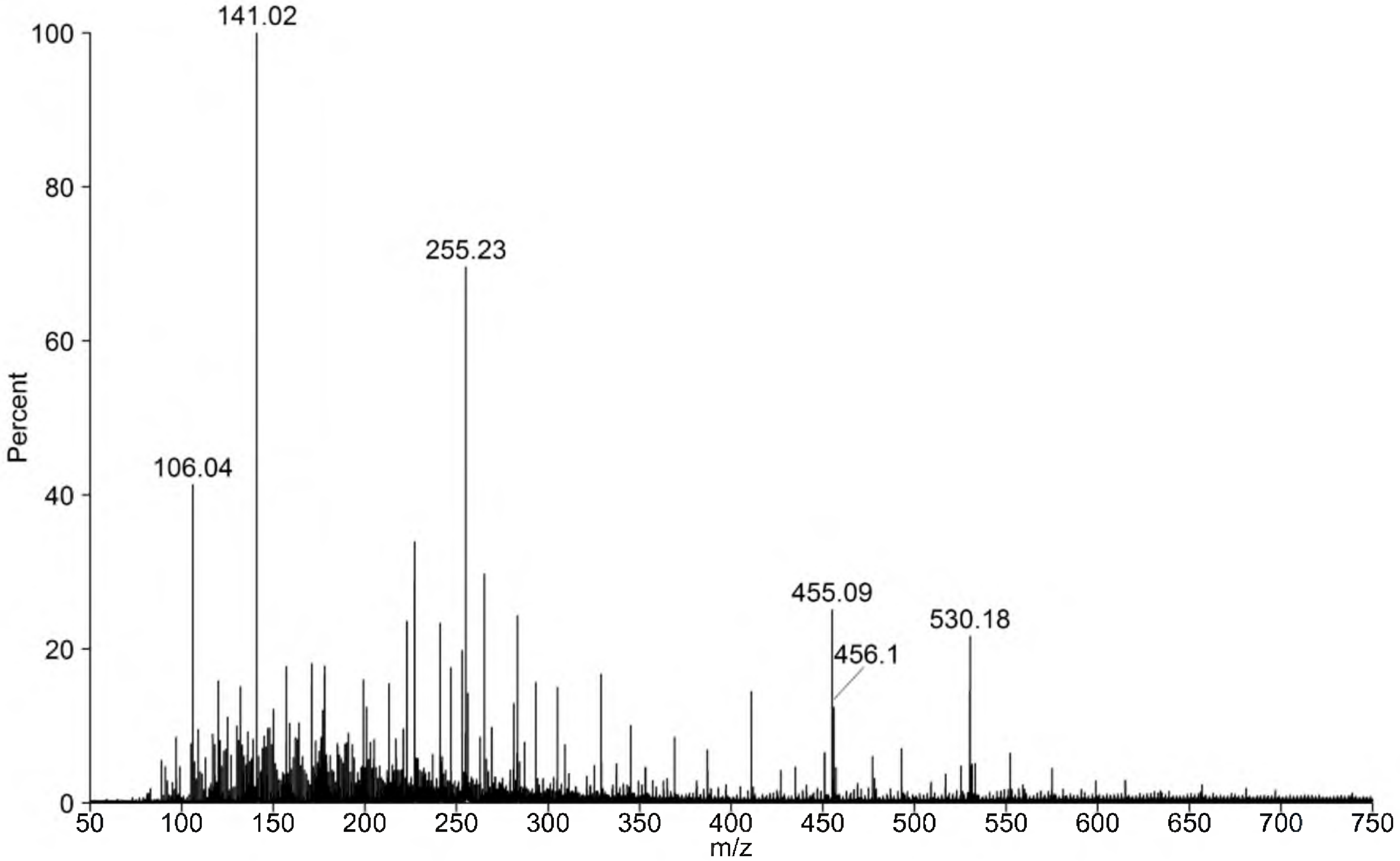

MS 7. Negative ion TOF ESI Mass spectrum of FMN isolated from IDI-2 after a 24 h incubation with $^{13}C_5$-IPP.

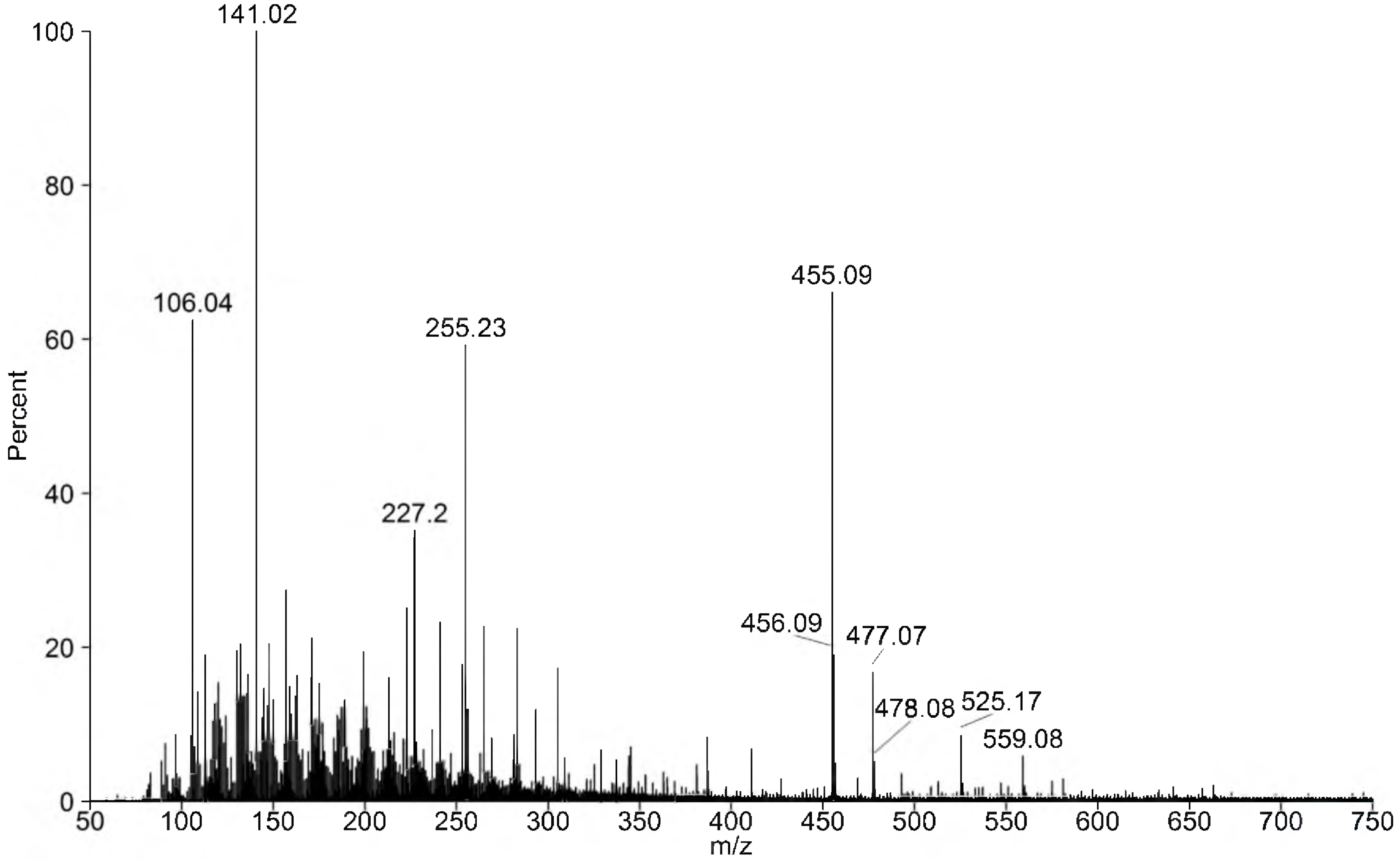

MS 8. Negative ion TOF ESI Mass spectrum of FMN isolated from IDI-2 after a 24 h incubation without substrate.

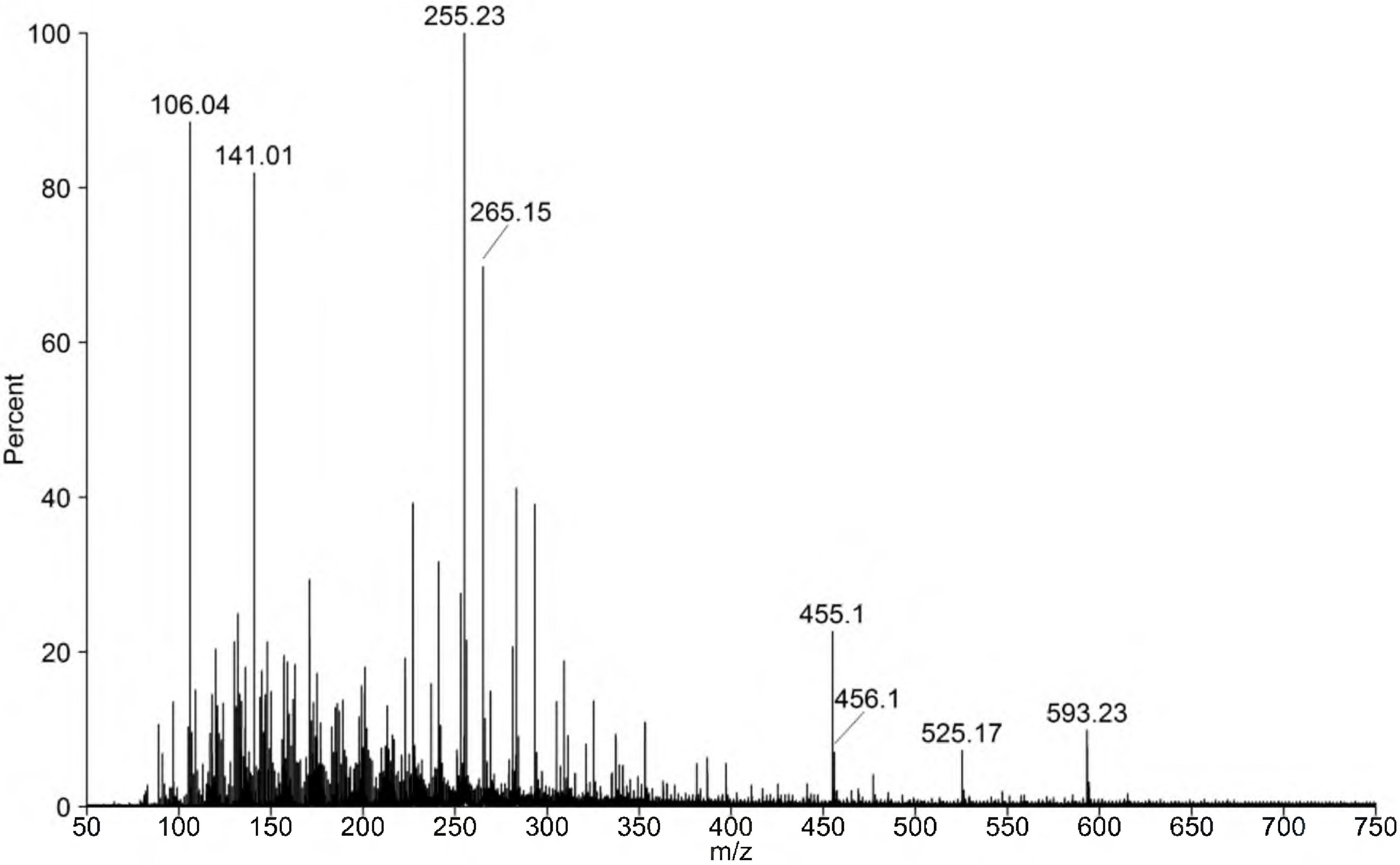

MS 9. Negative ion TOF ESI Mass spectrum of FMN isolated from IDI-2 after a 27 d incubation with IPP.

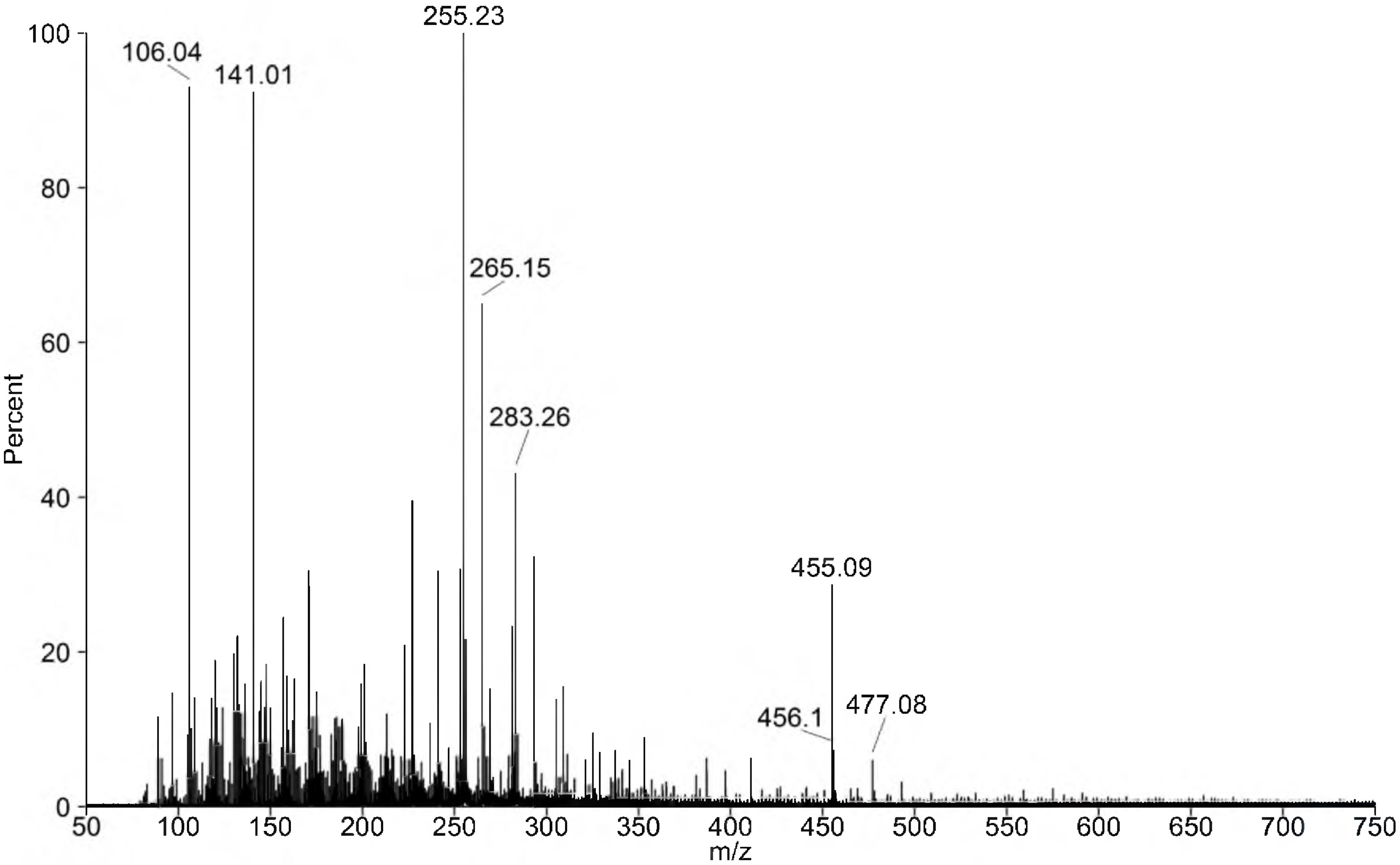

MS 10. Negative ion TOF ESI Mass spectrum of FMN isolated from IDI-2 after a 27 d incubation with GPP.

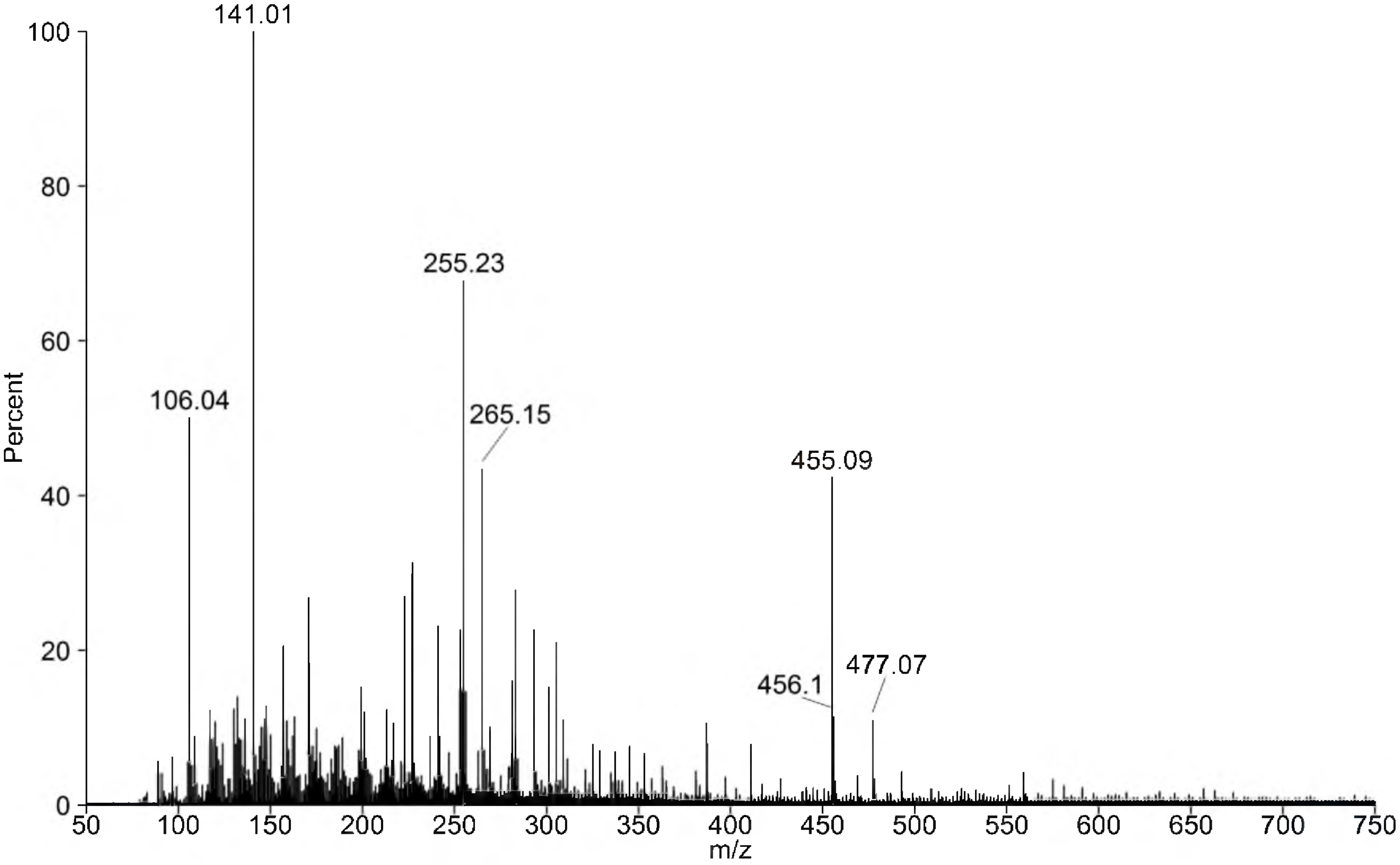

MS 11. Negative ion TOF ESI Mass spectrum of FMN isolated from IDI-2 after a 27 d incubation with FPP.

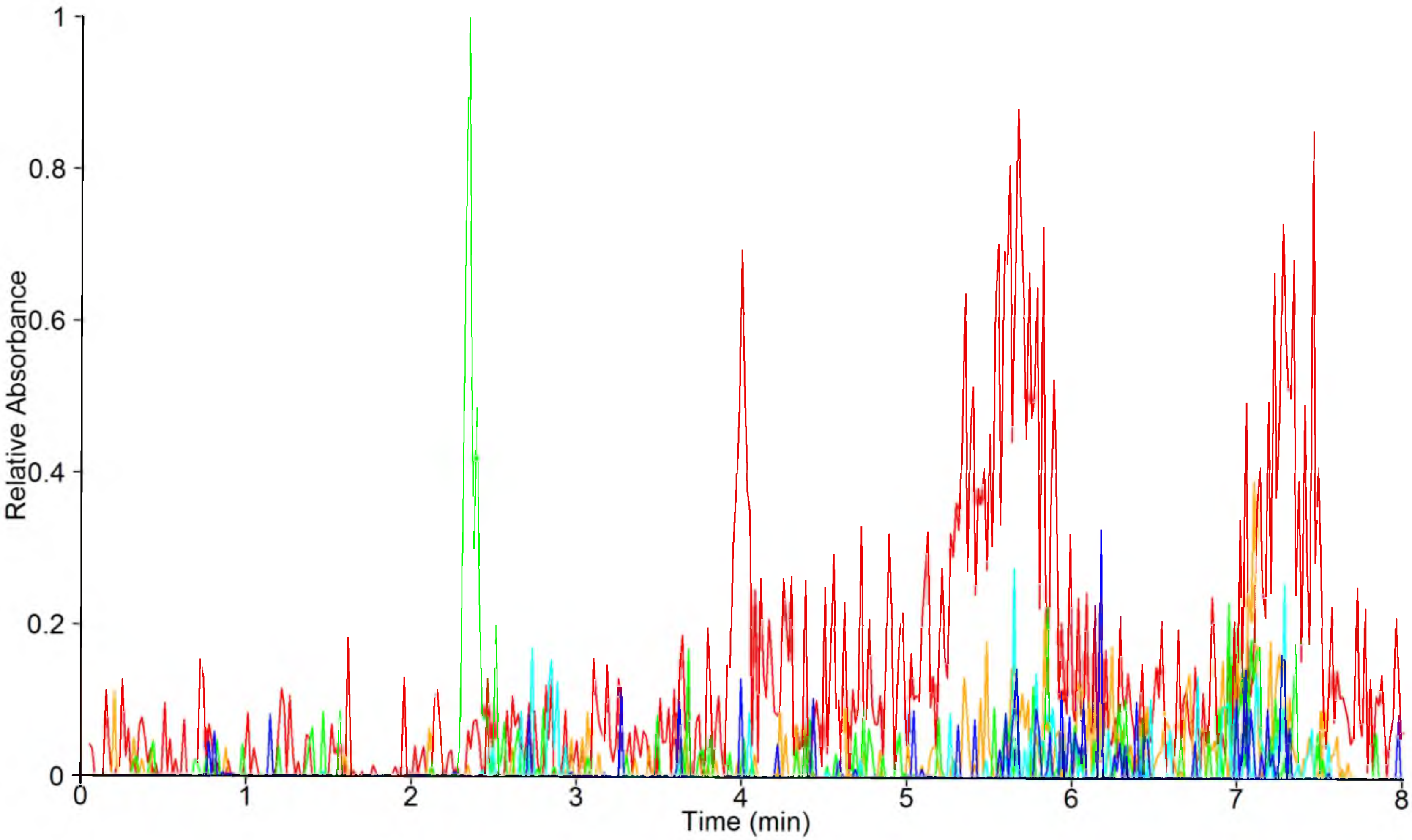

MS 12. UPLC-MS chromatograms of a 24 h incubation of *Tt*-IDI-2 without substrate of masses 255.2 (red), 375.2 (orange), 455.1 (green), 525.2 (cyan), 593.2 (blue).

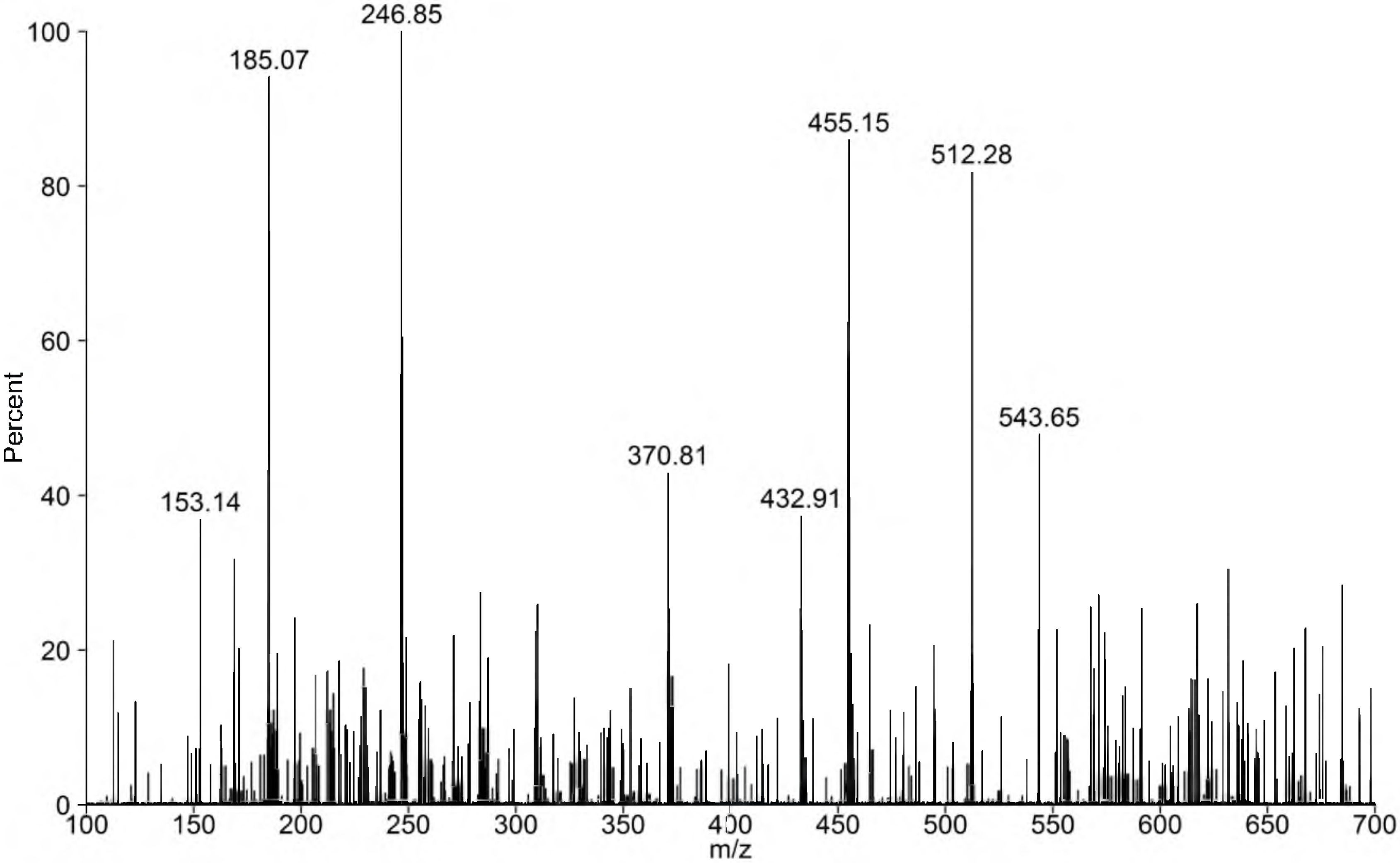

MS 13. UPLC-MS trace at 2.4 min of a 24 h incubation of *Tt*-IDI-2 without substrate.

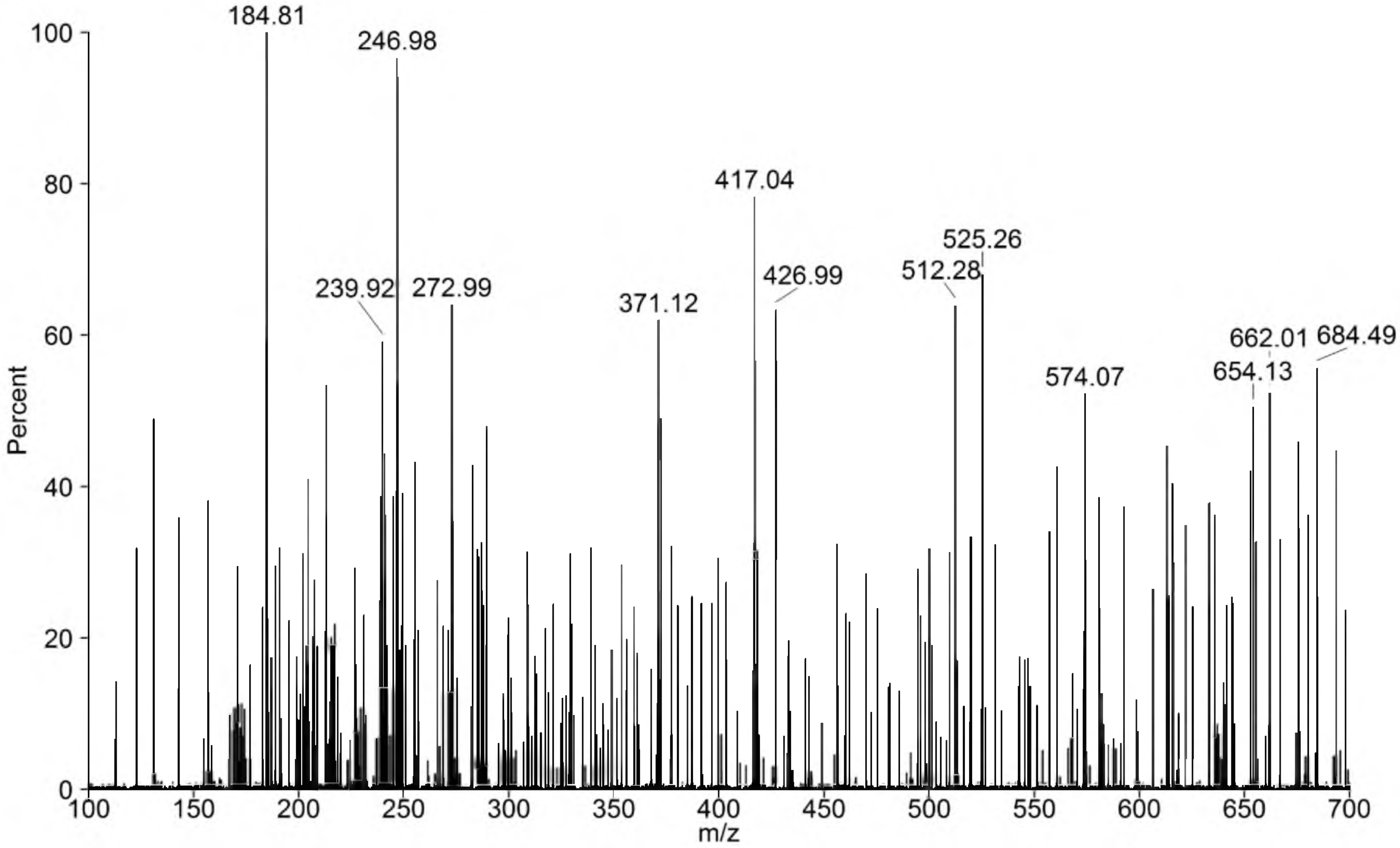

MS 14. UPLC-MS trace at 2.9 min of a 24 h incubation of *Tt*-IDI-2 without substrate.

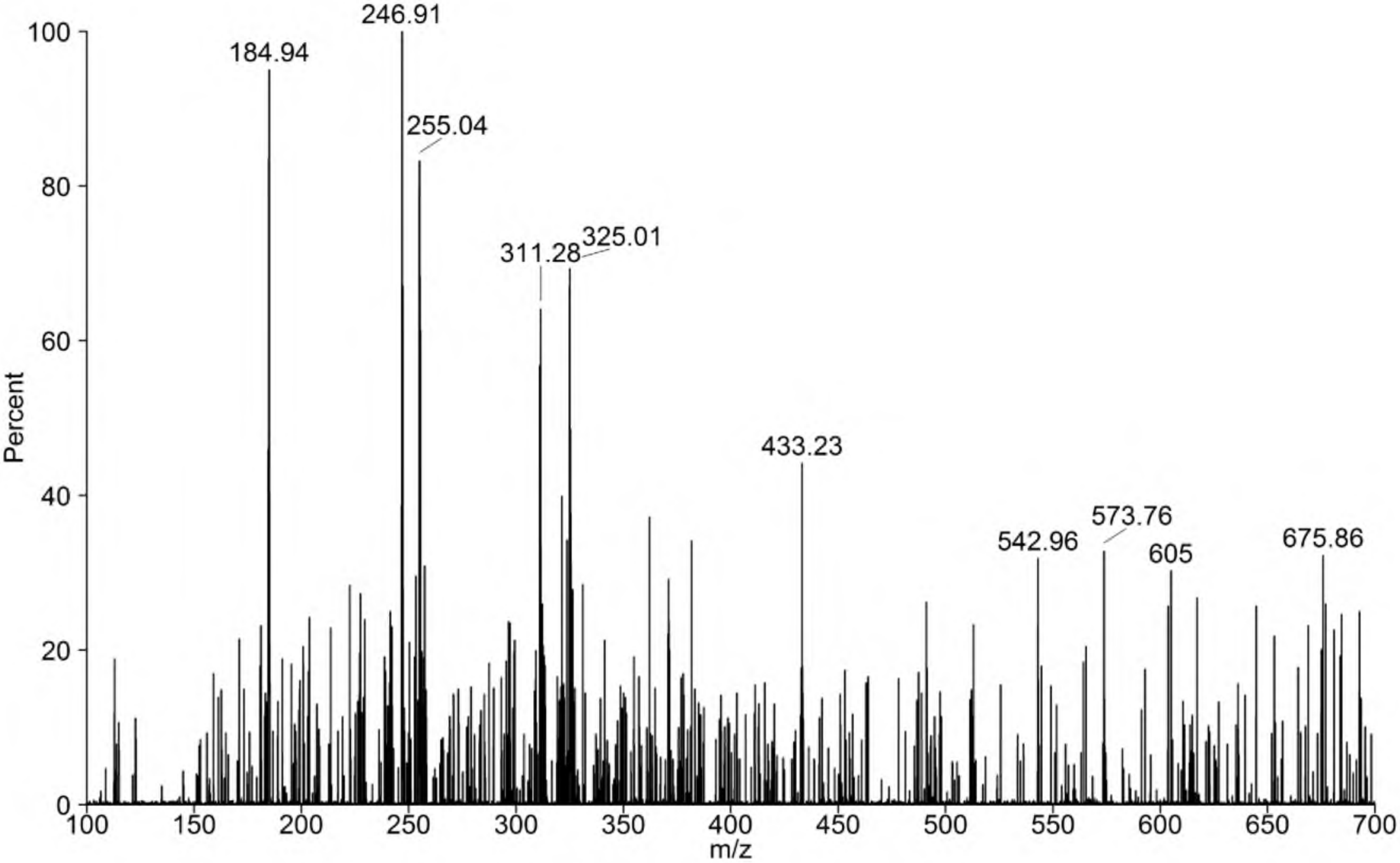

MS 15. UPLC-MS trace at 4.0 min of a 24 h incubation of *Tt*-IDI-2 without substrate.

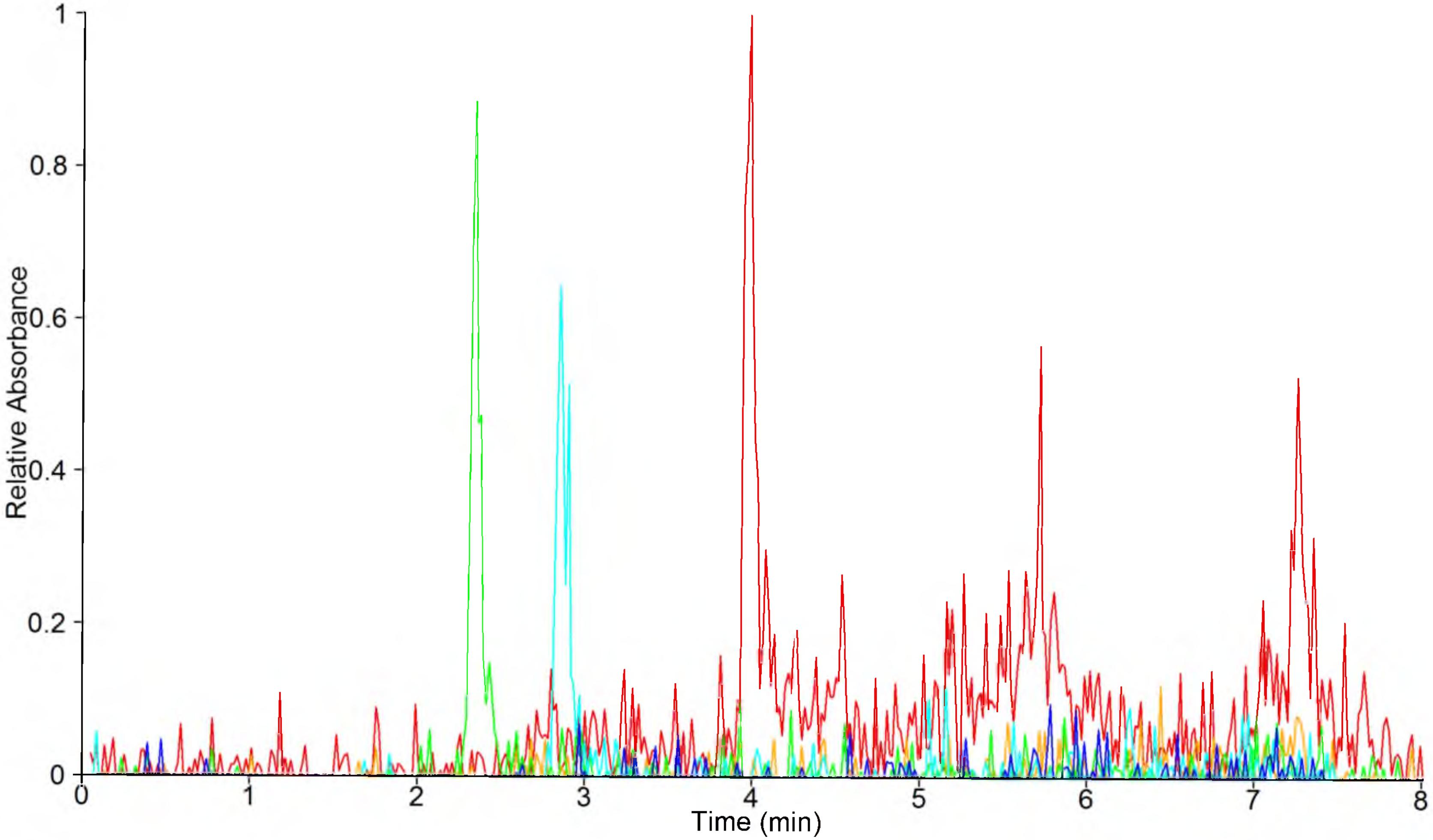

MS 16. UPLC-MS chromatograms of a 24 h incubation of *Tt*-IDI-2 with IPP of masses 255.2 (red), 375.2 (orange), 455.1 (green), 525.2 (cyan), 593.2 (blue).

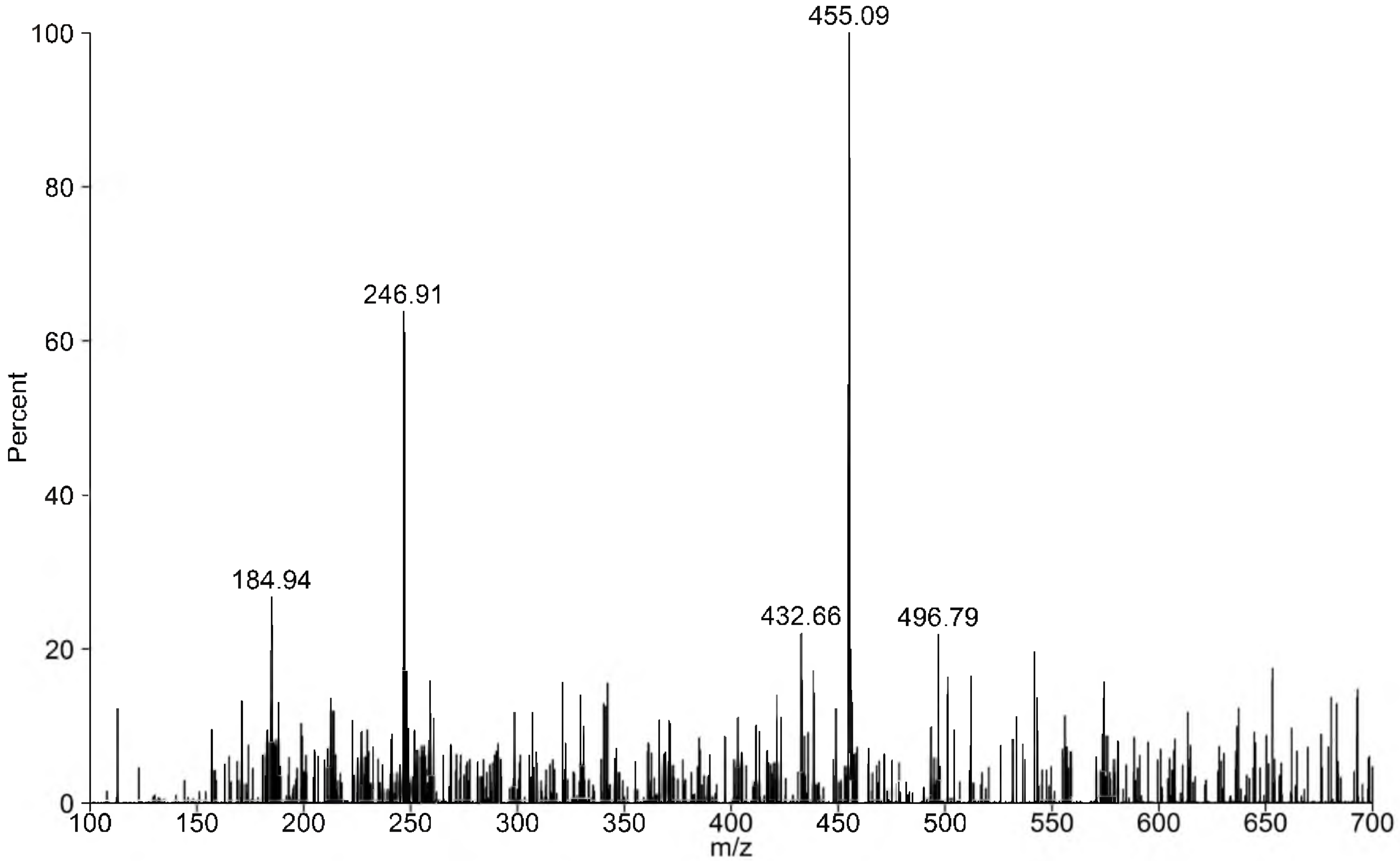

MS 17. UPLC-MS trace at 2.4 min of a 24 h incubation of *Tt*-IDI-2 with IPP.

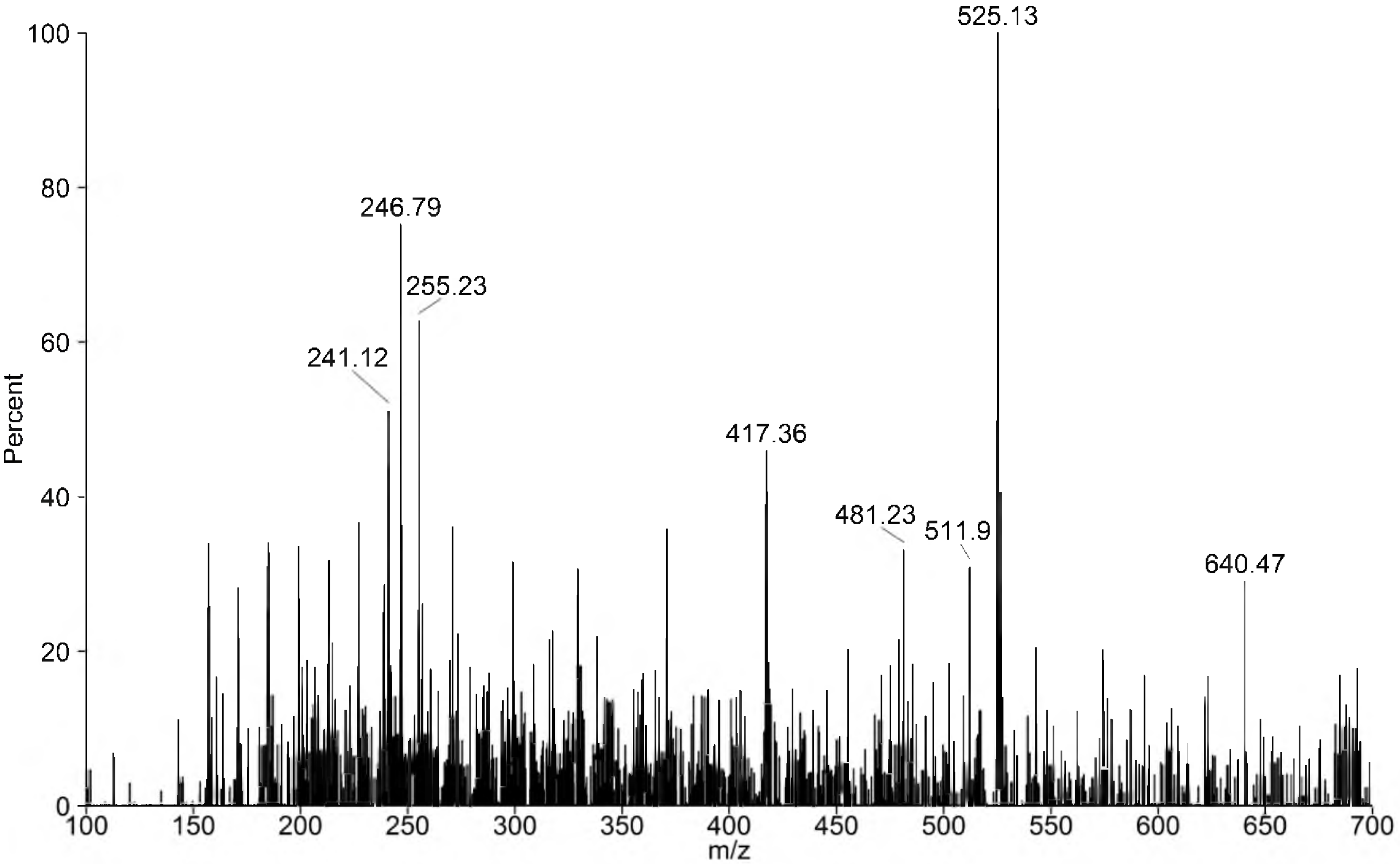

MS 18. UPLC-MS trace at 2.8 min of a 24 h incubation of *Tt*-IDI-2 with IPP.

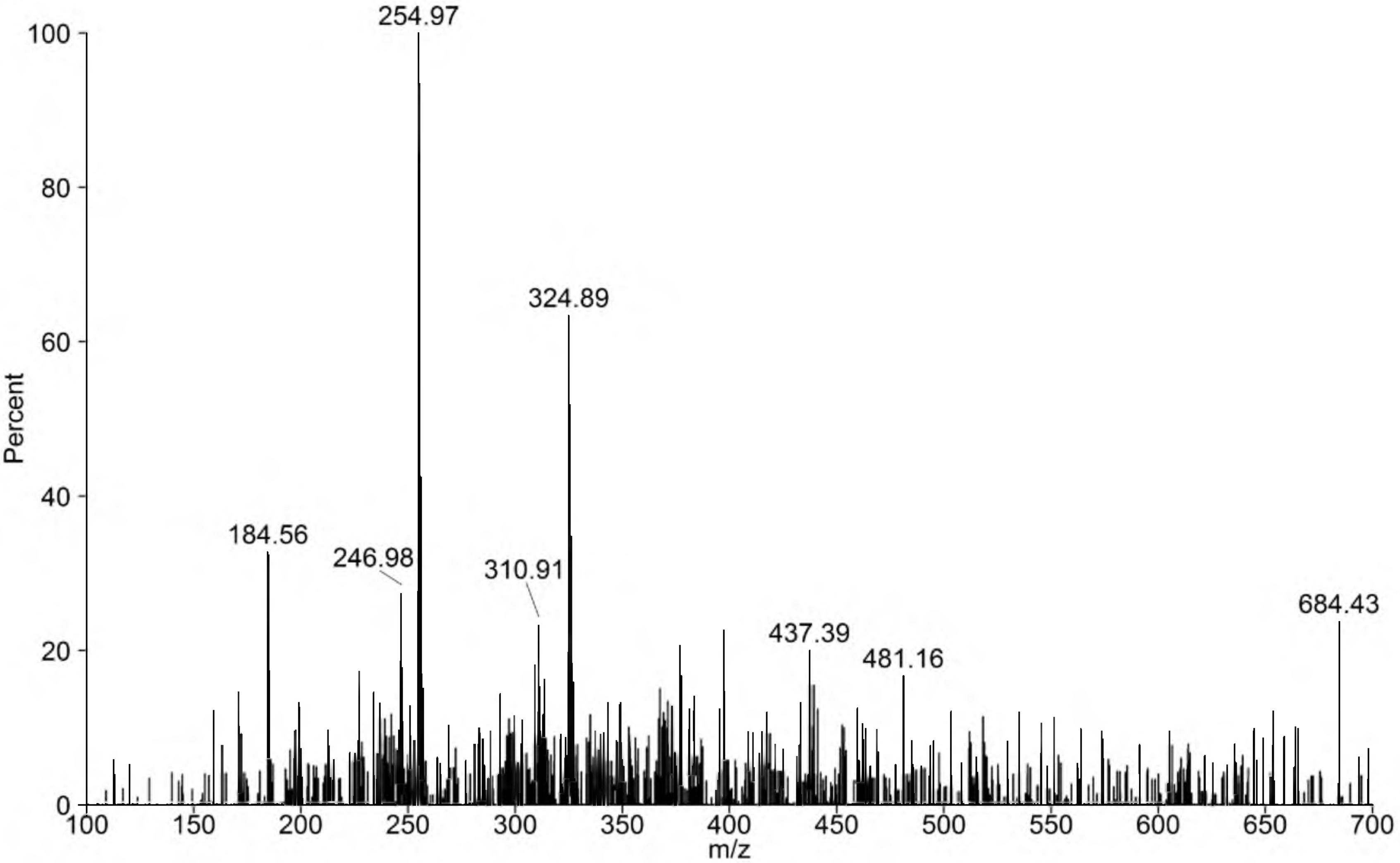

MS 19. UPLC-MS trace at 4.0 min of a 24 h incubation of *Tt*-IDI-2 with IPP.

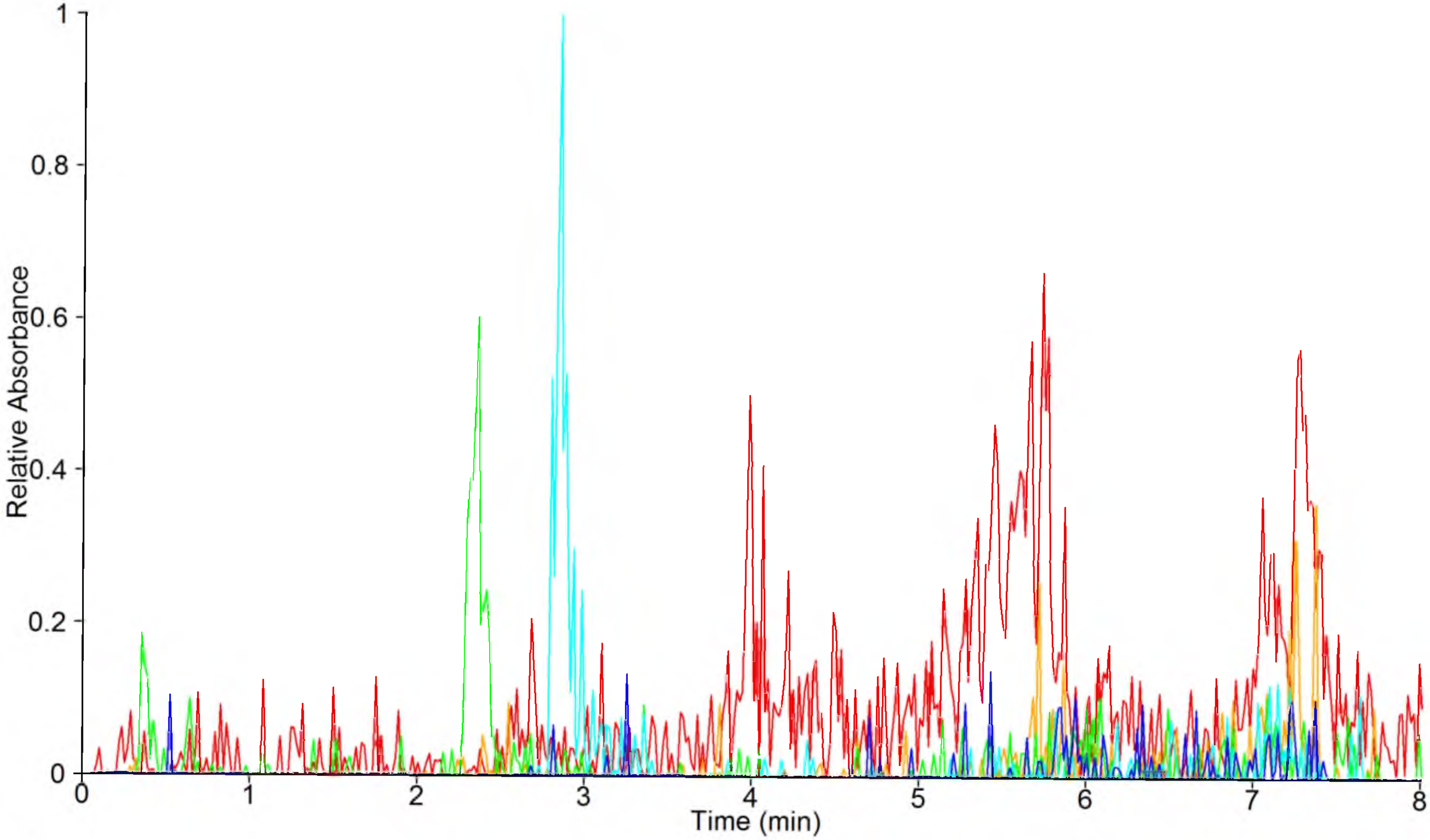

MS 20. UPLC-MS chromatograms of a 24 h incubation of *Tt*-IDI-2 with DMAPP of masses 255.2 (red), 375.2 (orange), 455.1 (green), 525.2 (cyan), 593.2 (blue).

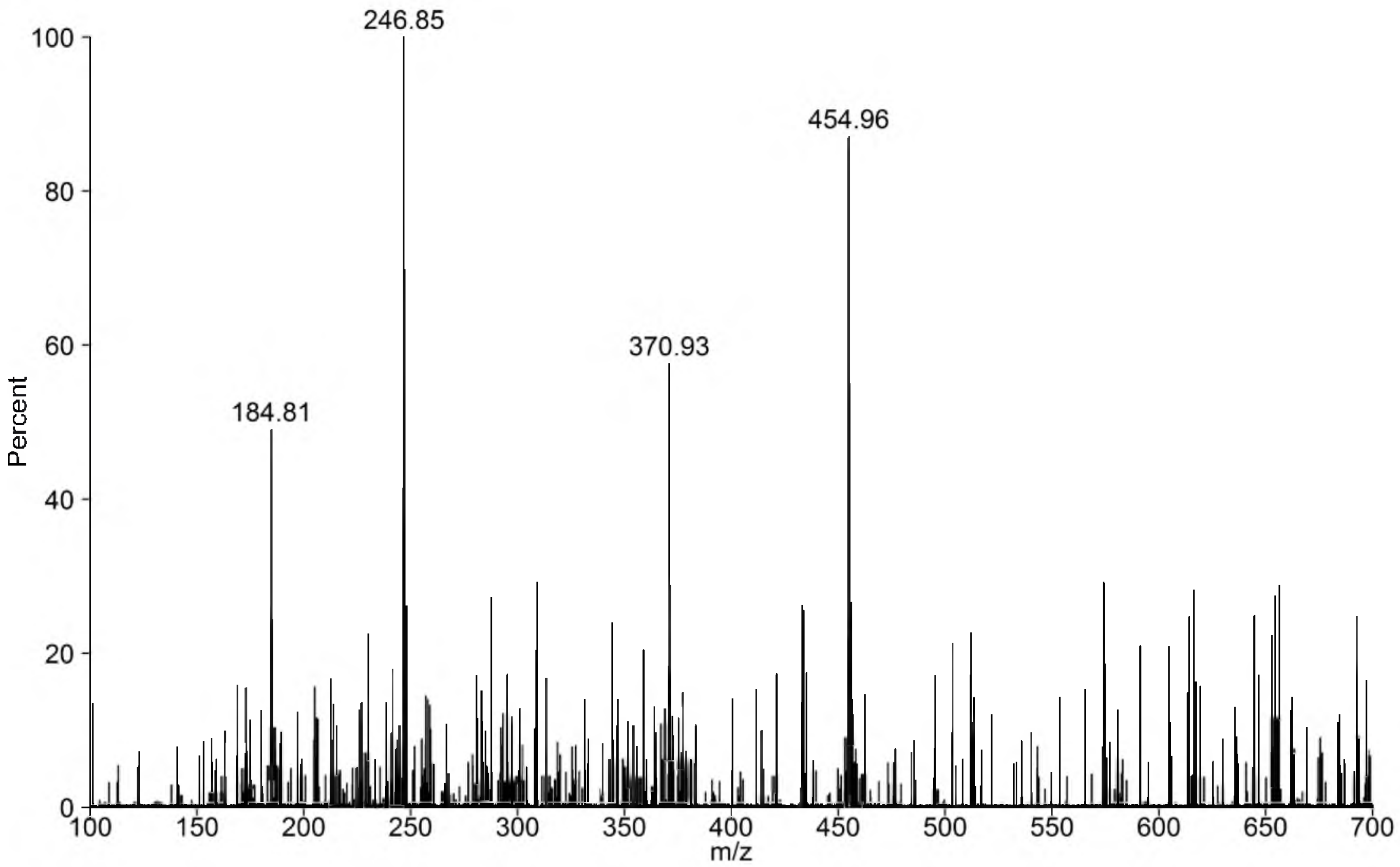

MS 21. UPLC-MS trace at 2.4 min of a 24 h incubation of *Tt*-IDI-2 with DMAPP.

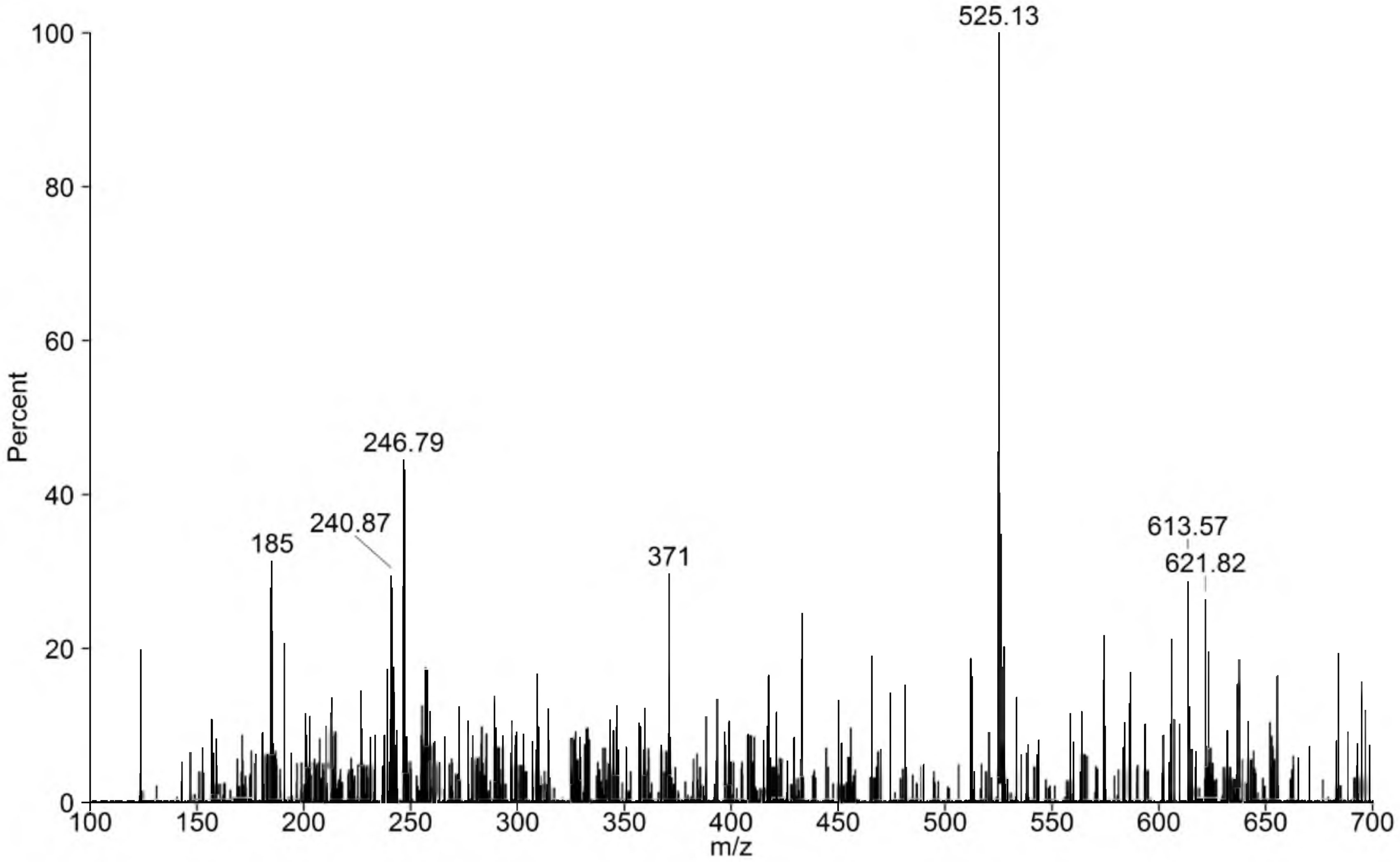

MS 22. UPLC-MS trace at 2.8 min of a 24 h incubation of *Tt*-IDI-2 with DMAPP.

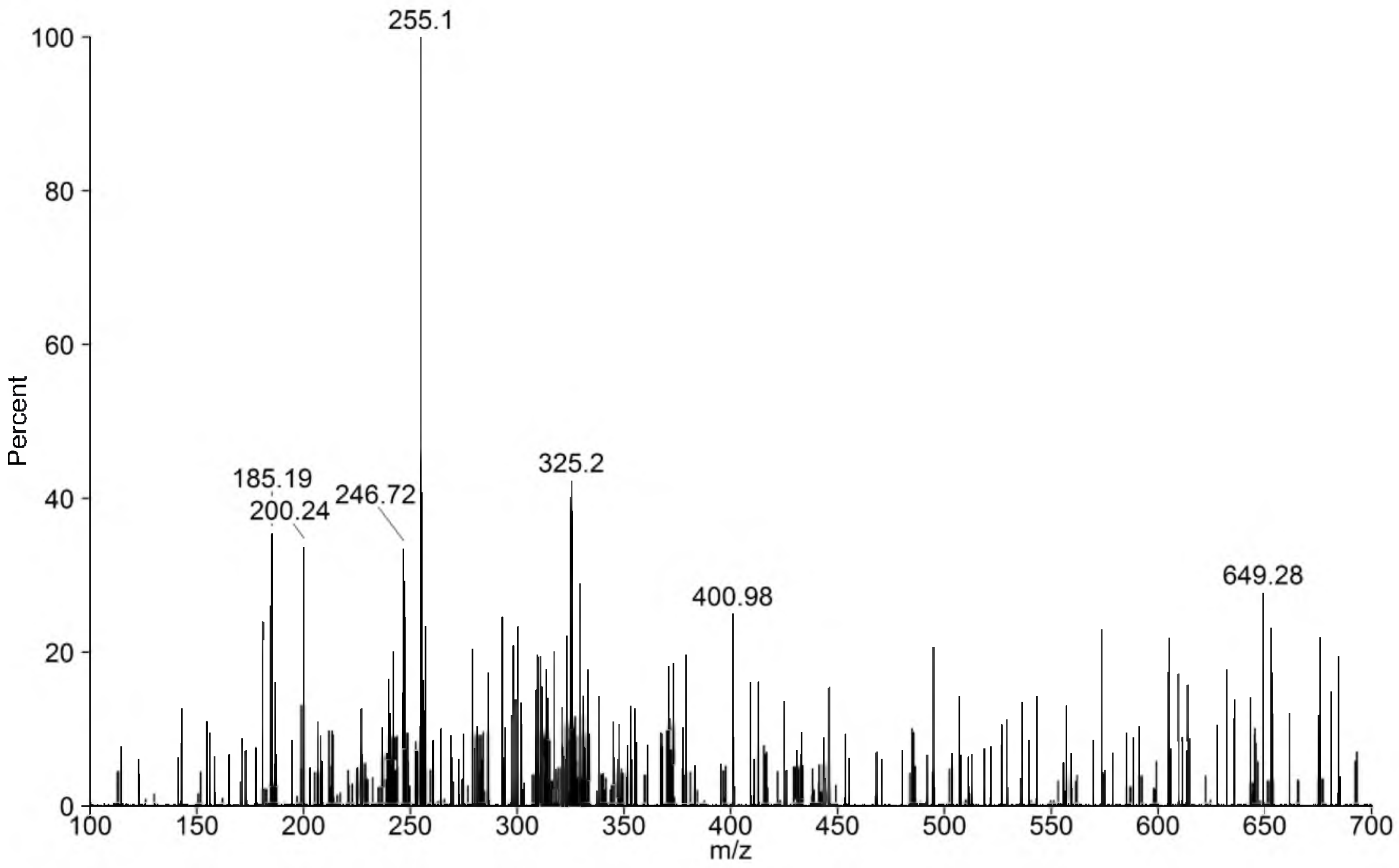

MS 23. UPLC-MS trace at 4.0 min of a 24 h incubation of *Tt*-IDI-2 with DMAPP.

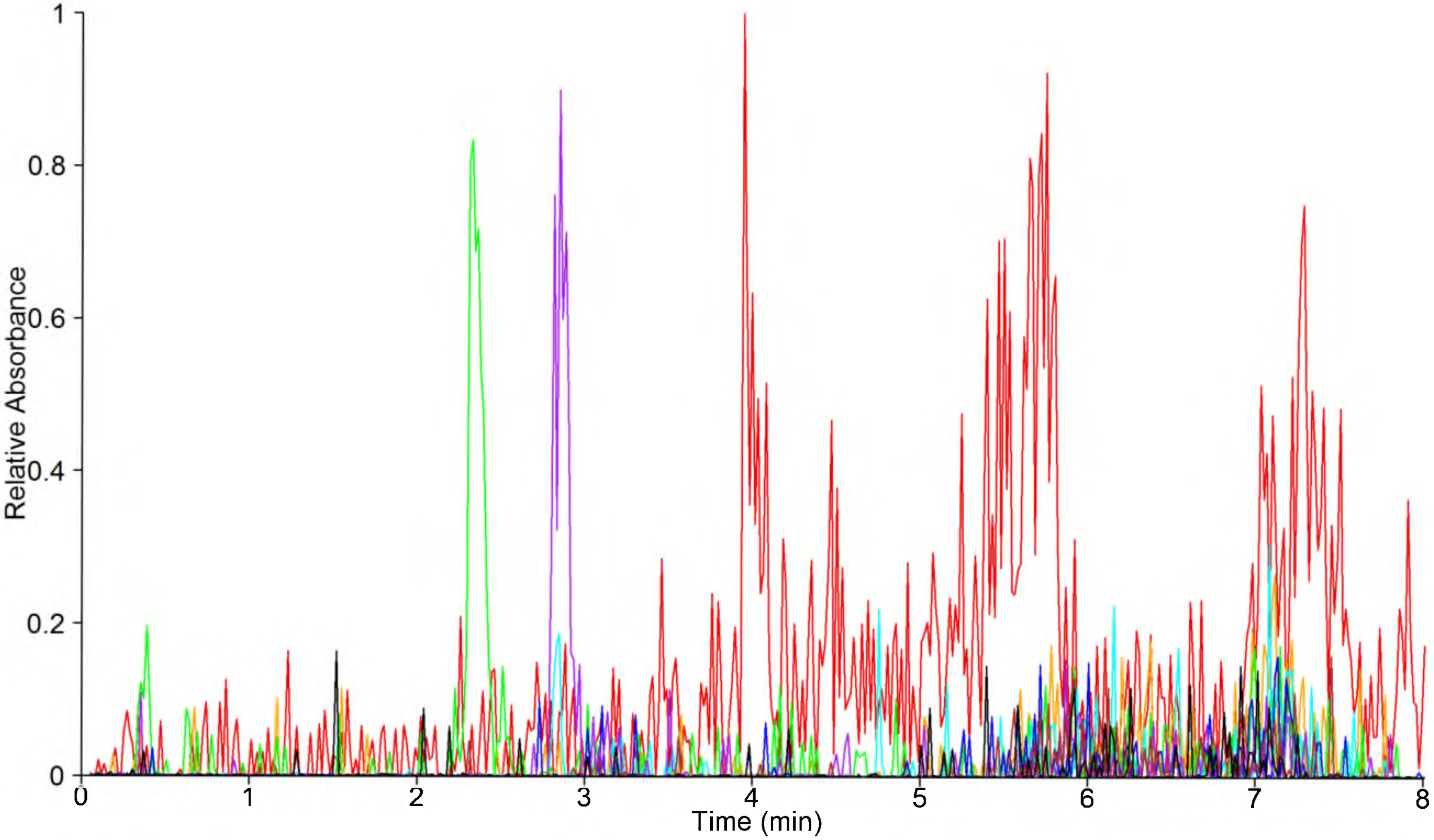

MS 24. UPLC-MS chromatograms of a 24 h incubation of *Tt*-IDI-2 with $^{13}C_5$-IPP of masses 255.2 (red), 375.2 (orange), 455.1 (green), 525.2 (cyan), 530.2 (purple), 593.2 (blue), 598.2 (brown), 603.2 (black).

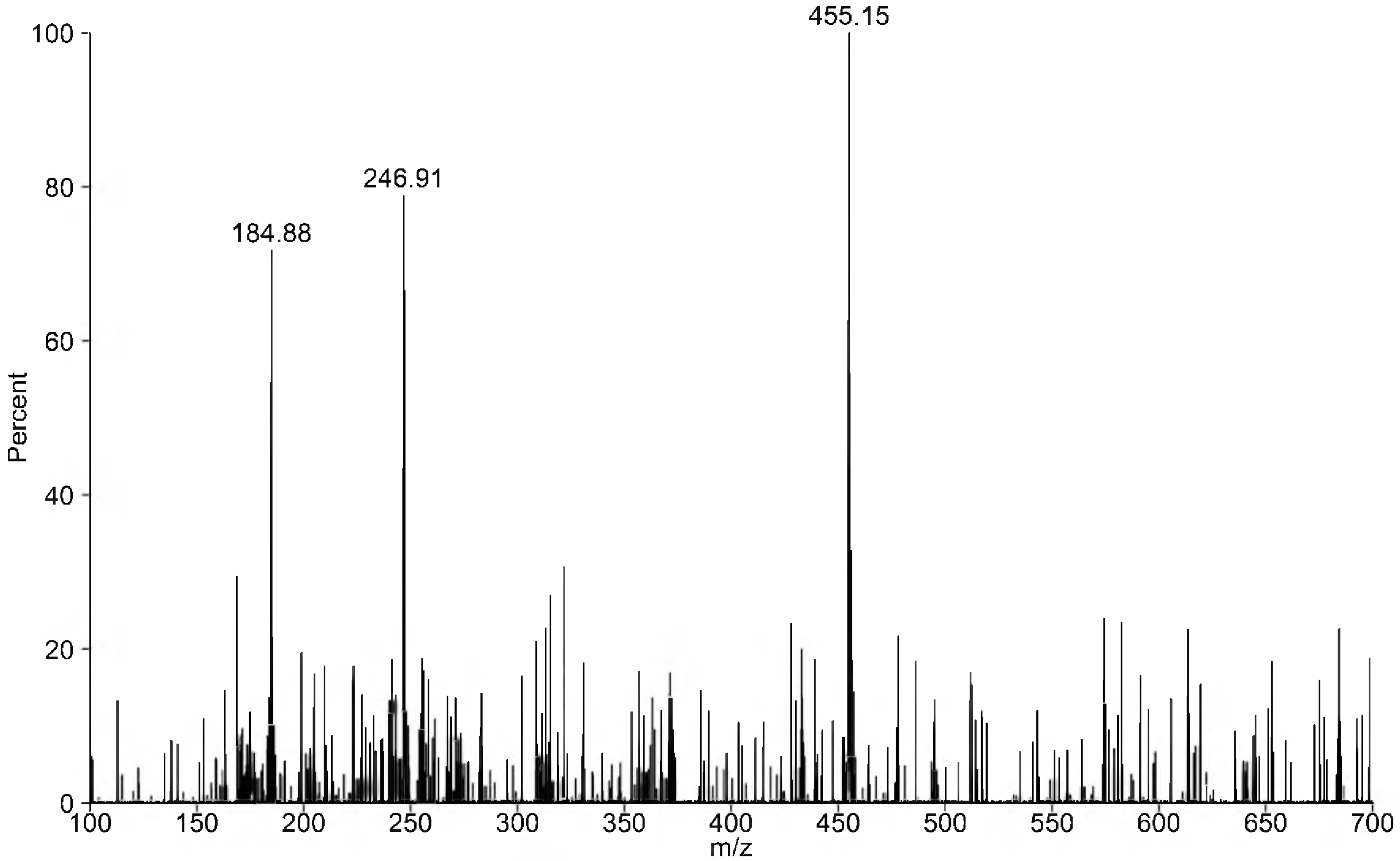

MS 25. UPLC-MS trace at 2.4 min of a 24 h incubation of *Tt*-IDI-2 with $^{13}C_5$-IPP.

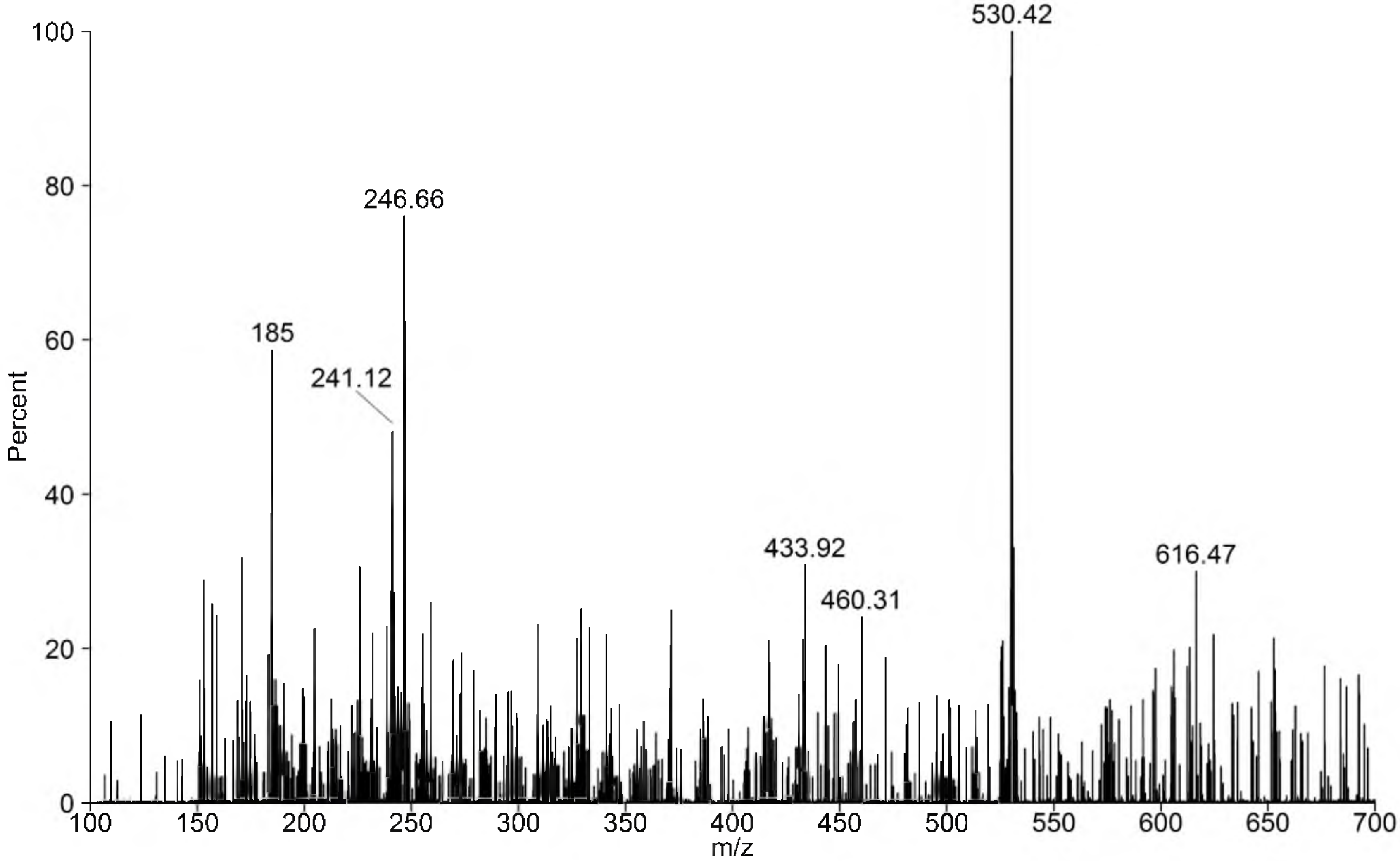

MS 26. UPLC-MS trace at 2.8 min of a 24 h incubation of *Tt*-IDI-2 with $^{13}C_5$-IPP.

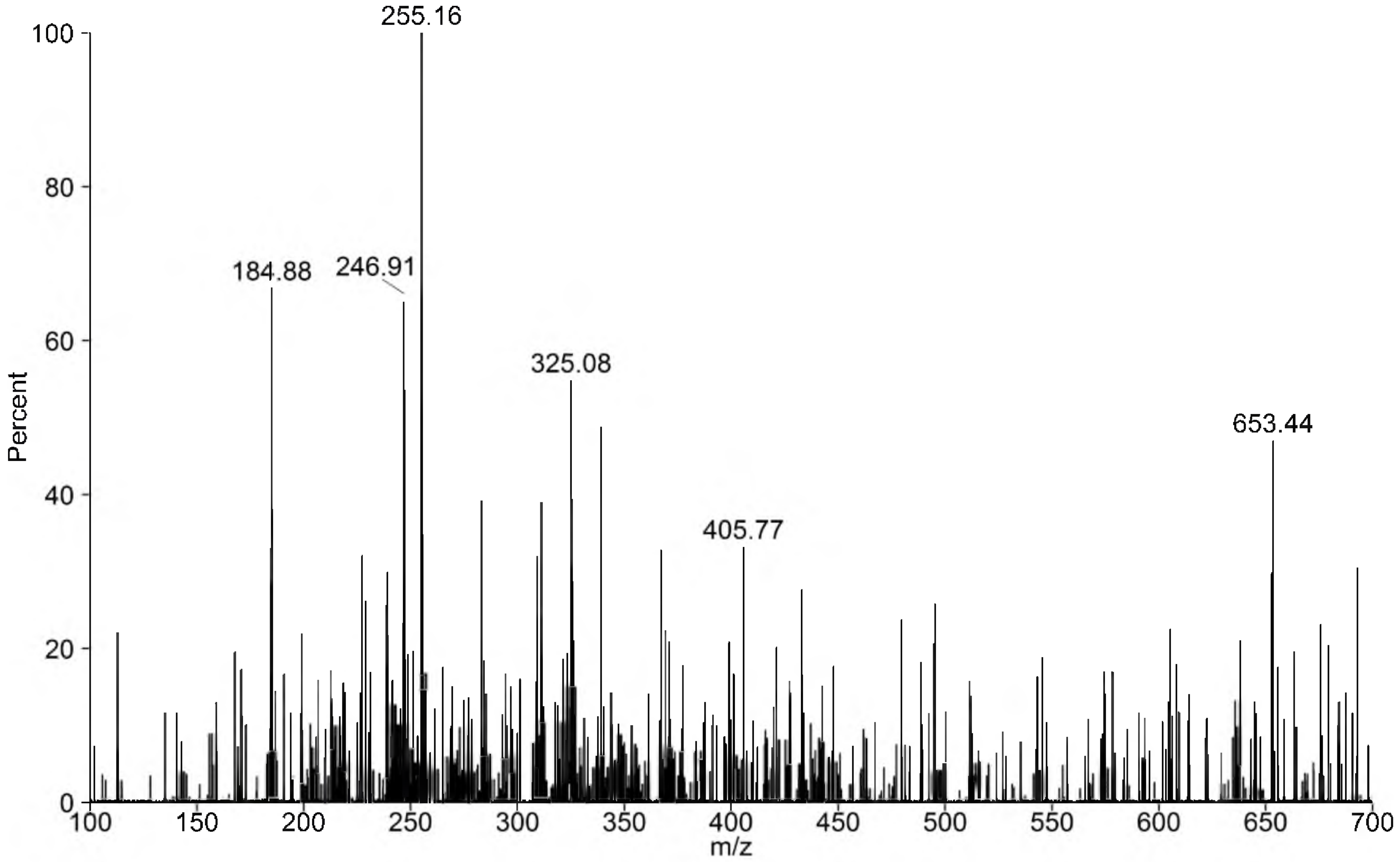

MS 27. UPLC-MS trace at 3.9 min of a 24 h incubation of *Tt*-IDI-2 with $^{13}C_5$-IPP.

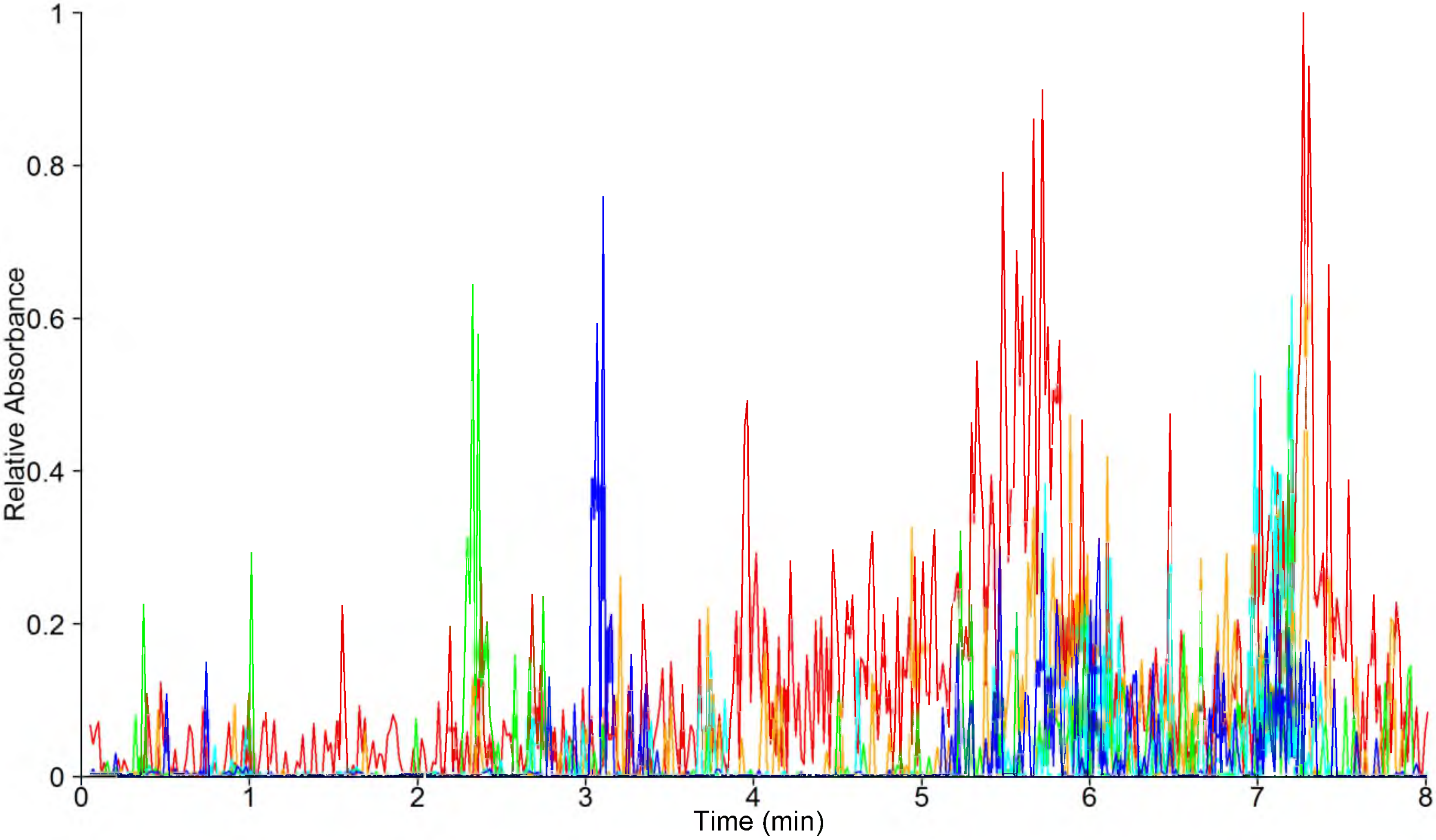

MS 28. UPLC-MS chromatograms of a 27 d incubation of *Tt*-IDI-2 with IPP of masses 255.2 (red), 375.2 (orange), 455.1 (green), 525.2 (cyan), 593.2 (blue).

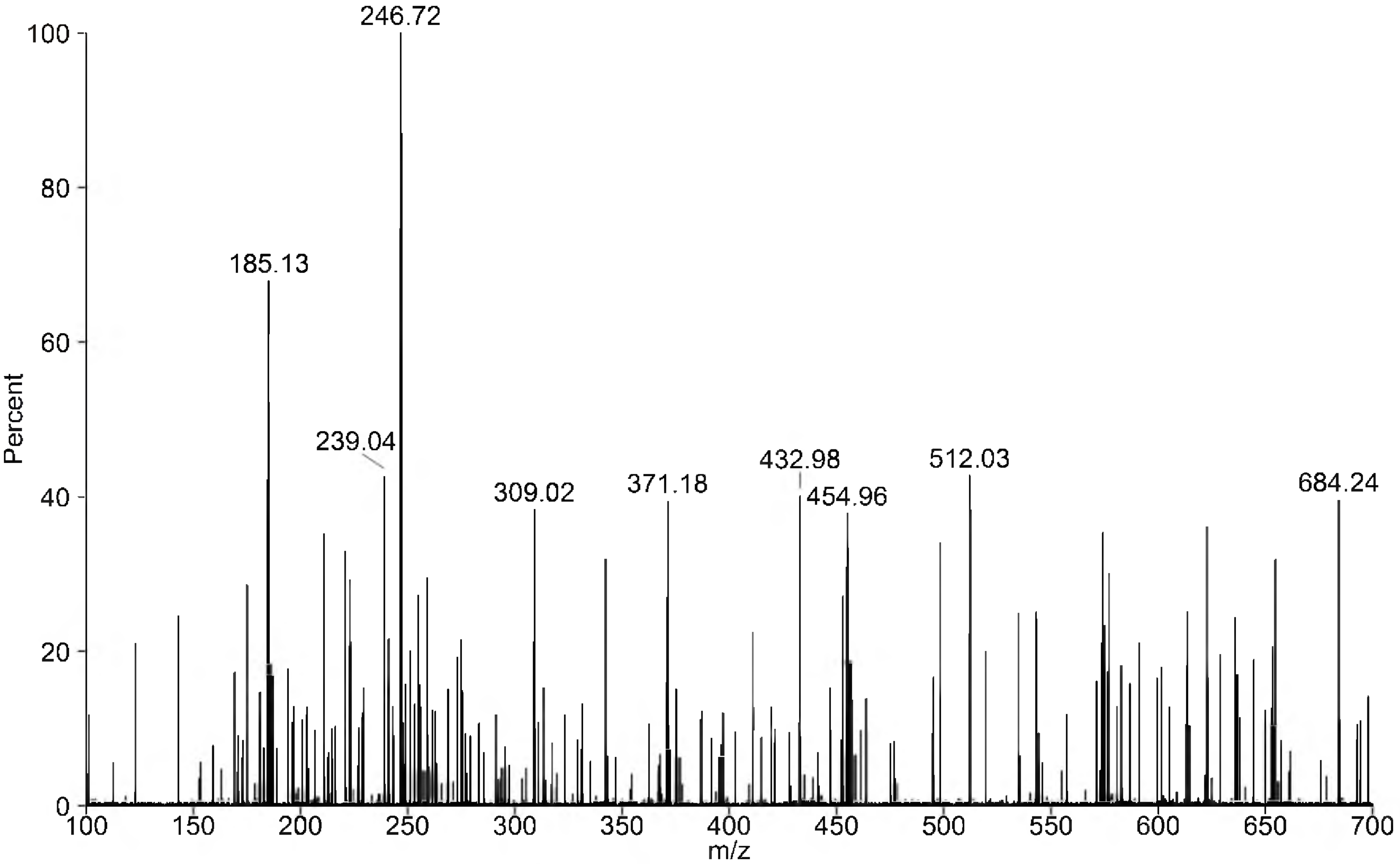

MS 29. UPLC-MS trace at 2.4 min of a 27 d incubation of *Tt*-IDI-2 with IPP.

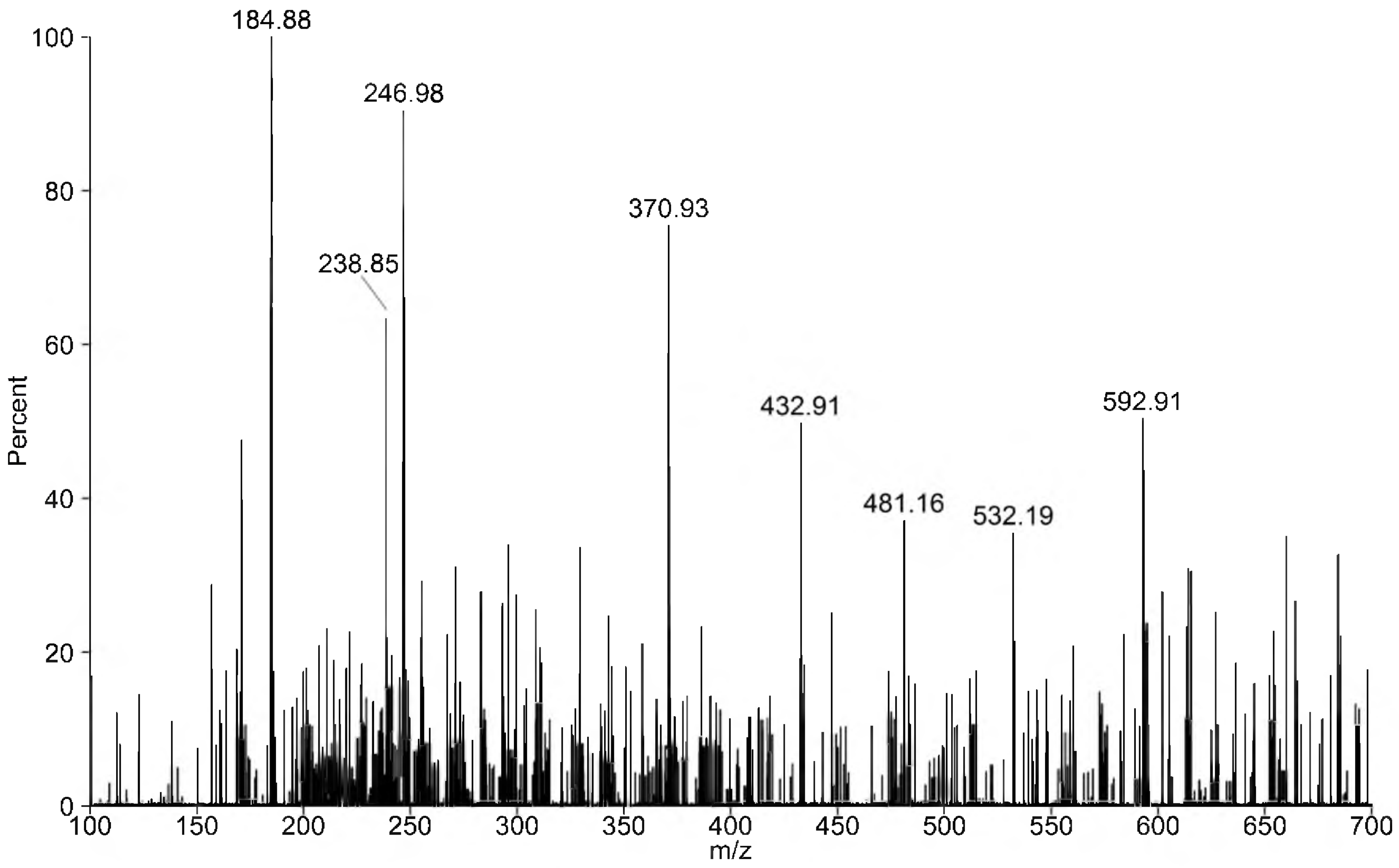

MS 30. UPLC-MS trace at 3.1 min of a 27 d incubation of *Tt*-IDI-2 with IPP.

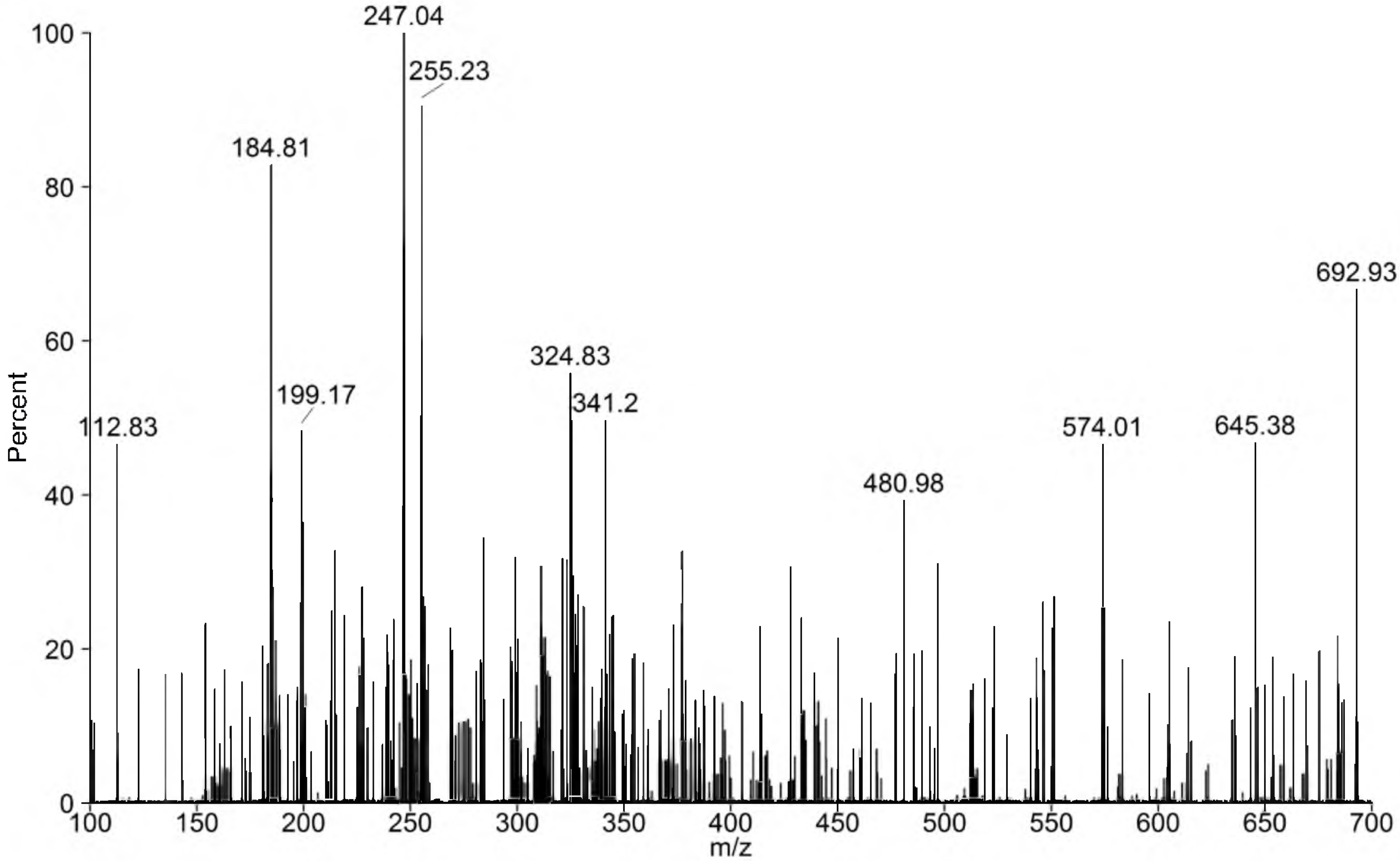

MS 31. UPLC-MS trace at 4.0 min of a 27 d incubation of *Tt*-IDI-2 with IPP.

APPENDIX C

CODED DATA FOR FARNESYL SYNTHASE

Sample	Time (s)	Deuterated Product	Deuterated Substrate	Unlabeled Product	Unlabeled Substrate
1	0.01	181.00	1547.71	72.25	419.40
2	0.01	260.82	4081.07	30.50	2617.19
3	0.01	152.28	5346.21	82.98	2953.73
4	0.01	69.40	2218.46	118.82	1371.93
5	0.01	184.09	3274.86	149.53	1988.00
6	0.01	286.77	3430.84	677.16	3220.29
7	0.01	143.96	4186.53	319.46	3974.77
8	0.01	85.42	3634.26	215.22	3512.94
9	0.01	112.32	3423.18	255.48	3248.78
10	0.02	209.67	1439.15	83.17	380.38
11	0.02	285.91	4851.77	203.41	2667.39
12	0.02	346.06	3254.07	201.65	1915.41
13	0.02	491.74	3712.01	290.37	2159.65
14	0.02	279.26	3299.18	480.27	3052.97
15	0.02	226.58	3295.85	390.07	3043.26
16	0.02	296.78	3870.48	423.04	3709.97
17	0.02	190.53	3291.68	305.89	3097.22
18	0.04	334.28	2355.56	110.75	544.43
19	0.04	291.11	2694.37	172.62	1651.60
20	0.04	352.89	4297.60	220.74	2271.20
21	0.04	151.43	2984.30	83.88	1795.98
22	0.04	470.14	624.90	285.58	364.33
23	0.04	241.78	2865.93	464.60	2709.63
24	0.04	302.51	3018.82	432.99	2785.88
25	0.04	186.18	2629.40	359.32	2461.88
26	0.04	232.20	2267.59	340.14	2537.69
27	0.066	765.69	1501.76	826.36	569.69
28	0.066	747.87	2447.86	378.88	1510.23
29	0.066	500.05	3641.28	283.97	1889.54
30	0.066	784.06	3180.73	507.60	1818.77
31	0.066	475.12	2350.41	725.50	2127.84
32	0.066	420.64	3056.65	648.08	2807.96
33	0.11	555.07	1311.83	150.67	320.04
34	0.11	627.86	1672.01	299.04	863.88
35	0.11	744.57	2487.19	425.14	1330.35
36	0.11	968.77	1951.30	628.41	1130.26
37	0.11	505.43	2267.03	706.47	2086.47
38	0.11	504.10	1907.85	1555.74	1837.98
39	0.182	952.68	966.16	372.16	255.01
40	0.182	1092.50	1065.82	612.72	503.59
41	0.182	1008.03	2372.93	646.11	1251.50
42	0.182	1428.18	1634.77	870.03	955.76
43	0.182	739.78	1660.82	1069.20	1498.29

44	0.182	679.76	1735.61	1063.17	1875.83
45	0.302	775.47	754.77	177.59	156.84
46	0.302	1211.27	1065.68	732.87	517.45
47	0.302	1185.23	2142.94	680.48	1119.82
48	0.302	1824.46	1424.19	1131.40	724.44
49	0.302	986.11	4677.19	2690.12	2590.54
50	0.302	694.08	1686.53	1023.85	1577.58
51	0.501	1140.56	710.15	584.78	298.16
52	0.501	1703.77	819.50	1016.88	395.54
53	0.501	1477.36	1391.35	857.02	695.77
54	0.501	726.58	1098.46	461.79	623.09
55	0.501	1780.94	942.50	1369.16	1501.95
56	0.501	1042.18	1073.65	1165.61	978.25

APPENDIX D

CODED DATA FOR FARNESYL TRANSFERASE

Sample	Time (s)	Deuterated Product	Deuterated Substrate	Unlabeled Product	Unlabeled Substrate
1	0.01	660.73	2287.79	639.92	2008.02
2	0.01	1124.02	9908.21	354.69	2784.18
3	0.01	822.71	3653.69	592.18	2409.04
4	0.01	818.20	3641.97	570.58	2395.76
5	0.01	1149.52	3364.93	769.83	2122.72
6	0.01	908.60	3672.73	314.36	1240.18
7	0.01	623.18	2926.17	553.36	2618.61
8	0.01	487.13	2716.78	696.61	3984.56
9	0.01	55.44	1065.75	85.31	1438.21
10	0.01	420.46	2660.49	766.67	3468.60
11	0.01	383.96	2555.38	477.10	3109.01
12	0.01	400.09	2928.33	495.75	3615.57
13	0.02	1215.62	1733.29	1198.38	1569.30
14	0.02	2210.74	9755.05	668.27	2741.23
15	0.02	1476.93	3071.02	1073.42	2007.01
16	0.02	1481.33	2949.73	1044.88	1895.36
17	0.02	1897.30	3128.04	1281.12	1945.76
18	0.02	1737.67	3033.34	610.19	1013.98
19	0.02	1086.24	2614.90	858.09	2189.81
20	0.02	824.35	2316.88	1224.27	3357.57
21	0.02	858.57	2370.75	1239.77	3335.58
22	0.02	84.80	879.40	119.04	1179.23
23	0.02	795.04	2344.55	1050.34	3093.85
24	0.02	724.74	2399.56	900.60	2932.03
25	0.02	806.71	1983.14	938.77	2346.21
26	0.03	1487.75	1522.64	1494.89	1361.96
27	0.03	2773.76	9692.99	826.69	2710.94
28	0.03	1789.89	2800.58	1307.35	1775.10
29	0.03	2272.40	2884.69	1518.24	1765.28
30	0.03	2054.79	2795.79	729.29	885.82
31	0.03	1315.31	2289.43	1009.78	2177.65
32	0.03	1033.31	2026.60	1518.32	2950.71
33	0.03	1023.24	2178.95	1479.05	3193.29
34	0.03	78.06	827.16	107.68	1103.63
35	0.03	981.61	2276.94	1279.64	2976.35
36	0.03	960.15	2565.44	1194.37	3151.00
37	0.03	955.78	1910.41	1141.69	2250.58
38	0.04	1773.07	1343.39	1814.64	1173.25
39	0.04	3289.80	9111.12	984.70	2552.80
40	0.04	2042.53	2586.30	1466.10	1680.71
41	0.04	2591.09	2497.42	1725.48	1518.01
42	0.04	2369.86	2410.12	876.19	750.32
43	0.04	1537.22	2126.12	1144.20	1897.31

44	0.04	1186.95	2111.42	1716.03	3047.35
45	0.04	149.09	762.09	207.30	1030.89
46	0.04	1107.57	2130.71	1492.64	2763.89
47	0.04	1078.07	2341.37	1340.18	2912.08
48	0.04	1103.68	1812.78	1295.07	2108.08
49	0.08	2342.27	862.07	2323.39	725.88
50	0.08	4372.22	7463.45	1301.56	2064.74
51	0.08	2770.78	2034.25	1975.15	1263.59
52	0.08	3166.30	1803.51	1159.92	549.97
53	0.08	2001.16	1454.21	1489.08	1406.10
54	0.08	1553.43	1729.17	2252.58	2490.17
55	0.08	1507.77	1816.17	2036.77	2453.80
56	0.1	2544.86	749.40	2520.36	581.04
57	0.1	7396.18	4839.45	2024.70	1439.97
58	0.1	2889.73	1755.17	2092.62	1063.54
59	0.1	3023.94	1537.87	1079.89	470.85
60	0.1	2203.50	1300.85	1636.91	1288.67
61	0.1	1755.52	1646.32	2530.11	2364.67
62	0.1	1654.95	1721.11	2231.85	2311.75
63	0.1	1643.24	1634.43	2168.19	2074.83
64	0.1	1408.88	1777.33	1727.08	2145.02
65	0.1	1625.41	1412.43	1901.97	1639.57

REFERENCES

(1) Dictionary of Natural Products Online, 22.1. Taylor & Francis Group. http://dnp.chemnetbase.com (accessed November 5, 2013).

(2) Bentley, R. (1999) Secondary metabolite biosynthesis: the first century. *Crit. Rev. Biotechnol. 19*, 1–40.

(3) Williams, C. G. (1860) On isoprene and caoutchine. *Philos. Trans. R. Soc. London 150*, 241–255.

(4) *Merriam-Webster's Collegiate Dictionary*, 10th ed.; Springfield, MA, 1998; p 1216-1217, 1275.

(5) Kremers, E. (1933) Phytochemical terminology - Terpene. *J. Am. Pharm. Assoc. 22*, 227–232.

(6) Schorlemmer, C. (1872) XII.—The chemistry of the hydrocarbons. *J. Chem. Soc. 25*, 425–446.

(7) Pichersky, E., and Gershenzon, J. (2002) The formation and function of plant volatiles: perfumes for pollinator attraction and defense. *Curr. Opin. Plant Biol. 5*, 237–243.

(8) Unsicker, S. B., Kunert, G., and Gershenzon, J. (2009) Protective perfumes: the role of vegetative volatiles in plant defense against herbivores. *Curr. Opin. Plant Biol. 12*, 479–485.

(9) Sharkey, T. D., Wiberley, A. E., and Donohue, A. R. (2008) Isoprene emission from plants: why and how. *Ann. Bot. 101*, 5–18.

(10) BASF. The cool freshness of menthol – BASF – The Chemical Company – Corporate Website. http://www.basf.com/group/corporate/en/news-and-media-relations/science-around-us/menthol/story (accessed November 1, 2013).

(11) Bautista, D. M., Siemens, J., Glazer, J. M., Tsuruda, P. R., Basbaum, A. I., Stucky, C. L., Jordt, S.-E., and Julius, D. (2007) The menthol receptor TRPM8 is the principal detector of environmental cold. *Nature 448*, 204–208.

(12) Rasmann, S., Köllner, T. G., Degenhardt, J., Hiltpold, I., Toepfer, S., Kuhlmann, U.,

Gershenzon, J., and Turlings, T. C. J. (2005) Recruitment of entomopathogenic nematodes by insect-damaged maize roots. *Nature 434*, 732–737.

(13) Köllner, T. G., Held, M., Lenk, C., Hiltpold, I., Turlings, T. C. J., Gershenzon, J., and Degenhardt, J. (2008) A maize (E)-β-caryophyllene synthase implicated in indirect defense responses against herbivores is not expressed in most American maize varieties. *Plant Cell 20*, 482–494.

(14) Degenhardt, J., Hiltpold, I., Köllner, T. G., Frey, M., Gierl, A., Gershenzon, J., Hibbard, B. E., Ellersieck, R., and Turlings, T. C. J. (2009) Restoring a maize root signal that attracts insect-killing nematodes to control a major pest. *Proc. Natl. Acad. Sci. U.S.A. 106*, 13213–13218.

(15) Klayman, D. L. (1985) Qinghaosu (Artemisinin): an antimalarial drug from China. *Science 228*, 1049–1055.

(16) White, N. J. (2008) Qinghaosu (artemisinin): the price of success. *Science 320*, 330–334.

(17) Krishnani, K. K., Ravichandran, P., and Ayyappan, S. (2008) Microbially derived off-flavor from geosmin and 2-methylisoborneol: sources and remediation, in *Reviews of Environmental Contamination and Toxicology* (Whitacre, D. M., Ed.), pp 1–27. Springer, New York, NY.

(18) Gerber, N. N., and Lechevalier, H. A. (1965) Geosmin, an earthly-smelling substance isolated from actinomycetes. *Appl. Microbiol. 13*, 935–938.

(19) Lu, G., Edwards, C. G., Fellman, J. K., Mattinson, D. S., and Navazio, J. (2003) Biosynthetic origin of geosmin in red beets (*Beta vulgaris* L.). *J. Agric. Food Chem. 51*, 1026–1029.

(20) Karahadian, C., Josephson, D. B., and Lindsay, R. C. (1985) Volatile compounds from *Pencillium sp.* contributing musty-earthy notes to brie and camembert cheese flavors. *J. Agric. Food Chem. 33*, 339–343.

(21) Bishopp, A., Mähönen, A. P., and Helariutta, Y. (2006) Signs of change: hormone receptors that regulate plant development. *Development 133*, 1857–1869.

(22) Springob, K., and Kutchan, T. M. (2009) Introduction to the different classes of natural products, in *Plant-derived Natural Products* (Osbourn, A. E., and Lanzotti, V., Eds.), pp 3–50. Springer US, New York, NY.

(23) Howitt, C. A., and Pogson, B. J. (2006) Carotenoid accumulation and function in seeds and non-green tissues. *Plant. Cell Environ. 29*, 435–445.

(24) Burri, B. J. (1997) Beta-carotene and human health: a review of current research.

Nutr. Res. 17, 547–580.

(25) Beytía, E. D., and Porter, J. W. (1976) Biochemistry of polyisoprenoid biosynthesis. *Annu. Rev. Biochem. 45*, 113–142.

(26) Whitehead, S. R., and Bowers, M. D. (2013) Iridoid and secoiridoid glycosides in a hybrid complex of bush honeysuckles (*Lonicera spp.*, Caprifolicaceae): implications for evolutionary ecology and invasion biology. *Phytochemistry 86*, 57–63.

(27) Beerhues, L. (2006) Hyperforin. *Phytochemistry 67*, 2201–2207.

(28) Van Cleemput, M., Cattoor, K., De Bosscher, K., Haegeman, G., De Keukeleire, D., and Heyerick, A. (2009) Hop (*Humulus lupulus*)-derived bitter acids as multipotent bioactive compounds. *J. Nat. Prod. 72*, 1220–1230.

(29) Ostash, B., Saghatelian, A., and Walker, S. (2007) A streamlined metabolic pathway for the biosynthesis of moenomycin A. *Chem. Biol. 14*, 257–267.

(30) Hemming, F. W. (1983) Biosynthesis of dolichols and related compounds, in *Biosynthesis of Isoprenoid Compounds* (Porter, J. W., and Spurgeon, S. L., Eds.), pp 305–354. John Wiley & Sons, New York, NY.

(31) Pennock, J. F., and Threlfall, D. R. (1983) Biosynthesis of ubiquinone and related compounds, in *Biosynthesis of Isoprenoid Compounds* (Porter, J. W., and Spurgeon, S. L., Eds.), pp 191–303. John Wiley & Sons, New York, NY.

(32) Chong, P. L.-G. (2010) Archaebacterial bipolar tetraether lipids: physico-chemical and membrane properties. *Chem. Phys. Lipids 163*, 253–265.

(33) Schafer, W. R., and Rine, J. (1992) Protein prenylation: genes, enzymes, targets, and functions. *Annu. Rev. Genet. 30*, 209–237.

(34) Ochocki, J. D., and Distefano, M. D. (2013) Prenyltransferase inhibitors: treating human ailments from cancer to parasitic infections. *MedChemComm 4*, 476-492.

(35) Dumelin, C. E., Chen, Y., Leconte, A. M., Chen, Y. G., and Liu, D. R. (2012) Discovery and biological characterization of geranylated RNA in bacteria. *Nat. Chem. Biol. 8*, 913–919.

(36) Spurgeon, S. L., and Porter, J. W. (1981) Introduction, in *Biosynthesis of Isoprenoid Compounds* (Porter, J. W., and Spurgeon, S. L., Eds.), pp 1–46. John Wiley & Sons, New York, NY.

(37) Chen, M., and Poulter, C. D. (2010) Characterization of thermophilic archaeal isopentenyl phosphate kinases. *Biochemistry 49*, 207–217.

(38) Matsumi, R., Atomi, H., Driessen, A. J. M., and van der Oost, J. (2011) Isoprenoid biosynthesis in Archaea-biochemical and evolutionary implications. *Res. Microbiol. 162*, 39–52.

(39) Flesch, G., and Rohmer, M. (1988) Prokaryotic hopanoids: the biosynthesis of the bacteriohopane skeleton. Formation of isoprenic units from two distinct acetate pools and a novel type of carbon/carbon linkage between a triterpene and D-ribose. *Eur. J. Biochem. 175*, 405–411.

(40) Zhou, D., and White, R. H. (1991) Early steps of isoprenoid biosynthesis in *Escherichia coli*. *Biochem. J. 273*, 627–634.

(41) Rohmer, M., Knani, M., Simonin, P., Sutter, B., and Sahm, H. (1993) Isoprenoid biosynthesis in bacteria: a novel pathway for the early steps leading to isopentenyl diphosphate. *Biochem. J. 295*, 517–524.

(42) Rohmer, M., Seemann, M., Horbach, S., Bringer-meyer, S., and Sahm, H. (1996) Glyceraldehyde 3-phosphate and pyruvate as precursors of isoprenic units in an alternative non-mevalonate pathway for terpenoid biosynthesis. *J. Am. Chem. Soc. 118*, 2564–2566.

(43) Altincicek, B., Duin, E. C., Reichenberg, A., Hedderich, R., Kollas, A.-K., Hintz, M., Wagner, S., Wiesner, J., Beck, E., and Jomaa, H. (2002) LytB protein catalyzes the terminal step of the 2-C-methyl-D-erythritol-4-phosphate pathway of isoprenoid biosynthesis. *FEBS Lett. 532*, 437–440.

(44) Omelchenko, M. V, Galperin, M. Y., Wolf, Y. I., and Koonin, E. V. (2010) Non-homologous isofunctional enzymes: a systematic analysis of alternative solutions in enzyme evolution. *Biol. Direct 5*, 31.

(45) Laupitz, R., Hecht, S., Amslinger, S., Zepeck, F., Kaiser, J., Richter, G., Schramek, N., Steinbacher, S., Huber, R., Arigoni, D., Bacher, A., Eisenreich, W., and Rohdich, F. (2004) Biochemical characterization of *Bacillus subtilis* type II isopentenyl diphosphate isomerase, and phylogenetic distribution of isoprenoid biosynthesis pathways. *Eur. J. Biochem. 271*, 2658–2669.

(46) Rohdich, F., Bacher, A., and Eisenreich, W. (2004) Perspectives in anti-infective drug design. The late steps in the biosynthesis of the universal terpenoid precursors, isopentenyl diphosphate and dimethylallyl diphosphate. *Bioorg. Chem. 32*, 292–308.

(47) Chaykin, S., Law, J., Phillips, A. H., Tchen, T. T., and Bloch, K. (1958) Phosphorylated intermediates in the synthesis of squalene. *Proc. Natl. Acad. Sci. U.S.A. 44*, 998–1004.

(48) Agranoff, B. W., Eggerer, H., Henning, U., and Lynen, F. (1960) Biosynthesis of terpenes VII. Isopentenyl pyrophosphate isomerase. *J. Biol. Chem. 235*, 326–332.

(49) Carrigan, C. N., and Poulter, C. D. (2003) Zinc is an essential cofactor for type I isopentenyl diphosphate:dimethylallyl diphosphate isomerase. *J. Am. Chem. Soc. 125*, 9008–9009.

(50) Lee, S., and Poulter, C. D. (2006) *Escherichia coli* type I isopentenyl diphosphate isomerase: structural and catalytic roles for divalent metals. *J. Am. Chem. Soc. 128*, 11545–11550.

(51) Wouters, J., Oudjama, Y., Barkley, S. J., Tricot, C., Stalon, V., Droogmans, L., and Poulter, C. D. (2003) Catalytic mechanism of *Escherichia coli* isopentenyl diphosphate isomerase involves Cys-67, Glu-116, and Tyr-104 as suggested by crystal structures of complexes with transition state analogues and irreversible inhibitors. *J. Biol. Chem. 278*, 11903–11908.

(52) Wu, Z., Wouters, J., and Poulter, C. D. (2005) Isopentenyl diphosphate isomerase. Mechanism-based inhibition by diene analogues of isopentenyl diphosphate and dimethylallyl diphosphate. *J. Am. Chem. Soc. 127*, 17433–17438.

(53) Poulter, C. D., and Rilling, H. C. (1981) Prenyl transferases and isomerase, in *Biosynthesis of Isoprenoid Compounds* (Porter, J. W., and Spurgeon, S. L., Eds.), pp 161–224. John Wiley & Sons, New York, NY.

(54) Reardon, J. E., and Abeles, R. H. (1986) Mechanism of action of isopentenyl pyrophosphate isomerase: evidence for a carbonium ion intermediate. *Biochemistry 25*, 5609–5616.

(55) Muehlbacher, M., and Poulter, C. D. (1988) Isopentenyl-diphosphate isomerase: inactivation of the enzyme with active-site-directed irreversible inhibitors and transition-state analogues. *Biochemistry 27*, 7315–7328.

(56) De Ruyck, J., Durisotti, V., Oudjama, Y., and Wouters, J. (2006) Structural role for Tyr-104 in *Escherichia coli* isopentenyl-diphosphate isomerase: site-directed mutagenesis, enzymology, and protein crystallography. *J. Biol. Chem. 281*, 17864–17869.

(57) Kaneda, K., Kuzuyama, T., Takagi, M., Hayakawa, Y., and Seto, H. (2001) An unusual isopentenyl diphosphate isomerase found in the mevalonate pathway gene cluster from *Streptomyces sp.* strain CL190. *Proc. Natl. Acad. Sci. U.S.A. 98*, 932–937.

(58) Nagai, T., Unno, H., Janczak, M. W., Yoshimura, T., Poulter, C. D., and Hemmi, H. (2011) Covalent modification of reduced flavin mononucleotide in type-2 isopentenyl diphosphate isomerase by active-site-directed inhibitors. *Proc. Natl. Acad. Sci. U.S.A. 108*, 20461–20466.

(59) Nakatani, H., Goda, S., Unno, H., Nagai, T., Yoshimura, T., and Hemmi, H. (2012) Substrate-induced change in the quaternary structure of type 2 isopentenyl diphosphate

isomerase from *Sulfolobus shibatae*. *J. Bacteriol. 194*, 3216–3224.

(60) Barkley, S. J., Desai, S. B., and Poulter, C. D. (2004) Proton exchange in type II isopentenyl diphosphate isomerase. *Org. Lett. 6*, 5019–5021.

(61) Kao, C., Kittleman, W., Zhang, H., Seto, H., and Liu, H. (2005) Stereochemical analysis of isopentenyl diphosphate isomerase type II from *Staphylococcus aureus* using chemically synthesized (S)- and (R)-[2-^{2}H]isopentenyl diphosphates. *Org. Lett. 7*, 5677–5680.

(62) Calveras, J., Thibodeaux, C. J., Mansoorabadi, S. O., and Liu, H. (2012) Stereochemical studies of the type II isopentenyl diphosphate-dimethylallyl diphosphate isomerase implicate the FMN coenzyme in substrate protonation. *ChemBioChem 13*, 42–46.

(63) Rothman, S. C., Helm, T. R., and Poulter, C. D. (2007) Kinetic and spectroscopic characterization of type II isopentenyl diphosphate isomerase from *Thermus thermophilus*: evidence for formation of substrate-induced flavin species. *Biochemistry 46*, 5437–5445.

(64) Kittleman, W., Thibodeaux, C. J., Liu, Y., Zhang, H., and Liu, H. (2007) Characterization and mechanistic studies of type II isopentenyl diphosphate:dimethylallyl diphosphate isomerase from *Staphylococcus aureus*. *Biochemistry 46*, 8401–8413.

(65) Mayhew, S. G. (1999) The effects of pH and semiquinone formation on the oxidation-reduction potentials of flavin mononucleotide. A reappraisal. *Eur. J. Biochem. 265*, 698–702.

(66) Thibodeaux, C. J., Mansoorabadi, S. O., Kittleman, W., Chang, W., and Liu, H. (2008) Evidence for the involvement of acid/base chemistry in the reaction catalyzed by the type II isopentenyl diphosphate/dimethylallyl diphosphate isomerase from *Staphylococcus aureus*. *Biochemistry 47*, 2547–2558.

(67) Johnston, J. B., Walker, J. R., Rothman, S. C., and Poulter, C. D. (2007) Type-2 isopentenyl diphosphate isomerase. Mechanistic studies with cyclopropyl and epoxy analogues. *J. Am. Chem. Soc. 129*, 7740–7741.

(68) Rothman, S. C., Johnston, J. B., Lee, S., Walker, J. R., and Poulter, C. D. (2008) Type II isopentenyl diphosphate isomerase: irreversible inactivation by covalent modification of flavin. *J. Am. Chem. Soc. 130*, 4906–4913.

(69) Engel, P. S., He, S.-L., Banks, J. T., Ingold, K. U., and Lusztyk, J. (1997) Clocking tertiary cyclopropylcarbinyl radical rearrangements. *J. Org. Chem. 62*, 5656–5656.

(70) Krishnamurthy, V., and Rawal, V. H. (1997) Kinetics of the oxiranylcarbinyl radical rearrangement. *J. Org. Chem. 62*, 1572–1573.

(71) Sharma, N. K., Pan, J.-J., and Poulter, C. D. (2010) Type II isopentenyl diphosphate isomerase: probing the mechanism with alkyne/allene diphosphate substrate analogues. *Biochemistry 49*, 6228–6233.

(72) Heaps, N. A, and Poulter, C. D. (2011) Synthesis and evaluation of chlorinated substrate analogues for farnesyl diphosphate synthase. *J. Org. Chem. 76*, 1838–1843.

(73) Unno, H., Yamashita, S., Ikeda, Y., Sekiguchi, S.-Y., Yoshida, N., Yoshimura, T., Kusunoki, M., Nakayama, T., Nishino, T., and Hemmi, H. (2009) New role of flavin as a general acid-base catalyst with no redox function in type 2 isopentenyl-diphosphate isomerase. *J. Biol. Chem. 284*, 9160–9167.

(74) Spencer, R., Fisher, J., and Walsh, C. (1977) One-and two-electron redox chemistry of 1-carba-1-deazariboflavin. *Biochemistry 16*, 3586–3594.

(75) Macheroux, P., Ghisla, S., Sanner, C., Rüterjans, H., and Müller, F. (2005) Reduced flavin: NMR investigation of N5-H exchange mechanism, estimation of ionisation constants and assessment of properties as biological catalyst. *BMC Biochem. 6*, 26.

(76) Thibodeaux, C. J., Chang, W., and Liu, H. (2010) Linear free energy relationships demonstrate a catalytic role for the flavin mononucleotide coenzyme of the type II isopentenyl diphosphate:dimethylallyl diphosphate isomerase. *J. Am. Chem. Soc. 132*, 9994–9996.

(77) Cavelier, G., and Amzel, L. M. (2001) Mechanism of NAD(P)H:quinone reductase: ab initio studies of reduced flavin. *Proteins Struct. Funct. Genet. 43*, 420–432.

(78) Bhattacharyya, S., Stankovich, M. T., Truhlar, D. G., and Gao, J. (2007) Combined quantum mechanical and molecular mechanical simulations of one- and two-electron reduction potentials of flavin cofactor in water, medium-chain acyl-CoA dehydrogenase, and cholesterol oxidase. *J. Phys. Chem. A 111*, 5729–5742.

(79) Stankovich, M. T. (1991) Redox properties of flavins and flavoproteins, in *Chemistry and Biochemistry of Flavoenzymes* ((Müller, F., Ed.), pp 401–425. CRC Press, Boca Raton, FL.

(80) Massey, V. (2000) The chemical and biological versatility of riboflavin. *Biochem. Soc. Trans. 28*, 283–296.

(81) Eley, M., Lee, J., Lhoste, J. M., Lee, C. Y., Cormier, M. J., and Hemmerich, P. (1970) Bacterial bioluminescence. Comparisons of bioluminescence emission spectra, the fluorescence of luciferase reaction mixtures, and the fluorescence of flavin cations. *Biochemistry 9*, 2902–2908.

(82) Munro, A. W., and Noble, M. A. (1999) Fluorescence analysis of flavoproteins, in *Flavoprotein Protocols* (Chapman, K. S., and Reid, A. G., Eds.), pp 25–48. Humana

Press, Totowa, NJ.

(83) UN-SCAN-IT, version 7; graph digitizing software; Silk Scientific: Orem, UT 2013.

(84) Ghisla, S., Massey, V., Lhoste, J., and Mayhew, S. G. (1974) Fluorescence and optical characteristics of reduced flavines and flavoproteins. *Biochemistry 13*, 589–597.

(85) Visser, A. J., Ghisla, S., Massey, V., Müller, F., and Veeger, C. (1979) Fluorescence properties of reduced flavins and flavoproteins. *Eur. J. Biochem. 101*, 13–21.

(86) Ghisla, S. (1980) Fluorescence and optical characteristics of reduced flavins and flavoproteins. *Methods Enzymol. 66*, 360–373.

(87) Kao, Y.-T., Saxena, C., He, T.-F., Guo, L., Wang, L., Sancar, A., and Zhong, D. (2008) Ultrafast dynamics of flavins in five redox states. *J. Am. Chem. Soc. 130*, 13132–13139.

(88) Song, P.-S. (1971) Chemistry of flavins in their excited states, in *Flavins and Flavoproteins* (Kamin, H., Ed.), pp 37–61. University Park Press, Baltimore, MD.

(89) Christie, J. M. (2007) Phototropin blue-light receptors. *Annu. Rev. Plant Biol. 58*, 21–45.

(90) Cashmore, A. R., Jarillo, J. A., Wu, Y.-J., and Liu, D. (1999) Cryptochromes: blue light receptors for plants and animals. *Science 284*, 760–765.

(91) Gomelsky, M., and Klug, G. (2002) BLUF: a novel FAD-binding domain involved in sensory transduction in microorganisms. *Trends Biochem. Sci. 27*, 497–500.

(92) Barends, T. R. M., Hartmann, E., Griese, J. J., Beitlich, T., Kirienko, N. V, Ryjenkov, D. A, Reinstein, J., Shoeman, R. L., Gomelsky, M., and Schlichting, I. (2009) Structure and mechanism of a bacterial light-regulated cyclic nucleotide phosphodiesterase. *Nature 459*, 1015–1018.

(93) Van den Berg, P. A. W., Feenstra, K. A., Mark, A. E., Berendsen, H. J. C., and Visser, A. J. W. G. (2002) Dynamic conformations of flavin adenine dinucleotide: simulated molecular dynamics of the flavin cofactor related to the time-resolved fluorescence characteristics. *J. Phys. Chem. B 106*, 8858–8869.

(94) Li, G., and Glusac, K. D. (2009) The role of adenine in fast excited-state deactivation of FAD: a femtosecond mid-IR transient absorption study. *J. Phys. Chem. B 113*, 9059–9061.

(95) Heelis, B. P. F. (1982) The photophysical and photochemical properties of flavins (isoalloxazines). *Chem. Soc. Rev. 11*, 15–39.

(96) Wahl, P., Auchet, J. C., Visser, A. J. W. G., and Müller, F. (1974) Time resolved fluorescence of flavin adenine dinucleotide. *FEBS Lett. 44*, 67–70.

(97) Fritz, B. J., Matsui, K., Kasai, S., and Yoshimura, A. (1987) Triplet lifetimes of some flavins. *Photochem. Photobiol. 45*, 539–541.

(98) Heelis, P. F. (1991) The photochemistry of flavins, in *Chemistry and Biochemistry of Flavoenzymes* (Müller, F., Ed.), pp 171–193. CRC Press, Boca Raton, FL.

(99) Traber, R., Werner, T., Schreiner, S., Kramer, H. E. A., Knappe, W.-R., and Hemmerich, P. (1980) 1e- and 2e- Transfer in the photochemistry of flavins, in *Flavins and Flavoproteins* (Yagi, K., and Yamano, T., Eds.), pp 431–442. University Park Press, Baltimore, MD.

(100) Massey, V., Stankovich, M., and Hemmerich, P. (1978) Light-mediated reduction of flavoproteins with flavins as catalysts. *Biochemistry 17*, 1–8.

(101) Massey, V., and Hemmerich, P. (1978) Photoreduction of flavoproteins and other biological compounds catalyzed by deazaflavins. *Biochemistry 17*, 9–17.

(102) Ghisla, S., and Massey, V. (1986) New flavins for old: artificial flavins as active site probes of flavoproteins. *Biochem. J. 239*, 1–12.

(103) Massey, V., Ghisla, S., and Moore, E. G. (1979) 8-Mercaptoflavins as active site probes of flavoenzymes. *J. Biol. Chem. 254*, 9640–9650.

(104) Massey, V., Claiborne, A., Biemann, M., and Ghisla, S. (1984) 4-Thioflavins as active site probes of flavoproteins. *J. Biol. Chem. 259*, 9667–9678.

(105) Koehn, E. M., Fleischmann, T., Conrad, J. A, Palfey, B. A, Lesley, S. A, Mathews, I. I., and Kohen, A. (2009) An unusual mechanism of thymidylate biosynthesis in organisms containing the thyX gene. *Nature 458*, 919–923.

(106) Walsh, C. T. (1979) Enzymatic reaction mechanisms. W. H. Freeman and Company, San Francisco, CA.

(107) Francisco, Wilson, A., Abu-Soud, H. M., Topgi, R., Baldwin, T. O., and Raushel, F. M. (1996) Interaction of bacterial luciferase with 8-substituted flavin mononucleotide derivatives. *J. Biol. Chem. 271*, 104–110.

(108) Yorita, K., Misaki, H., Palfey, B. A, and Massey, V. (2000) On the interpretation of quantitative structure-function activity relationship data for lactate oxidase. *Proc. Natl. Acad. Sci. U.S.A. 97*, 2480–2485.

(109) Chaiyen, P., Sucharitakul, J., Svasti, J., Entsch, B., Massey, V., and Ballou, D. P. (2004) Use of 8-substituted-FAD analogues to investigate the hydroxylation mechanism

of the flavoprotein 2-methyl-3-hydroxypyridine-5-carboxylic acid oxygenase. *Biochemistry 43*, 3933–3943.

(110) Osten, D. W., and Kowalski, B. R. (1984) Multivariate curve resolution in liquid chromatography. *Anal. Chem. 56*, 991–995.

(111) Wehrens, R., Carvalho, E., Masuero, D., de Juan, A., and Martens, S. (2013) High-throughput carotenoid profiling using multivariate curve resolution. *Anal. Bioanal. Chem. 405*, 5075–5086.

(112) Jayaraman, A., Mas, S., Tauler, R., and de Juan, A. (2012) Study of the photodegradation of 2-bromophenol under UV and sunlight by spectroscopic, chromatographic and chemometric techniques. *J. Chromatogr. B 910*, 138–148.

(113) Seber, G. A. F., and Wild, C. J. (2003) Unconstrained optimization, in *Nonlinear Regression*, pp 587–618. John Wiley & Sons, Hoboken, NJ.

(114) Mebane, W. R., and Berkeley, U. C. (2011) Genetic optimization using derivatives: the rgenoud package for R. *J. Stat. Softw. 42*, 1–26.

(115) Dawson, R. M. C., Elliott, D. C., Elliott, W. H., and Jones, K. M. (Eds.). (1969) Data for biochemical research 2nd ed., pp 200–201. Oxford University Press, New York.

(116) Sekhon, J. S., and Mebane, W. R. (1998) Genetic optimization using derivatives. *Polit. Anal. 7*, 187–210.

(117) R Core Team (2013) R: a language and environment for statistical computing. R Foundation for Statistical Computing, Vienna, Austria. URL http://www.R-project.org/

(118) Mullen, K. M. (2012) ALS: multivariate curve resolution alternating least squares (MCR-ALS). R package version 0.0.5. URL http://CRAN.R-project.org/package=ALS

(119) Mullen, K. M. and van Stokkum I. H. M. (2012) nnls: the Lawson-Hanson algorithm for non-negative least squares (NNLS). R package version 1.4. URL http://CRAN.R-project.org/package=nnls

(120) Turner, R. (2013) Iso: functions to perform isotonic regression. R package version 0.0-15. URL http://CRAN.R-project.org/package=Iso

(121) Lumley, T. (2013) dichromat: color schemes for dichromats. R package version 2.0-0. http://CRAN.R-project.org/package=dichromat

(122) Tornoe, C. W. (2012) nlmeODE: non-linear mixed-effects modeling in nlme using differential equations. R package version 1.1. http://CRAN.R-project.org/package=nlmeODE

(123) Soetaert, K., and Petzoldt, T. (2010) Solving differential equations in R: package deSolve. *J. Stat. Softw. 33*, 1–25.

(124) Pinheiro, J., Bates, D., DebRoy, S., Sarkar, D., and the R Development Core Team (2013) nlme: linear and nonlinear mixed effects models. R package version 3.1-111.

(125) Sarkar, D. (2008) Lattice: multivariate data visualization with R. Springer, New York, NY.

(126) Walker, W. H., Hemmerich, P., and Massey, V. (1970) Light induced alkylation and dealkylation of the flavin nucleus. *Eur. J. Biochem. 13*, 258–266.

(127) Hevesi, L., and Bruice, T. C. (1972) 5 vs. 4a Addition to isoalloxazines. *J. Am. Chem. Soc. 94*, 8277–8278.

(128) Hemmerich, P., and Haas, W. (1975) Recent developments in the study of "fully reduced flavin" in *Reactivity of Flavins: The Proceedings of the Symposium Dedicated to the Late Professor Leonor Michaelis under the Auspices of the Japanese Biochemical Society* (Yagi, K., Ed.), pp 1–13. University of Tokyo Press, Tokyo.

(129) Ghisla, S., Massey, V., and Choong, Y. S. (1979) Covalent adducts of lactate oxidase. Photochemical formation and structure identification. *J. Biol. Chem. 254*, 10662–10669.

(130) Dudley, K. H., Ehrenberg, A., Hemmerich, P., and Müller, F. (1964) Spectra and structures of components of the flavin redox system. *Helv. Chim. Acta 47*, 1354–1383.

(131) Massey, V. (1994) Activation of molecular oxygen by flavins and flavoproteins. *J. Biol. Chem. 269*, 22459–22462.

(132) Kemal, C., Chan, T. W., and Bruice, T. C. (1977) Reaction of $^3O_2$ with dihydroflavins. 1. $N^{3,5}$-dimethyl-1,5-dihydrolumiflavin and 1,5-dihydroisoalloxazines. *J. Am. Chem. Soc. 99*, 7272–7286.

(133) Müller, F. (1983) The flavin redox-system and its biological function, in *Radicals in Biochemistry* (Boschke, F. L., Ed.), pp 71–107. Spring-Verlag, New York, NY.

(134) Sharma, N. K., and Poulter, C. D. (2013) Unpublished work.

(135) Ball, S., and Bruice, T. C. (1981) The chemistry of 1-carba-1-deaza-N5-ethyl-N3-methyllumiflavins. Influence of the N1 upon the reactivity of flavin 4a-hydroperoxides. *J. Am. Chem. Soc. 103*, 5494–5503.

(136) Dunn, J. D., Reid, G. E., and Bruening, M. L. (2010) Techniques for phosphopeptide enrichment prior to analysis by mass spectrometry. *Mass Spectrom. Rev. 29*, 29–54.

(137) Leitner, A. (2010) Phosphopeptide enrichment using metal oxide affinity chromatography. *Trends Anal. Chem. 29*, 177–185.

(138) Cuccurullo, M., Schlosser, G., Cacace, G., Malorni, L., and Pocsfalvi, G. (2007) Identification of phosphoproteins and determination of phosphorylation sites by zirconium dioxide enrichment and SELDI-MS/MS. *J. Mass Spectrom. 42*, 1069–1078.

(139) Gertler, G., Fleminger, G., and Rapaport, H. (2010) Characterizing the adsorption of peptides to TiO_2 in aqueous solutions by liquid chromatography. *Langmuir 26*, 6457–6463.

(140) Connor, P. A., and McQuillan, A. J. (1999) Phosphate adsorption onto TiO_2 from aqueous solutions: nn in situ internal reflection infrared spectroscopic study. *Langmuir 15*, 2916–2921.

(141) Larsen, M. R., Cordwell, S. J., and Roepstorff, P. (2002) Graphite powder as an alternative or supplement to reversed-phase material for desalting and concentration of peptide mixtures prior to matrix-assisted laser desorption/ionization-mass spectrometry. *Proteomics 2*, 1277–1287.

(142) Larsen, M. R., Graham, M. E., Robinson, P. J., and Roepstorff, P. (2004) Improved detection of hydrophilic phosphopeptides using graphite powder microcolumns and mass spectrometry. *Mol. Cell. Proteomics 3*, 456–465.

(143) Xing, J., Apedo, A., Tymiak, A., and Zhao, N. (2004) Liquid chromatographic analysis of nucleosides and their mono-, di- and triphosphates using porous graphitic carbon stationary phase coupled with electrospray mass spectrometry. *Rapid Commun. mass Spectrom. 18*, 1599–1606.

(144) Luo, W., Muller, J. G., Rachlin, E. M., and Burrows, C. J. (2000) Characterization of spiroiminodihydantoin as a product of one-electron oxidation of 8-oxo-7,8-dihydroguanosine. *Org. Lett. 2*, 613–616.

(145) Massey, V., Müller, F., Feldberg, R., Schuman, M., Sullivan, P. A., Howell, G., Mayhew, S. G., Rowena, G., and Foust, G. P. (1969) The reactivity of flavoproteins with sulfite. *J. Biol. Chem. 244*, 3999–4006.

(146) Müller, F., and Massey, V. (1969) Flavin-sulfite complexes and their structures. *J. Biol. Chem. 244*, 4007–4016.

(147) Mager, H. I. X., and Tu, S.-C. (1990) Dithionite treatment of flavins: spectral evidence for covalent adduct formation and effect on in vitro bacterial bioluminescence. *Photochem. Photobiol. 51*, 223–229.

(148) Heyerick, A., Huvaere, K., Keukeleire, D., and Forbes, M. D. E. (2005) Fate of flavins in sensitized photodegradation of isohumulones and reduced derivatives: studies

on formation of radicals via EPR combined with detailed product analyses. *Photochem. Photobiol. Sci. 4*, 412–419.

(149) Caballero, I., Blanco, C. A., and Porras, M. (2012) Iso-α-acids, bitterness and loss of beer quality during storage. *Trends Food Sci. Technol. 26*, 21–30.

(150) Hu, Y., Wang, K., and MacMillan, J. B. (2013) Hunanamycin A, an antibiotic from a marine-derived *Bacillus hunanensis*. *Org. Lett. 15*, 390–3.

(151) Jonnalagadda, V., Toth, K., and Richard, J. P. (2012) Isopentenyl diphosphate isomerase catalyzed reactions in D_2O: product release limits the rate of this sluggish enzyme-catalyzed reaction. *J. Am. Chem. Soc. 134*, 6568–6570.

(152) Yamashita, S., Hemmi, H., Ikeda, Y., Nakayama, T., and Nishino, T. (2004) Type 2 isopentenyl diphosphate isomerase from a thermoacidophilic archaeon *Sulfolobus shibatae*. *Eur. J. Biochem. 271*, 1087–1093.

(153) Rohmer, M., Grosdemange-Billiard, C., Seemann, M., and Tritsch, D. (2004) Isoprenoid biosynthesis as a novel target for antibacterial and antiparasitic drugs. *Curr. Opin. Investig. Drugs 5*, 154–162.

(154) Zhang, B., Watts, K. M., Hodge, D., Kemp, L. M., Hunstad, D. A., Hicks, L. M., and Odom, A. R. (2011) A second target of the antimalarial and antibacterial agent fosmidomycin revealed by cellular metabolic profiling. *Biochemistry 50*, 3570–3577.

(155) Andreassi, J. L., Dabovic, K., and Leyh, T. S. (2004) *Streptococcus pneumoniae* isoprenoid biosynthesis is downregulated by diphosphomevalonate: an antimicrobial target. *Biochemistry 43*, 16461–16466.

(156) Kudoh, T., Park, C. S., Lefurgy, S. T., Sun, M., Michels, T., Leyh, T. S., and Silverman, R. B. (2010) Mevalonate analogues as substrates of enzymes in the isoprenoid biosynthetic pathway of *Streptococcus pneumoniae*. *Bioorg. Med. Chem. 18*, 1124–1134.

(157) Hersh, B. L. B., and Walsh, C. (1980) Preparation, characterization, and coenzymic properties of 5-carba-5-deaza and 1-carba-1-deaza analogs of riboflavin, FMN, and FAD. *Methods Enzymol. 66*, 277–287.

(158) Segel, I. H. (1975) Enzyme kinetics, pp 274–329, 401. John Wiley & Sons, New York, NY.

(159) Baty, F., and Delignette-Muller, M. L. (2012) nlstools: tools for nonlinear regression diagnostics. R package version 0.0-13.

(160) Graffelman, J. (2012) calibrate: calibration of scatterplot and biplot axes. R package version 1.7.1.

(161) Markham, K. A, Steven Sikorski, R., and Kohen, A. (2003) Purification, analysis, and preservation of reduced nicotinamide adenine dinucleotide 2′-phosphate. *Anal. Biochem. 322*, 26–32.

(162) Wu, J. T., Wu, L. H., and Knight, J. A. (1986) Stability of NADPH: effect of various factors on the kinetics of degradation. *Clin. Chem. 32*, 314–319.

(163) De Ruyck, J., Janczak, M. W., Neti, S. S., Rothman, S. C., Schubert, H. L., Cornish, R. M., Matagne, A., Wouters, J., and Poulter, C. D. (2014) Determination of kinetics and the crystal structure of a novel type 2 isopentenyl diphosphate:dimethylallyl diphosphate isomerase from *Streptococcus pneumoniae*. *ChemBioChem 15*, 1452-1458.

(164) Filisetti, L., Fontecave, M., and Niviere, V. (2003) Mechanism and substrate specificity of the flavin reductase ActVB from *Streptomyces coelicolor*. *J. Biol. Chem. 278*, 296–303.

(165) Russell, T. R., Demeler, B., and Tu, S. (2004) Kinetic mechanism and quaternary structure of *Aminobacter aminovorans* NADH:flavin oxidoreductase: an unusual flavin reductase with bound flavin. *Biochemistry 43*, 1580–1590.

(166) Johnston, J. B., Walker, J. R., Rothman, S. C., and Poulter, C. D. (2007) Type-2 isopentenyl diphosphate isomerase. Mechanistic studies with cyclopropyl and epoxy analogs. *J. Am. Chem. Soc. 129*, 7740-7741.

(167) Heaps, N. A. Synthesis and evaluation of alternative substrates for farnesyl diphosphate synthase and isopentenyl diphosphate isomerase. Ph.D. Dissertation, University of Utah, Salt Lake City, UT, December 2008.

(168) Fromm, H. J. (1979) Use of competitive inhibitors to study substrate binding order. *Methods Enzymol. 63*, 467–486.

(169) Hoshino, T., and Eguchi, T. (2007) Functional analysis of type 1 isopentenyl diphosphate isomerase from *Halobacterium sp.* NRC-1. *Biosci. Biotechnol. Biochem. 71*, 2588–2591.

(170) Weiss, J. N. (1997) The hill equation revisited: uses and misuses. *FASEB J. 11*, 835–841.

(171) Thulasiram, H. V, Erickson, H. K., and Poulter, C. D. (2007) Chimeras of two isoprenoid synthases catalyze all four coupling reactions in isoprenoid biosynthesis. *Science 316*, 73–76.

(172) Nguyen, U. T. T., Goody, R. S., and Alexandrov, K. (2010) Understanding and exploiting protein prenyltransferases. *ChemBioChem 11*, 1194–1201.

(173) Dolence, J. M., and Poulter, C. D. (1995) A mechanism for posttranslational

modifications of proteins by yeast protein farnesyltransferase. *Proc. Natl. Acad. Sci. U.S.A. 92*, 5008–5011.

(174) Pais, J. E., Bowers, K. E., and Fierke, C. A. (2006) Measurement of the α-secondary kinetic isotope effect for the reaction catalyzed by mammalian protein farnesyltransferase. *J. Am. Chem. Soc. 128*, 15086–15087.

(175) Weller, V. A., and Distefano, M. D. (1998) Measurement of the α -secondary kinetic isotope effect for a prenyltransferase by MALDI mass spectrometry. *J. Am. Chem. Soc. 120*, 7975–7976.

(176) Huang, C., Hightower, K. E., and Fierke, C. A. (2000) Mechanistic studies of rat protein farnesyltransferase indicate an associative transition state. *Biochemistry 39*, 2593–2602.

(177) Sousa, S. F., Fernandes, P. A., and Ramos, M. J. (2009) The search for the mechanism of the reaction catalyzed by farnesyltransferase. *Chem. A Eur. J. 15*, 4243–4247.

(178) Yang, Y., Wang, B., Ucisik, M. N., Cui, G., Fierke, C. A, and Merz, K. M. (2012) Insights into the mechanistic dichotomy of the protein farnesyltransferase peptide substrates CVIM and CVLS. *J. Am. Chem. Soc. 134*, 820–823.

(179) Fisher, H. F., and Saha, S. K. (1996) Interpretation of transient-state kinetic isotope effects. *Biochemistry 35*, 83–88.

(180) Fisher, H. F., Palfey, B. A, Maniscalco, S. J., and Indyk, L. (2006) Relationship between the time-dependence of a transient-state kinetic isotope effect and the location of complexes in a reaction sequence. *J. Phys. Chem. A 110*, 4465–4472.

(181) Canty, A., and Ripley, B. (2013) boot: bootstrap R (S-plus) functions. R package version 1.3-9.

(182) Davison, A. C., and Hinkley, D. V. (1997) Bootstrap methods and their applications. Cambridge University Press, Cambridge.

(183) Wickham, H. (2009) ggplot2: elegant graphics for data analysis. Springer US, New York, NY.

(184) Baddeley, A., and Turner, R. (2005) spatstat: an R package for analyzing spatial point patterns. *J. Stat. Softw. 12*, 1–42.

(185) Efron, B. (1979) Bootstrap methods: another look at the jackknife. *Ann. Stat. 7*, 1–26.

(186) Felsenstein, J. (1985) Confidence limits on phylogenies: an approach using the

bootstrap. *Evolution 39*, 783–791.

(187) Preacher, K. J., and Hayes, A. F. (2008) Asymptotic and resampling strategies for assessing and comparing indirect effects in multiple mediator models. *Behav. Res. Methods 40*, 879–891.

(188) MacKinnon, J. G. (2006) Bootstrap methods in econometrics. *Econ. Rec. 82*, S2–S18.

(189) Meyer, J. S., Ingersoll, C. G., McDonald, L. L., and Boyce, M. S. (1986) Estimating uncertainty in population growth rates: jackknife vs. bootstrap. *Ecology 67*, 1156–1166.

(190) Maniscalco, S. J., Saha, S. K., Vicedomine, P., and Fisher, H. F. (1996) A difference in the sequence of steps in the reactions catalyzed by two closely homologous forms of glutamate dehydrogenase. *Biochemistry 35*, 89–94.

(191) Saha, S. K., Maniscalco, S. J., and Fisher, H. F. (1996) Mechanistic interpretation of tryptophan fluorescence quenching in the time courses of glutamate dehydrogenase catalyzed reactions. *Biochemistry 35*, 16483–16488.

(192) Parkin, D. W. (1991) Methods for the determination of competitive and noncompetitive kinetic isotope effects, in *Enzyme Mechanism from Isotope Effects* (Cook, P. F., Ed.), pp 269–290. CRC Press, Boca Raton, FL.

(193) Ali, J. A., and Lohman, T. M. (1997) Kinetic measurement of the step size of DNA unwinding by *Escherichia coli* UvrD helicase. *Science 275*, 377–380.

(194) Anderson, K. S., Milesll, E. W., and Johnson, K. A. (1991) Serine modulates substrate channeling in tryptophan synthase. *J. Biol. Chem. 266*, 8020–8033.

(195) Fenner, H., Grauert, R., Hemmerich, P., Michel, H., and Massey, V. (1979) 5-Thia-5-deazaflavin, a 1e$^-$-transferring flavin analog. *Eur. J. Biochem. 95*, 183–191.

(196) Edmondson, D., and Ghisla, S. Flavoenzyme structure and function, in *Flavoprotein Protocols* (Chapman, K. S., and Reid, A. G., Eds.), pp 157–179. Humana Press, Totowa, NJ.

(197) Moore, E. G., Ghisla, S., and Massey, V. (1979) Properties of flavins where the 8-methyl group is replaced by mercapto- residues. *J. Biol. Chem. 254*, 8173–8178.

(198) Eckstein, J. W., Hastings, J. W., and Ghisla, S. (1993) Mechanism of bacterial bioluminescence: 4a,5-dihydroflavin analogs as models for luciferase hydroperoxide intermediates and the effect of substituents at the 8-position of flavin on luciferase kinetics. *Biochemistry 32*, 404–411.

(199) Murthy, Y. V. S. N., and Massey, V. (1998) Synthesis and properties of 8-CN-flavin nucleotide analogs and studies with flavoproteins. *J. Biol. Chem. 273*, 8975–8982.

(200) Light, D. R., and Walsh, C. (1980) Flavin analogs as mechanistic probes of adrenodoxin reductase-dependent electron transfer to the cholesterol side chain cleavage cytochrome P-450 of the adrenal cortex. *J. Biol. Chem. 255*, 4264–4277.

(201) Walsh, C., Fisher, J., Spencer, R., Graham, D. W., Ashton, W. T., Brown, J. E., Brown, R. D., and Rogers, E. F. (1978) Chemical and enzymatic properties of riboflavin analogues. *Biochemistry 17*, 1942–1951.

(202) Mansurova, M., Koay, M. S., and Gärtner, W. (2008) Synthesis and electrochemical properties of structurally modified flavin compounds. *European J. Org. Chem. 2008*, 5401–5406.

(203) Ghisla, S., and Mayhew, S. G. (1976) Identification and properties of 8-hydroxyflavin-adenine dinucleotide in electron-transferring flavoprotein from *Peptostreptococcus elsdenii*. *Eur. J. Biochem. 63*, 373–390.